



HAL
open science

3D-hyperspectral imaging and optical analysis of skin for the human face

Lou Gevaux

► **To cite this version:**

Lou Gevaux. 3D-hyperspectral imaging and optical analysis of skin for the human face. Optics [physics.optics]. Université de Lyon, 2019. English. NNT : 2019LYSES035 . tel-02881115

HAL Id: tel-02881115

<https://theses.hal.science/tel-02881115v1>

Submitted on 25 Jun 2020

HAL is a multi-disciplinary open access archive for the deposit and dissemination of scientific research documents, whether they are published or not. The documents may come from teaching and research institutions in France or abroad, or from public or private research centers.

L'archive ouverte pluridisciplinaire **HAL**, est destinée au dépôt et à la diffusion de documents scientifiques de niveau recherche, publiés ou non, émanant des établissements d'enseignement et de recherche français ou étrangers, des laboratoires publics ou privés.



NNT: 2019LYSES035

PHD THESIS OF THE LYON UNIVERSITY

Jean Monnet University

Doctoral school N° 488
Sciences, Ingénierie, Santé

Publicly defended on the 16/10/2019, by:

Lou GEVAUX

3D-hyperspectral imaging and optical analysis of skin for the human face

In front of the jury composed by:

ANDRAUD Christine, Muséum National d'Histoire Naturelle,

GIOUX Sylvain, University of Strasbourg,

HARDEBERG Jon Yngve, Norwegian University of Science and Technology,

HEBERT Mathieu, Jean Monnet University,

CLERC Raphael, Institut d'Optique Graduate school,

TREMEAU Alain, Jean Monnet University,

DELAVAL Jean Michel, Newton Technologies,

SEROUL Pierre, Bull Atos Technologies,

Reporter

Reporter

Examiner

Director

Co-supervisor

Co-supervisor

Invited guest

Invited guest



N°d'ordre NNT : 2019LYSES035

THESE DE DOCTORAT DE L'UNIVERSITE DE LYON

Université Jean Monnet

Ecole doctorale N° 488
Sciences, Ingénierie, Santé

Soutenue publiquement le 16/10/2019, par :

Lou GEVAUX

Imagerie hyperspectrale 3D et analyse optique de la peau pour le visage humain

Devant le jury composé de:

ANDRAUD Christine, Muséum National d'Histoire Naturelle,

GIOUX Sylvain, Université de Strasbourg,

HARDEBERG Jon Yngve, Norwegian University of Science and Technology,

HEBERT Mathieu, Université Jean Monnet,

CLERC Raphael, Institut d'Optique Graduate school,

TREMEAU Alain, Université Jean Monnet,

DELAVAL Jean Michel, Newton Technologies,

SEROUL Pierre, Bull Atos Technologies,

Rapporteur

Rapporteur

Examinateur

Directeur

Co-encadrant

Co-encadrant

Invité

Invité

Funding

This work has been funded by the Région Auvergne-Rhône-Alpes, under the ARC 6 grant, and carried out in partnership with Newton Technologies.



We would like to thank Jean Luc Perrot (CHU Saint-Etienne) and Hugues Favrelière (SYMME, Université de Savoie) for their participation.



Example of skin translucency in art.
Joseph the Carpenter, Georges de La Tour
(Louvre, Paris)

Acknowledgements

First of all, I would like to express my gratitude to Mathieu Hébert, Pierre Sérout, Alain Trémeau and Raphael Clerc, who initiated this PhD project, for entrusting me with this project at Laboratoire Hubert Curien and Newton Technologies, and for patiently guiding me these last three years. I would like to especially acknowledge Mathieu Hébert, the director of my PhD, for his steadfast support, enthusiasm, creativity and scientific rigor, and Raphael Clerc, for his punctilious instruction and for his fastidious input, particularly pertaining to optical modeling.

I would like to acknowledge the members of the jury. Thank-you to Christine Andraud and Sylvain Gioux for agreeing to report this PhD manuscript, and for dedicating the time to read this work. I would also like to thank Jon Yngve Hardeberg for traveling to Saint-Etienne to attend my PhD defense as an examiner.

Additional thanks go to Jean Michel Delaval, owner and CEO of Newton Technologies, for welcoming me into his company, and for the freedom and trust he gave me in this project. A huge thank-you to the lab and imaging teams as well for their precious help. Without their expertise in prototyping, their aid in coding in C++ and their support in image processing, the project could not have been brought to completion. I am especially grateful to Marie Cherel, who allowed me to take hyperspectral images of her and use them in our communications about the project. I would like to thank the entire Newton team for all the moments we spent together, both during and outside working hours. Were it not for the exigencies of brevity, I would mention each of you by name; but rest assured, you have all become much more to me than mere colleagues.

I would like to acknowledge a number of other researchers and students that I've had the pleasure to work with at Laboratoire Hubert Curien and within the wider material appearance and skin optics community: Dorian Saint-Pierre, Nicolas Dalloz, Lionel Simonot, Anthony Cazier, Caroline Ponte, Emmanuel Marin, Loïc Denis, Jean Luc Perrot and Hugues Favrelière. I have learnt so much by working and conversing with you, and will keep great memories of the moments spent together at the lab and at conferences.

Finally, I would like to thank my family and friends for their unwavering encouragement, for always lending an attentive ear, and for their good-humored advice during this adventure. I reserve the final words of these acknowledgements for Simon. Thank you for proof-reading this manuscript, more than once. Thank you for proof reading most of my work, more times than I can count. And thank you for everything that has nothing to do with this PhD. I am forever in your debt.

Abstract

Hyperspectral imaging, a non-invasive, in vivo imaging method that can be applied to measure skin spectral reflectance, has shown great potential for the analysis of skin optical properties on small, flat areas: by combining a skin model, a model of light-skin interaction and an optimization algorithm, an estimation of skin chromophore concentration in each pixel of the image can be obtained, corresponding to quantities such as melanin and blood. The purpose of this work is to extend this method to large, non-flat areas, in particular the human face. The accurate measurement of complex objects such as the face must account for variances of illumination that result from the three-dimensional geometry of an object, which we call irradiance drifts. Unless they are accounted for, irradiance drifts will lead to errors in the hyperspectral image analysis.

In the first part of the work, we propose an extended measurement setup, comprising a wide field hyperspectral camera (with an acquisition range of 400 nm to 700 nm, in 10 nm width wavebands) and a 3D measurement system using fringe projection. As short acquisition time is crucial for in vivo measurement, a trade-off between resolution and speed has been made so that the acquisition time remains under 5 seconds.

To account for irradiance drifts, a correction method using the 3D geometry of the surface and radiometry principles is proposed. The irradiance received on the face is computed for each pixel of the image, and the resulting data used to suppress the irradiance drifts in the measured hyperspectral image. This acts as a pre-processing step to be applied before image analysis. This correction method, however, failed to yield satisfactory results on those parts of the face almost perpendicular to the optical axis of the camera, such as the sides of the nose, and was therefore discarded in favor of using an optimization algorithm robust to irradiance drifts in the analysis method.

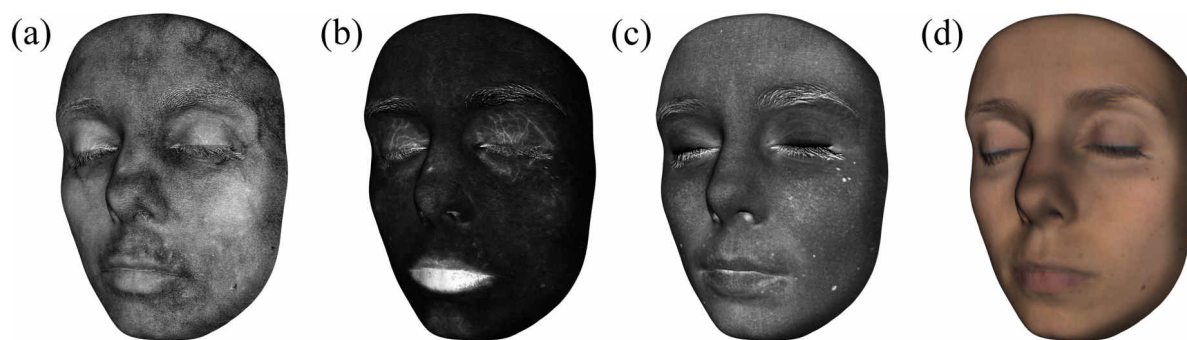


Figure 0.1. 3D hyperspectral acquisition results: (a) oxygen rate, (b) blood volume fraction, (c) melanin concentration, and (d) color.

Skin analysis from the measured hyperspectral image is performed using optical models and an optimization method. Skin is modeled as a two-layer translucent material whose absorption and scattering properties are determined by its composition in chromophores. Light-skin interactions are modeled using a two-flux method. An inverse problem is solved by optimization to retrieve information about skin composition from the measured reflectance. The chosen optical models represent a trade-off between accuracy and acceptable computation time, which increases exponentially with the number of parameters in the model. The resulting chromophore maps can be added to the 3D mesh measured using the 3D-hyperspectral camera for display purposes, as shown in Figure 0.1.

In the spectral reflectance analysis method, skin scattering properties are assumed to be the same for everyone and on every part of the body, which represents a shortcoming. In the second part of this work, the fringe projector originally intended for measuring 3D geometry is used to acquire skin modulation transfer function (MTF), a quantity that yields information about both skin absorption and scattering coefficients. The MTF is measured using spatial frequency domain imaging (SFDI) and analyzed by an optical model that relies on the diffusion equation to estimate skin scattering coefficients. On non-flat objects, retrieving such information independently from irradiance drifts is a significant challenge. The novelty of the proposed method is that it combines hyperspectral imaging and SFDI to obtain skin scattering coefficient maps of the face independently from its shape.

We emphasize throughout this dissertation the importance of short acquisition time for in vivo measurement. The hyperspectral image analysis method, however, is extremely time-consuming, preventing real time image analysis. A preliminary attempt to address this shortcoming is presented, using neural networks to replace optimization-based analysis. Initial results of the method have been promising, and could drastically reduce calculation time from around an hour to a second.

Résumé

L'imagerie hyperspectrale, une méthode non invasive permettant de mesurer in vivo la réflectance spectrale, a démontré son fort potentiel pour l'analyse des propriétés optiques de la peau pour des zones planes et de petite taille : l'association d'un modèle optique de peau, d'une modélisation de ses interactions avec la lumière et d'une méthode d'optimisation permet d'analyser l'image hyperspectrale en chaque pixel et d'estimer des cartographies de concentrations en chromophores, comme la mélanine et le sang. Le but de ce travail est l'extension de la méthode pour la mesure et l'analyse de surfaces larges et non planes, et en particulier du visage humain. Les mesures d'objets complexes comme le visage sont affectées par des variations spatiales d'éclairement, que l'on appelle dérives d'éclairement. Les dérives d'éclairement créent des erreurs dans l'analyse des images hyperspectrales, à moins que celles-ci soient prises en compte dans le modèle.

Dans la première partie de ce travail, nous proposons une évolution du système d'acquisition, qui inclut une caméra hyperspectrale grand-champ (permettant l'acquisition de bandes spectrales de 10 nm de largeur entre 400 et 700 nm) et un système d'acquisition de la géométrie 3D basé sur la projection de franges. Une acquisition courte étant cruciale pour les mesures in vivo, un compromis entre résolution et vitesse d'acquisition a été trouvé pour que le temps d'acquisition soit inférieur à 5 secondes.

La caméra hyperspectrale a été combinée avec un scanner 3D dans le but de proposer une méthode de correction des dérives d'éclairement utilisant la géométrie 3D et des principes de radiométrie. L'éclairement reçu par le visage en chaque pixel de l'image est calculé puis cette valeur est utilisée pour supprimer les dérives d'éclairement dans l'image hyperspectrale. Ceci constitue une étape de prétraitement à appliquer avant l'analyse de l'image hyperspectrale. Cependant, les résultats de cette méthode ne sont pas satisfaisants sur les zones du visage qui sont pratiquement perpendiculaires à l'axe optique de la caméra, comme les côtés du nez. La méthode a donc été rejetée en faveur de l'utilisation d'un algorithme d'optimisation robuste aux dérives d'éclairement dans la méthode d'analyse.

L'analyse de la peau à partir des images hyperspectrales est basée sur l'utilisation de modèles optiques et d'une méthode d'optimisation. La peau est modélisée comme un matériau translucide à deux couches, dont les propriétés d'absorption et de diffusion dépendent de sa composition en chromophores. Les interactions entre la peau et la lumière sont modélisées à l'aide d'une approche à deux flux. La résolution d'un problème inverse par optimisation permet de retrouver de l'information sur la composition de la peau en chromophores à partir de la réflectance spectrale mesurée. Les modèles optiques choisis sont un bon compromis entre une description fidèle de la peau et un temps de calcul acceptable.

Ce dernier augmente de manière exponentielle lorsque le nombre de paramètres du modèle augmente. Les cartes de chromophores estimées peuvent être affichées sous forme 3D lorsque cette information a été mesurée à l'aide de la caméra 3D-hyperspectrale, comme illustré en Figure 0.1.

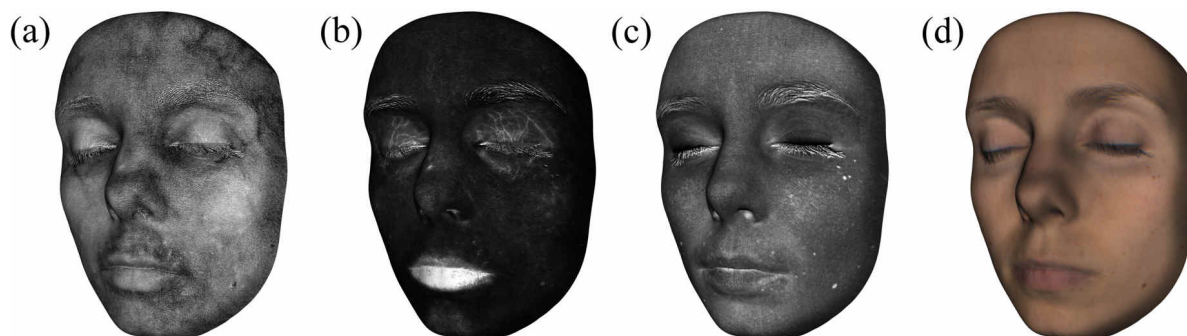


Figure 0.1. 3D hyperspectral acquisition results: (a) oxygen rate, (b) blood volume fraction, (c) melanin concentration, and (d) color.

Un point faible de la méthode d'analyse de la réflectance spectrale est le manque d'information sur les propriétés de diffusion de la peau, considérées comme identiques d'une personne à l'autre, et d'une partie du corps à l'autre. Dans la seconde partie de ce travail, nous utilisons le projecteur de franges, initialement dédié à l'acquisition 3D, pour mesurer la fonction de transfert de modulation (FTM) de la peau, qui fournit de l'information à la fois sur les propriétés d'absorption et de diffusion. La FTM est mesurée par imagerie dans le domaine des fréquences spatiales (SFDI) et analysée à l'aide d'un modèle optique reposant sur l'équation de la diffusion dans le but d'estimer le coefficient de diffusion de la peau. Sur des objets non-plats, l'extraction d'information indépendamment des dérives d'éclairage est un défi important. L'originalité de la méthode proposée repose sur l'association de l'imagerie hyperspectrale et de la SFDI dans le but d'estimer des cartes de coefficient de diffusion sur le visage indépendamment de sa forme.

Nous insistons régulièrement sur l'importance du temps d'acquisition court pour des mesures *in vivo*, cependant, l'analyse des données par optimisation demande plusieurs heures de calcul, ce qui empêche l'utilisation de la méthode en temps réel. Afin de lever cette limitation, nous nous sommes penchés sur l'utilisation des réseaux de neurones, dans le but de remplacer la méthode d'analyse par optimisation. Les premiers résultats ont montré la possibilité de fortement réduire le temps de calcul, d'environ une heure à une seconde.

Le mémoire est structuré en 10 chapitres :

Le premier chapitre, l'introduction, présente les enjeux de ce projet et permet de le situer dans son contexte applicatif ;

Le chapitre 2 rappelle les définitions et lois d'optiques utiles à la compréhension de la mesure et de la modélisation optique des matériaux translucides ;

Le chapitre 3 rappelle la structure et composition de la peau, ses propriétés optiques et la façon dont elle peut être mesurée optiquement ;

Le chapitre 4 présente le système d'acquisition hyperspectral grand-champ et le chapitre 5 présente le scanner 3D associé à la caméra hyperspectrale. Les performances de ces deux systèmes sont discutées en détails ;

Le chapitre 6 expose une méthode de correction des dérives d'éclairement dont la validité est discutée;

Le chapitre 7 détaille la méthode d'analyse des images hyperspectrales qui permet d'estimer des cartographies de concentration en chromophore.

Le chapitre 8 présente la méthode de mesure de la translucidité de la peau par imagerie dans le domaine des fréquences spatiales, qui peut être associée à la caméra hyperspectrale, et le chapitre 9 présente la méthode d'analyse des mesures SFDI, permettant d'estimer des cartographies du coefficient d'absorption ;

Les conclusions et perspectives de ce travail sont énoncées dans le chapitre 10.

Table of contents

Chapter 1. Introduction	21
Chapter 2. Bases of optics for the measurement and modeling of translucent materials.....	27
2.1. Basic radiometry concepts	28
2.1.a. Solid angle and geometrical extent	28
2.1.b. Radiometry quantities	29
2.2. Radiometry definitions for surfaces	30
2.2.a. Reflectance.....	31
2.2.b. BRDF and BSSRDF	32
2.2.c. Point spread function and modulation transfer function	34
2.3. Surface and volume light interactions for translucent materials	35
2.3.a. Surface reflection	35
2.3.b. Subsurface interactions	36
2.3.c. Multilayer materials.....	38
2.3.d. Light polarization	38
2.4. Modeling light propagation within random particle media.....	39
2.4.a. The radiative transfer theory.....	40
2.4.b. The diffusion approximation.....	43
2.4.c. The Kubelka-Munk model	46
2.4.d. Monte Carlo.....	48
2.5. Conversion of spectral information into color.....	49
2.6. Conclusion	52
Chapter 3. The optical study of human skin	53
3.1. Physiological structure and composition of skin.....	53
3.2. Skin optical properties.....	56
3.2.a. Skin absorption coefficient.....	57
3.2.b. Skin scattering coefficient	58
3.3. Skin study using optical methods.....	58

3.3.a.	Skin punctual acquisition.....	59
3.3.b.	Skin imaging	61
3.3.c.	Skin temporal variations.....	63
3.4.	Conclusion	64
Chapter 4. Capturing wavelength selective information: Hyperspectral imaging (HSI).....		65
4.1.	Spectral imaging methods.....	66
4.1.a.	Acquisition methods	67
4.1.b.	Spectral imaging of the body	70
4.2.	Full face hyperspectral camera	72
4.2.a.	Acquisition setup and software.....	72
4.2.b.	Calibration.....	77
4.3.	Efficacy of the method and acquisitions on skin.....	78
4.3.a.	Acquisition speed, resolution and accuracy of the method	78
4.3.b.	Skin hyperspectral imaging.....	81
4.4.	Conclusion	84
Chapter 5. Measuring non-flat parts of the body: 3D scanning.....		85
5.1.	Optical methods for 3D scanning	86
5.1.a.	Passive methods.....	87
5.1.b.	Active methods	88
5.1.c.	Body 3D scanning.....	89
5.2.	Full face 3D scanner using fringe projection.....	90
5.2.a.	Acquisition setup and software.....	92
5.2.b.	Triangulation principle	94
5.2.c.	Phase shift principle	95
5.2.d.	Phase unwrapping.....	97
5.2.e.	Radiometric calibration	101
5.2.f.	Geometric calibration	103
5.3.	Full face 3D geometry measurement	105
5.3.a.	3D meshes displayed with texture	105
5.3.b.	Acquisition speed, resolution and accuracy of the method	107
5.4.	Conclusion	112

Chapter 6. Measuring the spectral reflectance of curved surfaces: irradiance drift correction	113
6.1. Irradiance correction methods for simple and complex configurations	115
6.1.a. Analytical formula for the point source correction method	115
6.1.b. Implementation of the method.....	118
6.1.c. Case of a complex illumination geometry	121
6.2. Irradiance correction on hyperspectral images.....	123
6.3. Going further: using imaging methods to estimate skin BRDF.....	126
6.4. Conclusion	128
Chapter 7. Chromophore map estimation from HSI analysis	129
7.1. Model-based estimation of chromophore maps	130
7.1.a. Skin model	130
7.1.b. Light-skin interactions model.....	132
7.1.c. Resolution of the inverse problem using an optimization	135
7.2. Full face spectral reflectance analysis	136
7.2.a. Robustness of the analysis method: theoretical study.....	139
7.2.b. Experimental validation of the method	146
7.2.c. Discussion	150
7.3. Going further: using artificial neural networks for skin chromophore map estimation	151
7.3.a. Architecture of the artificial neural network.....	151
7.3.b. Training dataset and process	153
7.3.c. Estimated chromophore maps.....	157
7.3.d. Discussions.....	158
7.4. Conclusion	159
Chapter 8. Measuring skin translucency: Spatial frequency domain imaging (SFDI)	161
8.1. Full face SFDI system	163
8.1.a. Acquisition setup and software	163
8.1.b. Multiple frequency contrast measurement using a projector	165
8.1.c. Calibration and normalization	167
8.2. SFDI acquisition on phantom samples and skin.....	168
8.2.a. Milk samples	168
8.2.b. Wax samples.....	169

8.2.c. Skin.....	171
8.3. Efficacy of the method.....	174
8.4. Conclusion	176
Chapter 9. Scattering map estimation from SFDI analysis	177
9.1. MTF model using the diffusion approximation	178
9.2. MTF analysis for a full face.....	183
9.3. Experimental measurement analysis.....	186
9.3.a. Phantom SFDI measurement.....	186
9.3.b. Face measurement using HSI and SFDI	190
9.3.c. Discussion on the limitations of the method.....	193
9.3.d. Using μ_s' maps to improve the analysis of hyperspectral images?.....	194
9.4. Going further: “seeing” through a scattering material by using deconvolution techniques.....	195
9.5. Conclusion	196
Chapter 10. Conclusion	199
Appendix 1: Reproduction of Figure 4.18	203
Appendix 2: Reproduction of Figure 7.5.....	204
Communications	205
References.....	207

Chapter 1.

Introduction

Skin, by which we interface with the environment, plays an important role in protecting our body against pathogens, regulating our temperature, synthesizing vitamin D, and mediating sensation. When skin is damaged or afflicted by disease, the consequences can be painful, debilitating or even fatal, making the identification and treatment of skin injuries and pathologies a major public health issue. From a sociological perspective, our skin is one of the first things others notice about us and plays an important role in the perception of a person's beauty, health and age [Mattis et al. 2007]. Our collective fascination in the way our skin looks is such that an estimated 140 billion dollars are spent every year on cosmetology products. It is no surprise then, that the study of human skin has been an important field of research for some time, spanning the fields of medicine, dermatology, cosmetology, but also in entertainment and art. In painting, for example, the faithful reproduction of skin color has long been a challenge for artists, with even a dedicated name in French, *carnation*, literally meaning *skin tone* [Magnain 2009]. Using glazing and *sfumato*, Leonardo Da Vinci was able to achieve in the *Mona Lisa* skin tones that are very similar to actual skin not only in terms of color but also in terms of spectral reflectance [Elias and Cotte 2008]. This shows the capacity of human observers to perceive much more than what a RGB-color camera captures, perhaps because we are used to observing skin under different spectral illuminations. Returning to a biological perspective of skin, we are also able to instinctively judge whether a person is living a healthy lifestyle or not from looking at their skin color, most likely because the eye is capable of capturing a light signal that is richer than RGB-color. The spectral dimension of skin color is therefore crucial to its accurate description, and skin color cannot be reduced to tri-chromatic color only.

The evaluation of skin in dermatology and cosmetology

Throughout much of the history of dermatology and cosmetology, skin study has mainly been conducted through visual inspection by specialists. Occasionally, this has been complemented by invasive biopsy to better understand skin cellular structure or to decide

on the benignity or malignancy of a lesion. Relying on human assessment only, however, is susceptible to certain shortcomings: it requires highly trained assessors whose time is both in demand and costly; it is limited to what is visible at the skin surface; and some evaluations are difficult to perform, such as accurately estimating the color of a lesion, or quantifying change over time. The development of tools for measuring skin in recent decades has proved invaluable to supplementing the judgments of the specialists as well as making the study of skin easier, by revealing information that is difficult to assess or that remains invisible to the naked eye.

Challenges of skin optical measurement

Skin measurement, however, presents many challenges, as skin is alive, soft, with a non-flat surface and a complex structure and composition. In particular, methods that require applying pressure to the skin invariably modify its properties, and in the case of in vitro measurements, these properties are even more drastically altered. In light of this, the use of optical methods for skin analysis has grown markedly in recent years, as they allow for non-invasive, in vivo and non-contact measurements. In vivo measurements have real advantages over in vitro measurements as they are less invasive for the patient. Non-contact solutions are also preferable over contact methods because the measurements they yield cannot be affected by how much pressure is applied by the operator.

Among contactless methods, imaging methods have shown particular promise. Unlike punctual methods, which provide an average value over a certain area, imaging can be applied to heterogeneous materials and yields quantitative information as well as shape information. As such, skin images can be analyzed using automatic computation, or can be used as a supplement to visual inspection by a specialist. Many imaging methods for skin study are now available, with examples given in Chapter 3. These methods are neither equivalent nor interchangeable; rather, each is adapted to a specific range of purposes, for which their resolution and field of view is adapted. For example, the method that is best-adapted to study the cellular structure of a melanoma differs from that which is best-suited to assess the efficacy of a cosmetic product made to reduce skin redness. Or to give another example, a method that is used to study skin cells is likely to have a very high resolution, but a field of view that is less than a few mm²; conversely, an imaging system designed to study skin at a full body scale is more limited in terms of resolution.

Context of the project: from research to application

The project has been developed in collaboration with an industrial partner, Newton Technologies (Lyon, France). The core business of Newton Technologies is the development of image acquisition methods and analysis algorithms to evaluate the efficacy of cosmetology products on skin, hair and nails. The general aim of this project is to further develop the hyperspectral instrumentation of Newton Technologies and its skin analysis methods. Throughout this work, we have oriented the design of the experimental systems

to make them suitable for use outside of a research context. Our particular interest in this project is full face imaging. The face is one of the most challenging parts of the body to measure because of its size and complex 3D geometry. As such, a method that is capable of imaging a full face can in theory also be applied to any other part of the body. The face is also of particular interest for applications in cosmetology, the market targeted by the industrial partner of the project.

Skin analysis using optical modeling

Besides seeing skin from a biomedical point of view, skin can also be considered as an optical material: it is a heterogeneous translucent material with which light interacts under the form of absorption and scattering, depending on its structure and composition [Igarashi et al. 2007; Jacques 2013]. When we look at skin, information about its physiology is therefore “hidden” within the optical signal captured by our eye, or by a camera. Optical models that describe light propagation within translucent materials can be applied to retrieve some of this hidden information, using an inverse approach.

In addition to imaging, an important part of this work is dedicated to optical modeling and analysis methods with the aim of retrieving the information contained in the measured signal. Skin is a complex organ which is best described using many parameters. However, when applying an inverse approach, the capacity to retrieve information from the measured signal tends to be much better when the optical model has fewer parameters than the available quantity of information. The selected imaging method should therefore try to capture as much information as possible.

Skin hyperspectral imaging

Limiting our study to so-called “surface imaging”, hyperspectral imaging (HSI) is one of the most promising methods for full face imaging and high resolution measurement, in terms of spatial resolution, to be able to discern fine details, and in terms of spectral resolution, to be able to gather as much information as possible and allow accurate physiological analysis. HSI consists of measuring skin spectral reflectance over many narrow and non-overlapping bandwidths that contiguously cover a part of the radiative spectrum. In our application, we focus on visible light, between 400 and 700 nm.

Previous works by Séroul et al. have shown that skin HSI combined with an optical model-based analysis can yield information about skin composition, under the form of oxygen rate, blood volume content and melanin concentration maps [Seroul et al. 2017]. The hyperspectral camera developed by Newton Technologies and used in Séroul’s work is however limited to the acquisition of small and relatively flat areas of the body. Consequently, applying such a method on a full face requires further developments, both in terms of instrumentation and analysis method. The measurement of a full face presents several challenges: for in vivo measurement, acquisition time must be as short as possible to reduce the chances of a person moving during acquisition; high resolution and good signal

to noise ratio are more difficult to achieve within a large field of view; and finally, although illumination is controlled, the measured spectral reflectance is affected by irradiance drifts on the curved parts of the face.

Skin spatial domain frequency imaging

Once the aforementioned issues are solved, another limitation of skin HSI can be identified: the spectral reflectance of skin is determined by both scattering and absorption properties, however, these two optical properties cannot be retrieved separately from a single measurement. In the analysis of hyperspectral images, this limitation is tackled by assuming skin scattering as constant and using a value taken from literature, in order to retrieve skin absorption properties. The analysis of skin scattering is however of great interest to the field of medicine, and could also pave the way to new analysis methods in cosmetology that would allow for more accurate descriptions of skin aging, hydration, inflammation, and scar healing. In addition, we are also interested in understanding whether the assumption that scattering is constant is generally valid or not, in order to better judge the accuracy of the hyperspectral image analysis method that we are using. In order to estimate maps of scattering, an additional method for measuring how light is spatially spread within skin must be implemented, such as spatial frequency domain imaging (SFDI), a method that measures skin modulation transfer function [Cuccia et al. 2009].

General content of the work

In the work reported in this dissertation, we propose firstly to combine wide field of view HSI with the measurement of the 3D geometry of the face. This will allow us to tackle the issue of irradiance drifts, and to interpret hyperspectral measurements independently from the shape of the face. The design of a 3D-HSI system for in vivo measurement is a significant challenge, mainly due to the difficulty of acquiring a large quantity of data within few seconds. Although 3D-spectral imaging is currently an active field of research, the few existing near-field 3D-spectral imaging systems are not entirely suited to broad spectral and spatial measurement on living organs: they are either multispectral systems [Paquit et al. 2009; Hirai et al. 2016; Zhang et al. 2016] providing spectral resolutions that are too low to be used for optical analysis, or in the case of those 3D-spectral imaging systems that do provide sufficiently high spectral resolutions [Kim 2013], the acquisition process is not adapted to living subjects. As far as we know, none of the existing systems are able to achieve high resolution images within a short acquisition time, we therefore designed a 3D-HSI system dedicated to full face measurement.

Subsequently, we propose to apply SFDI to measure skin modulation transfer function on a full face, and then to estimate maps of scattering coefficient. As is the case with hyperspectral imaging, the measured modulation transfer function is strongly affected by irradiance drifts for complex surfaces like the face. To design an analysis method independent from irradiance drifts, we propose to combine SFDI with HSI. One of the main

challenges of SFDI-HSI in vivo acquisition lies in the necessity of acquiring a large quantity of data within a short duration of time (preferably below 5 seconds) which leads to significant constraints in the design of the acquisition method.

Validating the estimated skin parameters

As we do not have access to any “ground truth” values for the parameters that we are estimating in vivo, we are also faced with the challenge of validating the analysis methods throughout the work. For the validation of biomedical methods, it is common to use samples whose optical properties are similar to biological tissues, called “phantoms”. However, as such samples have a different composition and structure than skin, our analysis method cannot be applied to them. Hence, alternative methodologies to evaluate the pertinence and accuracy of the analysis results will be proposed throughout the dissertation.

Structure of the report

The present work is constructed in three main parts. The first part, comprising Chapters 2 and 3, gives an overview of the optical study of translucent material, and in particular of skin. Chapter 2 covers the optical concepts used in this work, along with few typical optical models used to describe light transport in translucent materials. Chapter 3 presents the specificities of skin as a biological material and as an optical material, as well as few acquisition tools commonly used for its study.

In the second part, Chapters 4 to 7 describe our methods for full face hyperspectral acquisition and for analysis that is robust to irradiance drifts. The work presented in this part have been the object of an oral presentation at the Material Appearance conference of the Electronic Imaging Symposium in 2018 [Gevaux et al. 2018] and has been published in a journal [Gevaux et al. 2019a]. Chapter 4 describes the hyperspectral camera, while Chapter 5 details the 3D measurement system with which the camera is combined. Chapter 6 proposes a method for irradiance drift correction that uses the 3D geometry of the measured face, and Chapter 7 presents the chromophore map estimation method and the optical model associated with it.

Finally, the third part of the dissertation, which comprises Chapters 8 and 9, is dedicated to skin scattering measurement using SFDI and its optical analysis, which has been orally presented in the Imaging, Manipulation, and Analysis of Biomolecules, Cells, and Tissues XVII conference of SPIE Bios in 2019 [Gevaux et al. 2019b]. Experiments are detailed in Chapter 8 and analysis presented in Chapter 9.

Chapter 2.

Bases of optics for the measurement and modeling of translucent materials

Throughout this work, many optical objects, including light sources, imaging systems, polarizers, surfaces, translucent materials and so on, will be manipulated, implicating a large range of optical concepts. This chapter gives an overview of the optical models and radiometry concepts necessary for understanding how light interacts with a translucent multilayer material such as human skin, as well as for understanding optical measurements, including imaging.

A translucent material is commonly described as a material that allows light to pass through. However, such a definition, based on transmission, remains ambiguous—according to this definition, a very thick piece of translucent material that does not allow light to pass through would be described as opaque rather than translucent, although its visual appearance is influenced by subsurface light transport. We define translucent materials as scattering and absorbing materials for which subsurface light transport is not negligible. We also prefer the term “strongly scattering material” rather than “opaque” to designate materials for which the subsurface light transport is strongly limited, that-is-to-say that any incident ray is absorbed or backscattered so quickly that the distance it can travel within the material is almost zero.

The chapter is organized as follows: Section 2.1 presents fundamental radiometric quantities, which characterize the geometrical distribution of energy in space. Section 2.2 describes the concepts used to characterize the reflection or transmission properties of objects. Section 2.3 describes the categories of light-material interaction and Section 2.4 gives an overview of some of the existing models for light propagation in random particle media. Finally, although we are mainly working with spectral quantities, images are often

displayed as color images for easier visualization. Section 2.5 describes the color conversion process used throughout this work.

2.1. Basic radiometry concepts

Radiometry is the process of measuring optical radiation emitted by a source, detected by a sensor, reflected at an optical interface or transmitted through an optical object. Optical radiation is measured in energy units, and its spectrum covers the wavelength range from about $0.01 \mu\text{m}$ to $1000 \mu\text{m}$. In practice however, the part of the radiative spectrum that is considered is often reduced according to the properties of the source or detector. The perception of light by a human observer is studied in a separate discipline called *photometry*, which uses a different set of units and takes into account the sensitivity of the human eye.

A fundamental quantity used in radiometry is the *flux* F , expressed in watts (W). Flux corresponds to the energy radiated per unit of time, and is used to define three other fundamental quantities that describe the geometrical distribution of energy in space: intensity, irradiance and radiance. Before explicitly defining these quantities, the geometrical concepts of solid angle and geometrical extent should be elucidated. In radiometry, radiation does not travel along a line from one point to another as is the case in geometrical optics, since the probability of a photon being precisely located on a line is zero. Radiation must rather be considered as flowing through a “pencil of light”, characterized by a geometrical extent, considering a small area around each point and a small set of directions, or solid angle.

2.1.a. Solid angle and geometrical extent

A *solid angle* measures the amount of field of view covered by an object from a particular point. If we consider a sphere of radius R centered at this point, the solid angle, in steradian (sr), is the area of the segment of sphere that corresponds to the field of view, divided by R^2 .

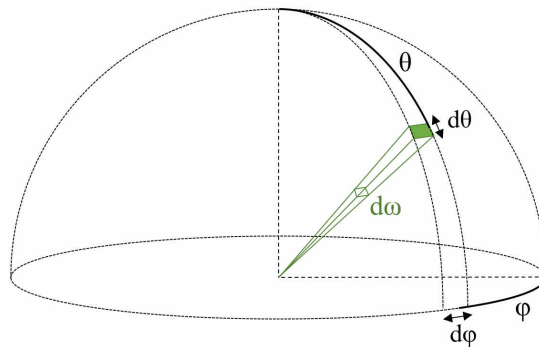


Figure 2.1. Infinitesimal solid angle in the direction (θ, ϕ) .

In spherical coordinates, the infinitesimal solid angle $d\omega$ in the direction characterized by the polar and azimuthal coordinates (θ, φ) (see Figure 2.1) is:

$$d\omega = \sin\theta d\theta d\varphi. \quad (2.1)$$

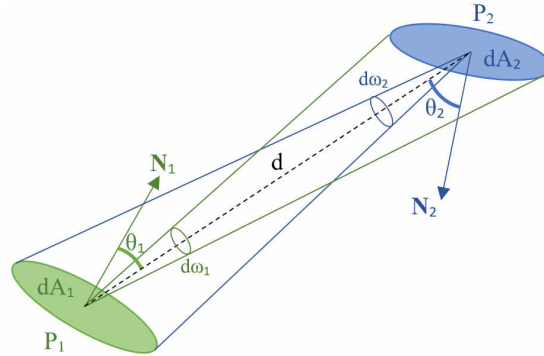


Figure 2.2. Geometrical extent between two small areas dA_1 and dA_2 .

Geometrical extent can be defined by considering two small area elements dA_1 and dA_2 which are located at P_1 and P_2 , with the distance between them being d , as illustrated in Figure 2.2. The normal directions to these areas form the angles θ_1 and θ_2 with the direction of the light ray given by the line (P_1P_2) . The geometrical extent can be written either from P_1 or from P_2 and is equal to the apparent area around the considered point, multiplied by the solid angle subtended by the opposite area:

$$d^2G = dA_1 \cos\theta_1 d\omega_1 = dA_2 \cos\theta_2 d\omega_2 = \frac{(dA_1 \cos\theta_1)(dA_2 \cos\theta_2)}{d^2}. \quad (2.2)$$

2.1.b. Radiometry quantities

Intensity I , expressed in $\text{W}\cdot\text{sr}^{-1}$, is the density of flux per unit solid angle that propagates in a specific direction characterized by the infinitesimal solid angle $d\omega$:

$$I = \frac{dF}{d\omega}. \quad (2.3)$$

Intensity is often used to describe how light is emitted from a point source. When the light emitted by a point source is the same in all directions, the source is isotropic.

Irradiance E , expressed in $\text{W}\cdot\text{m}^{-2}$, is the density of flux per unit area incident on an area dA :

$$E = \frac{dF}{dA}. \quad (2.4)$$

Exitance M , in $\text{W}\cdot\text{m}^{-2}$, is the opposite of irradiance in that it is the density of flux per unit area that is radiated from an area dA into a hemisphere.

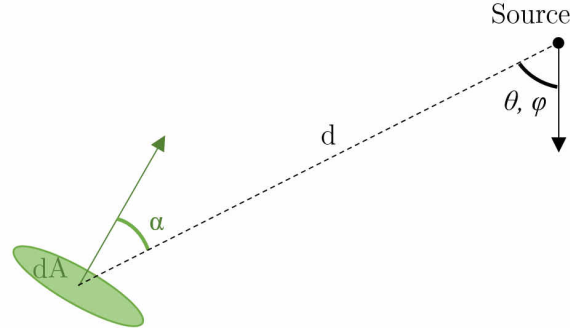


Figure 2.3. Useful notations in the definition of the inverse square law.

The relationship between irradiance and intensity is given by the *inverse square law*. Let us consider a source of intensity I that illuminates a small area dA , located at a distance d in the direction (θ, φ) and oriented with an angle α , as illustrated in Figure 2.3. When d is sufficiently large, the irradiance E received by this area is:

$$E = \frac{I(\theta, \varphi) \cos \alpha}{d^2}. \quad (2.5)$$

Radiance L , in $\text{W}\cdot\text{m}^{-2}\cdot\text{sr}^{-1}$, is the flux per unit extent d^2G , that-is-to-say the flux per unit area and per unit projected solid angle:

$$L = \frac{d^2F}{d^2G}. \quad (2.6)$$

A surface that is perfectly diffusing, i.e. that emits or reflects the same radiance in every direction, is called *Lambertian*. For a Lambertian reflector, the relation between radiance L and total exitance M is given by Lambert's law:

$$M = \pi L. \quad (2.7)$$

Radiance is the radiometric quantity best-adapted to describing light pencils, and can be used to describe light flowing through an optical system, toward a detector or from a surface source, i.e. a surface that emits or reflects light.

2.2. Radiometry definitions for surfaces

In physics, the light reflection and transmission properties of objects are characterized by various radiometric quantities, formalized by Nicodemus et al. [Nicodemus et al. 1977].

These quantities allow us to describe how much light is reflected (the concept of Reflectance), in which directions (the concept of Bidirectional Reflectance Distribution Function – BRDF), and how far light travels inside the material before emerging from it (the concept of Bidirectional Scattering-Surface Reflectance Distribution Function – BSSRDF).

For the study of translucent materials, the concept of Point Spread Function (PSF) can be added to these three definitions, and can be related to both the material Reflectance and BSSRDF. The definitions of these radiometry concepts are covered in this section.

2.2.a. Reflectance

Reflectance R , a dimensionless quantity, denotes any ratio of reflected flux F_r to incident flux F_i relative to a same surface element.

$$R = \frac{F_r}{F_i}. \quad (2.8)$$

It generally depends upon wavelength, illumination geometry and orientation (solid angle), observation geometry and orientation (solid angle), polarization and position on the surface [McCluney 1994]. This latter parameter is often ignored in the case of uniform materials. *Spectral reflectance* is defined as the reflectance in successive narrow wavebands of similar bandwidth.

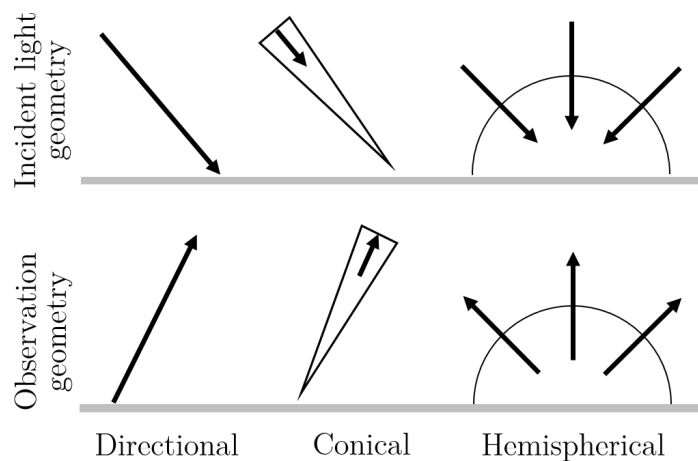


Figure 2.4. Most common geometries of illumination and observation for the definition of reflectance.

Reflectance is a general concept that has no signification until precise geometries for illumination and observation are specified, since different combinations of illumination and observation geometries generate very different reflectance values. For example, the reflectance of an aluminum mirror illuminated by collimated light at a certain angle is

around 0.8 if the observation system captures the specularly reflected light, and 0 otherwise. To allow simpler communication of these geometries, Nicomedus proposed a classification into nine geometries based on 3 types of solid angles for the incident light and for the captured light [Nicodemus et al. 1977]: infinitesimal, conical and hemispherical (Figure 2.4). Rigorously, when the incident light fulfills a non-infinitesimal cone, its radiance distribution should also be specified. In the cases of illumination through conical and hemispherical solid angles, it is assumed in Nicodemus classification that the incident radiance is constant (i.e. light is perfectly diffuse).

Reflectance is hardly measurable in practice, because this would require measuring the incident flux, which is difficult. The measurement of a slightly different quantity called *reflectance factor* is therefore often used instead. Reflectance factor is defined as a ratio of flux reflected by the surface F_{sample} to the flux reflected in the same observation direction by a perfect diffuser irradiated in exactly the same way as the sample F_{ref} :

$$\hat{R} = \frac{F_{sample}}{F_{ref}}. \quad (2.9)$$

Reflectance has values limited to the interval $[0, 1]$ from the law of conservation of energy. Reflectance factor, however, can have large values, such as in the case of a mirror measured in the specular direction.

Reflectance and reflectance factor do not describe the spatial and directional aspects of light reflection, which require the introduction of the notions of Bidirectional Reflectance Distribution Function (BRDF) and Bidirectional Scattering-Surface Reflectance Distribution Function (BSSRDF).

2.2.b. BRDF and BSSRDF

Bidirectional Reflectance Distribution Function (BRDF), expressed in sr^{-1} , is a function defined for every configuration of incidence and observation directions, denoted respectively as i and o and described by their spherical coordinates (θ_i, φ_i) and (θ_o, φ_o) in respect to the normal of the surface. BRDF is the ratio of the radiance L_o issued from an infinitesimal area going towards the direction o , to the irradiance E_i produced by a collimated illumination of this area from the direction i (Figure 2.5.a).

$$BRDF(\theta_o, \varphi_o, \theta_i, \varphi_i) = \frac{L_o(\theta_o, \varphi_o)}{E_i(\theta_i, \varphi_i)}. \quad (2.10)$$

BRDF can also depend on the position on the surface, the wavelength and the polarization state of the incident light. In this work, the influence of the polarization state of light is ignored, on the assumption that it plays a negligible role in the scattering materials that we are studying.

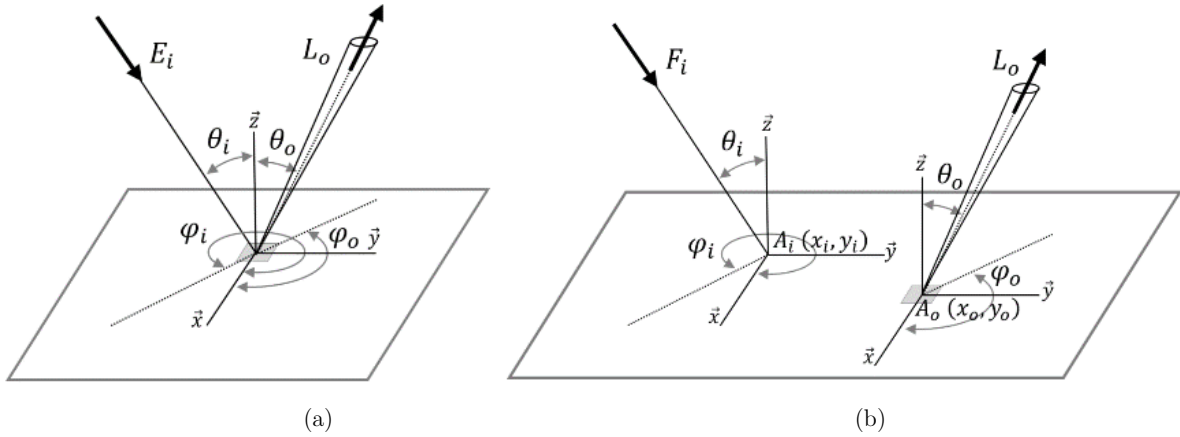


Figure 2.5. Scheme of the angles and coordinates used in the definition of (a) the BRDF and (b) the BSSRDF.

In his article, Nicodemus states that for uniform irradiance over a “large enough” area of a uniform and isotropic surface, BRDF is the basic quantity that characterizes the reflection properties of the surface [Nicodemus et al. 1977]. Nicodemus, however, does not go into any further detail about the meaning of “large enough”, which depends on the properties of the material. For strongly scattering materials, the effects of light subsurface scattering are not noticeable, and BRDF is sufficient to characterize the material even for very small illuminated areas. For translucent materials however, light can travel further in the material, and subsurface scattering affects the reflected radiance, unless a very large area is illuminated. Thus, it is necessary to refer to the Bidirectional Scattering-Surface Reflectance Distribution Function (BSSRDF) for an accurate description of a translucent material. Contrary to BRDF, BSSRDF can fully describe the appearance of a translucent object when illumination is non-uniform or punctual, as it takes into account the subsurface light transport in addition to the angular distribution of the reflected light.

Bidirectional Scattering-Surface Reflectance Distribution Function (BSSRDF), expressed in $\text{m}^2 \cdot \text{sr}^{-1}$, relates the radiance L_o leaving the surface in a point $A_o(x_o, y_o)$, and towards a direction $o(\theta_o, \varphi_o)$, and the incident flux F_i received from a given direction $i(\theta_i, \varphi_i)$ at a point $A_i(x_i, y_i)$ (Figure 2.5.b).

$$BSSRDF(\theta_o, \varphi_o, \theta_i, \varphi_i, x_o, y_o, x_i, y_i) = \frac{L_o(x_o, y_o, \theta_o, \varphi_o)}{F_i(x_i, y_i, \theta_i, \varphi_i)}. \quad (2.11)$$

The concept of BSSRDF has been widely used in image synthesis since the work of Jensen et al., who showed the importance of using the BSSRDF instead of the BRDF for realistic rendering of translucent materials such as marble, milk and human skin [Jensen et al. 2001].

2.2.c. Point spread function and modulation transfer function

Surface and subsurface interactions between light and a material can be fully described using BSSRDF, however it is a rather complex quantity to measure and to use. For the study of translucent materials, the *Point Spread Function* (PSF) is a simpler quantity describing the spatial aspects of subsurface light scattering. When translucent materials are illuminated punctually, some light exits further from the illuminated area due to subsurface scattering, creating a region of gradually diminishing brightness around the point of illumination. The pattern of light that is observed is the PSF of the material, expressed in m^{-2} . PSF is a function of the incident light geometry, observation geometry, wavelength, polarization state and location on the sample. It is defined as the ratio of the exitance of an infinitesimal area located in $A_o(x_o, y_o)$ to the flux F_i punctually received at the point $A_i(x_i, y_i)$. For homogeneous materials, PSF does not depend on the location of the point A_i that receives light. Similarly to reflectance, PSF can be characterized according to the classification of geometries of measurement shown in Figure 2.4.

PSF can be related to BSSRDF by integrating over the solid angles Γ_i and Γ_o , which define respectively the illumination and observation configurations. By considering the incident radiance $L_i(\theta_i, \varphi_i)$ flowing in the cone Γ_i , the relationship between PSF and BSSRDF can be written as:

$$PSF_{\Gamma_i, \Gamma_o}(x, y) = \frac{\int_{(\theta_i, \varphi_i) \in \Gamma_i} \int_{(\theta_o, \varphi_o) \in \Gamma_o} BSSRDF(x, y, \theta_i, \varphi_i, \theta_o, \varphi_o) L_i(\theta_i, \varphi_i) d\Omega_i d\Omega_o}{\int_{(\theta_i, \varphi_i) \in \Gamma_i} L_i(\theta_i, \varphi_i) d\Omega_i}, \quad (2.12)$$

where $d\Omega_i = \cos\theta_i \sin\theta_i d\theta_i d\varphi_i$ and $d\Omega_o = \cos\theta_o \sin\theta_o d\theta_o d\varphi_o$.

PSF can also be related to reflectance. When a surface receives a flux F_i punctually, its reflectance can be deduced from the PSF through a spatial integration over an area of observation A , which is large compared to the dimensions of the PSF:

$$R = \iint_{(x_o, y_o) \in A} PSF(x_o, y_o) dx_o dy_o. \quad (2.13)$$

PSF can be used to describe the light pattern $M_o(x_o, y_o)$ that results from a translucent material receiving a flux of spatial distribution $F_i(x, y)$:

$$M_o(x_o, y_o) = (PSF \otimes F_i)(x_o, y_o), \quad (2.14)$$

where \otimes denotes the two-dimensional convolution, defined as:

$$A(x, y) \otimes B(x, y) = \int_u \int_v A(x - u, y - v) B(x, y) du dv. \quad (2.15)$$

In biomedical optics, PSF has often been referred to as *diffuse reflectance* [Wilson and Jacques 1990], however, we prefer the term of PSF which, in our opinion, makes clear the

fact that this quantity describes the diffuse reflectance when illumination is punctual. The PSF used to describe the performance of an imaging system is often normalized to unity, which means that it does not account for how much light is transmitted (or reflected) by the system. In this thesis, the PSF that we use is normalized to the reflectance, as expressed in Eq. (2.13).

Modulation Transfer Function (MTF), the Fourier transform of PSF in the spatial frequency domain, can also be used to characterize translucent materials. It describes the loss of contrast of a pattern image projected onto the material according to the spatial frequency of the pattern. Contrary to the MTF commonly used to describe the performances of imaging systems, it also contains information about the reflectance (or transmittance, when considering light travelling through a translucent material) of the material: as PSF is normalized to the reflectance, MTF at zero is the reflectance.

2.3. Surface and volume light interactions for translucent materials

When a translucent material (often referred to as “turbid” in biomedical optics) is illuminated, light undergoes a number of events at the surface of the material and within its volume, illustrated by Figure 2.6. Photons can also be emitted in the material for fluorescent materials, however this possibility is not considered in this work.

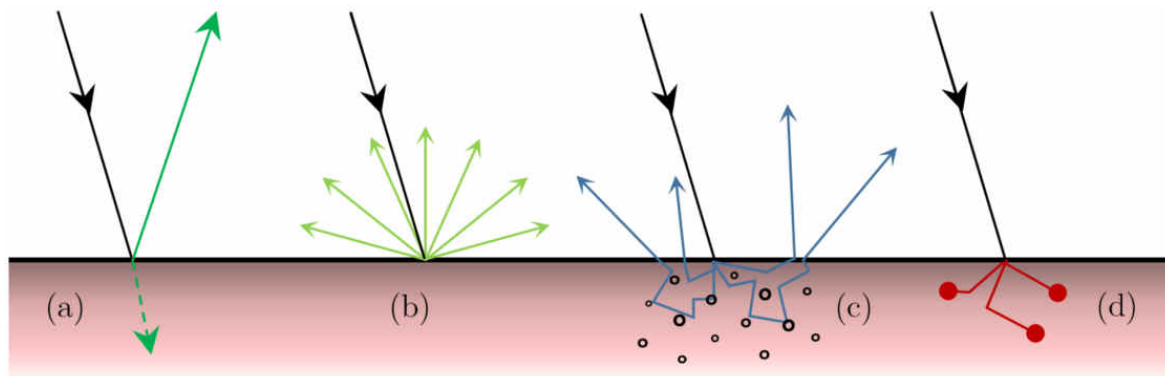


Figure 2.6. Types of light interaction with a translucent material: (a) Specular reflection and refraction, (b) surface scattering, (c) volume scattering (or subsurface scattering) and (d) volume absorption.

2.3.a. Surface reflection

The events can be reflections at the interface between the material and the outside media (generally air) due to a change of refractive index. The direction of reflection depends

on the surface topology. If the surface is perfectly smooth, such as a polished surface or a mirror, reflection is specular only (Figure 2.6.a) and can be described by the Snell-Descartes laws. The fraction of reflected light when the incident angle is θ is given by Fresnel formulae:

$$R_p(\theta) = \left(\frac{n^2 \cos \theta - \sqrt{n^2 - \sin^2 \theta}}{n^2 \cos \theta + \sqrt{n^2 - \sin^2 \theta}} \right)^2, \quad (2.16)$$

$$R_s(\theta) = \left(\frac{\sqrt{n^2 - \sin^2 \theta} - \cos \theta}{\sqrt{n^2 - \sin^2 \theta} + \cos \theta} \right)^2, \quad (2.17)$$

with R_p and R_s the respective reflection coefficients for p - and s -polarized light, and n the relative refractive index of the interface defined as n_2/n_1 when light propagates in a media of index n_1 and is incident on a media of index n_2 . The reflection coefficient for natural light is the average of R_p and R_s .

If the surface is rough, light is scattered (Figure 2.6.b). For many materials, surface reflection can be approximately described as a sum of specular reflection and diffuse reflection, a hypothesis used in some simple BRDF models for computer graphics such as the Phong reflection model [Phong 1975]. However, for more realistic rendering, slope distribution models allow a more accurate description of rough surface scattering by taking into account the surface topology. These models, such as the one developed by Torrance, Sparrow and Cook [Torrance and Sparrow 1967; Cook and Torrance 1982], model the rough interface as a set of randomly inclined microfacets reflecting and transmitting light as flat oblique interfaces. These models apply to rough surfaces for which the roughness characteristic length is much larger than light wavelength. Within these conditions, diffraction is negligible and light behavior relies on geometrical optics.

2.3.b. Subsurface interactions

Subsurface interactions, or volume interactions, are scattering and absorption events (Figure 2.6.c and d). Scattering and absorption events that occur in translucent materials can be modeled with a radiometric approach, such as the radiative transfer formalism, which is the subject of the next section.

Absorption, which occurs when the photon frequency is resonant with the transition frequencies of the atoms in the material, corresponds to a photon energy being taken up by matter and converted into another form of energy [Fox 2002]. Absorption is generally characterized by how much a light flux is attenuated when travelling through the material, using quantities such as the *absorption coefficient* μ_a , in m^{-1} , defined according to the surviving fraction of the incident light T travelling a unity length ∂L as in Eq. (2.18), or the *absorption mean-free-path* $l_{abs} = 1/\mu_a$ (in m).

$$\mu_a = -\frac{1}{T} \frac{\partial T}{\partial L}. \quad (2.18)$$

Scattering denotes a photon's deviation due to variations of refractive index within the volume. For simplicity, we consider that the scattering centers are particles. Depending on the shape and size of the particle, elastic scattering (the photon is deviated with no energy loss) can be modeled using the Rayleigh formalism [Rayleigh 1871] or the Mie theory [Mie 1908]. The Rayleigh formalism applies for particles much smaller than the wavelength and can be used to explain phenomenon such as the blue sky and the redness of sunsets. The Mie theory describes scattering by larger particles such as fat droplets in milk.

Scattering can be described using two parameters. The first parameter is the *scattering coefficient* μ_s , which represents the probability of a photon being scattered when travelling a unity length, and is expressed in m^{-1} , defined similarly as the absorption coefficient. The scattering coefficient can be replaced by the *scattering mean-free-path* $l_{sca} = 1/\mu_s$ (in m). The second parameter is the *scattering phase function* $P(\theta)$, the angular distribution of light intensity scattered by a particle at a given wavelength. This function, which shows the chances that a photon will be scattered in a particular direction θ , is normalized:

$$\int_{\text{sphere}} P(\theta, \varphi) d\omega = 1. \quad (2.19)$$

When multiple scattering occurs, it is common, for the sake of simplicity, to average this function over the whole sphere and use the *anisotropy coefficient* g :

$$g = \frac{1}{4\pi} \int_{\text{sphere}} P(\theta, \varphi) \cos\theta d\omega. \quad (2.20)$$

The anisotropy coefficient, which varies between -1 and 1, indicates whether light is mostly scattered forwards ($0 < g \leq 1$), as in the example shown in Figure 2.7, or backwards ($-1 \leq g < 0$). For isotropic scattering, $g = 0$.

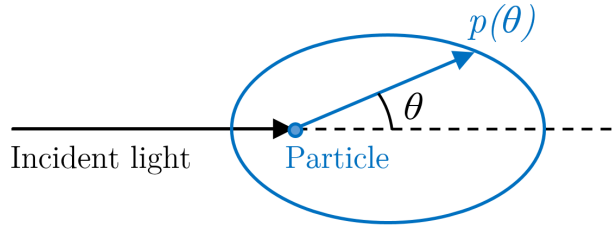


Figure 2.7. Example of phase function.

In order to take anisotropy into account, the reduced scattering coefficient $\mu_s' = (1 - g)\mu_s$ is often used instead of the scattering coefficient.

2.3.c. Multilayer materials

For multilayer materials, the material's overall reflectance properties depends on each layer properties.

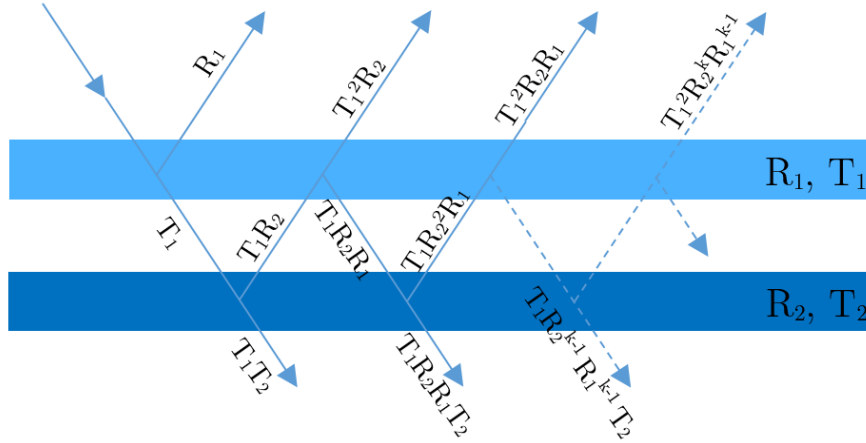


Figure 2.8. Light propagation in a two-layer material.

We consider a two-layer material, illustrated by Figure 2.8, composed of homogeneous layers for which the direction of measurement, i.e. whether light travels from top to bottom or inversely, does not impact reflectance and transmittance. They are described by their reflectance and transmittance, (R_1, T_1) for the top layer and (R_2, T_2) for the bottom layer. The Kubelka formulae [Kubelka 1954] describes the total reflectance R and the total transmittance T of the two-layer material :

$$R = R_1 + \frac{T_1^2 R_2}{1 - R_1 R_2}. \quad (2.21)$$

$$T = \frac{T_1 T_2}{1 - R_1 R_2}. \quad (2.22)$$

2.3.d. Light polarization

The light-material interactions described above affect the polarization state of light. This property can be used to separate the surface specular reflection from the light exiting the material after being scattered inside the volume. Indeed, as long as light is not scattered, its polarization is maintained. Thus, the polarization state of light is preserved during a specular reflection. However, light is depolarized when it undergoes multiple scattering events, either within a translucent material, or at the surface of a rough material. Consequently, when a translucent material is illuminated with linearly polarized light, placing a second linear polarizer (called an analyzer) in front of the detector allows us to

either retain or remove the surface specular reflection, depending on the orientation of the analyzer.

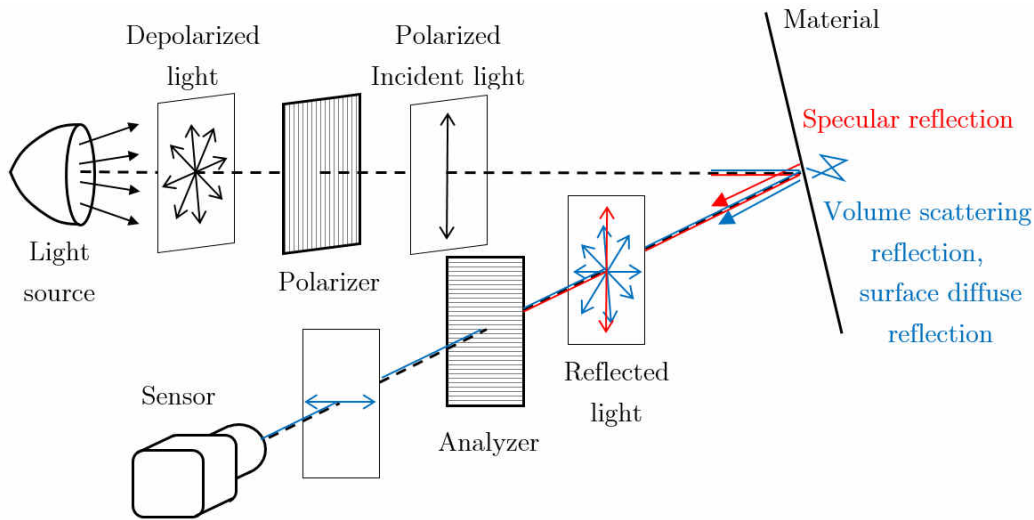


Figure 2.9. Principle of the cross-polarization (CP) configuration used to remove the specular component of reflection from the signal received by the sensor.

When the surface is viewed in a *cross-polarization configuration* (CP), i.e. when the analyzer is oriented perpendicularly to the incident light polarization, the specular reflection is cut and the depolarized light, which comprises volume scattering reflection and surface diffuse reflection, is partly transmitted by the analyzer, as illustrated by Figure 2.9. When using a *parallel-polarization configuration* (PP), the specular reflection is completely transmitted and the volume scattering reflection is partly transmitted by the analyzer. Illustrations of applications of PP and CP configurations for skin imaging are presented in Chapter 3.

2.4. Modeling light propagation within random particle media

Historically, two approaches have been developed to model light scattering: analytical theory, which takes fundamental equations such as the Maxwell equations as its starting point, and transport theory, also called radiative transfer theory, which considers the transport of energy through a medium containing particles. The transport theory is based on the approximation that powers, rather than fields, can be added, neglecting any wave effects (such as interferential or diffraction effects), except for the description of scattering by a single center.

In this section, we consider only the transfer theory and the models that are based on it, as in most cases, this formalism is sufficient to model light propagation in translucent

materials. The transfer theory gives a general model to describe wave propagation in the presence of random particles. The resolution of the radiative transfer equation can, however, be complex, and simpler models which derive from the transfer theory are often preferred in practice. In the case of a parallel-plane problem, flux models or the diffusion approximation have the advantage of being simpler while maintaining an acceptable degree of accuracy. In this section, the construction of the radiative transfer model, the diffusion equation and the Kubelka-Munk model are summarized along with discussions about their range of validity.

2.4.a. The radiative transfer theory

The radiative transfer theory, initiated by Schuster in 1903 and to which Chandrasekhar significantly contributed [Chandrasekhar 1943; Chandrasekhar 1960], is a unified formulation of the transport of energy through a medium containing particles, without considering wave equations. The transfer theory is able to describe a wide range of light-material interactions, for materials including atmosphere, oceans, paper or biological tissue. Diffraction and interference effects are not included, as this model considers the addition of powers rather than the addition of waves. In this section, we use the same notations as Ishimaru [Ishimaru 1978].

The most important and fundamental quantity used in the radiative transfer theory is the *specific intensity* $I(r, \mathbf{s})$ also called spectral radiance, defined as follow: For a given direction defined by a unit vector \mathbf{s} , at a point r of a given random medium, the specific intensity is the average power flux density within a unit solid angle (illustrated in Figure 2.10.a) and within a unit frequency band centered at frequency ν . Its unit is $\text{W}\cdot\text{m}^{-2}\cdot\text{sr}^{-1}\cdot\text{Hz}^{-1}$. In our application, the frequency dependence is omitted as there is no energy exchange between frequencies.

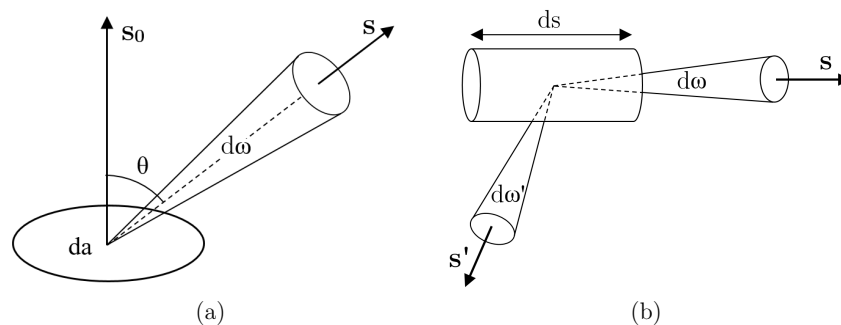


Figure 2.10. Useful notations in the definition of (a) the specific intensity and (b) elementary cylinder [Ishimaru 1978].

Several useful quantities in the radiative transfer theory can be defined from the specific intensity, such as flux (forward and backward) and average intensity:

- The *flux* dF flowing within a solid angle $d\omega$ through an elementary area da , respectively oriented in the directions \mathbf{s} and \mathbf{s}_0 as illustrated in Figure 2.10.a, is:

$$dF = I(r, \mathbf{s}) \mathbf{s} \cdot \mathbf{s}_0 da d\omega. \quad (2.23)$$

- The *forward flux* F_+ , which is the total flux passing through a small area da of normal vector \mathbf{s}_0 in the forward direction:

$$F_+(r, \mathbf{s}_0) = \int_{2\pi_+} I(r, \mathbf{s}) \mathbf{s} \cdot \mathbf{s}_0 d\omega. \quad (2.24)$$

- Similarly, the *backward flux* F_- , which denotes the total flux passing through da in the backwards direction, is given by the same expression as Eq. (2.24), with an integration over the hemisphere oriented according to the backward direction $-\mathbf{s}_0$.
- The *average intensity* U is defined as:

$$U(r) = \frac{1}{4\pi} \int_{4\pi} I(r, \mathbf{s}) d\omega. \quad (2.25)$$

Let us consider an elementary cylinder illustrated in Figure 2.10.b: it is centered on point r , of volume dS , and contains ρdS particles, with ρ the number of particles in a unit volume, called *number density*. For a specific intensity $I(r, \mathbf{s})$ incident on this volume, each particle scatters $\sigma_s I$ and absorbs $\sigma_a I$, with σ_s and σ_a the particle scattering and absorption cross sections. The intensity loss for all particles is therefore:

$$\begin{aligned} dI_{loss}(r, \mathbf{s}) &= -\rho ds (\sigma_s + \sigma_a) I(r, \mathbf{s}) \\ &= -\rho ds \sigma_t I(r, \mathbf{s}), \end{aligned} \quad (2.26)$$

with $\sigma_t = \sigma_a + \sigma_s$.

In addition to this intensity loss, some of the incident power flowing into the solid angle $d\omega'$ along the direction \mathbf{s}' can scatter inside the solid angle $d\omega$ along the direction \mathbf{s} . As there are ρdS particles in the cylinder, and scattered flux can come from any direction \mathbf{s}' , the intensity gain can be expressed in function of the amplitude function $f(\mathbf{s}, \mathbf{s}')$:

$$dI_{gain}(r, \mathbf{s}) = \int_{4\pi} \rho ds |f(\mathbf{s}, \mathbf{s}')|^2 I(r, \mathbf{s}') d\omega'. \quad (2.27)$$

In Eq. (2.27), the amplitude function can be replaced by the phase function defined by:

$$p(\mathbf{s}, \mathbf{s}') = \frac{4\pi}{\sigma_t} |f(\mathbf{s}, \mathbf{s}')|^2, \quad (2.28)$$

$$\frac{1}{4\pi} \int_{4\pi} p(\mathbf{s}, \mathbf{s}') d\omega' = w_0 = \frac{\sigma_s}{\sigma_t}, \quad (2.29)$$

where w_0 is called the *albedo* of a single particle. We can notice here that the scattering phase function $P(\theta)$ defined in Section 2.3 is slightly different from $p(\mathbf{s}, \mathbf{s}')$, as $P(\theta)$ is normalized to unity.

Finally, if light is emitted within the volume, the specific intensity increases by:

$$dI_{\text{gain,emission}} = dS \cdot \varepsilon(r, \mathbf{s}), \quad (2.30)$$

where ε denotes the power radiation per unit volume per unit solid angle in the direction \mathbf{s} .

The *radiative transfer equation* (RTE) is given by considering these three sources of specific intensity losses and gains. In the following equations, we introduce the absorption, scattering and total coefficients $\mu_a = \rho\sigma_a$, $\mu_s = \rho\sigma_s$ and $\mu_t = \rho\sigma_t$. The addition of Eqs. (2.26), (2.27) and (2.30), yields the following expression:

$$\frac{dI(r, \mathbf{s})}{dS} = -\mu_t I(r, \mathbf{s}) + \frac{\mu_t}{4\pi} \int_{4\pi} p(\mathbf{s}, \mathbf{s}') I(r, \mathbf{s}') d\omega' + \varepsilon(r, \mathbf{s}). \quad (2.31)$$

The specific intensity is often separated into two parts: the reduced incident intensity I_{ri} and the diffuse intensity I_d . The reduced incident intensity is the part of the incident flux which decreases due to absorption and scattering:

$$\frac{dI_{ri}(r, \mathbf{s})}{dS} = -\mu_t I_{ri}(r, \mathbf{s}). \quad (2.32)$$

The diffuse intensity is the specific intensity produced within the medium due to scattering. Replacing the specific intensity by $I_{ri} + I_d$ in Eq. (2.31), the RTE can be rewritten as a function of the diffuse intensity:

$$\frac{dI_d(r, \mathbf{s})}{dS} = -\mu_t I_d(r, \mathbf{s}) + \frac{\mu_t}{4\pi} \int_{4\pi} p(\mathbf{s}, \mathbf{s}') I_d(r, \mathbf{s}') d\omega' + \varepsilon_{ri}(r, \mathbf{s}) + \varepsilon(r, \mathbf{s}) \quad (2.33)$$

with

$$\varepsilon_{ri}(r, \mathbf{s}) = \frac{\mu_t}{4\pi} \int_{4\pi} p(\mathbf{s}, \mathbf{s}') I_{ri}(r, \mathbf{s}') d\omega'. \quad (2.34)$$

When there is no light emission within the material, ε is zero. The term ε_{ri} is called the *equivalent source function* generated by the reduced incident intensity. Equation (2.33) can be further simplified by defining the phase function p using a model, such as the Rayleigh or the Henyey-Greestrein phase function [Henyey and Greenstein 1941].

Except in simple cases, the solution to the radiative transport equation can only be done by simulation, such as by using Monte Carlo simulations. Approximated models exist in particular cases, as explained in the following.

2.4.b. The diffusion approximation

The diffusion equation is an approximated solution of the radiative transfer equation, valid for dense materials — where the particle content is much greater than 1%, and where a high number of scattering events occur: the diffuse intensity I_d defined in the previous section encounters many particles and is scattered almost uniformly in all directions. The diffusion approximation is valid for materials that are not too absorbing ($\mu_a \ll \mu_s$), such as is generally the case for biological tissues, and for samples whose dimensions are larger than the scattering mean free path ($\sim 1/\mu_s$). In order to allow for simpler expressions, we limit our study to materials in which there is no light emission within the material.

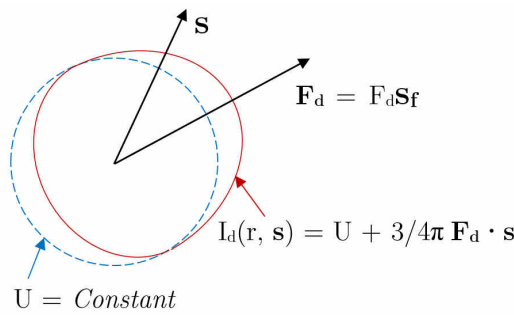


Figure 2.11. Almost uniform diffuse intensity I_d in the diffusion approximation [Ishimaru 1978].

In the diffusion approximation, the angular distribution of the diffuse intensity is almost uniform. It is not, however, completely uniform, as the total flux would then be zero. The diffuse intensity magnitude is thus a little higher in the direction of propagation, and is written in a first order approximation as a sum of an isotropic term and a non-isotropic term assumed to be proportional to the total flux, as described in Figure 2.11. With c a constant, we have:

$$I_d(r, \mathbf{s}) \approx U_d(r) + c \mathbf{F}_d(\mathbf{r}) \cdot \mathbf{s}, \quad (2.35)$$

with the diffuse flux vector

$$\mathbf{F}_d(\mathbf{r}) = F_d(r) \mathbf{s}_f = \int_{4\pi} I_d(r, \mathbf{s}) \mathbf{s} d\omega, \quad (2.36)$$

and the average diffuse intensity

$$U_d(r) = 1/4\pi \int_{4\pi} I_d(r, \mathbf{s}) d\omega. \quad (2.37)$$

Using the relationship between the magnitude of the diffuse flux F_d and the diffuse intensity I_d [Eq. (2.36)] in Eq. (2.35), we obtain:

$$c = 3/4\pi. \quad (2.38)$$

Combining Eqs. (2.35) and (2.38) with the RTE for a diffuse intensity [Eq. (2.33)] yields the *diffusion approximation equation* after performing the steps below [Ishimaru 1978].

- First, the integration of the RTE over 4π of solid angle gives:

$$\text{div}\mathbf{F}_d(\mathbf{r}) = -4\pi\mu_a U_d(r) + 4\pi\mu_s U_{ri}. \quad (2.39)$$

- Then, combining Eq. (2.35) with Eq. (2.33) and the additional hypothesis that $p(\hat{\mathbf{s}}, \hat{\mathbf{s}}')$ is function of only the angle between \mathbf{s} and \mathbf{s}' , yields:

$$\mathbf{s} \cdot \text{grad}U_d + \frac{3}{4\pi}\mathbf{s} \cdot \text{grad}(\mathbf{F}_d \cdot \mathbf{s}) = -\mu_t U_d - \frac{3}{4\pi}\mu_t \mathbf{F}_d \cdot \mathbf{s} + \mu_s U_d + \frac{3}{4\pi}\mu_t \mathbf{F}_d \cdot \mathbf{s} p_1 + \varepsilon_{ri} \quad (2.40)$$

with p_1 defined as

$$p_1 = 1/4\pi \int_{4\pi} p(\mathbf{s}, \mathbf{s}') \mathbf{s} \cdot \mathbf{s}' d\omega' = gw_0. \quad (2.41)$$

- Equation (2.40) multiplied by \mathbf{s} and integrated over 4π yields:

$$\text{grad}U_d = -\frac{3}{4\pi}\mu_t(1-p_1)\mathbf{F}_d + \frac{3}{4\pi} \int_{4\pi} \varepsilon_{ri}(r, \mathbf{s}) \mathbf{s} d\omega. \quad (2.42)$$

- Finally, Eq. (2.42) allows us to express \mathbf{F}_d , which can consequently be eliminated from Eq. (2.39) and yields the diffusion approximation equation:

$$\Delta U_d(r) - \kappa_d^2 U_d(r) = -3\mu_s \mu_{tr} U_{ri}(r) + \frac{3}{4\pi} \bar{\nabla} \int_{4\pi} \varepsilon_{ri}(r, \mathbf{s}) \mathbf{s} d\omega \quad (2.43)$$

with

$$\mu_{tr} = \mu_t(1-p_1) = \mu_a + \mu_s(1-g), \quad (2.44)$$

$$\kappa_d^2 = 3\mu_a \mu_{tr}, \quad (2.45)$$

and

$$U_{ri}(r) = 1/4\pi \int_{4\pi} I_{ri}(r, \mathbf{s}) d\omega. \quad (2.46)$$

The diffusion approximation equation [Eq. (2.43)] can be further simplified when the geometry of the problem is defined. Let us consider a thin collimated light beam illuminating a slab of particles along its normal direction. We consider the orthonormal coordinates system (X, Y, Z) centered on the illuminated area, with the Z axis normal to the surface and directed inward the material. With ρ the distance to the origin on the (X, Y) plane, and z the coordinate along the Z axis, the reduced incident intensity is:

$$I_{ri}(r, \mathbf{s}) = F_0(\rho) \exp(-\mu_t z) \delta(\mathbf{s} - \mathbf{z}), \quad (2.47)$$

and the corresponding average incident intensity is

$$U_{ri}(r) = \frac{F_0(\rho)}{4\pi} \exp(-\mu_t z). \quad (2.48)$$

The last term of Eq. (2.43) implies the equivalent source function ε_{ri} , defined in Eq. (2.34). This last term can be further simplified using Eq. (2.47):

$$\begin{aligned} \bar{\nabla} \int_{4\pi} \varepsilon_{ri}(r, \mathbf{s}) \mathbf{s} d\omega &= \bar{\nabla} \int_{4\pi} \left[\frac{\mu_t}{4\pi} \int_{4\pi} p(\mathbf{s}, \mathbf{s}') I_{ri}(r, \mathbf{s}) d\omega' \right] \hat{\mathbf{s}} d\omega \\ &= \bar{\nabla} \int_{4\pi} \left[\frac{\mu_t}{4\pi} F_0(\rho) \exp(-\mu_t z) \delta(\mathbf{s} - \mathbf{z}) \int_{4\pi} p(\mathbf{s}, \mathbf{s}') d\omega' \right] \mathbf{s} d\omega \end{aligned} \quad (2.49)$$

For isotropic scattering, $p(\mathbf{s}, \mathbf{s}')$ is constant, thus $\int_{4\pi} p(\mathbf{s}, \mathbf{s}') d\omega' = 0$, and the term expressed in Eq. (2.49) is zero.

Substituting Eqs. (2.48) and (2.49) into Eq. (2.43) yields a simplified diffusion equation applicable for collimated incident beams, with S a source term:

$$\Delta U_d(r) - \kappa_d^2 U_d(r) = -S(r). \quad (2.50)$$

$$S(r) = \frac{3\mu_s \mu_{tr}}{4\pi} F_0(\rho) \exp(-\mu_t z). \quad (2.51)$$

The diffusion equation can also be expressed as a function of the *fluence* $\varphi = 4\pi U_d$ (or *diffuse photon flux density*) and the *diffusion coefficient* $D = 1/3\mu_{tr}$:

$$\Delta \varphi(r) - \frac{\mu_a}{D} \varphi(r) = -\frac{\mu_s}{D} F_0(\rho) \exp(-\mu_t z). \quad (2.52)$$

The diffusion equation can be applied to simulate the fluence obtained when a translucent material of known optical parameters μ_a and μ_s is illuminated by a thin pencil of light. Such a model can be applied for homogeneous or multi-layer materials [Schmitt et al. 1990] using the appropriate boundary conditions. Figure 2.12, which represents simulations performed for various materials and has been reproduced after [Schmitt et al. 1990], shows that light subsurface transport presents different patterns depending on the material scattering and absorption properties: light travels wider in terms of radial distance from the entrance point when μ_a decreases, and deeper in the material when μ_s decreases.

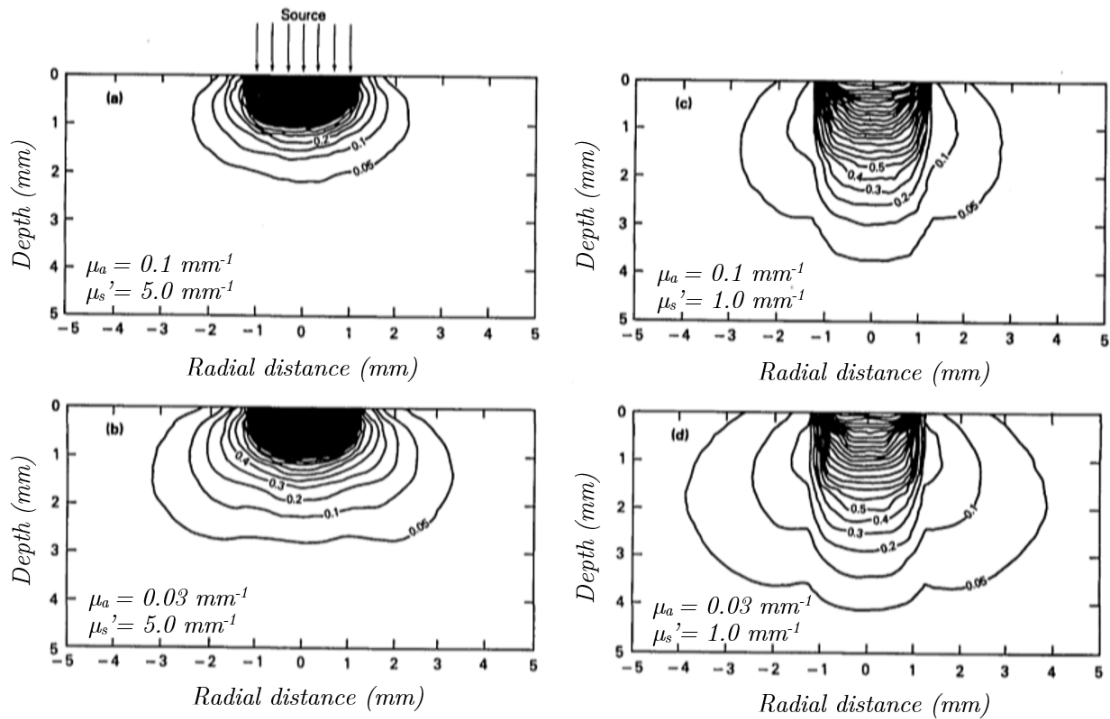


Figure 2.12. Fluence contour plot simulated using the diffusion approximation for homogenous materials of difference absorption and reduced scattering coefficients μ_a and μ_s' (reproduced from [Schmitt et al. 1990]).

2.4.c. The Kubelka-Munk model

The theory introduced by Kubelka and Munk in 1931 [Kubelka and Munk 1931] proposes a two-flux model for light propagation in parallel-plane materials illuminated by diffuse light. It models light propagation as two diffuse fluxes travelling perpendicularly to the layer in the forward and backward directions. The Kubelka-Munk (KM) model has been extensively used due to its simplicity and its relative accuracy as a predictive tool. Initially applied to printed materials, its use has been extended to the modeling of layered materials such as skin or makeup [Doi et al. 2006].

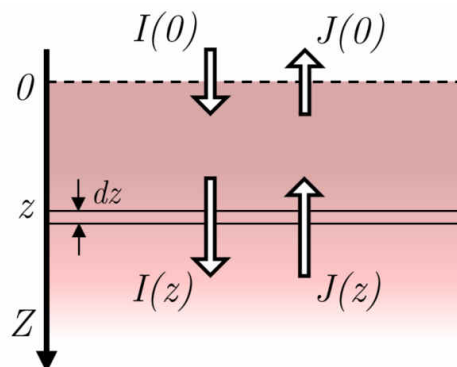


Figure 2.13. Positive and negative flux flowing through a slice of thickness dz located at a depth z .

Let us consider a homogeneous parallel-plane material which scatters and absorbs light, and a thin horizontal slice of this material, located at a depth z and of thickness dz .

This material is diffusely illuminated, and does not interact with light besides through absorption and scattering, characterized by the absorption and scattering coefficients K and S . Let us consider diffuse fluxes I and J , illustrated on Figure 2.13, traveling respectively in the positive and negative Z directions.

The variations of $I(z)$ when it crosses the slice dz are due to absorption and back-scattering: $I(z)$ decreases proportionally to the coefficient K when light is absorbed, and proportionally to the coefficient S when light is scattered. But $I(z)$ also increases due to the portion of $J(z)$ that has been back-scattered in the positive Z direction by this slice of material, proportionally to the coefficient S . The same principles also apply to $J(z)$ (with a negative sign as it is travelling in the negative Z direction), yielding a system of differential equations:

$$\begin{cases} \frac{dI}{dz} = -(K + S)I(z) + SJ(z) \\ \frac{dJ}{dz} = (K + S)J(z) - SI(z) \end{cases}. \quad (2.53)$$

Eq. (2.53) can be solved using approaches such as the Laplace transform or the matrix exponential (detailed in [Hébert et al. 2014; Ishimaru 1978]). Using the Laplace transform, the general solution for the differential system (2.53) is:

$$\begin{cases} I(z) = I(0) \cosh(Sbz) + \frac{1}{b} (J(0) - aI(0)) \sinh(bSz) \\ J(z) = J(0) \cosh(Sbz) + \frac{1}{b} (aJ(0) - I(0)) \sinh(bSz) \end{cases}, \quad (2.54)$$

with $a = (K + S)/S$ and $b = \sqrt{a^2 - 1}$.

Let us consider a parallel plane layer of thickness h , receiving an incident flux I_0 . Its transmittance and reflectance are $\tau = I(h)/I_0$ and $\rho = J(0)/I_0$. At $z = 0$, the forward flux is $I(0) = I_0$. At $z = h$, there is no backward flux incident upon the slab of material, and $J(h) = 0$. With these two boundary conditions, Eq. (2.54) expressed for $z = h$ yields the reflectance and transmittance of the layer:

$$\rho = \frac{\sinh(Sbh)}{b \cosh(Sbh) + a \sinh(Sbh)}. \quad (2.55)$$

$$\tau = \frac{b}{b \cosh(Sbh) + a \sinh(Sbh)}. \quad (2.56)$$

The K and S coefficients should be related to the μ_a and μ_s coefficients of the radiative transfer theory, as the Kubelka Munk theory corresponds to a special case of the radiative

transfer theory for which the phase function is reduced to two opposite directions. However, μ_a and μ_s' depend on the particle absorption and scattering cross-sections defined for a collimated beam of light, while the values of K and S are defined for a diffuse incident flux. For these reasons, the relationships between the Kubelka Munk coefficients and the RTE coefficients have been empirically estimated. The relationships given in literature [Thennadil 2008] are, with x a constant:

$$K = 2\mu_a. \quad (2.57)$$

$$S = \frac{3}{4}\mu_s' - x\mu_a. \quad (2.58)$$

Eq. (2.58) shows that K and S can be interdependent as S can contain absorption effects in addition to scattering when x is not zero. However, Thennadil [Thennadil 2008] has shown that for a diffuse incident flux and for not too absorbing materials ($\mu_a/\mu_s' < 75$), $x = 0$ yields a good approximation of the exact RTE.

2.4.d. Monte Carlo

Monte Carlo refers to a whole range of computational methods using repeated random samplings of a physical quantity to obtain numerical results. Monte Carlo methods are especially useful for dealing with physics-related problems that are difficult or impossible to solve by conventional and deterministic methods. In optics, Monte Carlo can be described as a non-deterministic ray tracing method: photons propagate in the media step by step, with a propagation direction sampled randomly according to a probability distribution, until it is completely absorbed or has reached the detector. Monte Carlo has been applied to biological tissue optics [Zhu and Liu 2013], as it can model light propagation in translucent materials with complex structures and solve the radiative transport equation at any accuracy as long as computation cost is not limited. In terms of calculation costs, Monte Carlo can be expensive as each ray propagation is computed. However, a variety of methods for speeding it up have been developed. In contrast with the other models presented in this section, results are not affected by boundary effects or limiting hypotheses. For these reasons, Monte Carlo is used in many applications and seen as a reference model.

Figure 2.14, reproduced from [Cuccia et al. 2009] and [Foschum et al. 2011], shows comparisons between simulations using Monte Carlo and the diffusion theory. Figure 2.14.a shows the difference in the spatial frequency domain. We can notice that the curves representing the two approaches are relatively similar at lower frequencies, but begin to deviate further and further from each other as frequency increases (with more error as μ_s' decreases). Figure 2.14.b shows the difference in the spatial domain, where ρ designates the distance between the source and the point of interest. On this graph, we can notice a significant difference between the Monte Carlo curves (MCd, MCs) and the diffusion theory (DT) for small ρ values, which is coherent with the observations in the frequency domain.

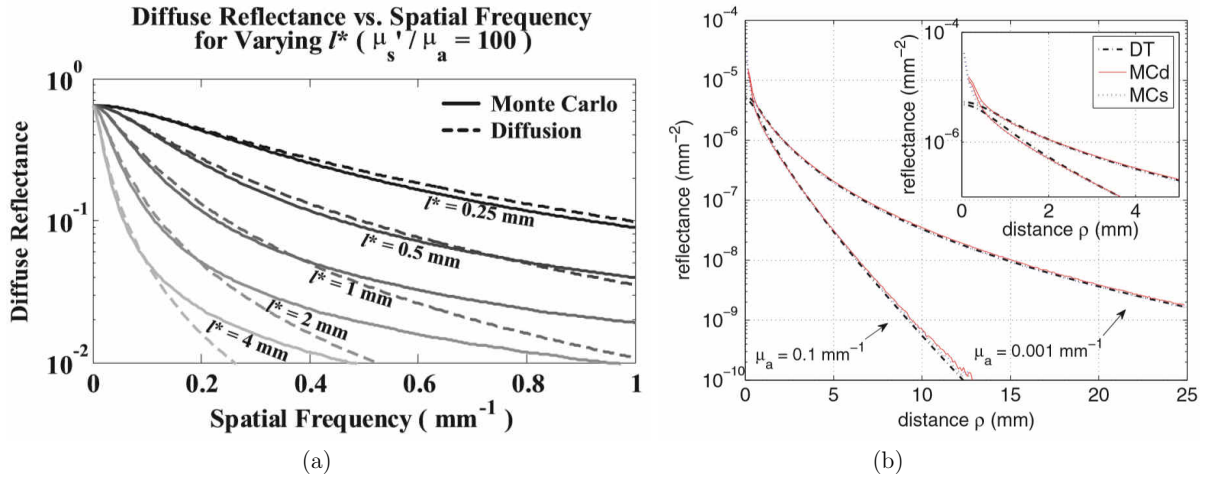


Figure 2.14. Comparison between Monte Carlo and diffusion theory (DT) simulations (a) in the frequency domain (with $l^* = 1/\mu_{tr}$) (reproduced from [Cuccia et al. 2009]) and (b) in the spatial domain (reproduced from [Foschum et al. 2011]).

These two graphs show that the diffusion approximation does not correctly describe light propagation close to the source, at distances smaller than the scattering mean free path $l^* = 1/\mu_{tr}$. More precisely, the diffusion approximation is valid only after several scattering events, and not for the light rejected back at the early entrance of the turbid material. In its valid range however, diffusion approximation is quite accurate, i.e., for isotropic scattering, $\mu_a \ll \mu_s'$ and dimensions larger than the scattering mean free path ($\sim 1/\mu_s'$).

2.5. Conversion of spectral information into color

The spectral reflectance of a surface, or the spectral luminance measured by a hyperspectral camera, contains significantly more information than color. The choice to convert this information to color is for illustration purposes, as color information corresponds to the way we are used to seeing. As such, color information will often be displayed in this work rather than spectral information. In this section, we summarize the rules of spectral to color conversion as well as the possible color systems that can be used, as defined by the Commission Internationale de l'Eclairage (CIE).

In this work, spectral images are converted into RGB color images, in the CIE 1931 RGB color space. However, when visual perception is involved, such as when color difference needs to be assessed, color systems derived from the CIE 1931 XYZ color space are used.

In the case of the CIE 1931 XYZ color space, spectrum conversion into the tri-stimulus values (X , Y , Z) requires contextualized observation and illumination conditions. By itself, spectral reflectance $R(\lambda)$ does not contain any information about the scene (illumination and observation context). Its conversion into color is possible only by setting illumination and observation conditions. The observation condition is given by the *color matching*

functions $\bar{x}(\lambda)$, $\bar{y}(\lambda)$ and $\bar{z}(\lambda)$ of the CIE 1931 XYZ color space, for either a 2° or a 10° standard observer [Wyszecki and Stiles 1982] (see Figure 2.15). The illumination $I(\lambda)$ is generally a standard illuminant, such as one of the illuminants of the D series, meant to represent natural daylight. In particular, D65 is intended to represent average daylight with a correlated color temperature of approximately 6500°K. Unless there are specific reasons for using a different illuminant, D65 is recommended by the CIE for colorimetric calculations in which daylight is to be represented [ISO/CIE 1999].

The spectral reflectance $R(\lambda)$ is converted into color values (X , Y , Z) by applying the following formula:

$$K = \frac{\gamma}{\int_{\lambda} I(\lambda)\bar{y}(\lambda)d\lambda} \int_{\lambda} R(\lambda)I(\lambda)\bar{k}(\lambda)d\lambda, \quad (2.59)$$

where (K, \bar{k}) represents alternately (X, \bar{x}) , (Y, \bar{y}) and (Z, \bar{z}) and γ is a factor (generally 100). In this work, we have chosen the color matching functions for a 2° standard observer.

When spectral luminance $L(\lambda)$ is measured, the illumination context is already defined, and the conversion only relies on the color matching functions:

$$K = \int_{\lambda} L(\lambda)\bar{k}(\lambda)d\lambda, \quad (2.60)$$

where (K, \bar{k}) represent alternately (X, \bar{x}) , (Y, \bar{y}) and (Z, \bar{z}) .

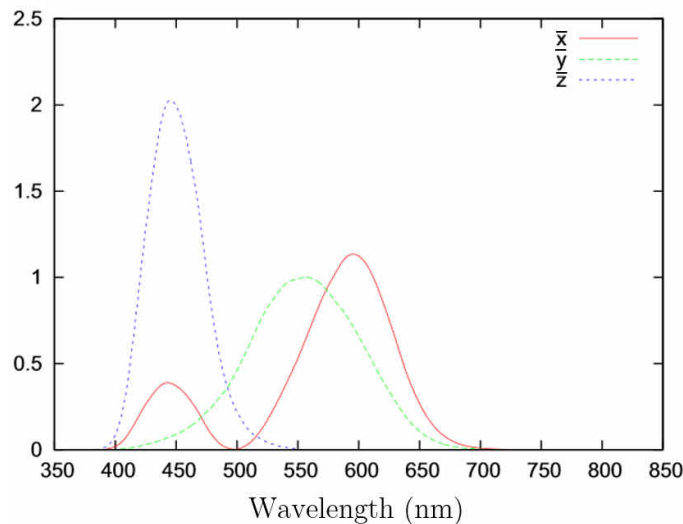


Figure 2.15. Color matching functions $\bar{x}(\lambda)$, $\bar{y}(\lambda)$ and $\bar{z}(\lambda)$ for a 2° standard observer as defined by the CIE for the CIE1931 XYZ color space.

In the CIE 1931 RGB color space, $\bar{r}(\lambda)$, $\bar{g}(\lambda)$ and $\bar{b}(\lambda)$ color matching functions have been defined by the CIE from visual experiments, and formulae similar to Eqs. (2.59) and (2.60) can be used for conversion. As the $\bar{x}(\lambda)$, $\bar{y}(\lambda)$ and $\bar{z}(\lambda)$ color matching functions are

linear combinations of the RGB color matching functions, it is also possible to retrieve (R, G, B) tristimulus from (X, Y, Z) by matrix multiplication.

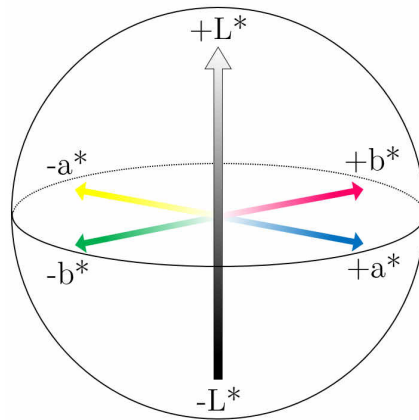


Figure 2.16. Illustration of the CIE 1976 $L^*a^*b^*$ color space.

Colors expressed in the XYZ space can then be converted into other color spaces, such as the CIE 1976 $L^*a^*b^*$ space (or CIELAB), which is perceptually uniform and in which it is possible to compute a distance between two colors. The $L^*a^*b^*$ space is often used in image analysis, as it offers a more intuitive interpretation of color than RGB. As illustrated in Figure 2.16, the L^* coordinates represent lightness, the a^* coordinates correspond to the red-green axis, and b^* to the blue-yellow axis.

Cylindrical color space in which colors are classified in function of their appearance to the human eye are also used here. For example, Munsell uses a color space that combines hue, value and chroma. In such a system, for a given hue, it is easy to organize colors according to their chroma and value.

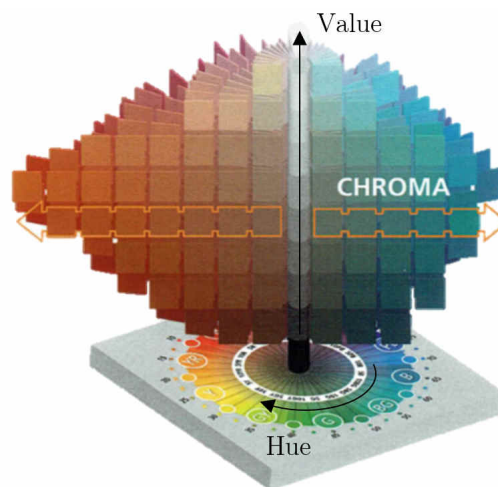


Figure 2.17. Hue, chroma and value color diagram of the system used by Munsell Color (USA) in its book of color.

In this thesis, spectral reflectance will often be converted into color. Unless a different method is specified, conversions are done into the CIE 1976 RGB color space using the D65 illuminant.

2.6. Conclusion

This chapter gives an overview of the most important concepts used throughout the thesis. Describing how light interacts with translucent materials involves complex quantities: BSSRDF must be used rather than BRDF and light subsurface transport can be described accurately by the radiative transfer equation, whose resolution is complex unless several simplifying assumptions are made. Up to this point, we have only been looking at light interaction with homogenous materials; in Chapter 3, we will consider the specific problems of modeling skin, which is a heterogeneous and translucent material.

Chapter 3.

The optical study of human skin

Skin is an organ that is made up of a complex arrangement of different cells, glands and fibers, which determine its optical and visual properties at a macroscopic scale. Optical measurement methods capture a light signal. When they are used on skin, our objective is to provide an interpretation of the measured light signal into a quantity that can be related to skin physiology, for applications in dermatology and cosmetology. It is therefore important to have a basic understanding of how the different skin elements are arranged together and how their interactions with light can be described by optical concepts.

The chapter is organized as follows: Section 3.1 gives a brief summary on skin physiological structure and composition. In Section 3.2, we present typical skin optical properties. Finally, we propose an overview of the existing methods used for skin punctual study and for skin imaging in Section 3.3.

3.1. Physiological structure and composition of skin

Skin, the largest organ in the body in terms of surface area, acts as a barrier to the exterior environment. Its complex structure, illustrated by Figures 3.2 and 3.1, is composed of three main layers: epidermis, dermis and hypodermis [Igarashi et al. 2007].

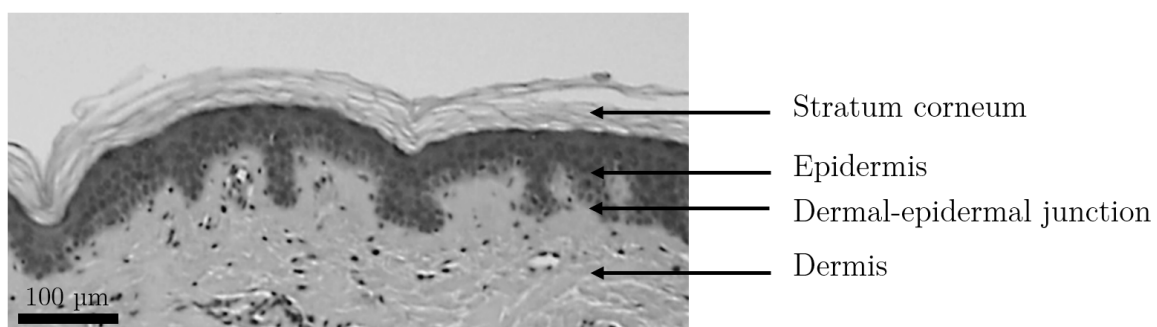


Figure 3.1. Skin histological section [Newton et al. 2017].

The epidermis can be further divided into sub-layers, from the stratum basal, which constitutes the boundary with the dermis, to the stratum corneum, which interfaces with the air. The stratum basal is composed of a single layer of basal cells producing keratinocytes. Melanocytes are also located in this sub-layer. They generate melanin when exposed to sunlight and distribute it to their neighboring keratinocytes. As new keratinocytes are produced by basal cells, the old keratinocytes travel upward and change shape. In the stratum granulosum sub-layer, they start deteriorating and finish by losing their nuclei and becoming totally flat. The oldest cells, the corneocytes, constitute the stratum corneum. They are dry, dead, and contain keratin fibers only. The stratum corneum plays an important role in retaining skin moisture and can deteriorate with age or skin dryness.

The interface between the dermis and the epidermis is called the dermal-epidermal junction. This interface is not flat: the dermal-epidermal junction forms epidermal protrusions down into the dermis (rete ridges) and dermal projections up into the epidermis (dermal papillae) [Newton et al. 2017]. The shape of this junction depends on the location on the body (for example, it is relatively flat on the face), but also on age. The junction flattens with age, leading to a decrease in skin elasticity.

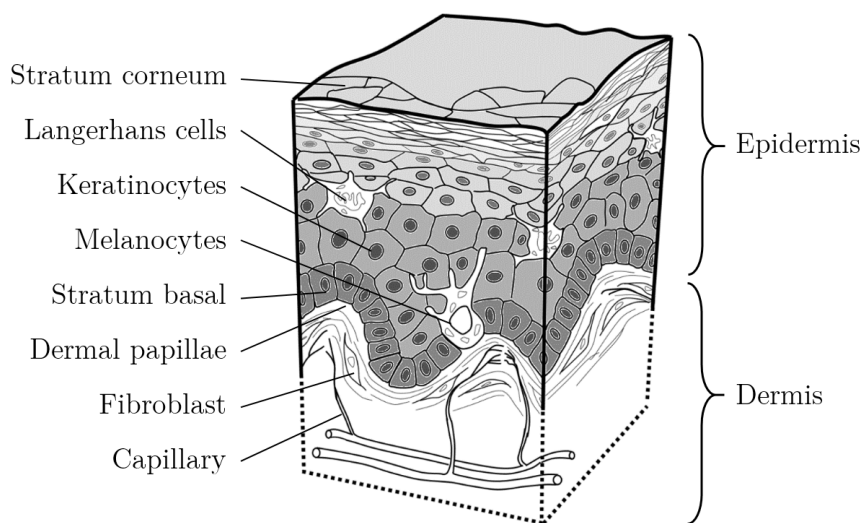


Figure 3.2. Schematic diagram of skin showing some of its structure and composition.

The skin's intermediary layer is called the dermis. Its thickness varies from less than a millimeter to half a centimeter. It is mainly composed of collagen and elastin fibers, and contains blood vessels, nerves and a variety of elements such as fibroblasts, the cells that synthesize extracellular matrix and collagen. Dermis is generally sub-divided between the papillary layer and the reticular layer. The papillary layer contains more nerves, more capillaries and a finer network of collagen than the reticular layer, in which the dense network of collagen aggregates into thick bundles. Collagen fibers, which represent around 70% of dermis dry weight, evolve over a person's lifetime [Varani et al. 2006], with significant variations between newborn skin, adult skin and aged or photodamaged skin.

The hypodermis is the deepest layer of the skin, located beneath the dermis. It typically has a thickness of several millimeters and includes a large number of fat cells and blood vessels.

Table 3.1 summarizes the typical structures of skin as described above, imaged at various depths using a Confocal Microscope [Hofmann-Wellenhof et al. 2012].

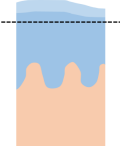
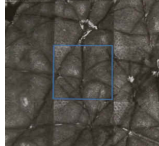

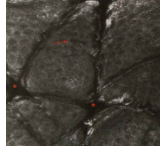

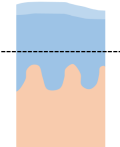

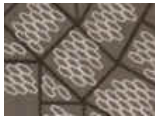
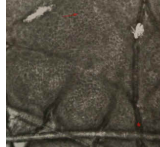

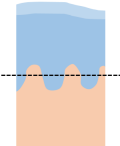
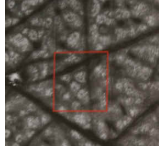



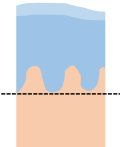
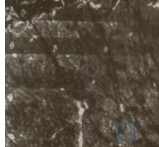

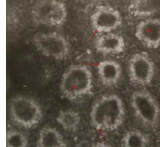

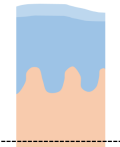
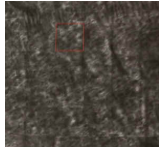
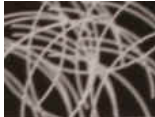
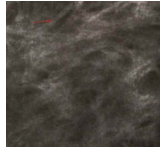

Location of the observed area	Confocal microscopy image	Schematic structure	Confocal microscopy image, zoom in	Schematic structure
				
				
				
				
				

Table 3.1. Reflectance Confocal Microscopy of healthy skin at various depths [Hofmann-Wellenhof et al. 2012].

Skin composition in light-absorbing chemical compounds, or *chromophores*, strongly influences skin optical properties. Melanin is the main chromophore in the epidermis. It is a polymer produced inside melanocytes, and stored and transported within the epidermis in melanosomes. It has a photoprotective role and strongly absorbs ultraviolet (UV) and visible light. Melanin content in the epidermis is generally expressed as a volume fraction of melanosomes within the tissue [Jacques 2013], although in following the conventions of the existing literature, we will refer to this as a *melanin concentration* in this thesis. This quantity varies between 1% and 43%, and is influenced by the person's genetic traits and UV radiation exposure. Two chemically distinct types of melanin exist: eumelanin, which

is black to brown, and pheomelanin, which is yellow to red. Regardless of skin color, the proportion of the two types of melanin in the human epidermis is approximately 74% eumelanin and 26% pheomelanin [Del Bino et al. 2015].

Hemoglobin, the protein contained in red blood cells (95% of a blood cell dry weight), is responsible for oxygen transportation. It can be found in blood vessels in the dermis, and its quantity influences skin color as it absorbs some of the light that has reached the dermis. A typical blood mass concentration within blood is 150 g.L^{-1} [Jacques 2013], but this varies with gender and age. Each hemoglobin protein can carry up to four oxygen molecules, and is called oxyhemoglobin (HbO₂) or deoxy-hemoglobin (Hb) depending on whether it is carrying oxygen or not. Hemoglobin is responsible for the red color of blood, as it absorbs light within most of the visual spectrum but is almost transparent for the large visible wavelengths (see Figure 3.3). Its shape changes when it binds with oxygen, resulting in different spectral absorption properties between Hb and HbO₂. Blood oxygen rate, the ratio of oxyhemoglobin to total hemoglobin content, is called oxygen saturation.

Other chromophores, generally present in low quantities in healthy skin, can also affect skin color. Methemoglobin, bilirubin and biliverdin, which are the products of hemoglobin deterioration, are three chromophores that are present in blood, in generally much lower quantities than hemoglobin. In cases of jaundice or hematoma, an abnormally high amount of bilirubin is present, giving the skin a yellowish color.

3.2. Skin optical properties

From the point of view of optics, skin is a turbid (or translucent) material which reflects, absorbs and scatters light.

Skin specular reflection properties, which are related to the visual attribute called gloss, can vary with sebum and transpiration secretions, or according to the state of the stratum corneum. Cells in the superficial layer can, for example, become detached from the rest of the layer due to skin dryness or deterioration, which alters light reflection and transmission at the skin surface. In this work, we use a cross-polarization (CP) configuration in most acquisition, and the specular reflection, which is discarded, will not be studied.

Considering only skin volume absorption and scattering properties, skin can be described using the quantities defined in Chapter 2: its anisotropy coefficient g , its refractive index n , its absorption coefficient μ_a and its scattering coefficient μ_s .

The anisotropy coefficient g varies between 0.5 and 0.75 and appears to increase as wavelength increases [Jacques 2013]. The anisotropy of light propagation in human skin can be studied on its own [Nickell et al. 2000], however, in this thesis, we do not separate the anisotropy coefficient from scattering and use the reduced scattering parameter $\mu_s' = \mu_s(1 - g)$, which accounts for both scattering and anisotropy.

The real refractive index of skin n depends, in a first approximation, on skin water content and varies between 1.5 for completely dry skin to 1.33 for water only. For skin, $n = 1.37$ or $n = 1.4$ is often used [Igarashi et al. 2007].

3.2.a. Skin absorption coefficient

The spectral absorption coefficient $\mu_a(\lambda)$ of skin is the sum of contributions from all absorbing chromophores i and depends on their concentration C_i and their individual absorption coefficient $\mu_{a,i}(\lambda)$. It can be described by the Beer-Lambert-Bouguer law [Bouguet 1729]:

$$\mu_a(\lambda) = \sum_i C_i \mu_{a,i}(\lambda). \quad (3.1)$$

Measurements of skin chromophore spectral absorption coefficients have been published in literature, for example by Jacques and Prahl, with their data tables available on their website [Jacques; Prahl]. Spectral values for melanin and hemoglobin are shown in Figure 3.3.

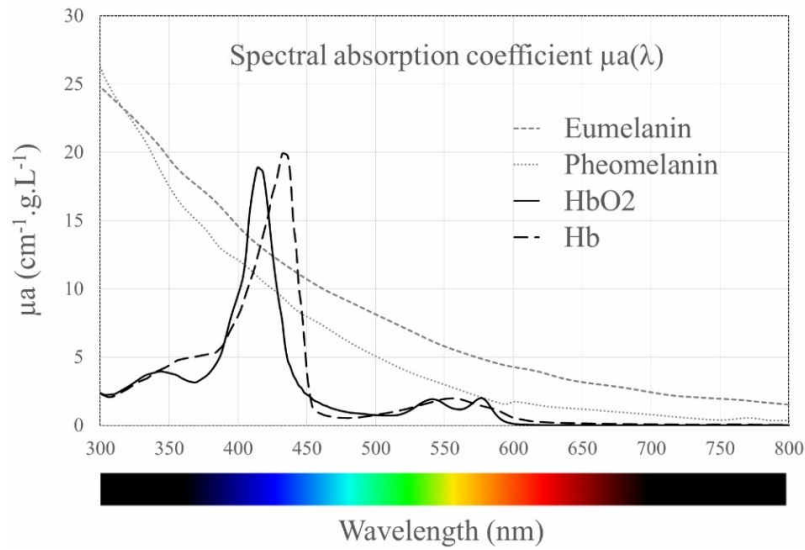


Figure 3.3. Spectral absorption coefficients $\mu_a(\lambda)$ for 1 g.L⁻¹ of eumelanin, pheomelanin, oxyhemoglobin (HbO2) and deoxy-hemoglobin (Hb) [Jacques; Prahl].

In this work, we will often mention the *blood volume fraction* c_{blood} , which is related to the apparent Hb and HbO2 molar concentration in the tissue $c_{Hb,mol}$ and $c_{HbO2,mol}$ using the following formula :

$$c_{blood} = \frac{c_{Hb,mol} + c_{HbO2,mol}}{c_{Hb,mass}} MW_{Hb}, \quad (3.2)$$

where MW_{Hb} is the molecular weight of hemoglobin, equal to 64 458 g.mol⁻¹ and $c_{Hb, mass}$ is the hemoglobin mass concentration within blood, chosen as 150 g.L⁻¹.

3.2.b. Skin scattering coefficient

Skin is a heterogeneous material composed of many structural elements, resulting in many variations in the refractive index, which lead to light scattering. The collagen fibers of the dermis strongly influence skin scattering properties. However, the influence of each element (cells, fibers, blood vessels, glands, shape of the dermal-epidermal junction, etc.) on scattering in skin is still little understood.

In contrast to the absorption coefficient, the scattering coefficient varies monotonically with wavelength: it decreases as wavelength increases. Skin contains elements that are small compared to visible wavelengths as well as larger elements. A possible model for skin scattering properties is a combination of Rayleigh and Mie scattering:

$$\mu_s'(\lambda) = a' \left(f_{ray} \left(\frac{\lambda}{500(nm)} \right)^{-4} + (1 - f_{ray}) \left(\frac{\lambda}{500(nm)} \right)^{-b_{mie}} \right), \quad (3.3)$$

with a' the value of the scattering coefficient at 500 nm, b_{mie} the Mie scattering power and $f_{ray} \in [0..1]$ the fraction of Rayleigh scattering.

Jacques' measurements [Jacques 1996] yield $a' = 4.29 \text{ mm}^{-1}$, $b_{mie} = 0.351$ and $f_{ray} = 0.76$. However, other studies [Jonasson et al. 2018] provide slightly different values, with μ_s' average values of 2.8 mm⁻¹ and 1.5 mm⁻¹ at 500 and 700 nm, while Jacques gives 4.3 mm⁻¹ and 1.8 mm⁻¹ at the same wavelengths.

Aging-related changes in skin structure impact skin scattering properties. For example, Branchet et al. have shown that the mean thickness of the collagen fibers increases and the distribution of fiber diameters becomes more heterogeneous with age [Branchet et al. 1991]. Iglesias-Guitan et al. showed in a study on skin aging modeling for applications in computer graphics that these variations mainly affect the wavelength dependence of the Mie scattering component [Iglesias-Guitan et al. 2015]. It can therefore be said that the way in which aging affects skin scattering properties is dependent on wavelength: the $\mu_s'(\lambda)$ curve becomes flatter with age, which corresponds to skin color becoming more and more dull.

3.3. Skin study using optical methods

Optical methods for skin acquisition have the advantage of being fast, non-invasive and capable of being performed in vivo. The existing measurement methods can be classified into punctual methods and imaging methods. Punctual methods provide an average value on a given area. Imaging methods provide a value in each pixel, making it possible to study skin heterogeneity. Both punctual and imaging methods can be sub-divided into two

categories depending on the type of measurement. Some methods deliver information that is directly related to skin visual appearance such as color, gloss and translucency, while others deliver information that can then be interpreted in terms of skin properties using an optical model. In this section, various skin acquisition methods and system used in dermatology and cosmetology are presented. We will also see that skin optical properties fluctuate with each beat of the heart.

3.3.a. Skin punctual acquisition

Spectrophotometers and colorimeters dedicated to skin measurement are probes which can be used on any part of the body.

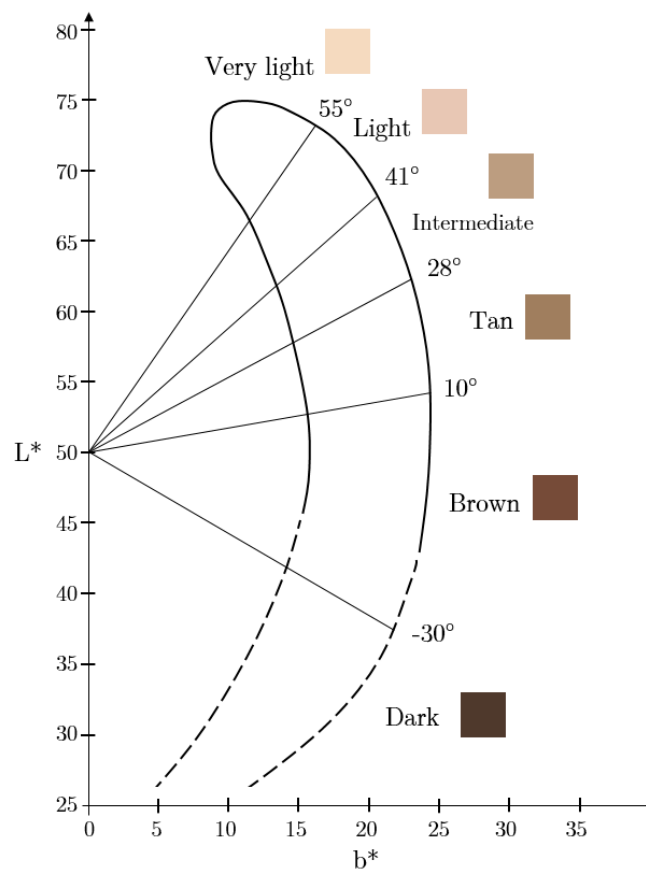


Figure 3.4. Skin $L^*a^*b^*$ color volume projected on the L^*b^* plane, used to classify skin between different shades of color [Chardon et al. 1991].

Skin color is often expressed in the Commission Internationale de l’Eclairage (CIE) $L^*a^*b^*$ 1976 colorimetric system, and can be classified according to an index such as the Individual Typology Index (ITA) developed by Chardon [Chardon et al. 1991]. When represented in the $L^*a^*b^*$ 1976 colorimetric space, the distribution of skin colors corresponds to a “banana shaped” volume (see Figure 3.4). The ITA angle, given by Eq. (3.4), can be used to classify color according to different degrees of lightness and darkness.

$$ITA^\circ = \arctan\left(\frac{L^* - 50}{b^*}\right) \times \frac{180}{\pi}. \quad (3.4)$$

Measuring skin spectral reflectance gives more information than color and can be used to determine specific skin properties. For example, reflectance pulse oximetry consists of measuring skin spectral reflectance at two wavelengths to determine peripheral oxygen saturation (SpO₂).

As skin is a translucent material, the types of measurement device should be carefully chosen. Most measurement devices designed for strongly scattering materials have identical illumination and observation areas. If such a device is used to measure skin, the light scattered outside of the illumination area due to subsurface transport is not detected. It results in errors on the amplitude and shape of the measured spectrum in the case of spectrophotometers, and on the measured color in the case of colorimeters. To overcome this issue, which has been named “red loss” artefact [Vidovič et al. 2015], the measurement device must be designed with an observation area smaller than the illumination area, or vice versa. The Konika Minolta (Japan) spectrophotometer CM-700d, which diffusely illuminates the sample on a 11 mm diameter area and measures it in the normal direction on an 8 mm diameter area, is adapted to skin measurement and often used for applications in cosmetology. Spectro2guide (BYK-Gardner, Germany) is another example of a spectrophotometer suitable for skin measurement.

Skin is a soft, non-planar material that becomes distorted under the pressure of a measurement probe. Consequently, measuring skin gloss using a glossmeter is not recommended as it is very difficult to ensure a constant viewing angle (generally 60° for gloss). A few instruments offer punctual gloss measurement for skin, such as Goniolux (Orion Concept, France) or Seelab GP (Seelab, France). They use multi-angle acquisition to compute a gloss index by estimating the BRDF peak width obtained for a certain directional illumination.

Skin translucency measurement has mainly been investigated for applications in medicine. The most common measurement method is Diffuse Reflectance Spectroscopy (DRS), first presented in 1990 by Wilson and Jacques [Wilson and Jacques 1990]. This method consists in measuring the point spread function (PSF) of the material by illuminating punctually a surface and measuring the exitance profile of the halo of light around the illuminated area. The shape of the PSF, which is a function of wavelength, can be analyzed using an optical model to retrieve absorption and scattering coefficients. However, rather than measuring skin optical coefficients, most DRS applications aim at determining the presence or absence of an “optical signature” which allows the diagnosis of a pathology. This method has been used to monitor glucose rate in diabetics [Bruulsema et al. 1997] or to interpret the results in tuberculin skin tests [Koenig et al. 2015]. Instruments using the same principle also exist for applications in cosmetology, such as Transluderm (Orion Concept, France) or Translucymètre (Monaderm, Monaco). These methods are,

however, less accurate than DRS probes dedicated to medical applications, and do not separate absorption and scattering in the interpretation of the measured signal.

3.3.b. *Skin imaging*

The methods presented in § 3.3.a provide an average measurement on a small area. However, skin is not a uniform surface and shape is also an important marker in the analysis of skin structures. An average measurement is generally not enough: a high quantity of melanin can either mean a darker skin color if it is spread uniformly, or a stain if melanin is concentrated on a small area; for dermatologists, the shape of a suspicious lesion provides important clues in the diagnosis of pathologies.

Historically, the diagnosis of skin pathologies has been performed by the naked eye, with skin imaging used only for illustration purposes to characterize the different types of skin lesions. In recent decades however, a number of imaging methods dedicated to the study of skin have been developed, and their role in dermatological consultations can be expected to dramatically increase.

Many skin imaging methods exist, with various specificities in term of spatial resolution and field of view. However, none are able to study skin at all scales, from the cell to a full body. For example, Reflectance Confocal Microscopy (RCM) and Optical Coherence Tomography (OCT) are two sophisticated optical methods that can image inside skin with a high resolution but on a very small area, generally in the order of a few mm². RMC can image inside skin (see Table 3.1) using a pinhole to block out-of-focus light, capturing only information close to the focal plane, whose depth can be chosen. RMC has a very high resolution, generally 1 μm; its main limitation is its weak penetration depth of only 200 μm. OCT is an interferometric modality producing images corresponding to a vertical section with a resolution of a few micrometers, with a penetration depth in the order of 1 mm.

A method which provides high resolution images on a relatively larger area, in the order of few cm², is dermatoscopy. Quite likely the most commonly used optical device in dermatology, a dermatoscope is a magnifier (typically × 10, and up to × 400) that also suppresses skin specular reflection. Gloss suppression can be achieved by creating optical contact using an immersion liquid, and in this way the optical index variation at the interface is small enough to remove perceptible surface reflection. It can also be achieved by using light polarization in a CP configuration (see Chapter 2). Recent dermatoscopes can capture digital images.

For larger zones of interest, such as the full body, “surface” imaging is generally used. Skin can be captured using color cameras or spectral cameras. All these imaging modalities require controlled acquisition conditions and color or radiometric calibration. In dermatology, color images can be used to follow the evolution of a pathology, but two images can be compared only if they have been taken in similar conditions—in particular, similar illumination and observation geometries—necessitating dedicated acquisition

benches. The acquired information can be used to study skin color, which can be used to address cosmetic claims such as redness or pigmented spots.

Multispectral and hyperspectral cameras provide more information than skin color and can be sensitive in the visible spectrum as well as the infrared spectrum. Spectral information can for example be used for diagnosis purposes, as is the case with the multispectral camera SIAscope® (MedX Health, USA), which measures 8 wavebands of the visible spectrum and close infrared for mole analysis [Moncrieff et al. 2002]. The MelaFind® system (Mela Science, USA), a 10-waveband multispectral system, is even more diagnosis oriented, using big data analysis to assist the dermatologist in its biopsy decision making [Monheit et al. 2011]. With hyperspectral imaging, the measured signal can also yield skin absorption properties estimation by applying an optical model. The potential uses of this application will be further developed in Chapter 7.



Figure 3.5. Images of the same area of skin acquired (a) in a cross-polarization (CP) configuration and (b) a parallel-polarization (PP) configuration (right).

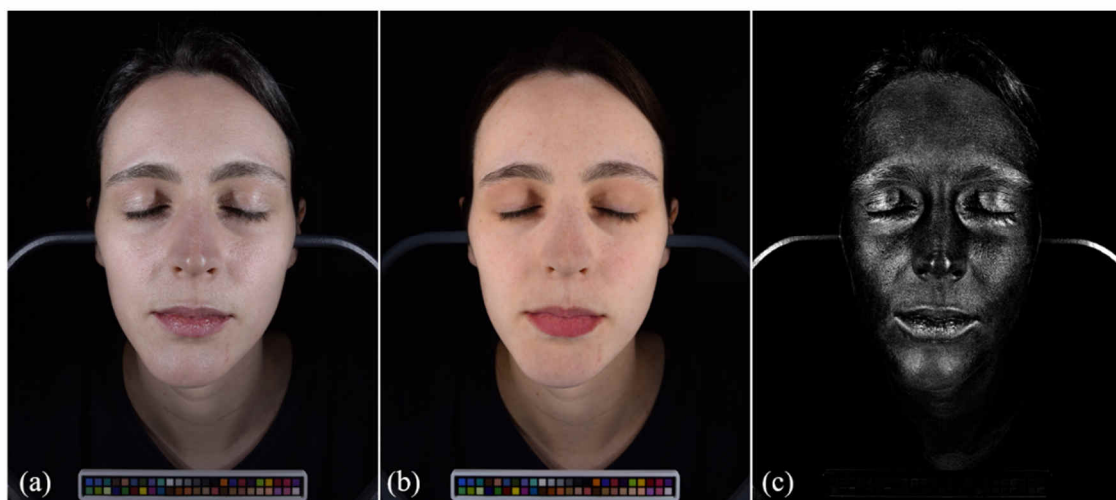


Figure 3.6. Example of gloss measurement on the ColorFace® (Newtone Technologies, France): (a) PP configuration, (b) CP configuration and (c) difference between the two images which shows the glossy areas.

Imaging methods are also used to measure skin gloss by capturing two images in a CP and PP configuration, and analyzing the difference (Figure 3.5). This method is used in many commercial systems dedicated to cosmetology, such as Samba (Bossa Nova Technologies, USA) or ColorFace® (Newtone Technologies, France) (Figure 3.6).

Finally, skin translucency can also be captured using imaging methods. Whilst punctual methods rely on measuring skin PSF, imaging methods work in the spatial frequency domain, measuring skin modulation transfer function (MTF). The method equivalent to DRS in the spatial frequency domain is Spatial Frequency Domain Imaging (SFDI). The principles, methods and applications of SFDI will be elaborated in Chapters 8 and 9.

3.3.c. Skin temporal variations

Skin properties vary with time. At a slow pace, skin evolves throughout a lifetime due to natural aging, or from the influence of the exterior environment such as weather conditions, ultra-violet exposure and pollution. Skin is also alive and its optical properties can change very rapidly, from moment to moment. Such variations occur with every beat the heart makes and every breath taken, oblivious to the naked eye. These variations can however be captured using an optical device, as it has been demonstrated in several studies [Poh et al. 2010; Wu et al. 2012]. The heartbeat especially affects the a^* component of skin $L^*a^*b^*$ color, as illustrated in Figure 3.7.

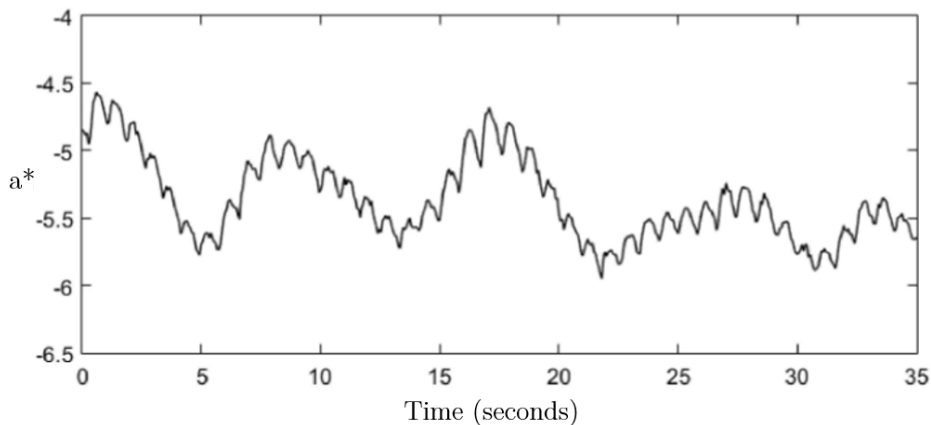


Figure 3.7. Evolution of the a^* component of skin $L^*a^*b^*$ color in regard to time.

The curve of Figure 3.7 has been measured on the face, on a person with a light skin color. The acquisition system comprises a CMOS color camera, LED lights and polarizing filters arranged in a CP configuration. The acquisition rate was set to 15 frames per second, which offers an adequate temporal sampling to study heartbeat. Images, acquired in RGB, were finally converted into $L^*a^*b^*$ (CIE 1976) and the average color on the forehead was computed. From this measurement, we have estimated 72 heartbeats and 8 breathing cycles per minute.

Heartbeat rate camera-based measurement is an interesting method to monitor patients in a non-invasive way and has been used to monitor newborns in hospital nurseries [Wu et al. 2012].

3.4. Conclusion

The brief (and incomplete) overview of optical methods for skin measurement given in this chapter reveals some of the challenges present when working on skin, a complex, alive, soft, heterogeneous and non-planar material. When possible, non-contact measurement methods are preferable to contact probes, which are prone to change skin properties. In terms of imaging methods, a compromise between being able to measure a large area and obtaining a high resolution is necessary, and the preference of one over the other should be adapted to the application. Finally, acquisition time is particularly important. In this chapter, only skin temporal variations in terms of color due to the beating of the heart is mentioned. While this phenomenon affects measurements that take longer than a single heartbeat, it is likely to be negligible compared to the artefacts due to the person moving during acquisition. In this thesis, we will emphasize many times the importance of reducing acquisition time as much as possible, in order to limit the effects of body movement on the measurement accuracy.

This chapter also provides the basic grounding in skin physiology, structure, composition, and optical properties necessary for understanding how the measurement of an optical signal can be transformed into information that is intelligible to a dermatologist or that can be interpreted as a cosmetological claim. Understanding the complexity of skin also defines the limitations of model-base analysis. In this work, we will be generally looking at what we call “healthy skin”, as described in Section 3.1 of the chapter.

Chapter 4.

Capturing wavelength selective information:

Hyperspectral imaging (HSI)

Multispectral and hyperspectral imaging are methods for measuring the spectral radiance of scenes as well, if appropriate calibration is possible, as the spectral reflectance factor of surfaces. The spectral reflectance factor, already defined in Chapter 2, is a radiometric quantity describing how much incident light is reflected by an object according to the wavelength of the light [Hébert et al. 2014]. This quantity can be used to simulate color under any illuminant such as natural sunlight and indoor lighting. It can also be used to reveal information usually invisible to the naked eye and estimate the optical properties of a material, making it suited to applications in various fields including cultural heritage [Liang 2012], art [Cucci et al. 2016], agronomy [Lorente et al. 2012], biology [Manley 2014] and medicine [Lu and Fei 2014].

Originally developed for observing Earth from space, spectral modalities of imaging have become more and more prevalent in the last decade, thanks to progress in sensor performances and computational power. The development of applications that can be used for skin acquisition and analysis is still in its infancy today, but it is foreseeable that new optical tools for non-invasive diagnosis will be available in the future. In particular, the work of Séroul [Seroul et al. 2017] has shown the considerable potential of HSI for skin chromophore composition analysis. His acquisition method, however, is limited to small and planar parts of the body. To extend his work, we have built a wide field hyperspectral camera, able to acquire a full human face. We have decided to focus on the human face, the part of the body that presents the most significant challenge for 3D scanning, as well as being of greatest interest to cosmetology. The acquisition method, however, can be applied to any part of the human body.

In this chapter, we give in Section 4.1 a brief review of the existing spectral imaging methods with a few examples of systems that can be used for body imaging. Then, we detail the hyperspectral camera built for full face acquisition in Section 4.2 before discussing the efficacy of the method in Section 4.3 and reach conclusions in Section 4.4.

4.1. Spectral imaging methods

Spectral imaging extends conventional RGB color imaging by replacing the three channels corresponding to three large wavebands, usually referred to as “red”, “green” and “blue”, with a considerably higher number of wavebands [Garini et al. 2006].

Multispectral Imaging (MSI) and Hyperspectral Imaging (HSI) are based on a similar principle, and differ only in the number of channels acquired (see Figure 4.1). While MSI typically measures 4 to 15 wavebands with no constraints on the waveband width and the spectrum sampling, HSI comprises of up to hundreds of narrow wavebands of similar bandwidths covering contiguously the spectrum of interest (potentially covering the ultraviolet, visible and infrared domains). There is no clear consensus about the definition of HSI in literature, as the minimum number of wavebands is not precisely defined. However, we propose that the conditions of regular spectral sampling and non-overlapping narrow wavebands are the most important criterion defining HSI.

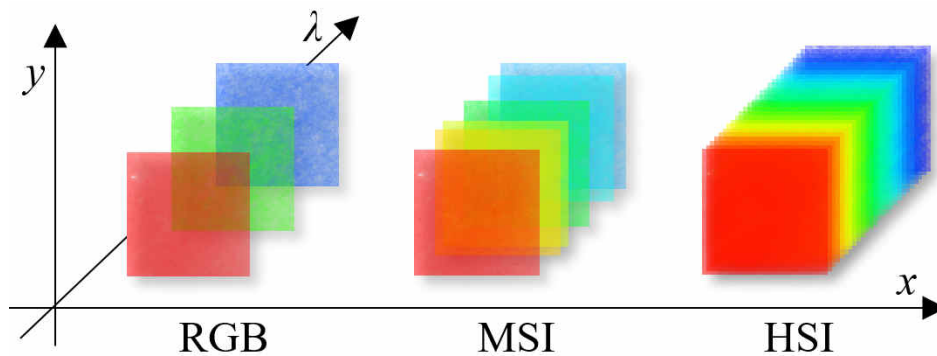


Figure 4.1. Difference between RGB imaging, multispectral imaging (MSI) and hyperspectral imaging (HSI).

Hyperspectral imaging can also be compared to spectroscopy, but whereas spectroscopy measures the average spectral reflectance of a given area, spectral imaging provides a spectrum for each pixel of the camera’s field. These measurements in many small areas on the observed surface makes hyperspectral imaging especially suitable for the observation of heterogeneous surfaces. Hyperspectral image data are often called “hypercubes” since they are three dimensional: two dimensions corresponding to the spatial domain, one dimension corresponding to the spectral domain.

4.1.a. Acquisition methods

Many near-field spectral imaging systems have been developed using various technologies and physical principles, with different specificities in terms of spatial resolution, spectral resolution, surface shape constraints and acquisition time. The targeted applications and their requirements often determine the choice of acquisition method.

The capacity to distinguish details on a spectral image depends on both spectral and spatial resolutions. A good spectral resolution allows discrimination between very subtle variations in the spectral reflectance, which can indicate variations in the material composition. A good spatial resolution makes it possible to see very fine details. As for acquisition time, with the exception of snapshot cameras, which acquire the spectral image instantaneously (providing multispectral data only), the acquisition of a hypercube requires a temporal scan. A short acquisition time allows working on live objects, such as the body, and a very short acquisition time can be used to capture videos.

Several methods, surveyed in [Lu and Fei 2014; Li et al. 2013; Garini et al. 2006], are commonly used: the staring approach, the pushbroom approach and the time-scan approach. Snapshot cameras, which simultaneously measure the spectral and spatial information, can be classified as a fourth category, although their acquisition principles are various [Hagen and Kudenov 2013].

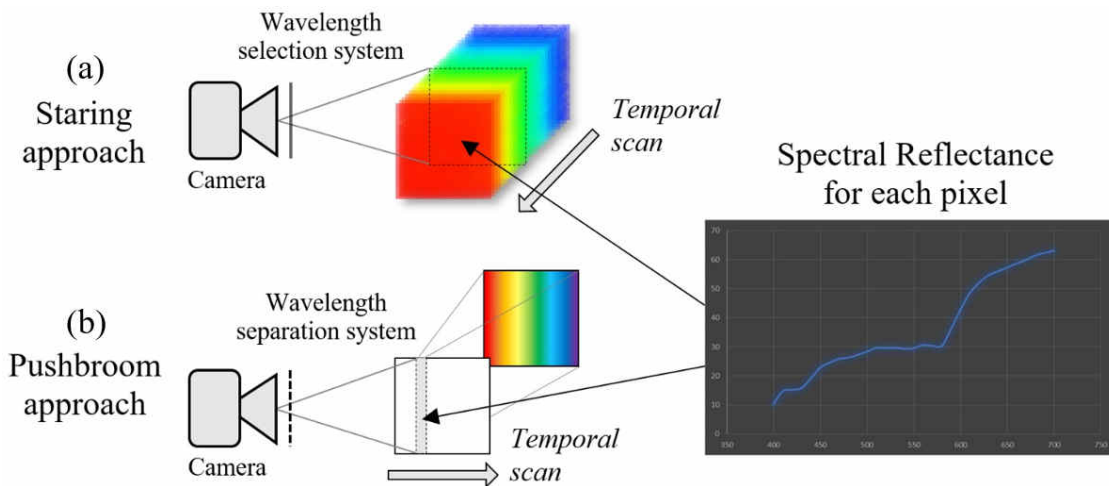


Figure 4.2. Concepts of the (a) staring and (b) pushbroom approaches for hyperspectral imaging.

The *staring approach*, illustrated in Figure 4.2.a, also called the *wavelength scanning approach*, records the full spatial information for each spectral band, and requires a temporal scan of the spectral dimension. When the acquisition system comprises a controlled illumination, this method can be implemented by using a wavelength selection system either at the level of the sensor or at the level of the light source. Several filtering tools can be

used, such as filtering wheels with a set of color filters or tunable filters. Filtering wheels offer a simple acquisition method [Zhang et al. 2016], however, as the filter plates are moving, a geometrical calibration is required [Brauers et al. 2008]. The spectral resolution of such a method is generally low, as the number of filters that can be placed on the wheel is limited.



Figure 4.3. (a) VariSpec™ LCTF (PerkinElmer, USA), (b) LCTF mounted in front of a monochromatic camera.

Tunable filters, such as liquid crystal tunable filters (LCTF) (Figure 4.3) or acousto-optical tunable filters (AOTF), are electro-optical components with no moving parts [Duempelmann et al. 2017; Jullien et al. 2017; Calpe-Maravilla 2006]. Their narrow transmission bandwidth is tuned during a temporal scan to obtain a hyperspectral image with a relatively good spectral resolution. Filtering wheels and tunable filters can be used to filter either the light reflected by the surface in the direction of the sensor, or the light emitted by the source under the condition that the light source power is within the filter acceptance [Jolivot et al. 2013].

In the recent years, systems comprising sets of monochromatic sources rather than filters have emerged. These methods, which consist of illuminating the object using multiple light sources with discrete narrow spectral bandwidths, are attractive in terms of cost and acquisition time, given the availability of a wide range of LEDs with different emission spectra. For example, several systems, using a monochromatic sensor and a set of monochromatic LEDs illuminating in turn the surface of interest, have been designed for applications in medicine [Goel et al. 2015; Li et al. 2012; Ohsaki et al. 2017; Islam et al. 2017]. These systems generally provide multispectral images. Nevertheless, some of them are able to acquire information at video rate and can be used in surgery. The main drawback of this method is the difficulty of achieving uniform illumination on large objects, which is crucial for wide field imaging. This is especially the case when the acquired surface is not flat, as the effects of lighting non-uniformities cannot be corrected using calibration for non-flat surfaces. Uniform lighting requires specific designs, such as integrating spheres, whose complexity increases with the size of the object of interest. Consequently, although this

solution is well-suited to the acquisition of small areas of interest, it presents certain challenges for full face acquisition.

The *pushbroom approach* or *line scanning approach*, illustrated in Figure 4.2.b, consists in acquiring the spectral information for a single line of an image. The complete image is then retrieved by performing a temporal scan of the second spatial dimension. This method generally uses a wavelength separating system such as a diffraction grating or a prism. Line scanning is very similar to single-point spectrometers, with spectral information measured on one line of the object using a 2D sensor: the spectral information is spread along one axis of the sensor, while the other contains spatial information. The temporal scan of the second spatial dimension can be achieved by moving the camera, the object, or the image of the object. When pushbroom cameras are integrated on an automated line for industrial applications such as food inspection or object sorting, the object moves. For applications on still objects for which there is no constraint on acquisition time, the camera can be mounted on a translation system [Pottier et al. 2019]. In both cases, this kind of HSI system is not portable. Recent developments aim at making line scanning faster, more compact and easier to use, by comprising elements designed to move the image of the object rather than the object itself, such as rotating mirrors [Gutiérrez-Gutiérrez et al. 2019]. Methods using line scanning generally provide very high spectral resolution images with more than a hundred wavebands within a wide spectral range. However, their spatial resolution is often limited. We had the opportunity to try the camera SPECIM IQ (Specim, Finland) (see Figure 4.4), a pushbroom system for which the temporal scan of the object image is integrated in the design of the camera. The acquisition time (around 5 seconds with appropriate lighting) was acceptable; the spectral range and resolution were very good (more than 200 wavebands between 400 and 1000 nm); however, the spatial resolution (512×512 pixels) was not sufficient to acquire fine details on a full face.



Figure 4.4. Full face hyperspectral acquisition using the SPECIM IQ camera (Specim, Finland), image displayed at (a) 446 nm and (b) 785 nm.

Time-scan methods, such as Fourier transform interferometry imaging [Bai et al. 2018], are a third category for which the acquired data are a superposition of spectral and spatial information from which the spectral image can be retrieved. Fourier spectroscopy measures the spectrum using light interference rather than filter, allowing it to collect more signal than wavelength scanning methods. These methods are mainly used for remote sensing applications, although some examples of their use in biomedical applications can also be found [Pham et al. 2000].

Finally, *snapshot cameras* use a variety of methods [Hagen and Kudenov 2013]. The simplest design relies on color filters placed on each pixel [Hirose et al. 2016], similarly to the way in which Bayer filters are used in color imaging. The drawback of such methods is the limited number of wavebands measured, leading to a necessary tradeoff between spectral and spatial resolution.

Whatever the acquisition method, spectral reflectance factor is obtained after a calibration step, generally using a perfectly diffusing white sample. The calibration consists in dividing the spectral radiance measured from the object with the spectral radiance measured from a reference surface (a perfectly white diffuser) that is illuminated and viewed in the same way as the object. For a Lambertian reflector (which we can assume skin to be if we ignore the specular reflection), this calibration also yields reflectance, which is equivalent to reflectance factor for perfectly diffusing surfaces. However, when measuring parts of the body that are not flat, the calibration method does not account for the illumination variations that can occur. On curved surface, the measured reflectance varies proportionally to the local irradiance of the surface.

4.1.b. Spectral imaging of the body

Several multispectral systems have been developed to acquire skin in vivo for applications in dermatology and cosmetology. A few hyperspectral cameras also exist for this purpose.

Various commercial systems relying on multispectral imaging have been developed for melanoma analysis since the early 2000s: SIAScope® (MedX Health, Canada) [Moncrieff et al. 2002], MelaFind (MELA Science, US) [Elbaum et al. 2001; Kupetsky and Ferris 2013] and SpectroShade (MHT Optic Research AG, Switzerland) [Tomatis et al. 2005]. These three systems measure between 8 and 15 bandwidths and are combined with software analysis to study melanoma, supplying information useful for diagnosis or even allowing for automatic detection. The target of these systems is however limited to small skin areas, and consequently, their field of view is relatively restricted.

VideometerLab (Videometer, Denmark), illustrated in Figure 4.5, is a commercial multispectral system which comprises a monochromatic sensor and 20 LEDs placed in an integrating sphere of a diameter around 50 cm. It measures the spectral reflectance between 365 and 970 nm under diffuse illumination. One version of the system aims at applications in dermatology and cosmetology and incorporates an articulated arm to allow easy

positioning on the body. The spatial resolution is 40 μm per pixel, which is very good, however the size of the measured area, around 10 cm^2 , is relatively small compared to the size of the system.

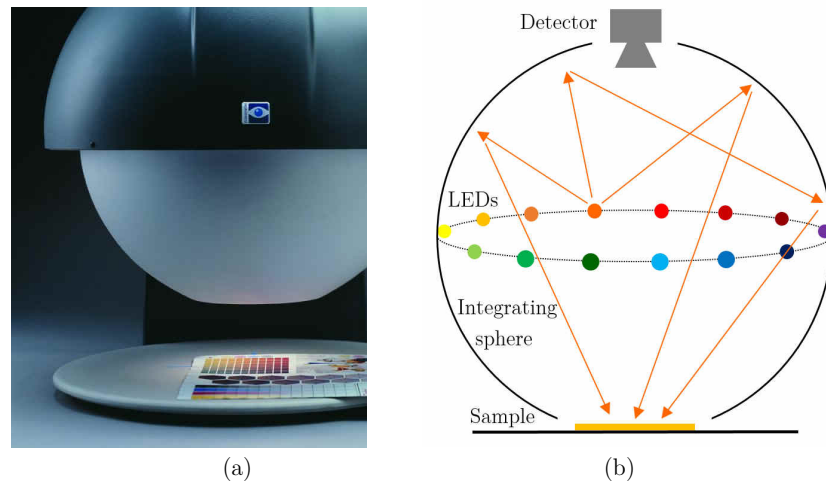


Figure 4.5. (a) VideometerLab multispectral acquisition system (Videometer A/S, Denmark), (b) principle of the setup, which uses a set of LEDs and an integrating sphere to uniformly lit the sample.

SpectraCam® (Newtone Technologies, France), in Figure 4.6, is one of the rare hyperspectral cameras specially designed for *in vivo* skin acquisition. In particular, it meets the requirement of short acquisition time, which is very important for acquisition on a live subject, which is prone to move. Its technical characteristics will be detailed in the next section, as SpectraCam® has been used as a starting point for the design of the full face acquisition system.

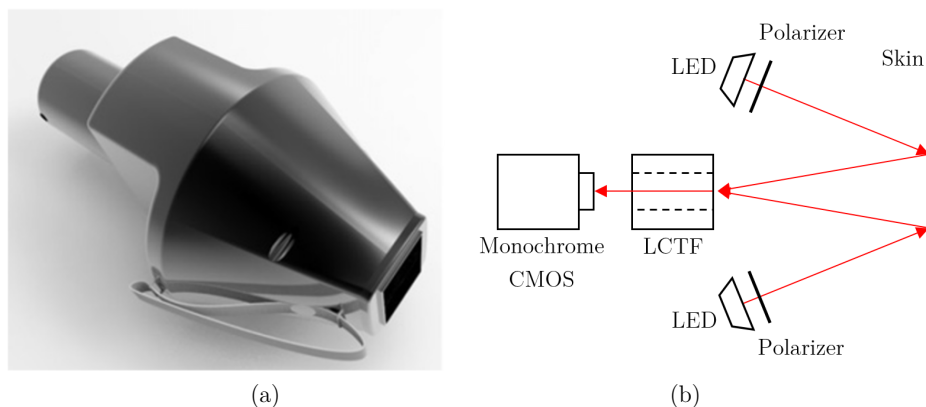


Figure 4.6. (a) SpectraCam® hyperspectral camera (Newtone Technologies, France) and (b) working principle.

4.2. Full face hyperspectral camera

The camera that we designed for full face acquisition has been conceived to provide hyperspectral images within the constraints of in vivo face acquisition: it must be safe for the skin and the eyes; adapted to the geometry of a face; its resolution must be sufficiently high; and its acquisition time must be short. It partly relies on the experience of Newton Technologies in the field of HSI, as the method implemented in SpectraCam® seems to be well-adapted to the specifications listed above. In this section, we detail the acquisition setup and the calibration step necessary to reconstruct the reflectance of the surface.

4.2.a. Acquisition setup and software

The full face hyperspectral imaging system, illustrated in Figure 4.7, is an extension of SpectraCam®, a portable system that can capture images of flat areas measuring 4×5 cm at 30 wavelengths [Nkengne et al. 2018; Seroul et al. 2017]. The wide field acquisition system has been named “SpectraFace”. The new system uses some of the elements already present in the SpectraCam®, but as full face acquisition requires a wider field of view and a deeper depth of field, the dimensions of the acquisition system have been adapted to suit these specific needs.

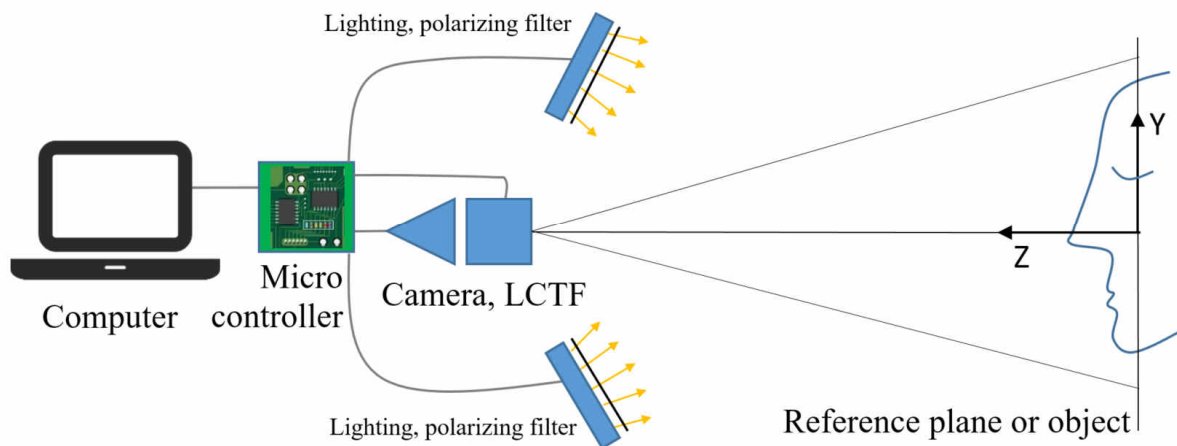


Figure 4.7. Hyperspectral acquisition setup for full face imaging.

The camera sensor comprises a monochrome CMOS 2048×2048 pixels camera (acA2040-90umNIR, Basler, Germany), a 35 mm focal length lens, and the liquid crystal tunable filter (LCTF) (VariSpec™, PerkinElmer, USA) shown in Figure 4.3.

The Basler camera has been selected for its good quantum efficiency in the visible spectrum, shown in Figure 4.8. The camera can encode gray level values on either 8 bits or 12 bits.

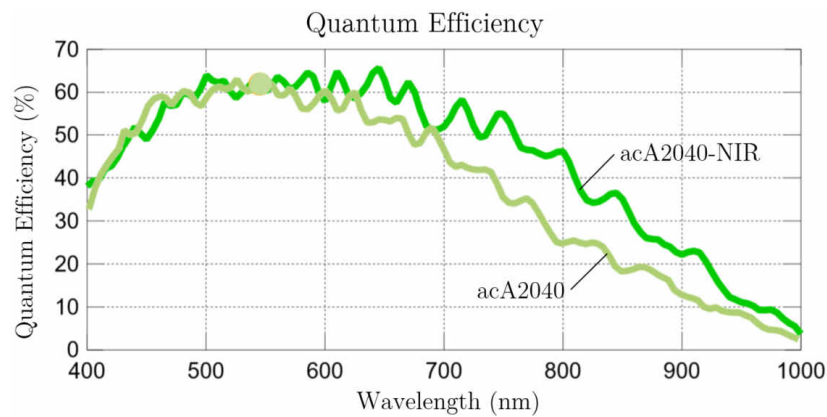


Figure 4.8. Quantum efficiency (%) as a function of wavelength for the acA2040 CMOS camera and its NIR version, given in the datasheet of the camera.

VariSpecTM allows light filtering within the visible spectrum (400 to 720 nm). It is based on the association of several Lyot filters [Gat 2000] (see Figure 4.9), and is equivalent to high quality interference filters with a bandwidth of 10 nm and a precision of 1 nm for the central wavelength. VariSpecTM tuning speed is around 50 milliseconds, which mainly corresponds to the liquid crystal relaxation time from “charge” to “no charge”. Two versions of VariSpecTM have been used, with respective apertures of 22 mm and a 35 mm. For both systems, the half angle of acceptance is 7.5°.

VariSpecTM transmission, illustrated in Figure 4.10, varies according to wavelength, with a very low transmission at 400 nm as well as in the shorter wavelengths. Transmission is weaker than 20% between 400 and 460 nm, which is one of the limitations of using a LCTF. Finally, VariSpecTM polarizes light linearly.

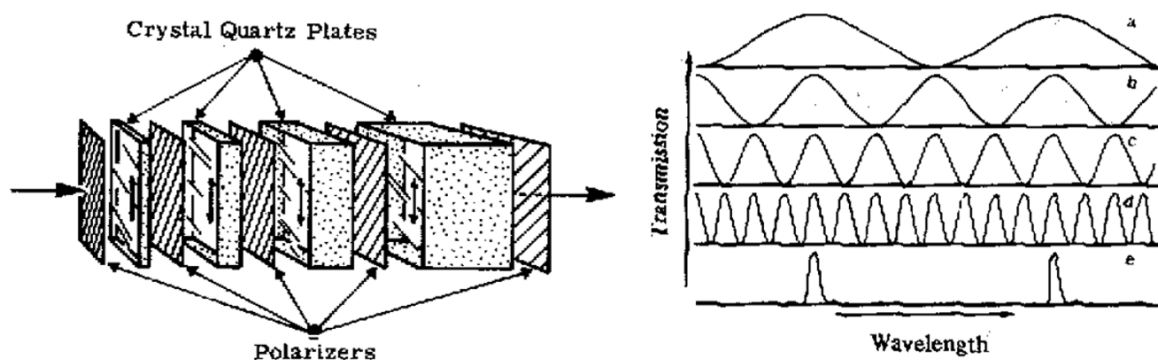


Figure 4.9. Operating principle of Lyot based LCTF [Gat 2000]. Transmission functions *a*, *b*, *c* and *d* are each associated with a crystal quartz plate, and *e* corresponds of the overall transmission. This illustration shows 4 elements, VariSpecTM comprises 6.

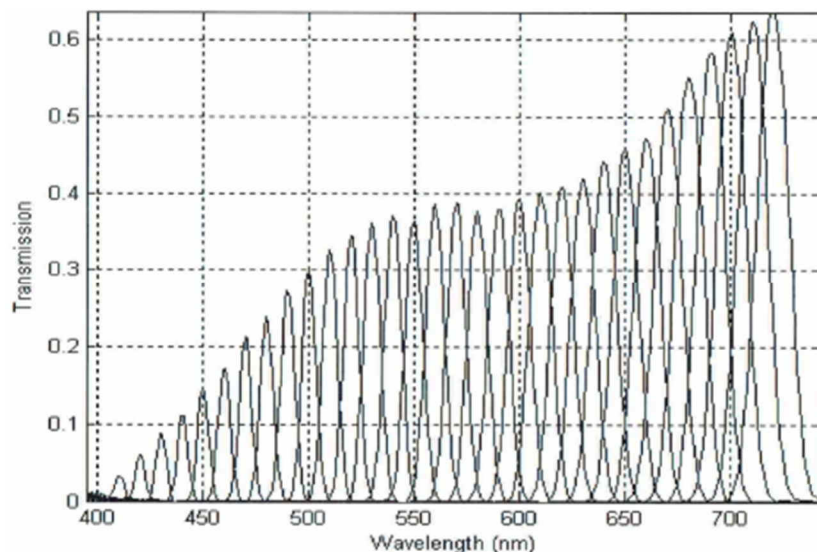


Figure 4.10. VariSpec™ transmission between 400 and 720 nm.

Other tunable filter technologies exist, such as acousto-optical tunable filters (AOTF), which uses a crystal in which vibrational waves at radio frequencies allow a single wavelength to cross. The transmission of an AOTF is relatively high and tuning speed can be quite fast. However, the field-of-view is narrow and the image quality is poor, which limits the potential applications of using AOTF for wide field imaging.

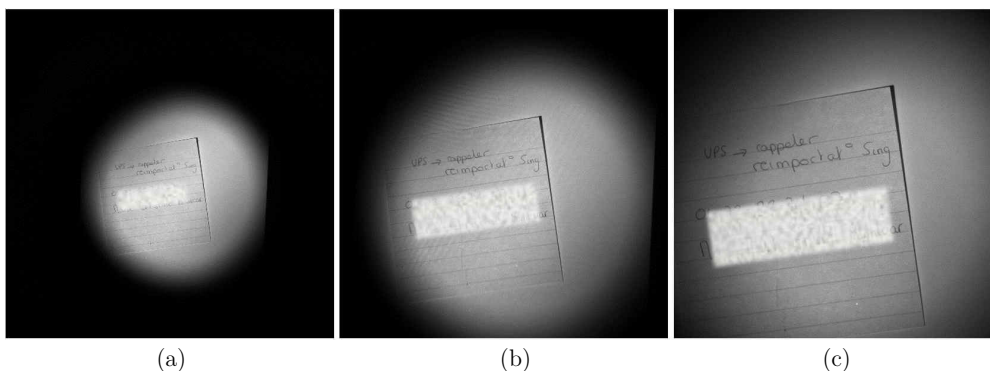


Figure 4.11. Images of the same scene taken with the 22 mm aperture VariSpec™, using three different lenses of focal length: (a) 16mm, (b) 24mm and (c) 35mm.

The focal length of the camera lens has been selected according to the limited acceptance angle of the LCTF. The LCTF is located in front of the camera, and introduces strong vignetting. Figure 4.11 shows the amount of vignetting produced for several focal lengths: the entire field of view was uniformly illuminated in all three images, with the loss of light that can be seen in the edges of the image are the result of vignetting. A 35 mm focal length was selected as a trade-off between minimizing vignetting and minimizing the distance between the camera and the face, so as to create a system that is as compact as

possible. When the large aperture LCTF is used with the 35 mm focal length lens, the recommended distance between the camera and the face is around 50 cm for a full face acquisition. A larger focal length could be chosen to prevent vignetting, but this would require a much longer distance between the camera and the face in order to have a sufficient field of view for full face imaging.

In order to reduce the amount of vignetting, VariSpec™ can also be placed between the sensor and the lens rather than in front of the lens. This would require an adaptor to be added to obtain proper focus. We have not tried such a configuration, but such an approach could improve the efficacy of the camera.

The focus of the camera cannot be adjusted between two acquisitions on two different persons, as the lens of the camera is difficult to access. The position of the face must therefore be constrained. Ear hooks, visible on Figure 4.12, are used to regulate the position of the person, so that the face is in the middle of the field of view and in focus when imaged by the camera. The ear hooks can also be oriented in the direction of the optical axis of the camera or at a 45° angle for side view acquisition.

To collect the highest light signal and obtain a better signal-to-noise ratio for the captured image, the lens entrance pupil is set as relatively open (around F/4). This reduces the camera's depth of field, but for the most part, we are able to obtain a relatively sharp image on the entire face.



Figure 4.12. Full face acquisition using the SpectraFace, side view configuration.

A reference plane is used for the black and white calibration acquisitions. On it, black and white Lambertian samples are successively mounted. These samples are 4A Munsell color sheets of references N 9.5/ for white and N 2/ for black (Munsell Color, USA).

The light sources are two LED lighting units shown in Figure 4.13.a, each one designed with 5 blue and 5 white LEDs aligned in the vertical direction, with LED plastic lens used to spread light horizontally. They provide sufficient irradiance on the skin over the whole visible spectrum for hyperspectral acquisition. Their position on each side of the camera has been set in order to provide uniform lighting on the reference plane: they are placed 30 cm

apart, and oriented in direction of the face at a distance of 40 cm (see details on Figure 4.13.b).

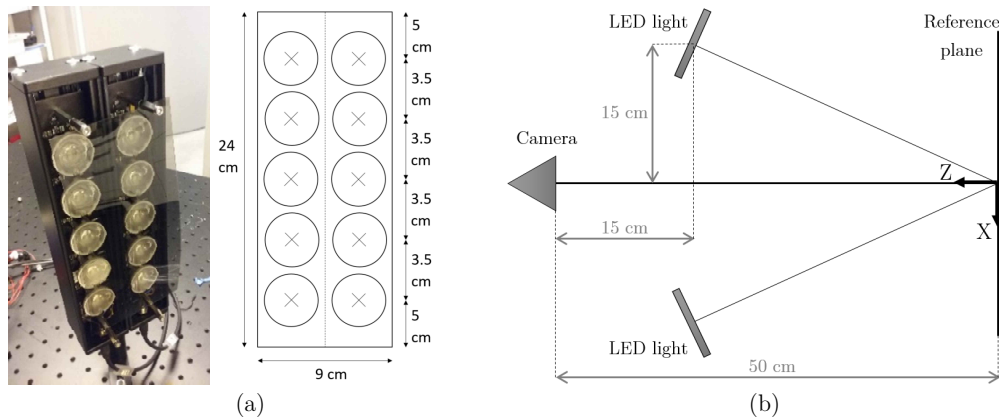


Figure 4.13. (a) Details on the LED lighting unit and (b) geometry of the acquisition system.

Linear polarizing filters are added to each lighting unit. They are oriented to create a cross-polarization (CP) configuration with the LCTF polarization direction, the latter playing the role of an analyzer for the reflected light. This CP configuration is used to remove the specular component of the reflected light, as explained in Chapter 2. The polarizing filters are made of polymer and are almost opaque at 400 nm. For these reasons, the hyperspectral images are acquired between 410 and 700 nm. Below 400 nm, light is harmful to the eyes and skin, and above 700 nm, blood and melanin are almost not absorbent. Therefore, we are not in any case interested in wavelengths outside this range.

A micro-controller is used to synchronize the image acquisition with the LCTF wavelength selection using the trigger mode of the camera for maximum acquisition speed.

The acquisition software has been developed in C++ using the Qt framework. It comprises a live preview tool to ensure that the subject is correctly positioned, and a GUI for settings. For each wavelength, exposure can be independently set to maximize the signal-to-noise ratio. The acquisition software currently used by Newtone Technologies is an improved version of the software developed as part of the PhD project. It includes additional features for clinical studies management. The post-processing of the hyperspectral images is done in Newtone's software NtImageAnalyzer, which includes a calibration function and color conversion tools.

The hyperspectral image acquisition time is around 2.5 seconds. The total acquisition time depends on the exposure time set for each wavelength acquisition as well as on the LCTF tuning time which constraints the delay between two wavelength acquisitions. The exposure time at each wavelength is selected to maximize the amount of light collected by the sensor without saturating the white reference plane used for the calibration described in the next paragraph.

4.2.b. Calibration

Once the hyperspectral acquisition has been performed, a radiometric calibration is necessary to retrieve the reflectance factor of the face from the captured signal. The signal $Q(x, y, \lambda)$ captured by the sensor in each pixel (x, y) for each wavelength λ is proportional to the radiance reflected by the imaged surface in the direction of the camera. Assuming that the surface is a Lambertian reflector, the determining factors are:

- the surface reflectance of the object $R(x, y, \lambda)$,
- the incident irradiance $E(x, y, \lambda)$,
- the sensor spectral response $S(\lambda)$, assumed to be independent from the location of the pixel,
- the optical system transmittance $T(x, y, \lambda)$,
- a coefficient $k(x, y)$ which depends on the angular location of the pixel in the field of view but is similar for all wavelengths,
- and the background noise n , estimated to be similar on all images.

$$Q = \frac{R}{\pi} E \cdot S \cdot T \cdot k + n. \quad (4.1)$$

E , S , T , k and n are unknown parameters that are calibrated via the acquisition of the signals $Q_w(x, y, \lambda)$ and $Q_k(x, y, \lambda)$ from respectively black and white reference Lambertian samples, of respective albedo $\rho_w(\lambda)$ and $\rho_k(\lambda)$. We have:

$$Q_w = \frac{\rho_w}{\pi} E \cdot S \cdot T \cdot k + n, \quad (4.2)$$

and

$$Q_k = \frac{\rho_k}{\pi} E \cdot S \cdot T \cdot k + n. \quad (4.3)$$

The calibration, illustrated by Figure 4.14, results in the object radiance factor (equal to reflectance for skin assumed to be Lambertian) for each pixel and each wavelength after applying the formula:

$$R = \frac{Q - Q_k}{Q_w - Q_k} (\rho_w - \rho_k) + \rho_k. \quad (4.4)$$

The camera calibration relies on the use of black and white reference samples, however, there is research showing that a better spectral calibration can be performed by using two shades of gray as reference samples [Doi et al. 2019]. Such an alternative could be used to improve the quality of the hyperspectral image, and could be especially useful for dark skin acquisitions, as the signal-to-noise ratio is a little low to provide satisfactory images with the current setting.



Figure 4.14. Acquired and corrected images at 590 nm: (a) Non-uniform illumination on the white reference plane, (b) uncalibrated image, (c) calibrated image.

The proposed calibration method gives satisfactory results when applied to flat objects. Applied to 3D objects, however, the incident irradiance on the reference samples differs from the incident irradiance on the measured object, which results in an error in the calibration output. For example, this is observable in Figure 4.14.c, where the sides of the nose appear darker than the rest of the skin. For non-planar objects, a “3D irradiance calibration” (see Chapter 6) is necessary to retrieve the spectral reflectance independently from irradiance variations, requiring a more complex photometric calculation and knowledge of the 3D geometry of the object.

4.3. Efficacy of the method and acquisitions on skin

In this section, the efficacy of the method is discussed and hyperspectral images acquired on skin are presented.

4.3.a. Acquisition speed, resolution and accuracy of the method

For in vivo application on skin, the efficacy of the system can be judged in terms of acquisition speed, resolution and accuracy.

Acquisition time is around 2.5 seconds. This acquisition time is satisfactory for static acquisitions and is short enough to mitigate the risk of the person moving during acquisition. A shorter acquisition time than this appears difficult to achieve for hyperspectral imaging using tunable filters.

The implemented hyperspectral camera captures hypercubes whose resolution is adequate for analysis: spatial resolution (one pixel roughly corresponds to 0.1 mm on the face) is high enough to discern fine details, and spectral resolution (30 narrow wavebands) is sufficient for estimating concentrations of skin components (see Chapter 7).

The spectral accuracy of the camera was investigated by measuring an A4 Munsell sheet (X-Rite, USA) representing the color of light skin (reference CC2 of the ColorChecker®). Two areas of different sizes were analyzed, as illustrated in Figure 4.15.

Area 1 corresponds to the entire field of view of the camera and is larger than a human face. Area 2 is of a smaller size, comparable to that of a human face. The spectrum and the $L^*a^*b^*$ color values of the acquired data were compared to values measured on the same sample using the X-Rite Color i7 spectrophotometer (X-Rite, USA). The measured spectral reflectance are shown in Figure 4.15.b and color values detailed in Table 4.1.

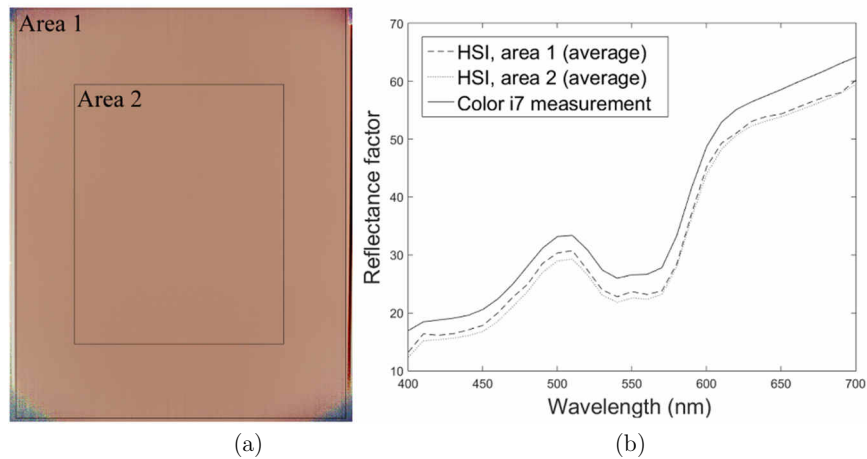


Figure 4.15. (a) Color image of an A4 light skin Munsell sheet measured using the hyperspectral camera, (b) average reflectance factor (%) on two different areas (dotted lines) and comparison with the spectrum acquired using the X-rite Color i7 spectrophotometer (solid line).

		Color i7	HSI area 1	HSI area 2
Mean Value	L^*	64.65	60.86	62.28
	a^*	13.57	14.77	14.20
	b^*	17.84	18.75	18.34
ΔE^*94		REF	3.86	2.41
Standard deviation	L^*	-	5.47	0.47
	a^*	-	18.77	0.89
	b^*	-	27.75	0.78

Table 4.1. CIE1976 $L^*a^*b^*$ values acquired on the Munsell sheet using the X-rite Color i7 spectrophotometer and the hyperspectral camera.

On average, the measured spectra of the two areas are similar. The high standard deviation observed in Area 1 can be explained by the border of the image being affected by noise. This is not the case for the measurement of Area 2. The camera can therefore be used for full face measurement as long as the corners of the image are not part of the area of interest. The ΔE^*94 color difference between the camera measurement and the Color i7

measurement on Area 2 is 2.41. This difference, which appears on the spectral reflectance factor graph (Figure 4.15.b) as a constant shift, results from using two different configurations for the measurements. The Color i7 spectrophotometer measurement was obtained using the “specular reflection excluded” mode of the device, which means that light in the specular direction is excluded, while light scattered everywhere else in the hemisphere is measured. The hyperspectral camera relies on a CP configuration to discard the specular reflection, so that all the scattered light is cut by the polarizer. In this CP configuration, more flux is discarded and the recorded reflectance factor is therefore lower. For skin analysis, this difference is not problematic, as it does not affect the shape of the spectrum containing the “spectral signature” of the measured area.

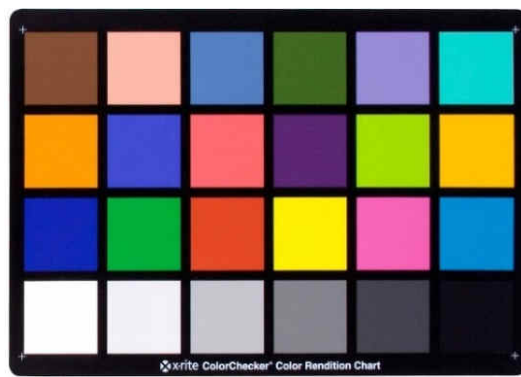


Figure 4.16. ColorChecker (X-Rite, USA) measured using SpectraFace and Metavue™ (X-Rite, USA).

A ColorChecker color chart (X-Rite, USA), shown in Figure 4.16, was also used to assess the system repeatability as well as the correlation between the system and a commercial spectrophotometer.

The system’s repeatability has been estimated in the CIE1976 L*C*h* color space, giving the lightness, chroma and hue of a color. Each patch of the ColorChecker has been imaged three times in a row and the quantity $k = \text{abs}(\sqrt{\text{variance}(x)}/\bar{x})$ has been calculated for each coordinate (denoted as x in the expression). The lower the k parameter, the more repeatable the system. The average value for k is 0.2% for lightness, 1.3% for chroma and 1% for hue. The value is higher for the last two components due to a lower repeatability on achromatic surfaces (i.e. the black and gray patches of the ColorChecker) for chroma and hue. The maximum k value is 7% for the hue of the black patch. This was expected, as chroma and hue are theoretically equal to zero for achromatic samples. Consequently, low levels of noise yield high relative error on the C* and h* and thus lower repeatability.

MetaVue™ from X-Rite is a spectrophotometer used to perform reference measurements on the same ColorCheker. The correlation between Metavue™ and

SpectraFace was investigated in the CIE1976 $L^*a^*b^*$ color space, and the calculated values show a very high correlation: more than 0.99. The high repeatability and correlation with a commercial device on the ColorChecker validates the accuracy of the camera on homogeneous samples.

For applications on a face, which comprise many small elements, both the LCTF and camera contribute to chromatic distortion. This results in spectral errors on small objects in the image, such as spots and hairs. This chromatic error, which can be described as a geometrical distortion for each spectral channel of the camera, is not visible to the eye, but can lead to errors of analysis, discussed in Chapter 7.

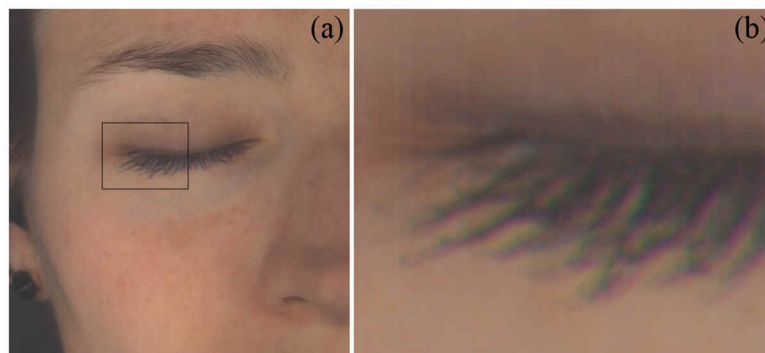


Figure 4.17. Example of chromatic error on eyelashes due to small movements: (a) part of the face image, (b) zoom on the eyelashes.

Chromatic errors can also result from the subject moving during the acquisition process. The eyelashes are especially susceptible to involuntary micro-movements during acquisition. When zooming in the eyelashes, some rainbow effects can be observed on the color image when the person has moved during acquisition, as shown in Figure 4.17.

4.3.b. Skin hyperspectral imaging

The calibrated images can be visualized at any desired wavelength as a grayscale image (see Figure 4.18.a, b and c) or converted into a color image (Figure 4.18.d).

Each of the wavelengths shown in Figure 4.18 highlights a specific skin characteristic and are coherent with the skin optical properties described in Chapter 3. At short wavelengths (Figure 4.18.a), melanin stains are particularly visible, since melanin mainly absorbs UV and blue light. Skin is also strongly scattering for these wavelengths, which means that blue light cannot travel very deeply into the skin before exiting: skin is strongly opaque in this spectral domain. The consequence of this property on the hyperspectral image is that the superficial skin structure and fine lines are clearly visible. Blood vessels can be seen with high contrast between 530 nm and 600 nm (Figure 4.18.b), due to a peak absorbance of hemoglobin in this part of the visible spectrum. Beyond 650 nm (Figure 4.18.c), skin is less scattering and its chromophores are less absorbent, therefore skin is more

translucent, which allows light to travel deeper into the tissue. Consequently, skin appears more uniform and surface details are blurred. In addition, blood absorption coefficient is close to zero for red light, and lips and skin have similar gray levels at 700 nm.



Figure 4.18. Example of channels of a hyperspectral image of a face: Image (a) at 420 nm, (b) at 590 nm, (c) at 700 nm, and (d) color image after conversion into RGB values. (These images can be found in large format in Appendix 1).



Figure 4.19. Color image under several illuminants: (a) D50, (b) D65, (c) D75 and (d) E illuminant.

The hypercube can also be used to model the color of the face under any illuminant, an operation called “relighting”, illustrated by Figure 4.19.

Various effects that can be observed on pathological skin are illustrated by two examples in Figure 4.20, which are images acquired using the SpectraCam® on pathological skin at the University Hospital of Saint-Etienne (France) in collaboration with Pr. Jean Luc Perrot. Figure 4.20.a shows the presence of angiomas and lentigos, whose appearance varies according to two distinct patterns when looking at different wavelengths. These distinct patterns may constitute a classification criterion. On the image at 440 nm, both angiomas and lentigos appear as dark spots, as a consequence of light absorption by melanin and hemoglobin in this waveband. At higher wavelengths, blood contained in angiomas, visible with a high contrast at 520 nm and 580 nm, suddenly “disappears” from the image between 620 nm and 700 nm, since it is almost transparent in this spectral range. The visual signature of lentigos is different: their visibility decreases as wavelength increases.

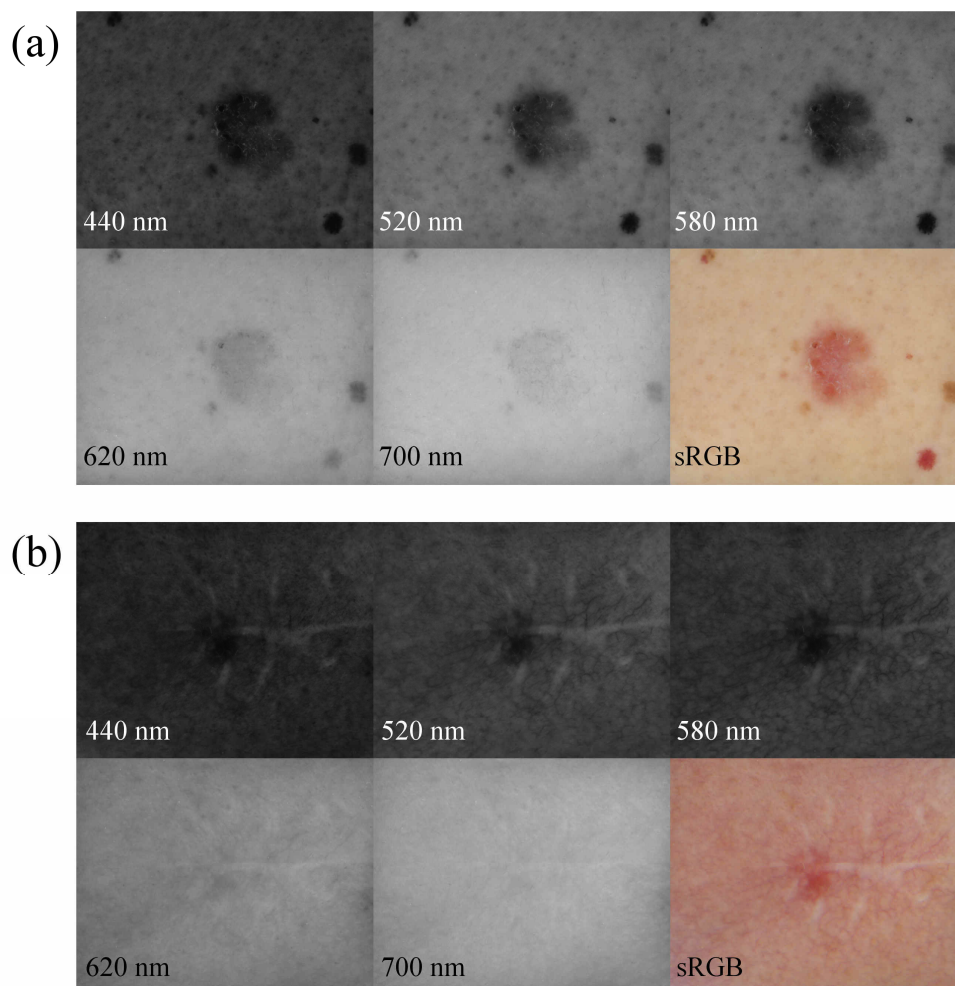


Figure 4.20. Spectral images of a 5×4 cm area of skin at various wavelengths and color representation for (a) angiomas and lentigos, and (b) for an hemangioma and a scar.

The second example (Figure 4.20.b), showing a hemangioma and a scar, demonstrates how spectral imaging can reveal information about how deep blood vessels are in skin. At 440 nm, a few blood vessels can be distinguished, but since skin is very scattering at this wavelength, light cannot propagate very deeply into the tissue, and we can deduce that these blood vessels are very close to the surface. As wavelength increases (see for example at 520 nm and 580 nm), skin becomes more and more translucent, and we can see more and more vessels. For each spectral image, the newly visible vessels are located a bit deeper in the skin than the ones visible at the shorter wavelength. At 620 nm and 700 nm, blood is not very absorbent, therefore blood vessels are no longer visible and skin appears very homogeneous. The scar color does not vary according to wavelength, as scar tissue generally does not contain blood vessels or melanin.

The wavelengths shown in Figure 4.20 have been selected by looking at the images. The automatic selection of wavelengths of interest is not part of this work.

4.4. Conclusion

The developed system meets the requirements of wide field of view, high resolution and short acquisition time that are crucial for obtaining satisfactory full face hypercubes, but achieving such efficacy depends on certain constraints: the lighting must be controlled, and the position of the subject must be fixed. Furthermore, the hyperspectral camera developed in this thesis relies on a technology which is now obsolete, as the key component, VariSpecTM, is no longer commercially available. Other LCTF or tunable filters could in theory be substituted, but we have not so far been able to find a replacement that is adequate in terms of both size and efficacy. If a completely different system had to be developed, spectral acquisition using monochromatic LEDs should definitely be explored. Although it might not work for a full face camera, a system with an average field of view could be designed (e.g. able to image half or a quarter of a face). Such an instrument could provide high spatial resolution images at a favorable cost.

With the emergence of artificial neural networks, hyperspectral cameras could be replaced by multispectral cameras, as discussed later in Chapter 7. If a sufficiently large quantity of diverse skins were to be acquired using both hyperspectral and multispectral cameras, a neural network could be trained to retrieve a complete spectrum from multispectral acquisitions [Setiadi and Nasution 2019]. The accuracy of such a method, however, would highly depend on the quality and diversity of the learning database.

Chapter 5.

Measuring non-flat parts of the body: 3D scanning

Methods for measuring the three-dimensional (3D) geometry of a scene have been an intense topic of research for more than half a century. 3D scanning is now part of our daily life and used in many applications including numerical modeling and virtual reality, which can make it easier to study objects that are fragile or non-accessible; carrying out inspections in manufacturing and healthcare; or simulating immersive environments in games. These applications cover a wide range of fields such as healthcare, industry, cultural heritage and entertainment.

Decades of research in 3D scanning has generated a number of methods surveyed in [Blais 2004], each of which have specific advantages and limitations for a given application. Nowadays, the physical principles of these methods are generally well defined, and recent research axes have focused on improving efficacy, whether in terms of resolution, sensitivity, robustness, speed, sensor miniaturization, or cost.

The 3D measurement of a human body, including the face, is of interest to many applications, spanning the sectors of entertainment, healthcare, virtual reality and augmented reality. For some of these applications, high resolution is sought to create realistic content; in healthcare, this becomes even more crucial, for example if 3D scanning is used as an aid to surgery. With regard to the latter, obtaining high resolution measurements of a living person or part of the body is especially challenging. High resolutions can be obtained either by performing multiple acquisitions, or by using several sensors to simultaneously acquire the necessary information. The former runs the risk of the person moving during the acquisitions, thus affecting the quality of the acquisition, whilst the latter can be prohibitively expensive. Unless price is not a limitation, as for some medical applications, the choice of acquisition method is constrained: a tradeoff must be made between acquisition time, price and quality. In our project, we wish to combine 3D

measurement with hyperspectral imaging, which adds further limitations. The challenge is to find an acquisition method suitable for full face acquisition and hyperspectral imaging that can be produced at an affordable price.

In Section 5.1 of this chapter, we first review the different types of 3D acquisition methods and discuss the existing setups for skin acquisition to determine the best-suited method for full face acquisition. Details about the implemented method and the acquisition system are given in Section 5.2. Acquisitions on a full face and discussion of the method implemented are presented in Section 5.3, and conclusions made in 5.4.

5.1. Optical methods for 3D scanning

Various optical and imaging technologies provide non-contact methods for collecting the geometrical shape of an object. These methods, recapitulated in Figure 5.1, can be categorized into those that are passive and active, with the main point of difference between the two being whether lighting conditions are controlled as part of the method [Remondino and El-Hakim 2006]. Hybrid methods combining both active and passive principles also exist. A good representation of commercially-available 3D scanners can be found on the website <<https://all3dp.com>> [All3dp].

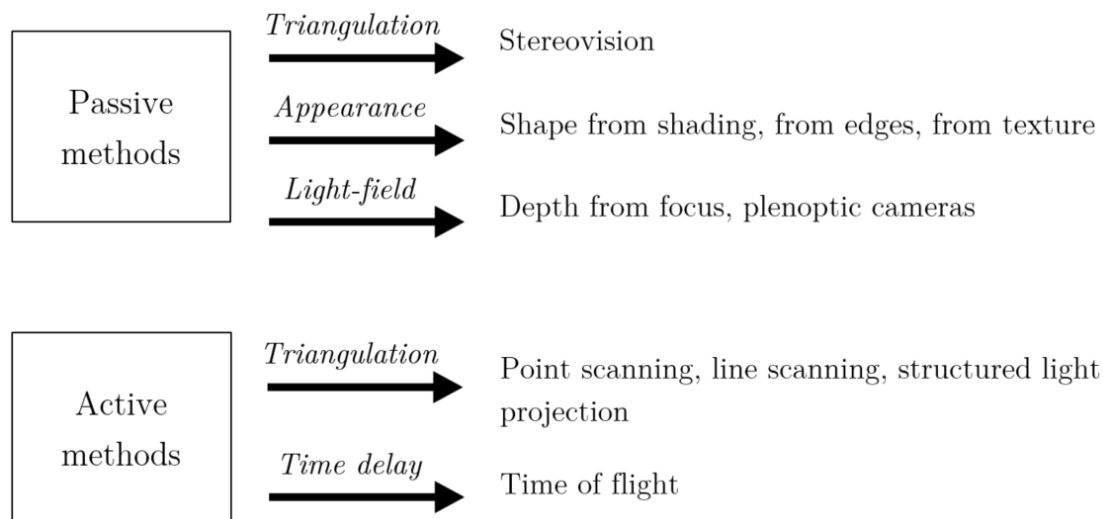


Figure 5.1. Examples of optical methods for 3D scanning, with the acquisition principle involved for each method in italic.

3D information obtained using a 3D scanner is generally in the form of a point cloud that can be visualized as a polygon mesh using a dedicated software (e.g. MeshLab, ISTI – CNR, Italy). Some methods, which can be qualified as “2.5D”, yield depth maps.

Depending on the geometry of the scene, some objects might be occluded and absent from the reconstruction. This limitation can be compensated by merging several acquisitions taken from different points of view.

In this section, some of the existing active methods, passive methods, and their potential applications to body 3D scanning are discussed.

5.1.a. *Passive methods*

Passive methods do not require any controlled illumination and utilize ambient light. Among these methods, *Stereovision*, or *photogrammetry*, is one of the most-used techniques [Zheng et al. 2007]. It is inspired by binocular vision: by recording a scene from at least two points of view, the 3D geometry can be estimated using triangulation. A given point of the scene must be located in each of the acquired images to compute its location in 3D space, and the scene is subsequently reconstructed in 3D by gathering these points. Consequently, binocular and multi-view stereovision consist in solving a correspondence problem. As the development of matching algorithms to find corresponding points is a challenging task for uniform objects, light patterns can be projected onto the surface to create a texture and improve the quality of 3D reconstruction using a hybrid approach. Many systems, of varying scales, cost and quality of results obtained, use stereovision. Some examples are given in Figure 5.2.

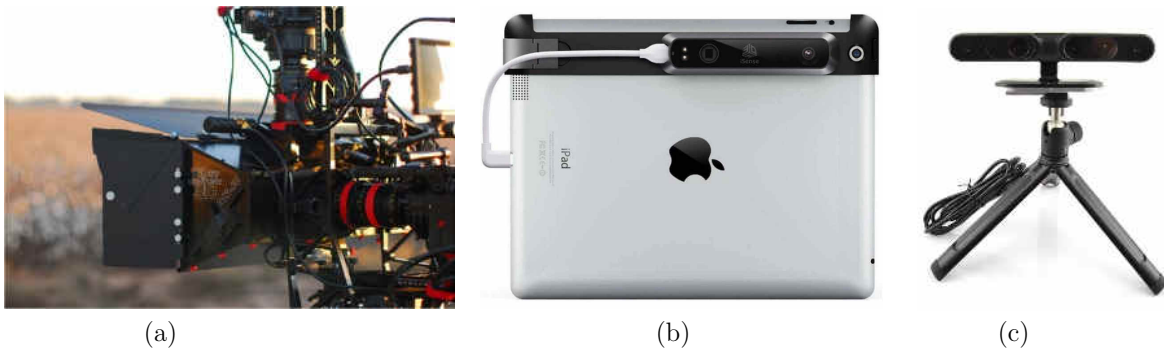


Figure 5.2. (a) Stereoscopic video acquisition system for the production of 3D movies (Angénieux, France), (b) Structure Sensor (Occipital, USA), (c) PrimeSense™ 3D depth scanner combining two cameras and an infrared projector (PrimeSense, Israel).

3D reconstruction from stereovision requires precise knowledge of the position of each camera, which can be determined through calibration. This calibration step can be avoided by using multiple images that contain redundant information. This is, for example, the method used in the Agisoft Metashape software (Agisoft LLC, Russia), which can build a precise 3D model of a scene or object (such as a human face as shown in Figure 5.3.a).

However, quantity and quality of input data is crucial for accurate 3D measurement, as illustrated in Figure 5.3.b, which shows an example of a poor 3D reconstruction.

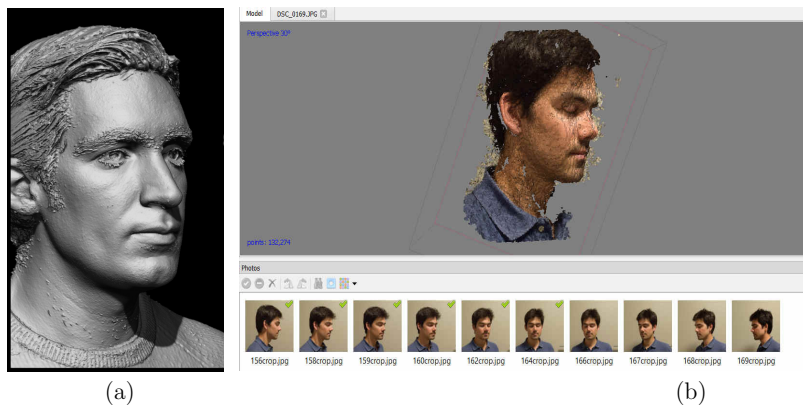


Figure 5.3. (a) Example of very high quality result obtained using the Agisoft Metashape software (data provided by Ten24: <<https://ten24.info/sample-scan/>>). (b) Test of the software in our lab, without a sufficiently high number of images, yielding poor accuracy.

While multi-view 3D scanning remains a classical passive 3D acquisition method, several single view methods sidestep the point-to-point correspondence problem and offer low cost solutions. One of them is the *depth from focus*, or *shape from focus* method [Moeller et al. 2015], which consists in imaging an object at different focus settings and using the defocus to identify the distance to the camera.

Passive methods are preferred when the lighting environment cannot be controlled. However, whilst they provide 3D information within a large field of view, their accuracy is generally lower than most active methods. As such, active methods are generally better-suited for acquisitions where accuracy and the ability to discern small details is a priority.

5.1.b. Active methods

Many active methods are also based on triangulation [Lanman and Taubin 2009]. In contrast to stereovision, active methods use only one camera, with the other (in a stereovision set-up) replaced by a controlled light source that projects onto the object a spot, line or structured light. *Single point laser scanning*, which first emerged in the 1970s, is an example of an early active method which allows 3D acquisition without any ambiguity.

As this process is quite slow, a similar approach using a sweeping line, called a *slit scanner*, is often preferred for the 3D acquisition of small static scenes. Examples of a single point laser scanner and a slit scanner are presented in Figure 5.4. The slit scanner is adequate for scanning small objects that can fit on a turntable, and several “Do it yourself” kits are available at a fairly low cost [Herakleous and Poullis]. Nevertheless, slit scanning is limited to static scenes or objects that can be placed on a turntable.



Figure 5.4. (a) 3D laser scanner (FARO, USA), (b) FabScan Pi slit scanner (Open source kit [Herakleous and Poullis]).

An alternative method is *structured light projection*, which involves projecting a light structure into a full field-of-view. This method is not ambiguity-free, as several identical patterns are projected on the object, but solutions have been proposed to overcome the correspondence problem: coded pattern projection using spots, colour coded fringes and binary coded fringes, or sinusoidal fringe projection with phase unwrapping algorithms being two [Gorthi and Rastogi 2010; Geng 2011].

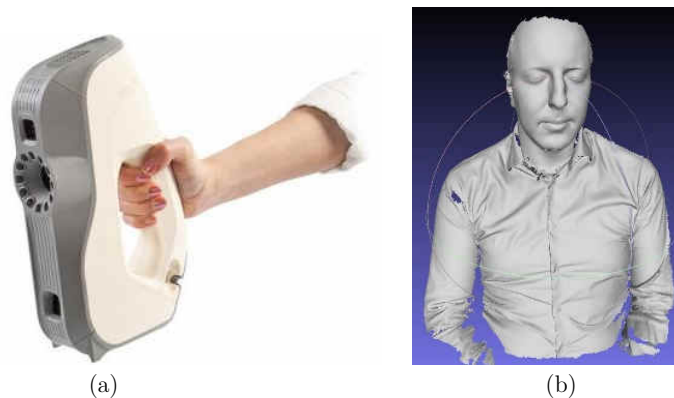


Figure 5.5. (a) Artec EVA 3D scanner and (b) an example of 3D scan obtained when we had the opportunity to test the system.

Figure 5.5 shows the EVA 3D scanner (Artec 3D, Luxembourg), an example of a device using structured light. The 3D geometry of a scene takes several minutes to record, requiring the object to be scanned from several points of view to overcome the limitations of its small field of view (the operator has to move around the object), with the final 3D reconstruction created by stitching the acquired 3D meshes together.

5.1.c. Body 3D scanning

The requirements that must be met to obtain an adequate 3D scan of the human body vary widely in terms of field of view, resolution and acquisition speed, depending on

the type of application. Among passive methods, stereovision is often used for applications in computer graphics, as the limited resolution of the 3D data can be balanced by applying a high quality image, named *texture*, on top of the 3D mesh. Another example of stereoscopic system used for body acquisition is Vectra M3 (Canfield, USA), a solution for full face 3D acquisition combining 3 stereoscopic cameras arranged in a triangle. This system can be used for applications such as face volume analysis in cosmetic surgery. However, its relatively poor resolution (the length of the polygon mesh edge is 1.2 mm) is not sufficient for detailed analysis on fine features such as wrinkles.

For applications where accuracy and resolution are critical, active methods are generally preferred. For example, the EVA fringe projection scanner (Figure 5.5) can be used for applications in healthcare, such as assisting the design of better-fitting custom-made prostheses and orthoses.

For many years in the field of cosmetology, wrinkles have been measured by first replicating skin topology using silicon, then measuring the silicon replica using methods adapted to small samples [Grove et al. 1989; Hatzis 2004]. The study of wrinkles using silicon replicas is today mostly replaced by optical measurements, as it is faster and contactless. A device often used for wrinkle characterizations is Primos^{CR} (Canfield, USA), a small system with field of view around 4×3 cm, which offers a depth resolution of $2 \mu\text{m}$ with pixels of $20 \mu\text{m}$ (Figure 5.6). This device, which relies on multiple fringe projections, can be used to study the efficacy of a cosmetic product in reducing the size of wrinkles. Dermatop-HE, commercialized by Aeva 3D (Luxembourg) is a competitor using the same method.

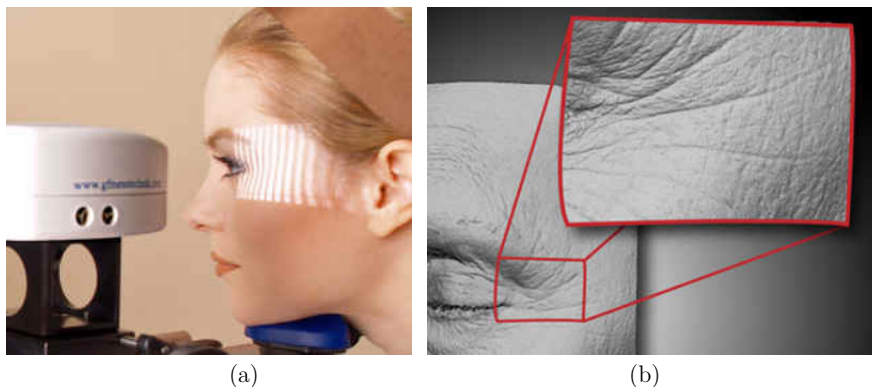


Figure 5.6. (a) Primos^{CR} (Canfield, USA) 3D scanner, using fringe projection for skin measurement and (b) associated high resolution results given as an example by the constructor.

5.2. Full face 3D scanner using fringe projection

The 3D scanning system that we have developed is based on a fringe projection method, which offers an excellent compromise between speed, quality and cost, within a

field of view that is compatible with full face acquisition. This method has already shown its efficacy in biomedical applications such as human body 3D shape measurements [Zhang and Yau 2006], deformation measurements and in vivo measurements [Wang et al. 2013]. Structured light projection also allows the use of a single camera for both hyperspectral and 3D acquisition, which ensures a good pixel to pixel correspondence between the measured polygon mesh and the color texture.

The overall acquisition process, illustrated in Figure 5.7, is as follows: After a radiometric calibration of the projector (detailed in 5.2.e), sinusoid fringes are projected onto the face and distorted by the geometry of the face. The difference between the measured phase on the face and the measured phase on a reference plane yields the 3D geometry using the triangulation principle. It should be noted however that in a first stage, this phase difference is “wrapped”, i.e. discontinuous and limited to $[-\pi, \pi]$. The continuous phase is retrieved from applying a phase unwrapping algorithm [Ghiglia and Romero 1994]. Finally, the phase can be converted into a depth map after a calibration step, and used to create a 3D mesh. Once the 3D reconstruction is completed, a color texture can be added for a better visual rendering.

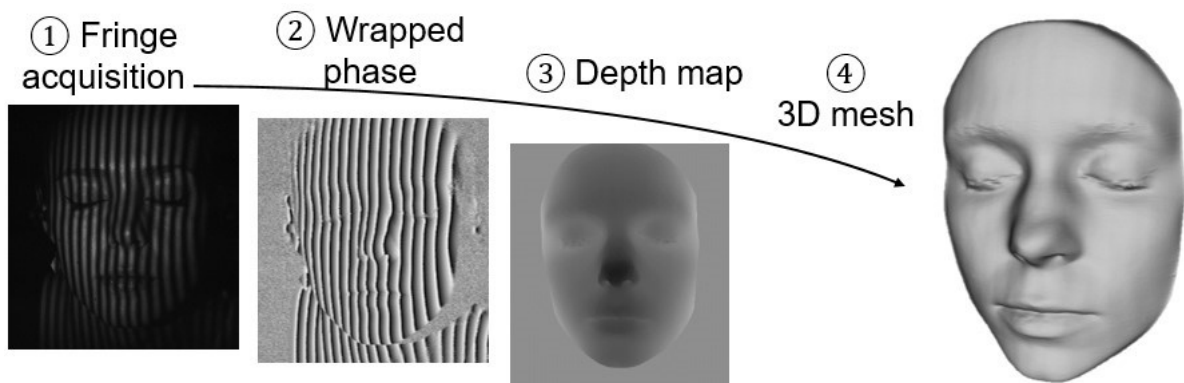


Figure 5.7. Illustration of the 3D scanner acquisition and reconstruction process.

In this section, we detail only the 3D scanner, but the system is combined with the hyperspectral camera presented in the previous chapter. The architecture of the system must therefore be compatible with the hyperspectral camera. The acquisition time must also be as short as possible, as the overall acquisition time (3D scanning and hyperspectral image) must remain within a few seconds for in vivo acquisition.

The acquisition setup and software are presented first. Then, the different tools that have been employed are detailed: the triangulation principle and the phase shift method are at the root of the method; phase unwrapping is required to solve the correspondence problem; finally, for a practical implementation, the radiometric and geometric calibrations that are necessary are presented.

5.2.a. Acquisition setup and software

The acquisition setup is illustrated in Figure 5.8. The sensor part is from the hyperspectral camera (Basler monochrome CMOS 2048×2048 pixel camera, 35 mm focal length lens, and liquid crystal tunable filter – LCTF). A distance of around 40 cm between the camera and the face is ideal for full face acquisition with the chosen focal length.

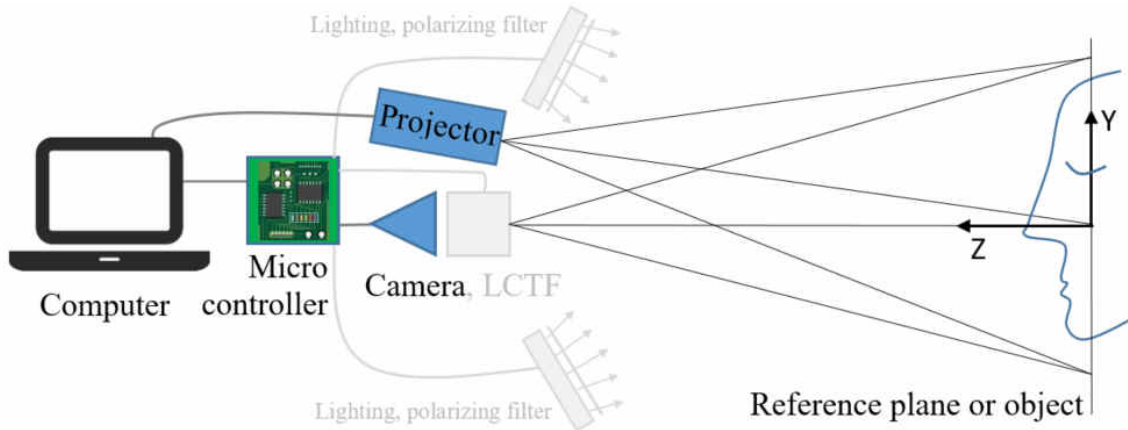


Figure 5.8. 3D scanner acquisition setup. Parts in gray correspond to the elements used for the hyperspectral acquisition.

For fringe projection, the system comprises a portable digital LED projector (DLP) (ML330, Optoma, Taiwan), connected to the computer. This DLP has been selected for its modest dimensions (it weighs 460 g), its short focal length (12 mm), its ability to focus at a distance as short as 30 cm, its acceptable luminous flux compared to most portable projectors (500 lumens according to the manufacturer), its acceptable resolution in its range (1280×800 pixels), and its relatively low price (now less than 500€). This projector is not the most powerful DLP on the market, but is one of the rare systems satisfying the conditions of a very short projection distance and sufficiently long focal length. The shorter the focal length, the larger the projected image for a fixed projector-to-image distance. For our application, we preferred a small field of projection, as long as it remained large enough to cover the human face, to maximize the resolution of the projected image and light power on the area of interest (the smaller the projection area, the higher the illuminance).

The light sources of the projector are red, green and blue LEDs, with maximum emission at 450 nm, 520 nm and 630 nm respectively. The spectral radiance of the white light emitted by the projector, corresponding to the three LEDs turned on together, is plotted in Figure 5.9. When 3D scanning is combined with hyperspectral imaging, the LCTF of the hyperspectral camera is a restricting element for the 3D scanner. It limits the field of view and reduces the amount of light transmitted to the sensor. More precisely, its transmission corresponds to a 10 nm wide waveband centered on a selected wavelength. The LCTF wavelength must be carefully chosen for the 3D scanning acquisition, depending

on the spectral power distribution of the projector light. The emission of the DLP limits our possibilities to 450 nm, 520 nm and 630 nm. For acquisition on translucent materials such as skin, a wavelength for which the material is most opaque should be selected (this point will be discussed in Section 5.3). For skin, red should be avoided and blue should be preferred. However, the LCTF transmission at 450 nm is very low (less than 15%) and skin reflectance at this wavelength is low as well, yielding a bad signal-to-noise ratio. The 3D acquisition wavelength is thus set to 520 nm.

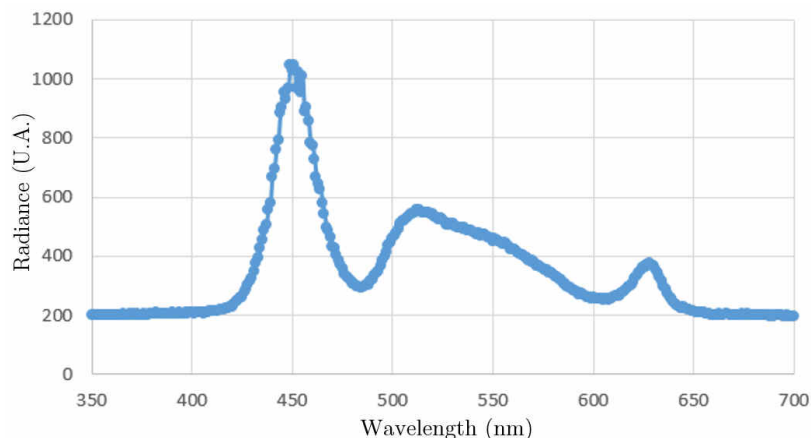


Figure 5.9. Spectral radiance of the white light emitted by the Optoma ML 330 DLP measured by using a spectrophotometer.

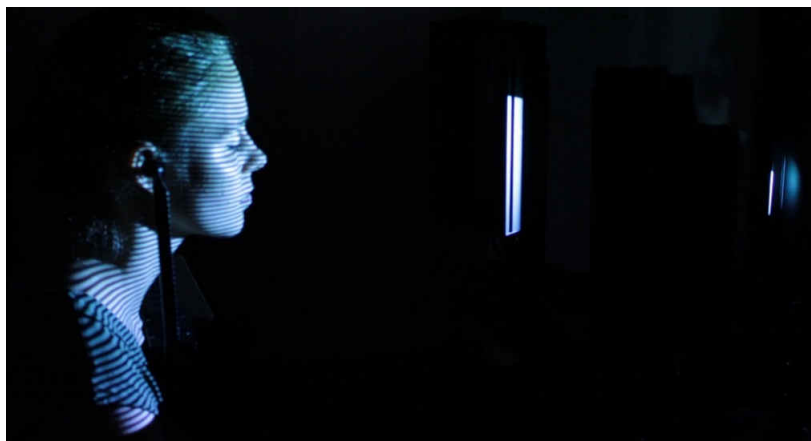


Figure 5.10. Example of 3D acquisition using SpectraFace, with the face illuminated by the Optoma projector.

The angle between the camera and the projector is approximately 10 degrees. It allows full face acquisition while minimizing occluded areas. Originally, the fringe direction was set as vertical, which is often the case for face 3D measurement using fringe projection: considering that the face is similar to a vertical cylinder, vertical fringes yield the best accuracy for this kind of topology. However, our experience has shown that the method

using vertical fringes was sensitive to the person's face orientation, and one side of the nose was often occluded when vertical fringes were used. Horizontal fringes were finally preferred, as they were more robust to such occlusions. Some 3D acquisition methods project both vertical and horizontal fringes to increase the accuracy of the measurement. For our application, however, this possibility has been rejected as it would increase acquisition time above what is reasonable for in vivo acquisition. The projector can be placed either above or beneath the camera, but we chose to place it beneath to obtain better results on the nose reconstruction. Figure 5.10 shows the fringes projected for 3D scanning.

A panel is used for reference and calibration, defining the X and Y axes of the Cartesian coordinate system shown in Figure 5.8. The panel is perpendicular to the optical axis of the camera (Z axis), and is mounted on a translation system which allows precise translations along the Z axis. The camera and projector pupils are located on the same (X , Y) plane.

The acquisition software used has already been mentioned in Chapter 4, and was developed in C++ using the Qt framework. This software provides a live preview of the scene and controls the 3D acquisition (as well as the hyperspectral acquisition). It can be used to perform a radiometric calibration of the projector (detailed below), and generate corrected fringe images. The SpectraFace system used by Newton Technologies is controlled using another software, developed by the company to manage clinical studies in addition to the basic acquisition and calibration features.

The fringe images acquired using this software correspond to the first step of the 3D scanning process. These images are then used to compute the object's 3D geometry using MatLab scripts (MathWorks, USA), written using the triangulation principle, the phase-shift method and the unwrapping algorithm described below.

Acquisition time is around 2 seconds.

5.2.b. *Triangulation principle*

Sinusoid fringes are projected onto an object and deformed according to the object geometry. Once the phase deformation is measured, the triangulation principle is applied to retrieve the depth information between the object and the reference plane.

Let us consider a perfect projector whose pupil is centered at a point E , and a perfect camera whose pupil is centered at a point D (Figure 5.11). Let us also consider a reference plane where the optical axes of the camera and the projector intercept at points G and C , respectively. Let us now consider a point F on the object, separated from the reference plane by a length h called the depth. Point F is illuminated by a ray from the projector that would intercept the reference plane at point A were it not for the presence of the object; point F is also viewed by the same pixel (x, y) in the camera as point B on the reference plane. We denote as L the distance DG between the reference plane and the camera's pupil; as b the distance DE between the camera and projector pupils; and as f the fringe frequency on the reference plane.

According to the pinhole model, the depth h satisfies the following equation:

$$\frac{AB}{DE} = \frac{h}{DG - h}. \quad (5.1)$$

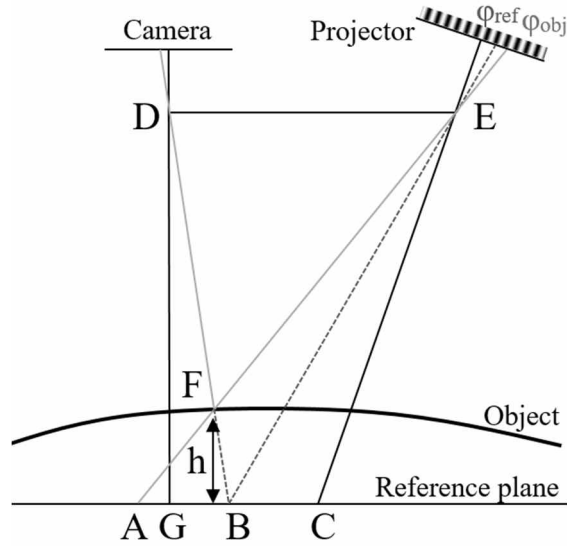


Figure 5.11. Illustration of the triangulation principle.

The phase difference between points A and B is

$$\Delta\varphi = \varphi_{obj} - \varphi_{ref}, \quad (5.2)$$

where φ_{obj} and φ_{ref} are respectively the phase at point F (or A) and at point B. Consequently,

$$\Delta\varphi = 2\pi f \cdot AB. \quad (5.3)$$

From Eqs. (5.1) and (5.3), it is possible to write the relationship between the depth and the phase difference:

$$h = \frac{L}{1 + 2\pi fb/\Delta\varphi}. \quad (5.4)$$

5.2.c. Phase shift principle

In order to retrieve the phase difference information in each pixel (x, y) , we use the phase shift method [Gorthi and Rastogi 2010]. Let us consider a perfect projector. N fringe images are projected, encoded into an 8 bit gray scale such that the radiance incident on a flat reference plane in each pixel (x, y) is defined by the following equation:

$$I_n(x, y) = I' + I'' \cos\left(2\pi fx + \frac{2\pi(n-1)}{N}\right), \quad n = 1, \dots, N, \quad (5.5)$$

where I' is the average radiance, I'' is the modulation and f is the fringe frequency on the reference plane.

The projected images represent identical fringes, each of which are successively shifted by $2\pi/N$. The phase, $2\pi fx$, depends on the pixel location x .

We denote as J_n ($n=1, \dots, N$) the images recorded by the camera (we do not model camera noise here), which are fringes whose phase $\varphi(x, y)$ is modified in function of the 3D geometry of the object:

$$J_n(x, y) = J'(x, y) + J''(x, y) \cos\left(\varphi(x, y) + \frac{2\pi(n-1)}{N}\right), \quad n = 1, \dots, N, \quad (5.6)$$

where J' is the average value and J'' is the modulation.

The phase $\varphi(x, y)$ can be computed in each pixel by using the following equation:

$$\varphi(x, y) = \arctan\left(\frac{\sum_{n=1}^N J_n(x, y) \sin\left(\frac{2\pi(n-1)}{N}\right)}{\sum_{n=1}^N J_n(x, y) \cos\left(\frac{2\pi(n-1)}{N}\right)}\right) \in [-\pi, \pi], \quad (5.7)$$

From the N acquired images, the grayscale image Q_{3D} that would be measured if the illumination was uniform (which also corresponds to the average value J') can be retrieved:

$$Q_{3D} = \frac{1}{N} \sum_{n=1}^N J_n. \quad (5.8)$$

The 3D scanning process is illustrated in Figure 5.12. The phase is computed from images projected on the object and on a reference plane (Figure 5.12.a-b) The information that yields the depth map of the object is the phase difference $\Delta\varphi$ (Figure 5.12.c).

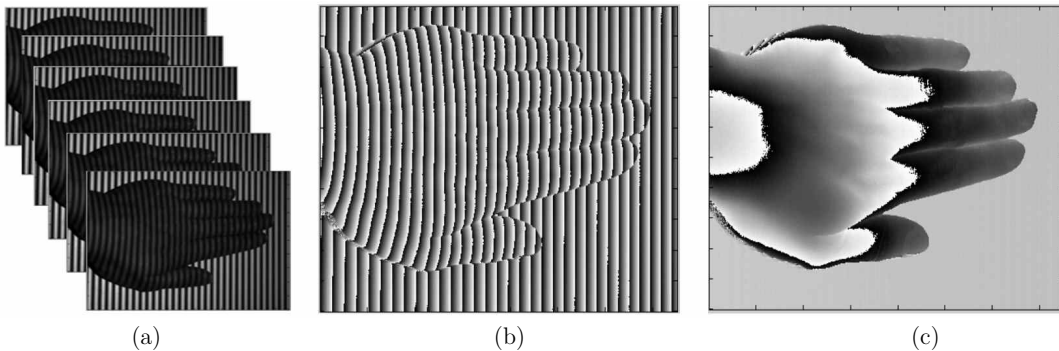


Figure 5.12. (a) Image acquisition ($N = 6$), (b) object wrapped phase and (c) phase difference between the object and the reference plane.

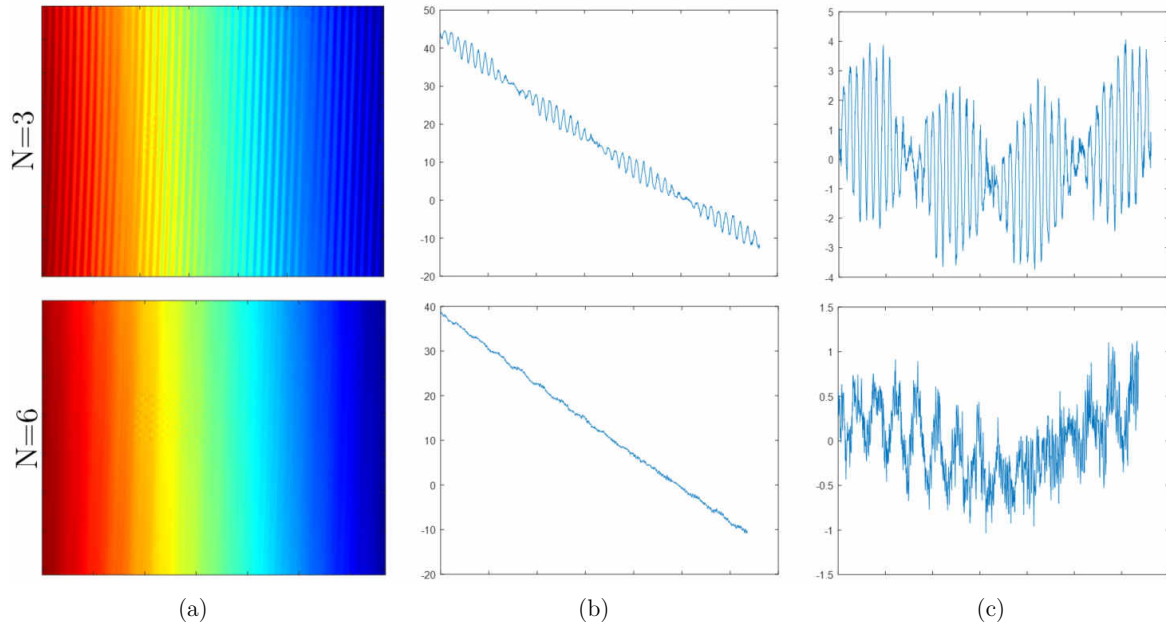


Figure 5.13. Phase shift method with $N = 3$ (top) and $N = 6$ (bottom): (a) depth map of a tilted plane (false color), (b) profile of the phase map and (c) error between the profile and the best linear fit. The variations are displayed in mm. The root-mean-square error is 1.6 mm for $N = 3$ and 0.4 mm for $N = 6$.

The selection of the value for N depends on the application requirements. When N increases, the acquisition time also increases but noise is reduced, as illustrated in Figure 5.13 [Li and Li 2011]. The observed noise, a consequence of the projector’s limitations, is specific to fringe projection acquisition: it is periodic, with a period of N times the period of the projected fringes. For our acquisition system, an N value around 5 or 6 is a good compromise between reduced noise and acquisition time.

5.2.d. Phase unwrapping

The phase calculated using Eq. (5.7) is discontinuous since its values are restricted to the interval $[-\pi, \pi]$. The continuous phase is retrieved through a phase unwrapping algorithm. Phase unwrapping techniques can be classified into two categories: temporal phase unwrapping and spatial phase unwrapping. *Temporal phase unwrapping* [Zuo et al. 2016] relies on the projection of a large number of images, such as using binary coded fringes, multiple frequency acquisition or coded structured light, in order to obtain the necessary information and solve the unwrapping problem. *Spatial phase unwrapping* uses the continuity between pixels to retrieve the original phase [Ghiglia and Pritt 1998]. As short acquisition time is of primary importance in our project, we ruled out the implementation of a temporal method.

An intuitive spatial phase unwrapping method is to assume that the phase difference between two neighboring pixels is always less than π : the phase has to be unwrapped each time the difference between two neighboring pixels is higher than π . Regrettably, this

method is not robust to noise and errors propagate, as illustrated in Figure 5.14, necessitating more complex solutions.

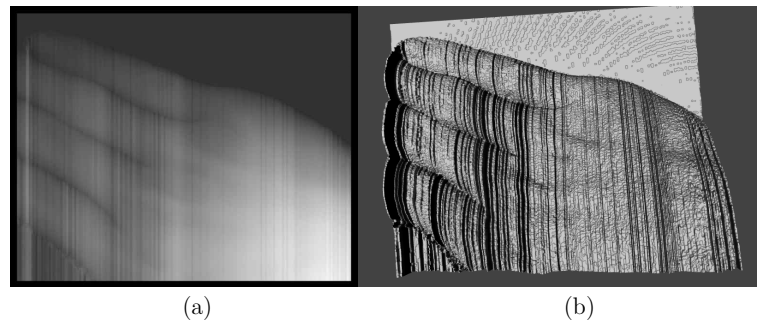


Figure 5.14. (a) Example of a depth map obtained after applying an unwrapping algorithm using phase continuity only, (b) corresponding 3D mesh display.

The solution that we selected is Ghilia’s “2D unweighted phase unwrapping” [Ghiglia and Romero 1994], a spatial method based on the discrete cosine transform (DCT). Ghilia’s method, however, yields distorted continuous phase, especially when the image contains the object’s borders or when parts of the image contain significant depth variations. As can be seen in Figure 5.15, which represents a hand in front of a plane, the phase is not very well reconstructed in the areas of transition between the hand and the background plane. This is especially visible on Figure 5.15.c, which shows the difference between the original wrapped phase and the unwrapped phase using the DCT algorithm. As phase unwrapping corresponds to the removal of 2π discontinuities, the difference between these two images should be exclusively multiples of 2π , which is not the case. Otherwise, Figure 5.15.c would display only 4 uniform areas.

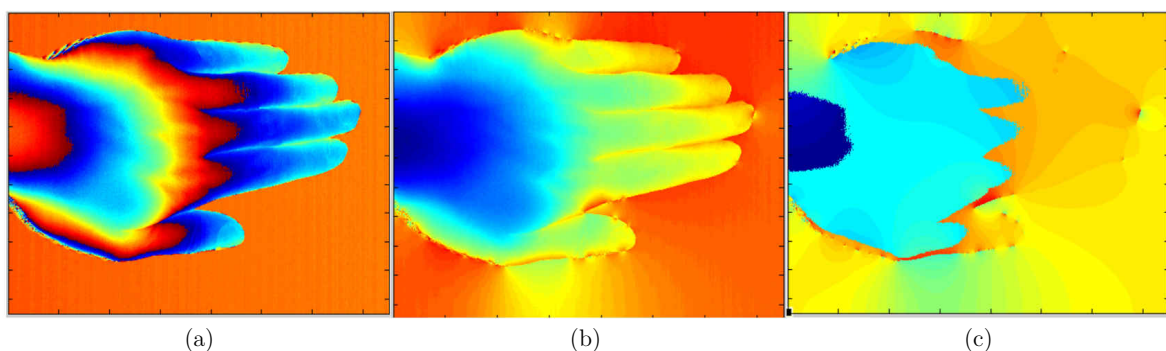


Figure 5.15. Example of Ghilia’s unwrapping method on a hand. (a) Original wrapped phase, (b) continuous phase obtained from the DCT method and (c) difference between the wrapped phase and the unwrapped phase (false colors display).

To prevent these deformations, we decided to add an additional step to the DCT method, as follows. Let us denote as $\phi_{i,j}$ the wrapped phase for each pixel (i, j) , $\varphi_{i,j}$ the

continuous phase and $\hat{\phi}_{i,j}$ the estimated phase using the DCT method, the latter two being given by Eqs. (5.9) and (5.10). The exact continuous phase is retrieved by applying Eq. (5.12), where $\lfloor \cdot \rfloor$ denotes the floor function. By definition, we can write:

$$\varphi_{i,j} = \phi_{i,j} + 2\pi k_{i,j}, \quad k \in \mathbb{Z}, \quad (5.9)$$

$$\hat{\phi}_{i,j} = \phi_{i,j} + 2\pi k_{i,j} + \varepsilon_{i,j}, \quad \text{abs}(\varepsilon_{i,j}) < 2\pi, \quad (5.10)$$

Thus:

$$\frac{\hat{\phi}_{i,j} - \phi_{i,j}}{2\pi} = \frac{2\pi k_{i,j} + \varepsilon}{2\pi} = k_{i,j} + \varepsilon_{i,j}', \quad \text{abs}(\varepsilon_{i,j}') < 1, \quad (5.11)$$

$$\varphi_{i,j} = \phi_{i,j} + 2\pi \cdot \left\lfloor \frac{\hat{\phi}_{i,j} - \phi_{i,j}}{2\pi} \right\rfloor. \quad (5.12)$$

This method yields very good results as long as there are no problematic discontinuities. We can see in the image of the hand (Figure 5.16) that the phase map of the background is not well reconstructed. However, when the original wrapped phase is cropped to eliminate significant phase variations, as in Figure 5.17, this method is quite effective and yields depth maps without artefacts with a short computation time.

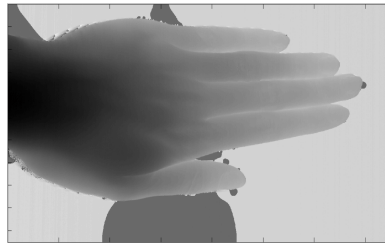


Figure 5.16. Continuous phase map of the hand obtained after applying the modified DTC method. We notice areas of errors on the background plane, due to high phase variations.

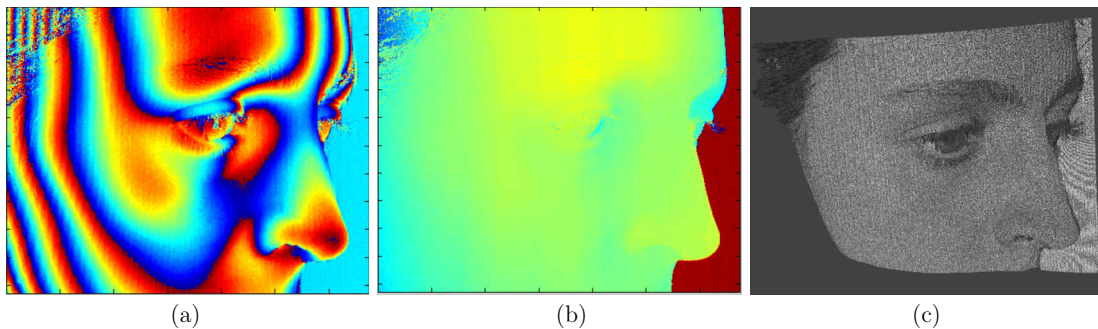


Figure 5.17. 3D reconstructions obtained using the modified DTC method on a cropped face: (a) wrapped phase, (b) unwrapped phase and (c) 3D mesh display.

For full face acquisition, the camera's field of view must necessarily include some of the background. As wrapped phase is especially noisy in pixels belonging to this background area (see Figure 5.18.a), a polygon area is created to delimit the area of interest (i.e. the face) and used as a mask to discard the background pixels in the phase reconstruction process. Then, the phase-unwrapping algorithm is applied to the discontinuous phase. If no precautions are taken, applying the phase unwrapping algorithm on a discontinuous image leads to substantial errors in the phase reconstruction. These errors occur for masked images because the new border created when masking the image adds very sharp discontinuities. These errors correspond to several phase "jumps" of 2π (see Figure 5.18.b).

In our first attempt to address this issue, we tried to identify the areas where the phase was not well-reconstructed, i.e. where there were phase "jumps" of 2π , assuming that the shape of the acquired face did not contain such discontinuities. The correct phase was then retrieved by adding or subtracting multiples of 2π on the erroneous pixels. This method was implemented using a watershed algorithm to locate the pixels that required correction. However, this approach was later abandoned as it was not sufficiently robust and required too much manual supervision to obtain a satisfactory phase reconstruction.

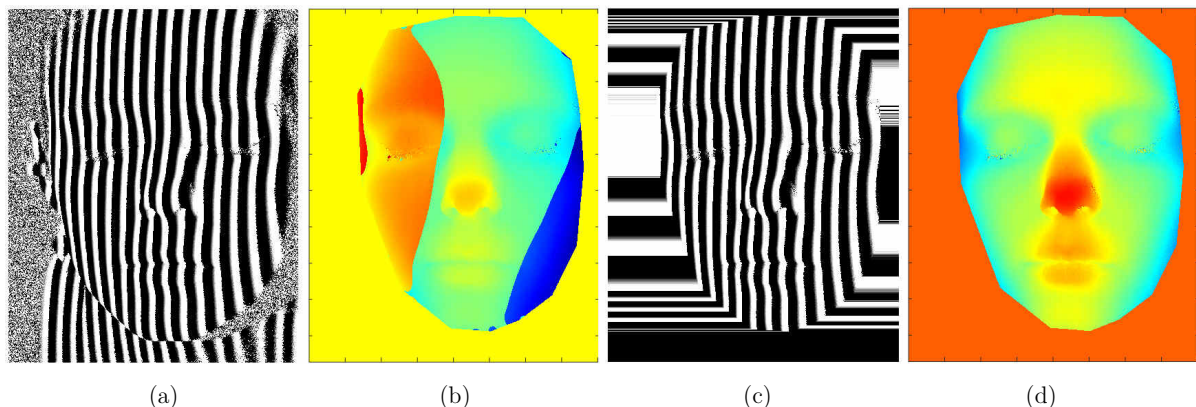


Figure 5.18. Unwrapping method for masked images using horizontal padding: (a) Original wrapped phase, (b) unwrapped phase when no padding is used, (c) masked and padded wrapped phase and (d) unwrapped phase when padding is used.

Our next idea was to directly remove the discontinuities at the edge of the mask. A typical method for achieving this purpose, which can also be used for computing the Fourier transform on masked images without obtaining all the frequencies created by the edge of the mask, is to "erase" the edge discontinuity by using the heat equation. The zeros in the area outside the zone of interest are replaced by values computed using the heat equation. However, this method requires a long computation time. We finally conceived a simpler solution, illustrated in Figure 5.18.c: the masked images are padded with the values of the pixels located at the edge, in the horizontal direction for vertical fringes and vice versa. This method does not totally remove the edge discontinuity, but discards most of the high

spatial frequencies resulting from the edge of the mask. It is sufficient for the unwrapping method to yield satisfactory unwrapped phase maps. The limitation of this method is that it requires a mainly convex mask, but this is generally the case for a human face.

Finally, noise on the phase map can produce phase errors within the masked area. This usually occurs when phase information is missing due to particular characteristics of the area of the object, such as on the eyelashes. In such cases, the error is a clear discontinuity of $2k\pi$ ($k \in \mathbb{Z}$) and it is relatively easy to correct it by manually adding $2k\pi$.

Once the continuous phase map is retrieved, the depth map of the object can be obtained by applying the triangulation principle given by Eq. (5.4) using parameters determined through calibration.

The acquisition process comprises three calibration steps for 3D scanning: a radiometric calibration which must be performed prior to generating the projected fringes, a depth calibration which allows the conversion of the phase onto a depth map, and an XY plane calibration which allows the conversion of the depth map into (x, y, z) coordinates expressed in millimeters, detailed in the following paragraphs.

5.2.e. Radiometric calibration

The projected fringes must be perfectly sinusoidal to ensure optimal 3D reconstruction quality. In practice, however, the sinusoidal profile of the projected image is distorted due to the radiometric non-linearity of the projector. Indeed, commercial digital projectors are designed to project nonlinear images in order to comply with human vision, which has a nonlinear sensitivity. As the selected DLP does not have a mode for projecting linear images, a radiometric calibration is necessary [Li and Li 2011; Zhang and Huang 2017]. The method we have chosen consists in measuring the projector non-linearity by successively projecting gray levels on a white plane. For each input gray level, the average value on the recorded image is calculated and we obtain an experimental curve. The projector's non-linearity is then modeled: the quadratic polynomial that best matches the experimental curve is computed using a least-square algorithm. Finally, this model is used to compute a new fringe image, closer to sinusoidal fringes after projection. This method accounts for both the projector's and camera's non-linearity. In practice, however, the selected camera is very linear and most of the grayscale distortion comes from the projector.

The projector's non-linearity is modeled by the following expression, relying on the gray level I_{output} measured by the camera, the gray level I_{input} given as an input of the projector, and constants (A, B, C) determined experimentally:

$$I_{output} = AI_{input}^2 + BI_{input} + C. \quad (5.13)$$

Figure 5.19 shows the gray images that are sent to the digital projector, and the corresponding acquired images. This example corresponds to a grayscale calibration performed using the hyperspectral camera described Chapter 4. The acquired images are

not uniform, mainly due to vignetting from the LCTF of the hyperspectral camera. The output gray level used in the calibration method is the average value on a central area of a 500×500 pixel dimension.

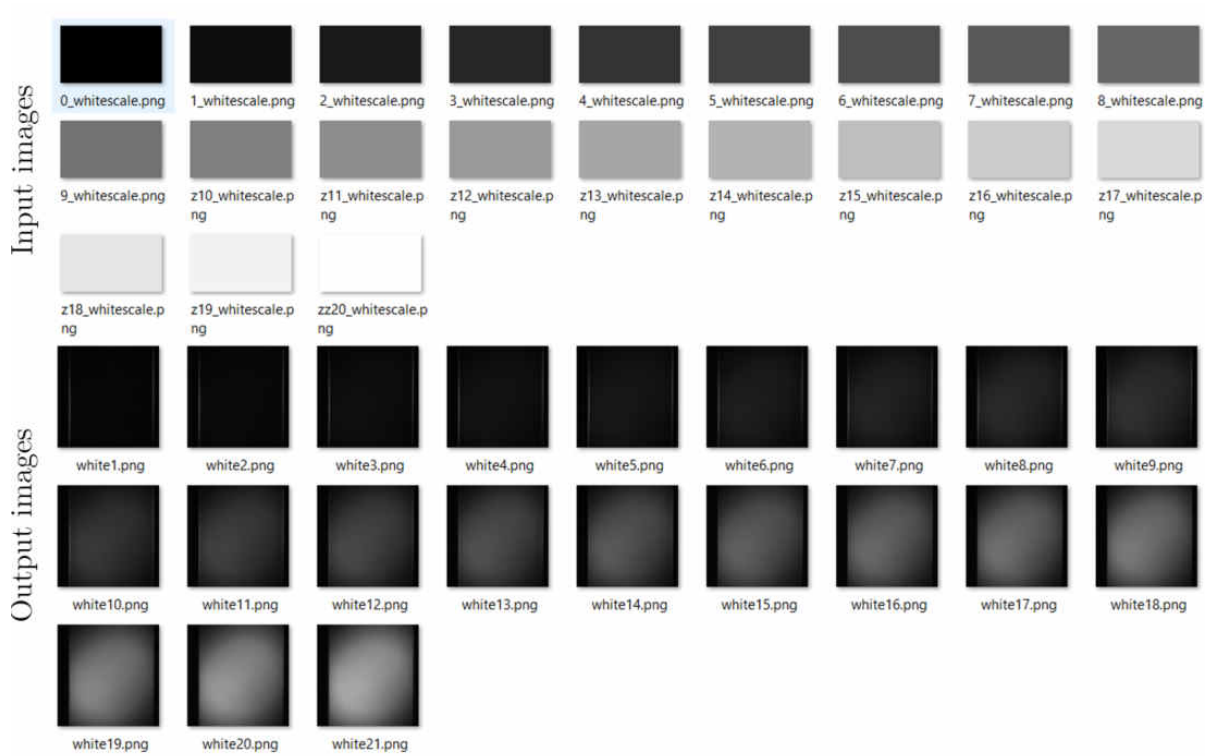


Figure 5.19. Input gray images and output images acquired by the camera.

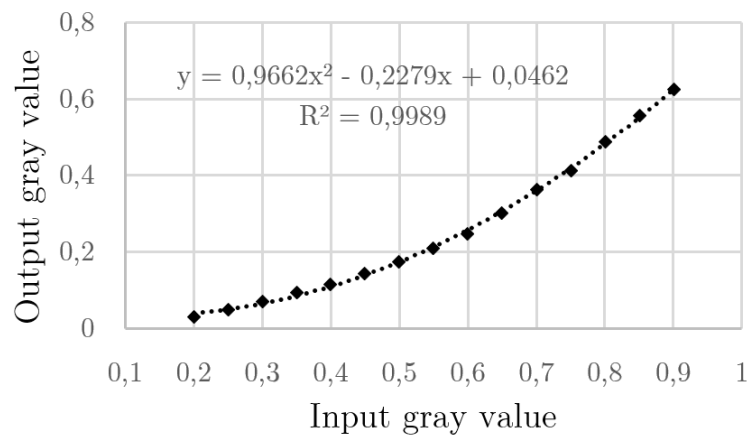


Figure 5.20. Output gray values for input gray levels limited to $[0.2; 0.9]$ (diamond markers) and fitting polynomial curve (dotted curve).

The projector is an 8 bit device with input values that are integers between 0 and 255. In this model, however, the gray level is expressed as a value between 0 (dark) and 1

(white). Since the projector used does not perform well at very dark and very bright gray levels, we chose to limit the gray level input between 0.2 and 0.9 (Figure 5.20).

The modified input image $I_{corrected}$ is computed from the sinusoidal fringe image I_{image} that we wish to project according to the following formula:

$$I_{corrected} = \frac{-B + \sqrt{B^2 + 4AI_{image}}}{2A}. \quad (5.14)$$

Figure 5.21 shows the difference between non-corrected and corrected fringes. Figure 5.21.d shows the Fourier transform of the fringe profiles. For the non-corrected fringes, we can observe several peaks that do not correspond to the frequencies of a sine curve. This is less the case for the corrected fringes, where the frequencies corresponding to the sine curve are predominant.

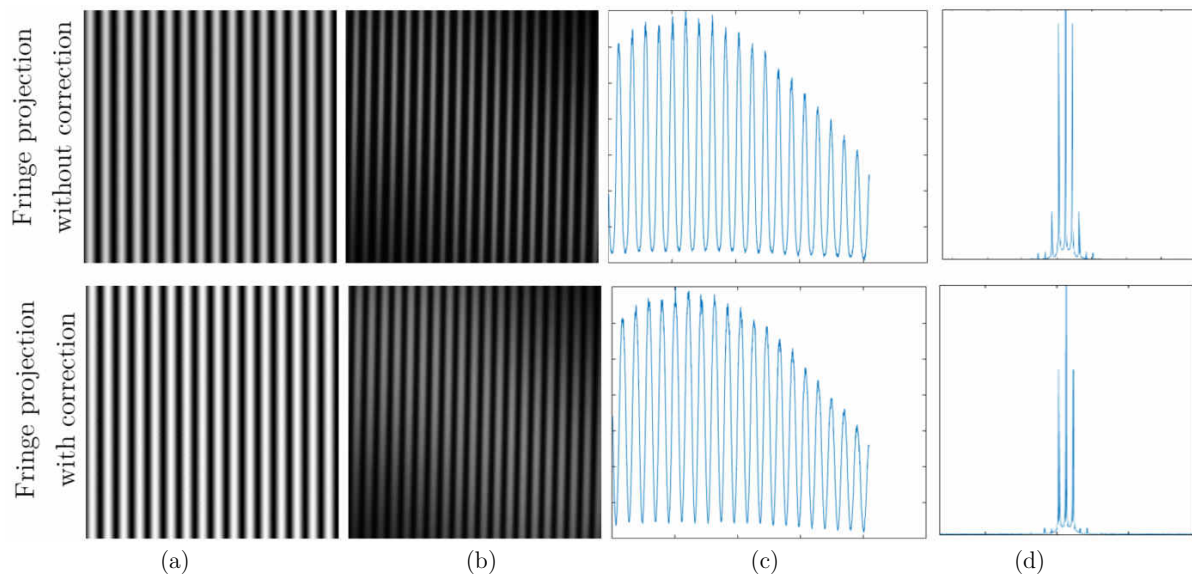


Figure 5.21. Difference between projecting non-corrected and corrected images: (a) input image, (b) image acquired by the camera, (c) fringe profile and (d) Fourier transform of the profile.

5.2.f. Geometric calibration

The conversion of the phase map into depth information from the triangulation principle described by Eq. (5.4) requires knowledge of the system geometrical parameters L , b and f . These parameters, in addition to being dependent on the pixel location for the fringe frequency f , are difficult to measure accurately. Therefore, a calibration must be performed. The simplest calibration is linear, based on the approximate assumption that the phase difference is directly proportional to the depth when L is much larger than h . A non-linear calibration which does not rely on this approximation is also possible.

The implemented calibration is non-linear, and has been described by Jia [Jia et al. 2007]. It requires the acquisition of several phase maps on planes located at various positions ($h_1, h_2 \dots$) along the Z axis (Figure 5.22) to find the two coefficients M and N :

$$h(x, y) = \frac{\Delta\varphi(x, y)}{M(x, y) + N(x, y)\Delta\varphi(x, y)}. \quad (5.15)$$

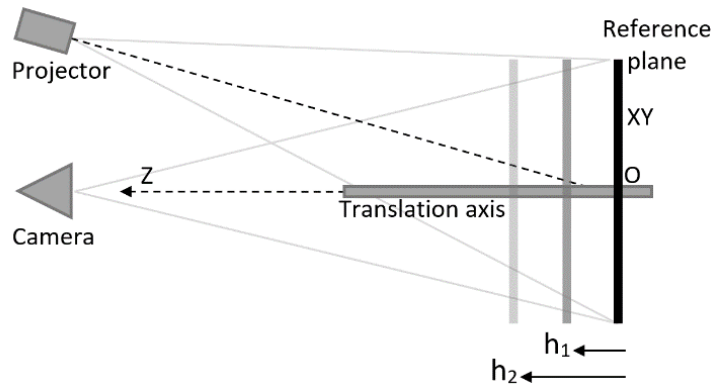


Figure 5.22. Scheme illustrating the depth calibration process.

A minimum of three acquisitions is required to evaluate the coefficients, but further measurements can be performed to give a better estimate of M and N by applying a least-squares algorithm. Figure 5.23 shows an example of the phase acquired for several h values and the regression curve that corresponds to Eq. (5.15).

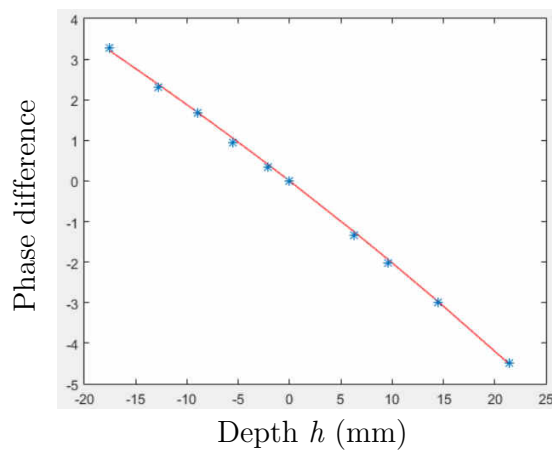


Figure 5.23. Acquisition of the phase on translated planes: Phase difference as a function of the depth h in mm, measurements (blue) and regression curve (red).

Finally, it is necessary to know the pixel to millimeter conversion to obtain the 2.5D information, which is a set of points with X, Y, Z coordinates in the 3D Cartesian space of the scene. This plane calibration is implemented by imaging a known object, such as a ruler.

In our system, one pixel of the camera roughly corresponds to 0.1 mm on the reference plane.

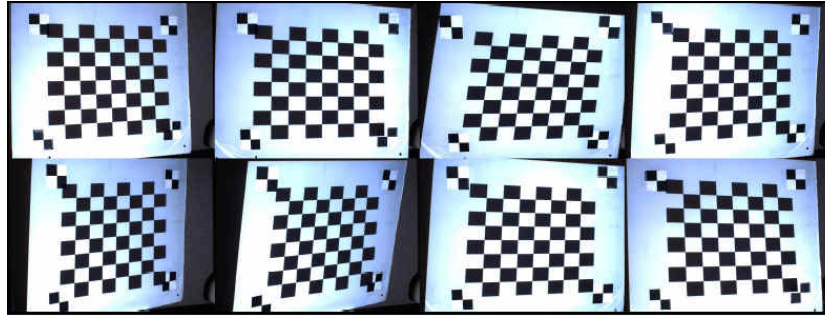


Figure 5.24. Example of the checkerboard images used in Bouguet’s camera calibration method [Bouguet].

The optical distortion of the camera and the projector can also be measured to fully calibrate the system. A typical camera geometrical calibration method is to acquire a known checkerboard at various positions and orientations, as illustrated in Figure 5.24 [Lanman and Taubin 2009]. The projector calibration can be done using a similar method [Moreno and Taubin 2012; Zhang and Huang 2006], in which a known checkerboard is projected onto a plane at various positions and orientations. The camera calibration is relatively easy to implement [Bouguet] so long as the camera depth of field can be set to keep the checkerboard to be in focus in all images. The projector calibration is more difficult to implement in our set-up, as the projector depth of field is not adapted to such a method. Ultimately, we decided not to correct the camera and projector geometrical distortions, given that the distortion on the area of interest, i.e. the center of the field of view only for full face acquisition, was acceptable.

5.3. Full face 3D geometry measurement

The 3D scanner, its acquisition methods and the 3D data reconstruction process presented in the previous section yield full face depth maps that can be visualized in 3D after a mesh conversion. Although the methods used have been fine-tuned to maximize accuracy, there remain some errors, discussed in this section, which might be due to shortcomings of the method itself, from the specificities of full face measurement, or from the specificities of translucent materials measurement.

5.3.a. 3D meshes displayed with texture

3D scanning produces depth maps that must then be converted into meshes in order to be displayed as a 3D object. A denoising filter is first applied to the depth map (either an average filter or a Gaussian filter, both using matrix convolution). The filtered depth

map looks smoother than the original depth map, but periodic noise is now even more visible (see Figure 5.25).

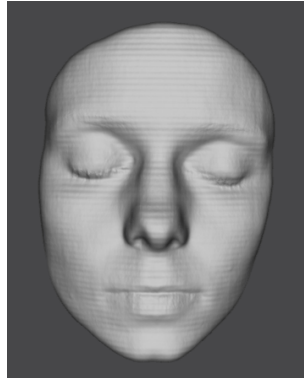


Figure 5.25. 3D display of a face depth map after an average filtering. The horizontal fringes result from the limitations of the fringe projection method.

This periodic noise is filtered using a 2D low pass Butterworth filter, which utilizes a multiplication in the Fourier domain. The parameters of the filter are chosen to reduce the frequency that corresponds to the periodic noise. The direction of the noise is dependent on the direction of the projected fringes. The Butterworth filter is asymmetric: only high frequencies are cut in the fringe direction, and the cutoff frequency is lower in the direction perpendicular to the fringes. Unfortunately, a small amount of facial shape information is also lost during the noise removal, as certain details on the face have similar frequencies to the noise. Consequently, this filtering step limits the resolution of the obtained image. Figure 5.26.a and b. shows the depth map before and after filtering.

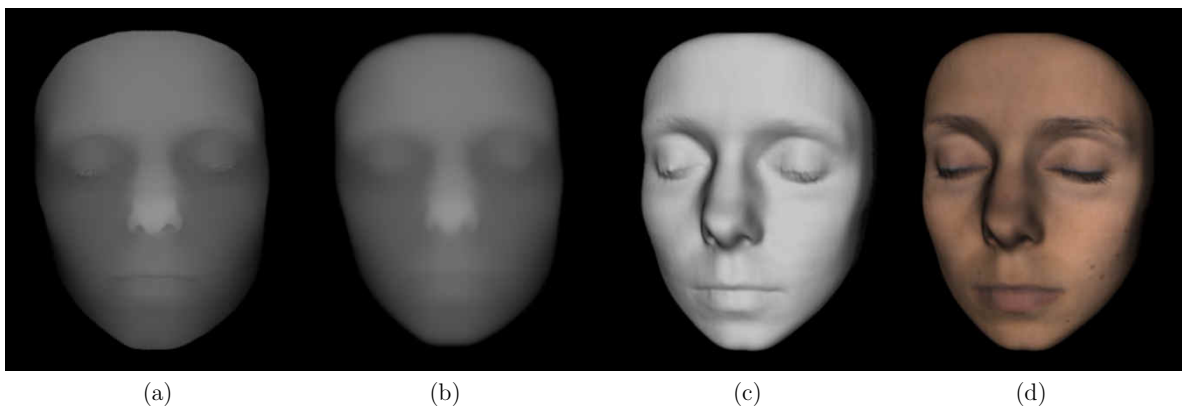


Figure 5.26. 3D hyperspectral acquisition of a full face: (a) depth map before smoothing, (b) depth map after smoothing, (c) 3D mesh without texture and (d) 3D mesh with color texture.

The depth map is converted into a .vtk 3D mesh file using a function from the Visual Toolkit library [Kitware]. During 3D mesh conversion, a texture can be added to represent

information such as reflectance for a given wavelength, or color. Figure 5.26.d shows the 3D-HSI measurement after conversion of the spectral reflectances into RGB color. These 3D meshes are displayed in Newton Technologies' SkinSurf software. This software includes a shader which adds shadows on the 3D face to give the impression of volume.

5.3.b. Acquisition speed, resolution and accuracy of the method

The efficacy of the implemented method can be assessed by its resolution, accuracy and acquisition time. Generally, it is much easier to achieve high resolution and accuracy when there are no constraints on acquisition time. Our method was designed to obtain maximum resolution and accuracy with an acquisition time that could be used for in vivo objects.

The method described in this chapter requires an acquisition time of around 2 seconds, which corresponds to the time needed for the projection of the different fringe images and their acquisition using a hyperspectral camera. The parameters that determine the acquisition time are the luminance of the projector, the sensitivity of the camera (i.e., the sensor response and the LCTF transmission at the 3D acquisition wavelength) and the projector refresh rate. The refresh rate of the chosen projector is not very high: the manufacturer indicates a vertical scan rate of 24 to 85 Hz, while 120 Hz is recommended for smooth videos. A delay of 100 milliseconds between two successive image acquisitions is thus necessary to avoid artefacts caused by refresh rate limitations. In addition, a satisfactory signal-to-noise ratio requires adequate exposure time, which was set at 150 milliseconds. For the projection of 5 fringe images, taking into account additional delay due to signal transfer between the camera and the computer, the approximate acquisition time is around 2 seconds.

The accuracy and precision of the system are determined by the limitations of both the hardware setup and software method. The fringe projection method has a limited resolution, while the hardware has shortcomings that degrade the accuracy of the acquisition. This is exacerbated when the measured surface is a translucent material such as skin. In this subsection, each source of limitation is separately investigated.

Precision of the fringe projection method

The fringe projection method relies on measuring the phase variation between a measurement on the object and a measurement on the reference plane. The minimum detectable height corresponds to a phase difference of one pixel of the projector, which corresponds to

$$\Delta\varphi_{min} = 2\pi f x_{pixel} , \quad (5.16)$$

with f the fringe frequency on the reference plane and x_{pixel} the size of a pixel of the projector on the reference plane. Using Eq. (5.4), this condition leads to the following minimum detectable height

$$\Delta h_{\min} = \frac{L}{1 + b / x_{\text{pixel}}}, \quad (5.17)$$

and minimum slope

$$\left| \frac{\partial h}{\partial x} \right|_{\min} = \frac{L}{b + x_{\text{pixel}}}. \quad (5.18)$$

The maximum measurable height difference between two neighboring pixels is 2π . Otherwise, the phase unwrapping algorithm cannot be applied. This yields a condition on the maximal measurable height difference

$$\Delta h_{\max} = \frac{L}{1 + fb}, \quad (5.19)$$

and the corresponding slope

$$\left| \frac{\partial h}{\partial x} \right|_{\max} = \frac{L}{x_{\text{pixel}}(1 + fb)}. \quad (5.20)$$

The minimum detectable height and minimum slope expressed in Eqs. (5.17) and (5.18) do not depend on the fringe frequency. The choice of fringe frequency, however, does have an impact on the minimum detectable height in practice: when the fringes are too large, the difference in radiance between two pixels is small, and a very small height difference is difficult to measure as it is likely to be of the same magnitude as the noise. The maximum height [Eq. (5.19)] also depends on the fringe frequency. If fringes are too small, the measurement can be performed only on objects that do not vary significantly in height. For these reasons, some methods targeting very high resolution acquisitions use multi-frequency projection [Yalla and Hassebrook 2005], to ensure both accuracy and high slope measurement. Such methods, however, increase acquisition time, which make them unsuited for vivo application. In this project, we selected an intermediate fringe frequency, of a value around 1 cm^{-1} .

Equations (5.17) and (5.19) show how b , the distance between the projector and the camera, and L , the distance between the camera and the reference plane, play a role in the system's resolution. These quantities b and L are related to the angle between the camera's and the projector's optical axis, which consequently greatly affects the resolution of the system [Geng 2011]: a large angle between the camera's and the projector's optical axis yields a better resolution. A large angle, though, increases the risk of having occluded areas. An angle of 10 degrees between the camera's and the projector's directions has been selected as a compromise to maximize resolution while minimizing occlusion.

The resolution is also influenced by the size of the projector pixels on the reference plane. This parameter is determined by the characteristics of the projector (pixel size,

resolution and focal length) and on the position of the reference plane. Although our choice of projector was informed by these considerations, it was equally limited by what was available and affordable on the market. In our system, the size of a projector's pixel on the reference plane is around 0.3 mm.

Quantitative error estimation on opaque objects

The precision of the acquisition method has been ascertained by measuring a tilted plane (Figure 5.27). The analysis of the 3D measurements shows that the noise is a combination of white noise, periodic noise and a low frequency deformation.

The low frequency deformation is caused by the geometrical distortions of the camera and the projector. It yields a higher disparity between the best-fitting plane and the acquired points on the corner of the image, as seen in Figure 5.27.b. As the region of interest is located in the center of the image for full face acquisition, the distortion observed in the corner of the image does not significantly affect the accuracy of the measurement of a full face. The maximum deviation between the acquired data and the best-fitting plane in the region of interest (which does not include the corners of the image) is 1.4 mm, the average deviation is 0.3 mm and the standard deviation is 0.4 mm.

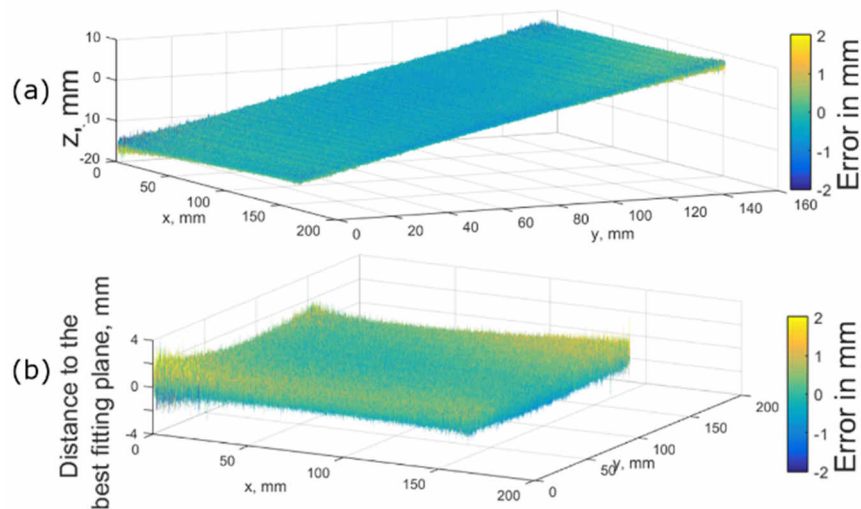


Figure 5.27. (a) Point cloud display of the measured titled plane before smoothing, (b) difference between the measured data and the best fitting plane.

Although the system's accuracy is theoretically determined by its dimensions, in practice, the quality of the projector significantly influences the results. Our chosen projector has a relatively low resolution (1200×800 pixels), and it displays images on an 8-bit gray scale. These two parameters determine the quality with which the projected signal is discretized and quantized. A low number of pixels per fringe results in high error between the projected signal and a perfect sinusoid. If the number of pixels per fringe is high (higher than 510 pixels), it is the 8 bit quantization that is limiting, as the projector

cannot render more than 255 gray levels. In addition to these limitations, the projector is not linear. A radiometric calibration has been performed to improve the quality of the projected fringes, however it is not sufficient to obtain a perfectly sinusoid signal. Finally, the depth of focus of the projector is shallow (an image projected on a plane translated of as little as 2 cm is out-of-focus), and the fringes projected can be blurred on some parts of the face. When the phase-shift method is used, the limitations listed above result in the periodic noise described above, visible on Figures 5.13 and 5.25.

As mentioned in Section 5.2, various solutions can be used to increase the quality of the measurement: in addition to performing a radiometric calibration, periodic noise can be reduced by increasing the number N of projected images in the phase shift method. The noise reduction, however, is not linear in respect to N : there is an optimum value for N when considering noise and acquisition time. After trying several configurations, we considered that $N = 5$ and $N = 6$ were the most appropriate configurations for full face 3D scanning.

The precision of the method was also characterized by measuring an opaque spherical object, namely a yellow ball, with a radius of $31 \text{ mm} \pm 0.5 \text{ mm}$, measured using a caliper.

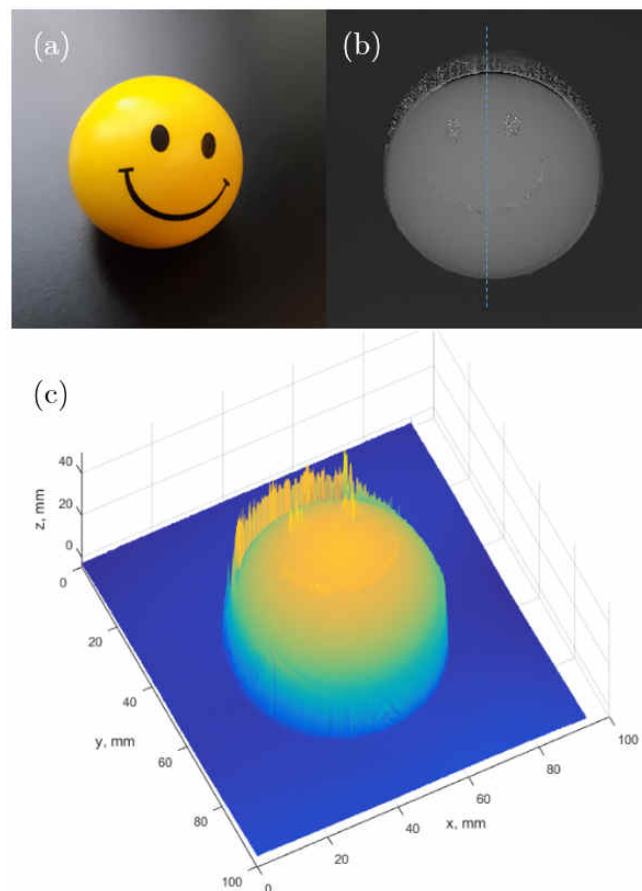


Figure 5.28. Acquisition on a spherical object: (a) object, (b) depth map and (c) 3D surface. The dotted line on (b) shows the location of the profile represented in Figure 5.29.

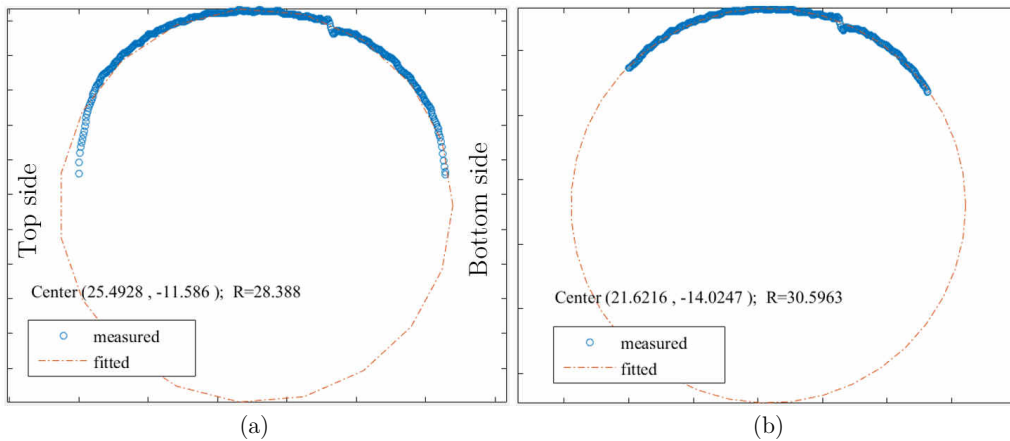


Figure 5.29. Profile of the depth map and best fitting circle calculated using the root-mean-square distance (a) when accounting for all the data and (b) when discarding the data at the border.

The depth map of the object has been reconstructed, and the vertical profile of the ball on the depth map has been used to assess the acquisition error. The 3D acquisition of the ball is illustrated by Figures 5.28 and 5.29.

When the entire profile is used to search for the best fitting circle using a method of least square (Figure 5.29.a), the corresponding circle radius is underestimated by 8%. However, when the pixels corresponding to the border of the ball are discarded (Figure 5.29.b), the ball radius estimated from the measurement is much closer to the manual measurement using a caliper.

Looking more closely at Figure 5.29.a, we can observe that the error is higher on the top of the ball (corresponding to the left of the profile) than the bottom. A possible explanation for this difference is the position of the projector: as the projector is located underneath the camera, the top of the ball receives less light, thus the signal-to-noise ratio is low and the measurement error is high. For an acquisition on a full face, it confirms that having the projector underneath the camera is the most appropriate position given the shape of a face.

The measured deviation on the tilted plane and on the ball are to be interpreted as minimum error values characterizing the acquisition method on non-translucent objects.

Efficacy of the method on skin

In vivo acquisitions on translucent materials such as skin are challenging for two reasons. The first is that unintentional movements of the person during the acquisition can generate noise. These movements can be more or less disadvantageous, but are in any case inevitable as the body moves when a person breathes. In order to minimize this source of noise, we have built an acquisition method with the aim of minimizing acquisition time. In the specific case of 3D acquisition, other strategies are also possible, such as using reconstruction methods that are more robust to movement [Cong et al. 2015].

The second challenge results from the fact that skin is a translucent material, causing subsurface scattering that deteriorates the quality of the projected fringes by blurring them. This subsurface scattering can be described by a point spread function (PSF), or by a modulation transfer function (MTF) in the Fourier domain. In theory, the effects of scattering on a pattern projected onto a medium can be estimated by the convolution of the PSF of the medium with the projected pattern. In the Fourier domain, this is equivalent to a multiplication of the MTF of the medium and the Fourier transform of the pattern. When the projected pattern is sinusoidal, its Fourier transform is a Dirac delta function. Hence, whatever the MTF of the medium, the result of the multiplication in the Fourier domain remains a Dirac delta function and the impact in the real domain is a loss of contrast of the sine function. In practice however, the implemented radiometric calibration was not sufficient to guarantee a perfectly sinusoidal output signal, resulting in distortion caused by subsurface scattering. This subsurface scattering can be minimized by limiting the acquisition to the channel of the projector for which skin is the most opaque [Wang et al. 2013]. As already discussed in Section 5.2.a, this is the blue channel for skin. However, as the camera in the proposed acquisition setup is more susceptible to noise in this waveband, we have chosen to perform 3D scanning at 520 nm.

5.4. Conclusion

The 3D scanning method detailed in this chapter allows us to measure the 3D geometry of a full face with a reasonable acquisition time. The precision and accuracy of the method are satisfactory, taking into account the simplicity of the setup. However, for applications targeting finer details such as wrinkles, higher precision would be necessary, while for applications targeting full face shape analysis, the acquisition of a single depth map is not sufficient.

If we wished to design a more effective system, two strategies could be considered: focusing on accurate full-face 3D scanning, or targeting high resolution wrinkle measurements on a small area. Both strategies would require a much more complex and expensive 3D scanner. For full face acquisition, it would be necessary to build a system comprising one or several projectors and several cameras (three for example) to perform multiple acquisitions with multiple points of view. For wrinkle measurements, the method implemented in Primos (Canfield, USA) and Dermatop-HE (Aeva 3D, Luxembourg), which uses multiple frequency fringe projection, appears to be an effective means of ensuring high precision. To build such a system however, a custom-built projector for which intensity, focal length and depth of field could be fully adjusted, would be required rather than a commercially available DLP.

Chapter 6.

Measuring the spectral reflectance of curved surfaces: irradiance drift correction

As already mentioned in Chapters 4 and 5, a simple radiometric correction based on a flat reference sample is not adequate to provide accurate spectral measurement of complex 3D objects. On a full face, the measured spectral reflectance is not a faithful representation of the actual spectral reflectance except in those areas that receive the same irradiance as that received by the flat panel used for calibration, e.g., the forehead and cheeks. On the other areas of the face, the measured spectral reflectance corresponds to the actual reflectance multiplied by a factor related to the irradiance deviation between the skin area and the flat reference plane. We propose to call this difference *irradiance drift*.

With respect to skin analysis, irradiance drifts can lead to errors in analysis. For example, an area that appears darker in the image because of lower illumination could be erroneously interpreted as an area containing more melanin. When working on a full face then, it is crucial that the image is pre-processed to manage irradiance drifts before attempting relevant skin analysis. This pre-processing takes the form of an irradiance correction method, and is a necessary step in the skin optical analysis.

Several methods are discussed in literature to address this problem, sometimes referred as a “curvature artefact”. We can categorize these methods into those using structured light or fringe pattern projection for 3D scanning [Westhäuser et al. 2008; Gioux et al. 2009; Paquit et al. 2008], and those relying on curvature intensity bias correction [Kainerstorfer et al. 2010], which do not require the additional acquisition of the 3D shape of the object. Certain 3D acquisition methods, such as shape from shading [Barron and Malik 2015], aim at retrieving surface reflectance information (and potentially more information, such as the lighting conditions) using similar principles.

The proposed method is an extension to a “3D irradiance correction” of the spectral calibration method detailed in Chapter 4. By assuming in a first approximation that skin is a Lambertian reflector, and acquiring the 3D geometry of the object, we can compute the irradiance of each pixel and subsequently perform an irradiance correction that takes into account the effects of the geometry of the object on the measured signal.

Knowledge of the 3D geometry, lighting conditions and BRDF of the surface allows us to render the visual appearance of the object using radiometric concepts described in Chapter 2. If the surface is Lambertian, the calculation is simplified, as BRDF is constant over the entire hemisphere whatever the illumination geometry. Reflected radiance, in every direction, is therefore proportional to irradiance. Figure 6.1 illustrates such an application by showing the visual appearance of a silicon skin replica (assumed to be a Lambertian reflector) under collimated illuminations at various angles. This rendering was computed in MatLab from the normal map of the object (Figure 6.1.a). The normal map has been acquired at the SYMME Laboratory (Annecy, France) using a LED dome which captures the object under many directional illuminations in order to reconstruct the 3D geometry of the surface.

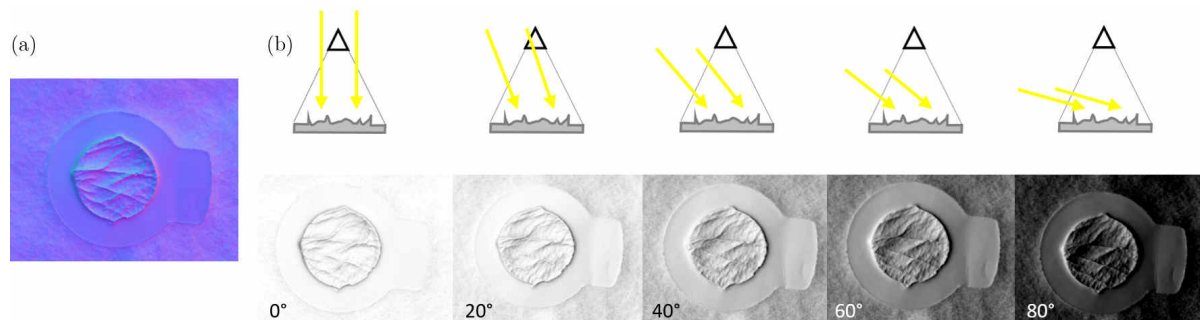


Figure 6.1. (a) Normal map of a white skin silicon replica and (b) rendering of the replica for a collimated illumination at various incident angles, assuming that the surface is Lambertian.

When an object whose 3D geometry is known is imaged under controlled lighting conditions, the same radiometry concepts that have been used to create the rendering of Figure 6.1 can be used to retrieve the reflectance factor of the object from the radiance measured by the camera. If the surface of the object is Lambertian, the reflectance factor corresponds to the reflectance (or albedo). In our case, skin is acquired using a cross-polarization (CP) configuration (the specular component is discarded), and only the diffuse reflectance component, which can be assumed as Lambertian for skin, is measured.

The method implemented by Gioux on spatially modulated imaging systems [Gioux et al. 2009] or Westhauser on color images [Westhäuser et al. 2008] uses the angle between the object surface and the optical axis of the camera. This method, however, is valid only

for a punctual illumination. As we have a complex illumination configuration in the hyperspectral imaging system, our approach must consider the full geometry of the acquisition system. Since we could not find any reference related to this issue in the literature, we conceived a new approach, in two steps. First, considering a point source, the amount of light received on each point of the object is computed so as to perform an irradiance drift correction, assuming that the surface is a Lambertian reflector. Secondly, the irradiance drift correction valid for point sources is extended to the full hyperspectral image (called hypercube) with the additional hypothesis that artefacts due to curvature are similar at every wavelength.

In this chapter, we detail in Section 6.1 the two-step irradiance correction method and its implementation, and discuss the efficacy of the method in Section 6.2. In Section 6.3, we present another possible application of the 3D imaging system: its use as a non-contact BRDF measurement device. Conclusions are drawn in Section 6.4.

6.1. Irradiance correction methods for simple and complex configurations

The irradiance drift correction method relies on computing the radiance reflected by the object toward the camera. This calculation is simple when the source is punctual, which can be assumed to be the case when the light source is a digital projector. However, this comes more complex when the object is illuminated by a series of lights, as it is the case for our hyperspectral acquisition system. In this section, the method valid for a point illumination is described first, then extended to the case of a complex illumination configuration.

6.1.a. Analytical formula for the point source correction method

Let us consider the following configuration: a point source (henceforth described to the “projector” to conform with our application) emits light in a cone, the object surface is Lambertian, and the area of interest is a small surface $dS(x, y)$ of the object that corresponds to one pixel (x, y) when imaged on the camera sensor.

The surface $dS(x, y)$ receives the irradiance $E(x, y)$, that can be expressed according to the inverse square law (already defined in Chapter 2) as a function of the source intensity $I(\theta, \varphi)$ in the direction of the object, the distance $d(x, y)$ between dS and the source and the angle $\alpha(x, y)$ between the normal of the surface and the lighting direction, illustrated in Figure 6.2:

$$E = I(\theta, \varphi) \frac{\cos\alpha}{d^2}. \quad (6.1)$$

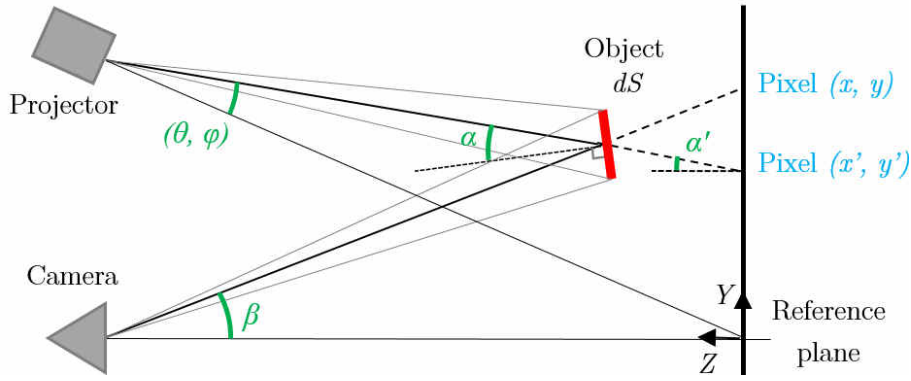


Figure 6.2. Geometry of the object, of the lighting, and useful quantities for the irradiance correction method.

Finally, the flux $F(x, y)$ received on the pixel of the camera is defined as the quantity of light flowing through the geometrical extent $dG(x, y)$ between the surface dS and the pupil of the imaging system.

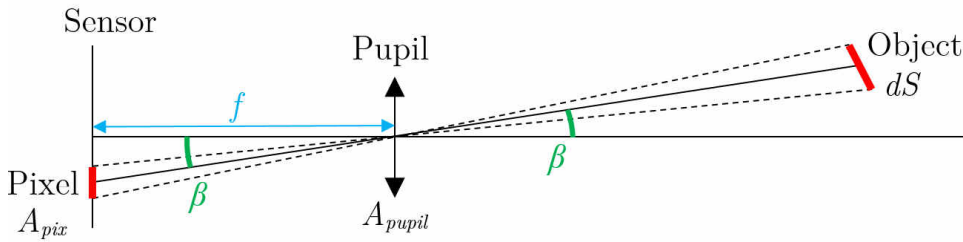


Figure 6.3. Simplified geometry of the imaging system.

As a property of geometric extent, dG is also equal to the geometrical extent between the pupil and the pixel (x, y) , and can be written as a function of the area of the pixel A_{pixel} , the area of the pupil A_{pupil} , the focal length of the system f and the angular position of the pixel in the field on view $\beta(x, y)$ (see Figure 6.3):

$$\begin{aligned}
 dG &= \frac{(A_{pixel} \cos \beta)(A_{pupil} \cos \beta)}{(f / \cos \beta)^2} \\
 &= A_{pixel} A_{pupil} \frac{\cos^4 \beta}{f^2}
 \end{aligned} \tag{6.2}$$

The flux $F(x, y)$ received on the pixel of the camera depends on the radiance $L(x, y)$ leaving the surface in the direction of the camera, the optics transmittance $T(x, y)$ and the angular position $\beta(x, y)$ of the pixel in the field of view of the camera:

$$F = k \cos^4 \beta \cdot L \cdot T, \quad (6.3)$$

where k is a coefficient that depends on the properties of the camera (focal length, aperture, pixel's size):

$$k = \frac{A_{pixel} A_{pupil}}{f^2}. \quad (6.4)$$

Finally, the electronic signal $Q(x, y)$ emitted by the sensor, which corresponds to the image, is proportional to the received flux:

$$Q = F \cdot S + n, \quad (6.5)$$

where S is the sensor sensitivity and n is the acquisition noise, both assumed to be independent from the location of the pixel.

The combination of Eqs. (6.1), (6.3) and (6.5) yields:

$$Q = \frac{R}{\pi} I(\theta, \varphi) \frac{\cos \alpha}{d^2} \cdot k \cos^4 \beta \cdot T \cdot S + n. \quad (6.6)$$

The surface reflectance $R(x, y)$, which is the parameter to be determined, can be retrieved by performing a calibration using a flat black sample and a flat white sample to provide the unknown quantities and remove the effect of noise. The source intensity can be calibrated by considering the pixel (x', y') , which corresponds to the area on the reference plane illuminated under the same angle (θ, φ) as the area on the object imaged in the pixel (x, y) .

The signal $Q_w(x', y')$ captured in the pixel (x', y') when the white reference plane of albedo ρ_w is measured can be written as:

$$Q_w = \frac{\rho_w}{\pi} I(\theta, \varphi) \frac{\cos \alpha'}{d'^2} \cdot k \cos^4 \beta' \cdot T' \cdot S + n, \quad (6.7)$$

where the quantities α' , d' , β' and T' are related to the pixel (x', y') : $d'(x', y')$ is the distance between the light source and the pixel on the reference plane; $\alpha'(x', y')$ is the angle between the normal of the reference plane and the illumination direction; $\beta'(x', y')$ is the angular position of the pixel in the camera's field of view; and $T'(x', y')$ is the transmission of the optical system

The signal Q_k captured on the black reference plane can be described by a similar expression, replacing ρ_w with ρ_k in Eq. (6.7). Combining Eqs. (6.6) and (6.7), we can express the reflectance factor of the surface as:

$$R(x, y) = \left(\frac{Q(x, y) - Q_k(x', y')}{Q_w(x', y') - Q_k(x', y')} (\rho_w - \rho_k) + \rho_k \right) \cdot \frac{\cos \alpha'(x', y') \cos^4 \beta'(x', y') T'(x', y') d(x, y)^2}{\cos \alpha(x, y) \cos^4 \beta(x, y) T(x, y) d'(x', y')^2}, \quad (6.8)$$

and thus becomes independent of the sensor response, source intensity and background noise.

Equation (6.8) involves values in two different pixels (x, y) and (x', y') , as well as the transmittance of the camera for this two pixels, which cannot be determined by calculation. In order to further simplify Eq. (6.8) and obtain an expression which is independent from T and T' , we assume that the light intensity of the projector is the same in the direction of pixel (x, y) and in the direction of pixel (x', y') . We obtain an expression that depends only on the pixel (x, y) :

$$R = \left(\frac{Q - Q_k}{Q_w - Q_k} (\rho_w - \rho_k) + \rho_k \right) \cdot \frac{\cos \alpha' d^2}{\cos \alpha d'^2}. \quad (6.9)$$

In our application, both the object-reference plane distance and camera-projector distance are small compared to the camera-reference plane distance, so that the pixels (x, y) and (x', y') are not far from each other. Consequently, the assumption mentioned above does not significantly affect the quality of the corrected images, which mainly depend on the quality of the 3D measurement, as discussed later in Section 6.2.

6.1.b. Implementation of the method

The irradiance correction method has been implemented in MatLab. In addition to the image acquired on the object and reference planes (Q , Q_w and Q_k), it requires information on the object (normal map and pixel location), on the camera (location) and on the lighting (position of the source). Eq. (6.9) gives the correction formula for each pixel, which is turned into a matrix expression, better suited to the computational facilities of MatLab. Parameters α , α' , d and d' become matrices with similar size as the whole image.

The 3D acquisition first yields a depth map which gives the location of the object surface for each pixel. From this depth map, the surface normal vectors $\mathbf{N} = [N^x, N^y, N^z]$ are computed using the following formulas, where \otimes refers to the 2 dimensional convolution [Barron and Malik 2015]:

$$\begin{aligned} N^x &= Z \otimes h_3^x / B \\ N^y &= Z \otimes h_3^y / B, \\ N^z &= 1 / B \end{aligned} \quad (6.10)$$

with

$$B = \sqrt{1 + (Z \otimes h_3^x)^2 + (Z \otimes h_3^y)^2}, \quad (6.11)$$

and

$$h_3^x = \begin{bmatrix} 1 & 0 & -1 \\ 2 & 0 & -2 \\ 1 & 0 & -1 \end{bmatrix} \text{ and } h_3^y = \begin{bmatrix} 1 & 2 & 1 \\ 0 & 0 & 0 \\ -1 & -2 & -1 \end{bmatrix}. \quad (6.12)$$

The map of normal vectors can then be encoded as an RGB color image: N^x is represented by the red coordinate, N^y by the green coordinate and N^z by the blue coordinate. Consequently, the background of the image, for which the normal vector is $[0 \ 0 \ 1]$, appears as blue. Figure 6.4 shows an example of normal map calculated from a depth map.

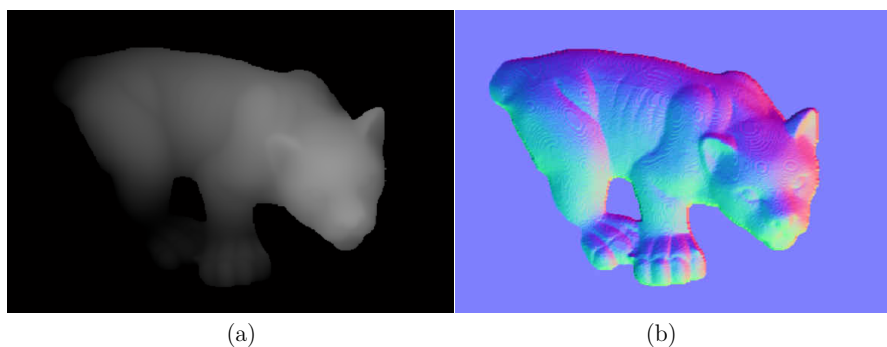


Figure 6.4. (a) Depth map and (b) corresponding normal vector map displayed as a color image.

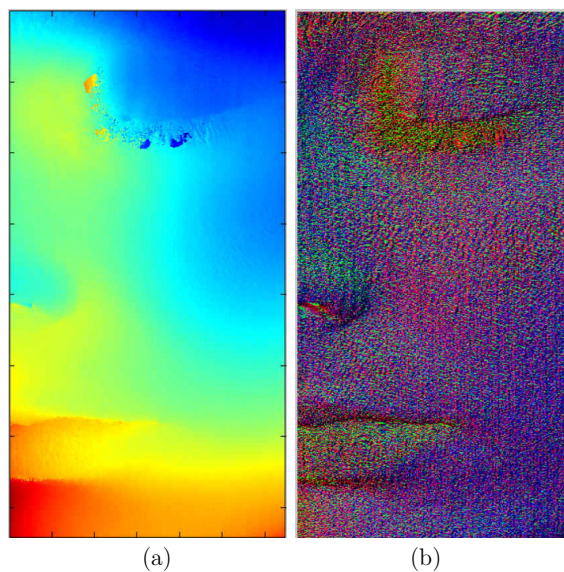


Figure 6.5. (a) Depth map of half a face (false color display) and (b) corresponding normal map when no smoothing has been applied.

The depth map must first be smoothed before computing the normal map. If no smoothing is applied, the computed normal map is very noisy, as can be seen in Figure 6.5. Noise reduction has been achieved by first applying a Gaussian filter, then an averaging filter. The averaging filter is larger in the horizontal direction to reduce the noise deriving from the 3D acquisition when vertical fringes are used (and vice versa when the 3D information is acquired using horizontal fringes).

Once the normal map is known, the quantities $\cos\alpha$ and $\cos\alpha'$ can be calculated: they are scalar products given by

$$\cos\alpha = \frac{\overrightarrow{O_{obj}O_{proj}} \cdot \overline{N}}{\left\| \overrightarrow{O_{obj}O_{proj}} \right\|}, \quad (6.13)$$

and

$$\cos\alpha' = \frac{\overrightarrow{O_{obj}O_{proj}} \cdot \overline{Z}}{\left\| \overrightarrow{O_{obj}O_{proj}} \right\|}, \quad (6.14)$$

with O_{proj} and O_{obj} respectively designating the location of the projector and considered pixel.

An example of cosine map is illustrated in Figure 6.6. We can notice on these images that the cosine map produces an impression of 3D shape. This is due to the fact that our brain uses information related to the quantity of reflected light to perceive volume, a quantity which is mainly determined by the cosine of the angle between the illumination direction and the surface normal vector.

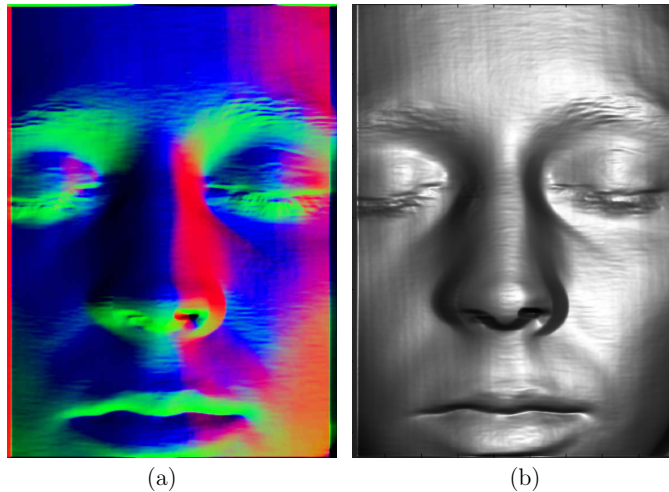


Figure 6.6. (a) Normal map and (b) cosine map representing the quantity $\cos\alpha$.

The term $\left\| \overrightarrow{O_{obj}O_{proj}} \right\|$ corresponds to the distance d between the source and the object.

The last quantity that is required to apply the correction method is the distance

$d' = \left\| \overrightarrow{O_{ref}O_{proj}} \right\|$. This distance is obtained after finding the location of the intersection $O_{ref} = (x_{ref}, y_{ref}, z_{ref})$ between the projector-object axis and the reference plane, defined by the equation $Z = 0$. The location of the intersection is given by the following expression:

$$O_{ref} = O_{proj} + c \times \overrightarrow{O_{proj}O_{obj}}, \quad (6.15)$$

where c is a constant satisfying $z_{ref} = 0$.

Figure 6.7 shows the results of an irradiance correction performed with a punctual source, a digital projector in our application. On the corrected image, we can see blood vessels on the left of the forehead that were not visible on the original image because of low contrast. However, the corrected image also contains artefacts, all of them resulting from quality issues in the normal map: irradiance drifts are sometimes over-corrected, such as on the eye, where some areas are lighter than they should be.

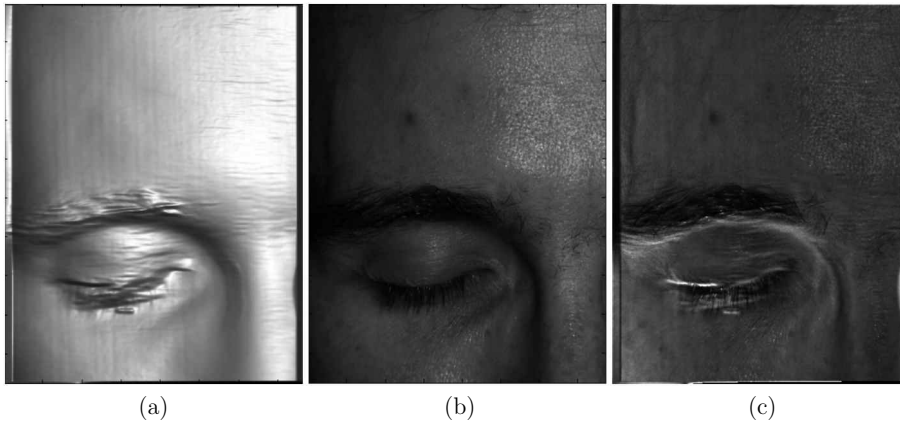


Figure 6.7. (a) Cosine map, (b) original image before correction and (c) image after correction.

This correction, valid when the illumination is punctual, is the first step to the general method that can be applied to images acquired using the hyperspectral camera, described below.

6.1.c. Case of a complex illumination geometry

In the proposed system, each lighting unit of the hyperspectral acquisition system comprises ten LEDs; the total incident irradiance is the sum the irradiances coming from each LED. The first idea for extending the method to a complex configuration was to consider the overall lighting configuration as a sum of point sources, 20 in our application. To implement this method, images on black and white reference planes had to be acquired for each point source, with all the other LEDs turned off. The correction method was then applied independently for each wavelength of the hypercube. However the quality of the corrected images was poor: it was difficult to accurately determine the position of each LED,

and although the assumption that illumination is punctual is valid for a digital projector, it is not clear whether this remains the case for LEDs combined with a plastic lens. The method described by Eq. (6.9) was therefore revised using an additional step to make it suitable to complex illumination configurations.

The hypercube correction is based on the assumption that once the radiometric calibration described in Chapter 4 has been applied, the remaining irradiance drifts are the same for all wavelengths. Indeed, the radiometric calibration detailed in Chapter 4 removes the effects of the illumination heterogeneities and camera transmission for each wavelength, and the irradiance drifts that remain after this first step derive from the shape of the face only. With this in mind, we can compute an irradiance correction on one image, corresponding to one wavelength, and apply it to the entire hypercube. Using our 3D-HSI system, the face is acquired a first time at a single wavelength during the 3D scanning (with the projector turned on and the LEDs turned off), then acquired again for all wavelengths using the hyperspectral camera (with the projector turned off and the LEDs turned on). We can apply the simple correction method on the image corresponding to the 3D acquisition. Consequently, we can identify the irradiance drifts at a single wavelength, and then use it to correct the whole hypercube.

Let us recall that the 3D scanning, performed for a single wavelength λ_{3D} (520 nm), provides Q_{3D} , the image that would be recorded by the camera if the object was illuminated by uniform light from the projector, with J_n , ($n = 1 \dots N$) the N fringe images recorded by the camera:

$$Q_{3D} = \frac{1}{N} \sum_{n=1}^N J_n . \quad (6.16)$$

For 3D acquisition, the lighting geometry is simple because there is only one source, the digital projector, which emits light within a cone. Its position can be determined by calibration. By performing an irradiance normalization using Eq. (6.9) on $Q_{3D}(\lambda_{3D})$, the normalized reflectance factor $\tilde{R}_{3D}(\lambda_{3D})$ for the wavelength λ_{3D} is obtained. For this wavelength, the output of the hyperspectral acquisition is $Q_{hsi}(\lambda_{3D})$. The ratio of $\tilde{R}_{3D}(\lambda_{3D})$ to $Q_{hsi}(\lambda_{3D})$ gives a correction factor K which stands for every wavelength:

$$K = \frac{\tilde{R}_{3D}(\lambda_{3D})}{Q_{hsi}(\lambda_{3D})} . \quad (6.17)$$

Finally, this correction factor is used on the hyperspectral image $Q_{hsi}(\lambda)$ and we can thereby obtain the normalized spectral reflectance factor $\tilde{R}_{hsi}(\lambda)$ for each wavelength:

$$\tilde{R}_{hsi}(\lambda) = K \cdot L_{hsi}(\lambda) . \quad (6.18)$$

This correction method is partly implemented in MatLab, where the correction factor K is calculated using the method already described in § 6.1.b, and partly implemented in

NtImageAnalysor, an image analysis software developed by Newton Technologies which allows the multiplication of hypercubes, to compute Eq. (6.18) for all wavelengths at once.

This method applies only if the hyperspectral image and the 3D image have been acquired in the same CP polarization configuration. Hence, a linear polarizing filter has been added to the projector to create a CP configuration with the LCTF polarization direction.

Notice that in the methods described in this section, shadows corresponding to light that is completely blocked by an obstacle are not modeled. We consider that the digital projector is positioned in such a way that there are not occluded areas visible on the acquired images. To account for shadowed areas in the current method, the location of the reference point O_{ref} (i.e. the point of the reference plane located in the direction (θ, φ) as the point on the object O_{obj} , calculated using Eq.(6.15)) could be used. If two pixels have the same reference point, then one of them receives light and one of them is occluded.

6.2. Irradiance correction on hyperspectral images

In this section, we present and discuss the efficacy of the method detailed above for irradiance drift correction applied to a full face.

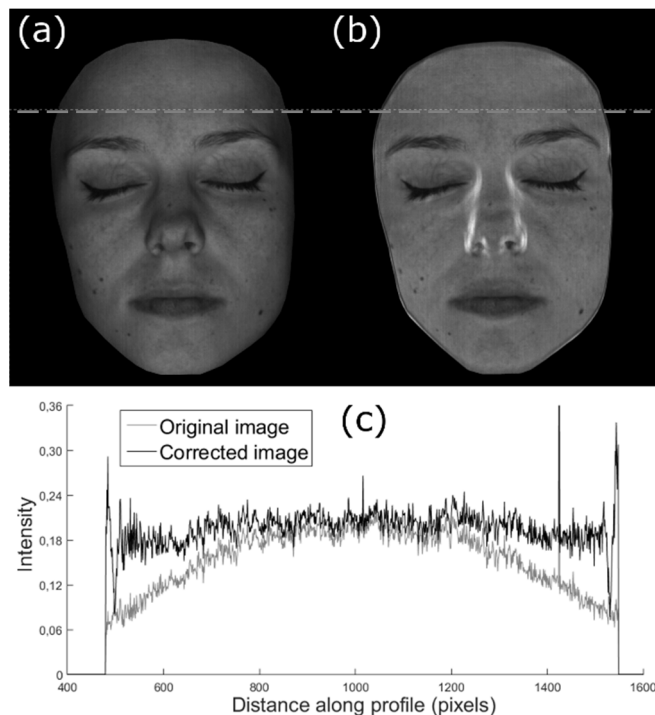


Figure 6.8. (a) Original image with incident irradiance non-uniformities, (b) image after correction and (c) profile of the radiance intensity on the forehead before (gray) and after correction (black). The dotted line on images (a) and (b) indicates the location of the profile. For display purposes, the maximum gray level corresponds to a reflectance of 0.5.

Figure 6.8 shows an example of a corrected image obtained in a simple configuration with the projector illuminating only the face, for a single wavelength (520 nm), before (Figure 6.8.a) and after (Figure 6.8.b) irradiance correction. Figure 6.8.c shows the irradiance horizontal profile on the forehead before and after correction.

The implemented method corrects the irradiance variation observed on the forehead. The curve observed on the gray line in Figure 6.8.c is the consequence of irradiance non-uniformities on the forehead but does not describe the skin reflectance on this zone. The black line shows that the reflectance profile is more homogeneous after applying the irradiance correction. Local variations are due to skin surface micro-reliefs.

Although this method yields good results for most parts of the face, there are areas for which it is not satisfactory. When the angle α between the lighting direction and the normal to the surface is high, the cosine of the angle is close to zero. Since in Eq. (6.9), the original radiance is divided by $\cos\alpha$, a small error on α yields a high error on the corrected reflectance factor. This can be seen on the sides of the nose, where the shadows are overcorrected.

Figure 6.9 shows an example of color images before and after applying the irradiance normalization method on a full hyperspectral image. The corrected hypercube has been converted into a color image for better visualization. Except for the overcorrected areas observed on the nose and border, the color obtained after correction is visually satisfactory. However, the errors observed on areas such as the nose, which appear to be unavoidable when generating a depth map acquired from a single point of view, is still present and must be considered as a limitation of the developed methodology.

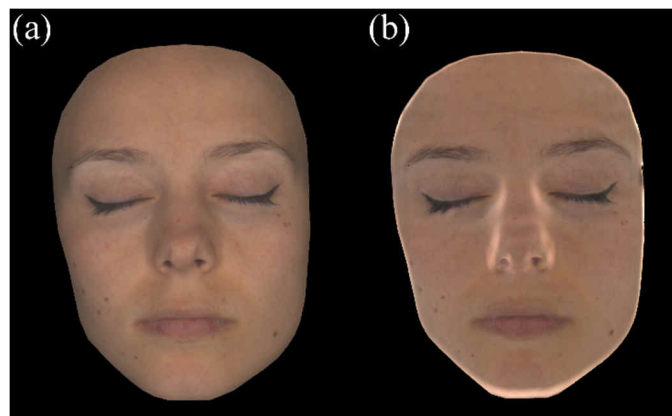


Figure 6.9. Full face color image (a) before correction and (b) after correction on a hyperspectral image (color conversion with a D65 illuminant).

Figures 6.8 and 6.9 show that the efficacy of the correction method depend highly on the quality of the depth map used. Unfortunately, using our 3D scanner, the depth map has to be heavily smoothed to prevent artefacts due to noise, which likely impacts the

accuracy of the 3D information. For example, we suspect that filtering the depth map slightly modifies the shape of the nose, directly impacting the quality of the correction method.

Figure 6.10 shows three slices of the hypercube corresponding to the wavelengths 420 nm, 600 nm and 700 nm, before and after correction. Examining them, certain observations concerning the validity of the two assumptions can be made:

- Assumption 1. Skin is a Lambertian reflector,
- Assumption 2. Irradiance drifts are independent of wavelength.

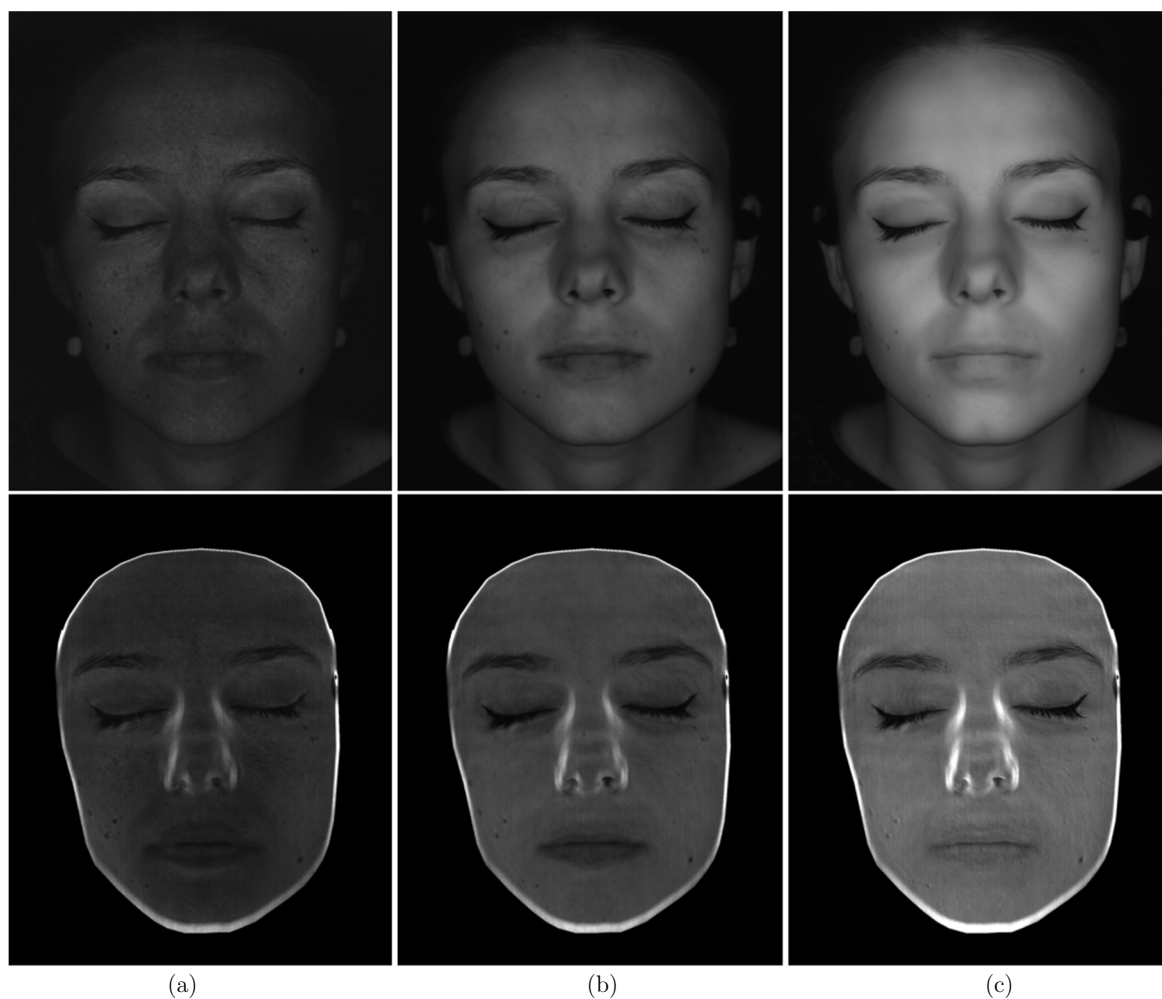


Figure 6.10. Images at (a) 420 nm, (b) 600 nm and (c) 700 nm before correction (top) and after correction (bottom). The gray levels of the images at 420 nm are multiplied by two for better contrast in the figure.

The image at 600 nm shows a mostly satisfactory corrected image when discarding the nose from the area of interest. On the images at 700 nm, however, the image after correction is much noisier than before correction. On the original image, the skin appears very smooth, and its micro-reliefs are not visible. This is due to the fact that skin is rather

translucent at this wavelength. However, when the correction is applied using the information acquired at 520 nm, the surface details that are visible on the image at 520 nm are artificially added to the corrected image. This shows that the validity of the second hypothesis is questionable when working on translucent materials, as light is blurred by skin according to wavelength.

The images at 420 nm also show less satisfactory correction than at 600 nm. Some areas are not perfectly corrected, such as the part underneath the eyebrows which remains slightly lighter than the rest of the face after correction. This artefact questions the validity of assumption 1: skin might be less Lambertian at 420 nm than at 600 nm. Such an explanation seems plausible, as skin translucency is not constant over the spectrum.

As the irradiance correction solution proposed was not as satisfactory as expected on a full face, we did not investigate any objective measure to quantify its accuracy.

6.3. Going further: using imaging methods to estimate skin BRDF

While working on the correction of irradiance drifts on skin, we were inclined to ask whether our system could also provide skin BRDF.

Measuring skin BRDF in vivo is a highly challenging task. Most commercial non-imaging BRDF measurement systems are gonio-reflectometers, which are designed to illuminate and measure flat samples at various angles. For non-contact instruments, it is difficult to properly position the part of the body to be measured and perform a reliable measurement. For contact measurements (with the acquisition device directly placed on top of the sample), skin is likely to be distorted into a less-than-flat surface under the weight of the system. In addition, BRDF measurement using a gonio-reflectometer can be too long for in vivo acquisitions: the person is likely to move if acquisition time is superior to a few seconds.

BRDF measurement based on imaging, on the contrary, permits for very short acquisition times. For example, using methods that require cylindrical homogeneous samples, a single image contains information about the reflectance factor at many incident and observation directions [Sole et al. 2018]. For in vivo skin measurement, it is not possible to control the shape of the sample, but it is possible to measure its 3D geometry and retrieve its BRDF from an image [Nielsen et al. 2017; Bintz et al. 2016; Marschner et al. 1999a; Marschner et al. 1999b]. Other methods are also possible, relying on light fields without requiring a 3D scan of the object [Debevec et al. 2000; Lu et al. 2017]. However, as our camera already includes a 3D scanner, we tried to retrieve information about the BRDF using “4D” information: the 3D geometry of the object and the luminance resulting from the object illuminated by the digital projector.

The method that we implemented is based on the same theory as that for irradiance correction for punctual sources detailed in Section 6.1.a. It yields the reflectance factor associated with two angles for each pixel: one angle for illumination and one angle for the direction of measurement. For simpler BRDF values, we consider only the angle between the specular reflection and the measurement direction, rather than both angles. In this case, the BRDF is a function of one angle only. We also assumed that the measured objects were uniform in order to sum the contribution of each pixel and obtain a single curve describing the object surface. We tested the method on still objects of different properties: a rough blue notebook and a smooth yellow mug. Results are presented in Figure 6.11.

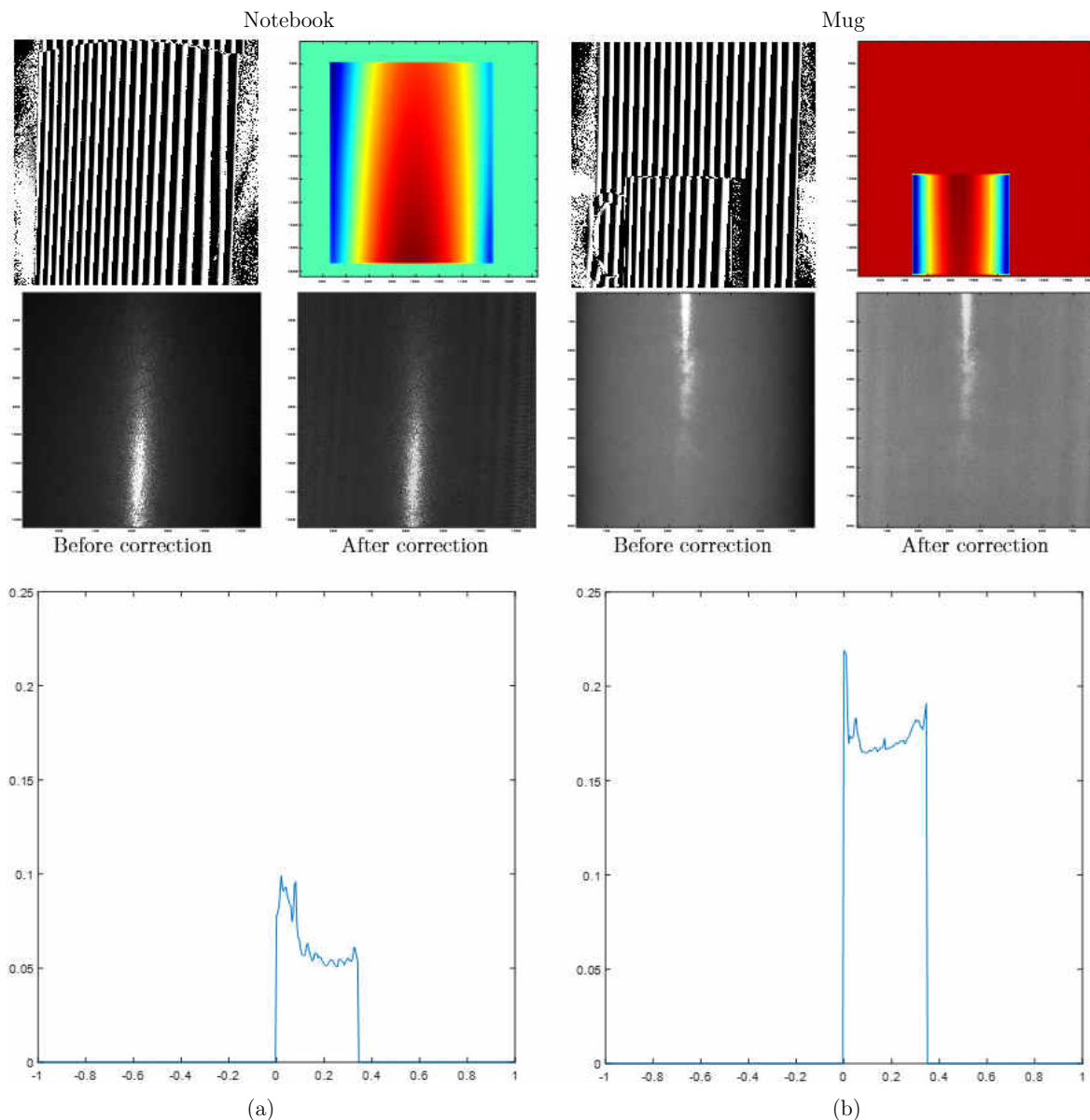


Figure 6.11. BRDF measurement using imaging and 3D scanning, (a) blue notebook and (b) yellow mug: From top to bottom, 3D acquisition using fringe projection, depth map (false color), image before and after correction and BRDF in relation to the angle to the specular direction (in radians).

The estimated BRDF of these two objects seem to correspond to their properties: for the yellow mug, which is highly specular, the central peak, which corresponds to the specular direction, is rather thin; in contrast, for the textured book surface, the central peak is wider: its size is almost twice the size of the peak of the mug. This is due to the fact that the surface of the book has micro-reliefs. We can also observe some measurement artefacts due to imprecisions in the 3D scanning (see the wave effects on the images after correction). In addition to these measurement errors, our setup is mainly limited by the narrow range of measured angles. The angle between the camera and the digital projector is around 10 degrees, which is required for 3D scanning. It is too limiting in the case of BRDF measurement, as the angles between illumination and observation remain small for a cylinder-like object in this configuration. The solution proposed by Marschner [Marschner et al. 1999b] is to move the sensor while the punctual source remains at the same location to increase the quantity of acquired data and increase the range of acquired angles. In our case, moving the camera would not be adapted for *in vivo* acquisition. Instead, several punctual sources at various location can be added at relatively low economic cost. In such a scenario, the image-based BRDF measurement would no longer be a one shot acquisition, but acquisition time would still remain relatively short (a few seconds).

6.4. Conclusion

The possibility of using 3D information for correcting irradiance non-uniformity and improving the measurement of spectral reflectance was the initial motivation for combining the hyperspectral camera with a 3D scanning system. The corrected images presented in this chapter, however, demonstrate that although geometry-based irradiance correction is a “physics-based” method, the chosen approach is too sensitive to acquisition noise. A more precise 3D acquisition system or a less “brute-force” method, which partially relies on optimization for example, should be considered to address this issue.

Given the limitations raised above, we have not implemented this irradiance correction method as a pre-processing step for skin analysis. Instead, we have used an analysis algorithm that is robust to irradiance shifts, described in Chapter 7.

As mentioned before, we can also wonder whether the assumption that skin is Lambertian is valid. The works of Marschner on the measurement of skin BRDF have shown that skin is mainly Lambertian near normal incidence, but as the angle of incidence increases, forward scattering also increases [Marschner et al. 1999a; Marschner et al. 1999b]. Skin reflection properties differ from those of a Lambertian reflector when high angles of incidence are involved.

Chapter 7.

Chromophore map estimation from HSI analysis

Skin structure and composition determine how light travels within skin and, consequently, influences its color. In particular, skin spectral reflectance, acquired using the hyperspectral camera described in Chapter 4, contains a “spectral signature” that can be linked to skin optical properties through modeling. It is thus possible to analyze skin spectral reflectance using an optical-model based method to retrieve information pertaining to skin physiology. The analysis of skin spectral reflectance consists of modeling how incident light on skin travels within it before being reflected back in the field of view of the camera. This is the direct approach, which predicts skin spectral reflectance when its optical properties are known. In our work, as we are aiming to retrieve skin optical properties from the measured spectral reflectance, the inverse problem must be solved.

In our application, we are seeking specifically to retrieve information about skin chromophore composition. As each skin chromophore has distinct absorption properties with regard to wavelength, their respective quantities can be estimated from the measured spectral signal. We model skin as a stack of two planar layers and use a two-flux model to describe light-skin interactions. Previous works have shown that this method yields highly satisfactory results on small and flat surfaces [Seroul et al. 2017]. The method, however, has not been tested on complex three-dimensional surfaces, on which the measurement is affected by irradiance drifts. We show in this chapter that the implemented method is robust to irradiance drifts and can consequently be applied to complex three-dimensional objects such as a full face.

In this chapter, we first detail in Section 7.1 the “skin analysis” method used to estimate maps of chromophore concentrations from the hyperspectral images, which comprises a model of skin, a model of light-skin interaction and an optimization method. In Section 7.2, the efficacy of the method is discussed by means of simulations and

experimental analysis. Finally, projects for going further using convolutional neuron networks are presented in Section 7.3 before drawing the conclusions.

7.1. Model-based estimation of chromophore maps

The hyperspectral image analysis method presented in this section, is the continuation of Seroul's work [Seroul et al. 2017]. It uses two optical models, both detailed in this section, that together define the direct approach: a model describes skin structure and composition in chromophores, and a model describes how light interacts with absorbing and scattering materials.

The overall optical model combines three laws, as illustrated in Figure 7.1. The first one corresponds to the relationship between each layer's optical properties and skin chromophore concentrations. The second one gives, for a given layer, the relationship between the absorption and scattering coefficients of the layer and its transmittance and reflectance. Finally, the third law accounts for both layer reflectance and transmittance in skin reflectance.

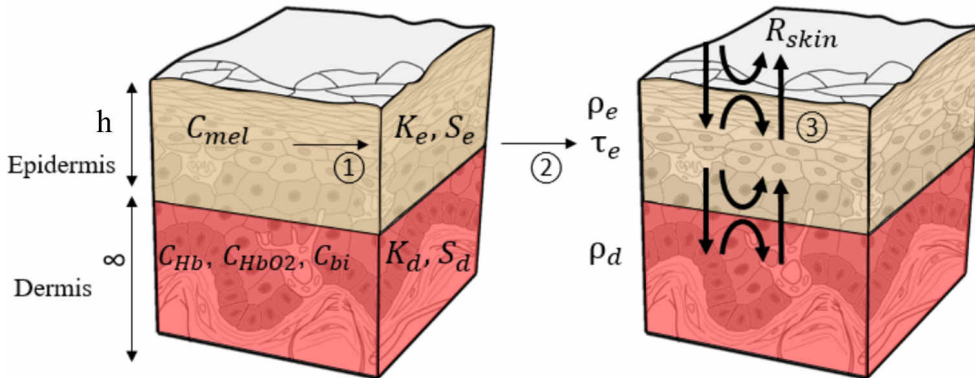


Figure 7.1. Skin model and light-skin interaction models used in the analysis method: ① Beer-Lambert-Bouguer laws, ② Kubelka Munk theory and ③ Kubelka formula and Saunderson correction.

The last part of this section details the optimization method used to compute chromophore concentration maps. For the analysis of full face hyperspectral images, the method must be as robust as possible to irradiance drifts, in order to limit the impact of curvature on the chromophore concentration estimation.

7.1.a. Skin model

The direct approach comprises a model for skin structure and composition. A trade-off between accuracy and simplicity must be found: a very simple skin model yields a model

easy to inverse, but its parameters do not accurately describe skin; a complex model that accurately describe skin with many parameters might provide more accurate analysis, but the calculation time needed for inversion is likely to be long, and errors arising from optimization are more likely to occur. As seen in Chapter 3, skin is a complex organ, made of two main layers, epidermis and dermis, themselves divided into several sub-layers, each of which have their own specific cell structures and chemical compositions.

The literature on tissue optics usually considers skin as a parallel plane comprising between one and 22 layers: some studies using Monte Carlo algorithms have limited their model to one layer to minimize calculation time [Cuccia et al. 2009]; the Kubelka-Munk method is often applied to two-layer models [Doi et al. 2016]; three layers have been used to account for the hypodermis beneath the dermis [Schmitt et al. 1990]; and Magnain showed that using the radiative transfer theory, the most accurate skin spectra were obtained using a 22-layer model [Magnain et al. 2007].

We have opted for a model that describes skin as a two-layer medium, roughly corresponding to the epidermis and the dermis, whose composition and optical properties are significantly different. Our decision to use two layers is a trade-off between a realistic description of skin structure and a model that is sufficiently simple to allow for optimization-based model inversion: the number of layer increases the number of parameters that have to be optimized – and concomitantly, the risk of failing to find the minimum of the cost function during the optimization process, which can result in significant errors.

Our two-layer model does not separate the stratum corneum from the epidermis. The stratum corneum is the outermost layer of the epidermis composed of dead cells filled with keratin [Igarashi et al. 2007], which especially affects skin specular reflection. For our application, the cross-polarization (CP) configuration used in the imaging system discards this reflection. In addition, the stratum corneum is a mainly scattering layer which has little impact on the absorption properties that we are estimating. Consequently, the nonseparation of the stratum corneum from the epidermis has a little effect on our analysis accuracy.

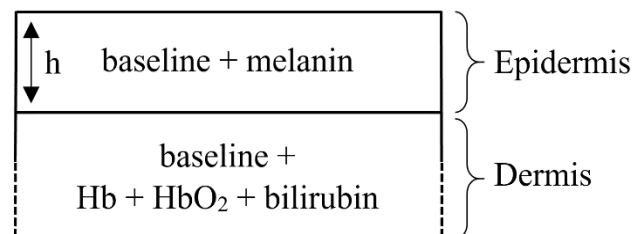


Figure 7.2. Skin model used in the optical analysis of hyperspectral reflectance.

The two-layer model for skin (Figure 7.2) is a simplification in which each layer is considered as flat and homogeneous. The epidermis is composed of a baseline and melanin,

and the dermis is composed of a baseline, deoxyhemoglobin (Hb), oxyhemoglobin (HbO₂) and bilirubin.

Each layer can be characterized by spectral absorption and scattering coefficients, $K(\lambda)$ and $S(\lambda)$ respectively. The absorption coefficient depends on the spectral absorbance of chromophores contained in the layer and their volume fraction: according to the Beer-Lambert-Bouguer law [Bouguet 1729], the spectral absorption coefficients of the epidermis $K_e(\lambda)$ and dermis $K_d(\lambda)$ can be written according to additive linear laws:

$$K_e(\lambda) = (1 - c_m)K_b(\lambda) + c_m K_m(\lambda), \quad (7.1)$$

and

$$K_d(\lambda) = (1 - c_{Hb} - c_{HbO_2} - c_{bi})K_b(\lambda) + c_{Hb}K_{Hb}(\lambda) + c_{HbO_2}K_{HbO_2}(\lambda) + c_{bi}K_{bi}(\lambda). \quad (7.2)$$

We refer to the work of Jacques [Jacques 2013] for the spectral absorption coefficient values of the baseline $K_b(\lambda)$, melanin $K_m(\lambda)$, hemoglobin $K_{Hb}(\lambda)$, oxyhemoglobin $K_{HbO_2}(\lambda)$ and bilirubin $K_{bi}(\lambda)$, as well as for the spectral scattering coefficients of the epidermis $S_e(\lambda)$ and dermis $S_d(\lambda)$. The volume fractions of melanin c_m , hemoglobin c_{Hb} , oxyhemoglobin c_{HbO_2} and bilirubin c_{bi} are unknown quantities that will be estimated through optimization, based on the two-flux model described in the next section.

7.1.b. *Light-skin interactions model*

Various optical methods have been used to describe light-skin interaction, including Monte Carlo methods [Nishidate et al. 2004; Meglinski and Matcher 2003], solutions of the radiative transfer equation [Magnain et al. 2007], models based on the diffusion approximation [Kienle et al. 1998; Zonios and Dimou 2006] or flux models [Jolivot et al. 2013; Doi et al. 2016]. The method that we have selected is framed by practical constraints: it must yield accurate parameter estimation but computation time must also remain reasonable.

The Monte Carlo methods are considered a benchmark in terms of accuracy but their inversion is time-consuming. For imaging applications, the calculation time required for one optimization on one pixel has to be multiplied by the number of pixels to estimate the overall calculation time. Consequently, while Monte Carlo can be used for punctual measurement analysis, it becomes prohibitively costly in terms of time when dealing with high resolution imaging. Pre-calculated look-up tables can be used as an alternative [Cuccia et al. 2009], but the number of parameters in the model must be low to allow affordable computation.

Two-flux models, such as the Kubelka Munk theory, are limited to diffuse illumination and materials with high scattering properties. However, they provide analytical reflectance and transmittance formulae, an advantage over other light scattering models.

Methods based on the radiative transfer theory describe more finely the scattering of light, in particular taking into account its angular distribution, and have been applied for accurate skin spectral reflectance modeling [Magnain et al. 2007]. Using such methods in applications that require the solving of an inverse problem is however difficult in practice, mainly due to computation time and complex angular measurements.

Finally, diffusion approximation can also be used to model skin spectral reflectance, but it is even more constrained than two-flux models as it describes materials whose absorbance is low in comparison to scattering. Diffusion approximation can be efficacious in modeling light transport for heterogeneous illumination but it is less effective than two-flux methods when considering multi-layer materials under homogeneous illumination.

For the reasons listed above, we chose to use a two-flux model for our application, as a trade-off between accuracy and simplicity.

The hyperspectral reflectances are analyzed with the two-flux model described in Seroul's work [Seroul et al. 2017], in which light propagation within each layer is described by the Kubelka-Munk formulae [Kubelka and Munk 1931]. The epidermis is characterized by its thickness h , spectral absorption coefficient $K_e(\lambda)$ and spectral scattering coefficient $S_e(\lambda)$. Its spectral reflectance $R_e(\lambda)$ and transmittance $T_e(\lambda)$ are, for each wavelength:

$$R_e = \frac{\sinh(b_e S_e h)}{b_e \cosh(b_e S_e h) + a_e \sinh(b_e S_e h)}, \quad (7.3)$$

and

$$T_e = \frac{b_e}{b_e \cosh(b_e S_e h) + a_e \sinh(b_e S_e h)}, \quad (7.4)$$

with

$$a_e = (K_e + S_e) / S_e \quad \text{and} \quad b_e = \sqrt{a_e^2 - 1}. \quad (7.5)$$

The dermis is assumed to be infinitely thick from an optical point of view, and its transmittance is zero. It is characterized by its spectral absorption coefficient $K_d(\lambda)$ and spectral scattering coefficient $S_d(\lambda)$. According to the Kubelka-Munk model, its spectral reflectance $R_d(\lambda)$ is given for each wavelength by:

$$R_d = a_d - b_d = \frac{K_d + S_d - \sqrt{K_d(K_d + 2S_d)}}{S_d}, \quad (7.6)$$

where a_d and b_d are functions of K_d and S_d , defined in the same way as in Eq. (7.5).

Finally, the spectral reflectance of skin, described as the superposition of dermis and epidermis, is given by Kubelka's formula [Kubelka 1954]:

$$R = R_e + \frac{T_e^2 R_d}{1 - R_e R_d}. \quad (7.7)$$

The effects of the air-skin interface have not been taken into account up to this point. Reflections at the interface also occur inside the skin. To account for the portion of light that is reflected back into the skin, we must apply the Saunderson correction [Saunderson 1942], illustrated in Figure 7.3:

$$R_{skin} = R_1 + \frac{(1 - R_2)(1 - R_1)R}{1 - R_2 R}. \quad (7.8)$$

In our application, the specular reflection at the surface, represented by the orange arrow in Figure 7.3, is discarded by the cross-polarization (CP) configuration. The measured quantity is:

$$R_{skin} = \frac{(1 - R_2)(1 - R_1)R}{1 - R_2 R}. \quad (7.9)$$

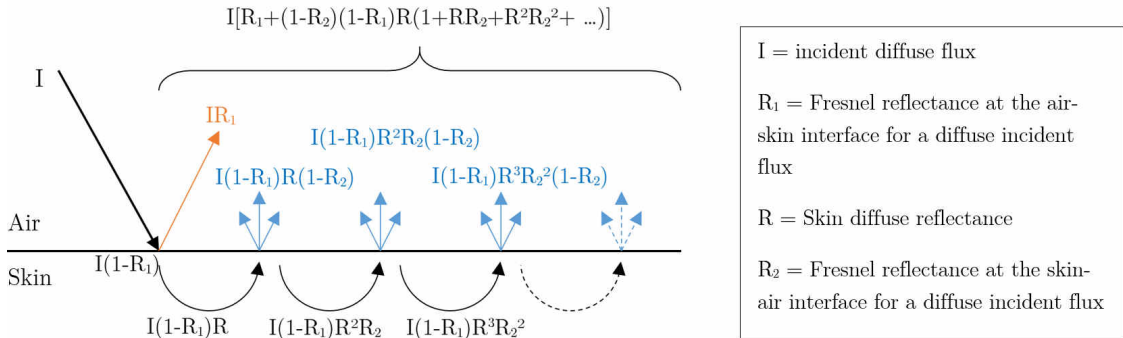


Figure 7.3. Principle of the Saunderson correction at the air-skin interface.

In this expression, the diffuse reflectance R is the only quantity that is dependent on skin chromophore concentration and epidermis thickness. The quantities R_1 and R_2 are functions of skin optical index n . The Fresnel reflectance at the interface from air to skin R_1 and at the interface from skin to air R_2 are given as a function of the Fresnel reflectance $R_{Fresnel}(\theta)$ given in Chapter 2 [§ 2.3.a, Eqs (2.16) and (2.17)]:

$$R_1 = \int_{\theta=0}^{\pi/2} R_{Fresnel}(\theta) \sin 2\theta d\theta, \quad (7.10)$$

and

$$R_2 = 1 - \frac{1 - R_1}{n^2}. \quad (7.11)$$

Equation (7.10) also has an analytical formula [Hébert et al. 2014]:

$$R_1 = \frac{1}{2} + \frac{(n-1)(3n+1)}{6(n+1)^2} - \frac{2n^3(n^2+2n-1)}{(n^4-1)(n^2+1)} + \frac{8n^4(n^4+1)\ln(n)}{(n^4-1)^2(n^2+1)} + \frac{n^2(n^2-1)^2}{(n^2+1)^3} \cdot \ln\left(\frac{n-1}{n+1}\right). \quad (7.12)$$

7.1.c. Resolution of the inverse problem using an optimization

The direct model described above gives skin spectral reflectance when skin chromophore composition is known. In our case however, we are required to determine the skin chromophore concentrations $\{c_{mel}, c_{Hb}, c_{HbO_2}, c_{bi}\}$ from the measured spectral reflectance by solving the inverse problem. This process consists of finding for each pixel the parameter values that minimize the distance $d(R_{skin}, R_m)$ between the measured spectrum $R_m(\lambda)$ and the predicted spectrum $R_{skin}(\lambda)$ computed using Eq. (7.9):

$$\{c_m, c_{Hb}, c_{HbO_2}, c_{bi}, h\} = \arg \min_{c_m, c_{Hb}, c_{HbO_2}, c_{bi}, h} [d(R_{skin}, R_m)]. \quad (7.13)$$

The parameters obtained by optimization are dependent on the definition of the distance d . A classical distance that can be used is the Euclidean distance, defined as:

$$d_E(R_{skin}, R_m) = \sqrt{\sum_{\lambda} (R_{skin}(\lambda) - R_m(\lambda))^2}. \quad (7.14)$$

On complex shapes like the face, some areas receive less light and the amplitude of the measured spectrum is consequently lower. Using the Euclidian distance in the analysis algorithm, these irradiance non-uniformities are interpreted as variations of chromophore concentrations. In order to prevent these errors, the metric must be independent from the spectrum amplitude, which is the case for the *Spectral Angle Mapper* (SAM) [Yuhus et al. 1992], defined as:

$$d_{SAM}(R_{skin}, R_m) = \arccos \left(\frac{\sum R_{skin}(\lambda) R_m(\lambda)}{\sqrt{\sum R_{skin}^2(\lambda) \sum R_m^2(\lambda)}} \right). \quad (7.15)$$

To illustrate the SAM properties, let us compare three areas of skin (Figure 7.4). The first is a reference area characterized by the measured spectral radiance $S_0(\lambda)$. The second area has the same chromophore composition as the first but with a lower incident irradiance, which implies that the perceived color is darker and the spectral radiance is $S_1(\lambda) = kS_0(\lambda)$ with $k < 1$. The third area of skin differs in chromophore composition from the first two areas and is characterized by the measured spectral radiance $S_2(\lambda)$.

When comparing the three spectral radiances using the root-mean-square (RMS) metric, $d_{RMS}(S_0, S_1)$ is high while $d_{RMS}(S_0, S_2)$ is low, due to the invariance of this metric in respect to lightness. The RMS metric is consistent with perceived color, which can be

affected by varying irradiance, but does not represent well the variations in skin chromophore properties. When comparing the three spectral radiances using the SAM metric, on the other hand, $d_{SAM}(S_0, S_1)$ is zero, while $d_{SAM}(S_0, S_2)$ is a not. The SAM metric evaluates only the shape difference between the two spectra, and is insensitive to irradiance variations. Owing to these properties, the SAM metric yields better results for the skin analysis algorithm.

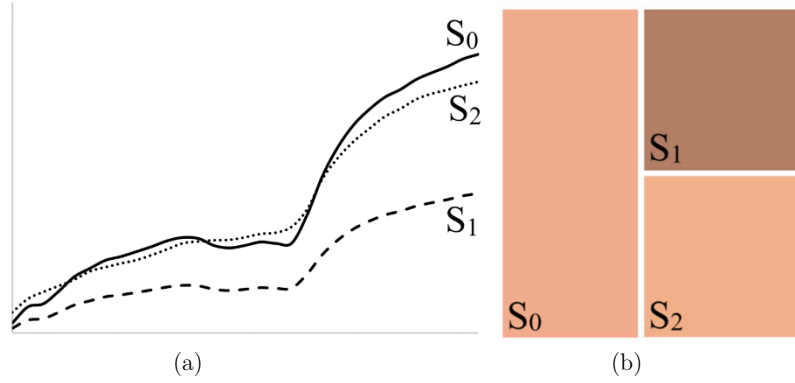


Figure 7.4. (a) Spectral radiance and (b) corresponding RGB colors. Distances to the reference spectrum S_0 according to the RMS metric and the SAM metric are: $d_{RMS}(S_0, S_1) = 14$; $d_{RMS}(S_0, S_2) = 2$; $d_{SAM}(S_0, S_1) = 0$; $d_{SAM}(S_0, S_2) = 6 \cdot 10^{-2}$.

7.2. Full face spectral reflectance analysis

The parameters of the model described so far are the skin chromophore concentrations $\{c_{mel}, c_{Hb}, c_{HbO_2}, c_{bi}\}$ and the epidermis thickness. In the outputs of the skin analysis optimization, the concentrations in Hb and HbO₂ are replaced by the total blood volume content c_{blood} and the oxygen rate α , defined as:

$$c_{blood} = c_{Hb} + c_{HbO_2}, \quad (7.16)$$

and

$$\alpha = c_{HbO_2} / c_{blood}. \quad (7.17)$$

The skin analysis outputs are displayed in the form of maps that show melanin concentration (actually corresponding to melanosome volume fraction, as mentioned in Chapter 3), oxygen rate and blood volume fraction (Figures 7.5.b, c and d). These maps, which correspond to estimated values, can be used to visualize and sort different structures such as veins, capillaries, hematoma, red spots and pigmented spots. They can also be used to follow the evolution of the skin conditions that affect chromophores or to monitor the effects of anti-dark circle cosmetic products on skin [Nkengne et al. 2018].

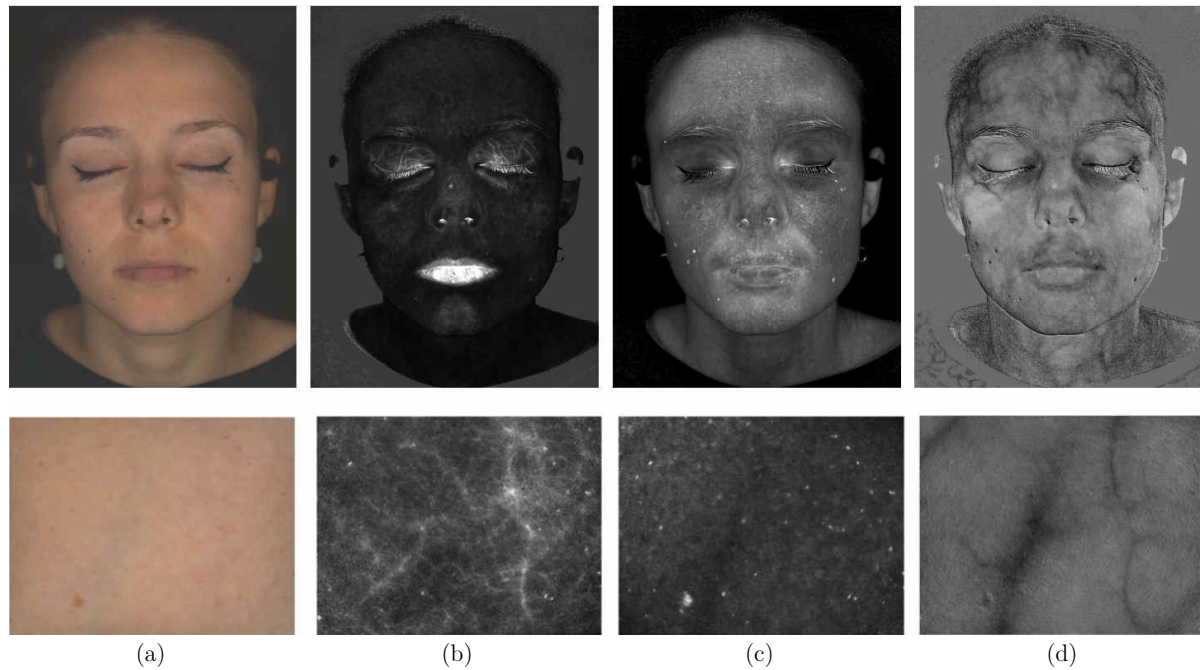


Figure 7.5. (a) Color image and maps of estimated chromophore concentration: (b) blood volume fraction, (c) melanin concentration and (d) oxygen rate. The top images correspond to a full face acquisition done using the SpectraFace camera (Chapter 4), the bottom images results from analysis on a SpectraCam® acquisition. (These images can be found in large format in Appendix 2).

The calculation time required to obtain these maps is around 5 hours for full face maps and one hour for smaller maps. On a full face, the calculation time could be reduced by removing the non-skin pixels from the input image. Indeed, for each pixel, a maximum number of iterations is set in the optimization algorithm, with an early stop possible when the error is lower than a certain threshold. Outside of skin areas, the model does not converge and the algorithm keeps running until the maximal number of iteration has been reached, which wastes time.

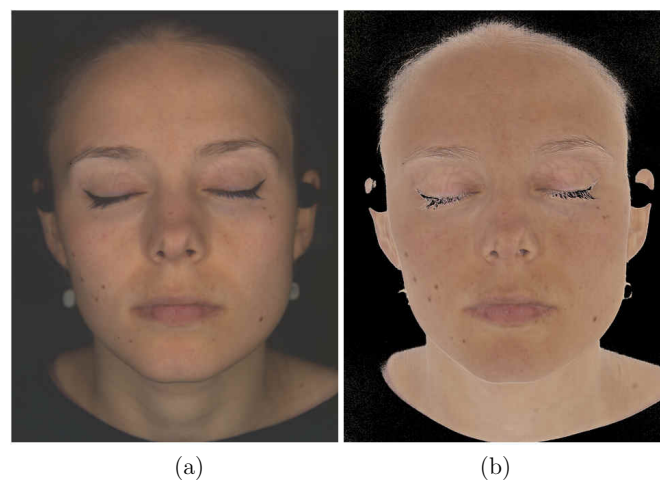


Figure 7.6. (a) Original color image and (b) reconstructed color image.

Figure 7.6.b shows the color image obtained after conversion of the predicted spectrum into color. The predicted spectrum was computed using the optical model [Eq. (7.9)] and the chromophore concentrations estimated by the skin analysis algorithm. As the computation erases irradiance drifts, we have the impression that the face has been flattened, especially in the reconstructed color image.

A map showing the residual distance of the optimization for each pixel allows us to compare the efficacy of the different optimization metrics and to validate our choice. The residual distance map gives a general idea of the quality of the analysis, but it is not an error map: it only indicates how well the model has converged, without accounting for the errors produced by model itself. Figure 7.7 shows the residual distance maps obtained using the RMS and SAM metrics, and the oxygen rate maps obtained for each analysis.

We notice that the values of the residual distance map for the RMS-based optimization are influenced by the shape of the face. As such, this metric cannot be applied on non-planar objects unless each pixel receives the same incident irradiance. The SAM, on the other hand, is more robust to irradiance drifts: the residual error map shows that the optical analysis using SAM is good at distinguishing skin (low residual distance) from other elements such as hair, fabric, make-up and background (high residual distance). This validates the use of SAM rather than RMS distance in the optimization process.

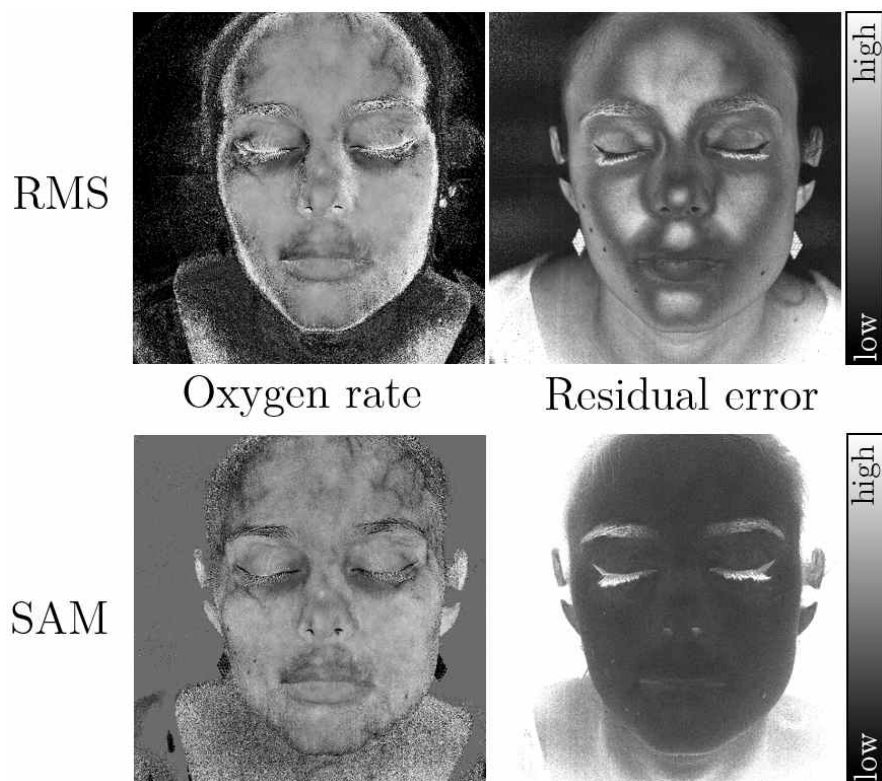


Figure 7.7. Maps of oxygen rate and residual distance from the skin optical analysis for a RMS-based optimization and a SAM-based optimization.

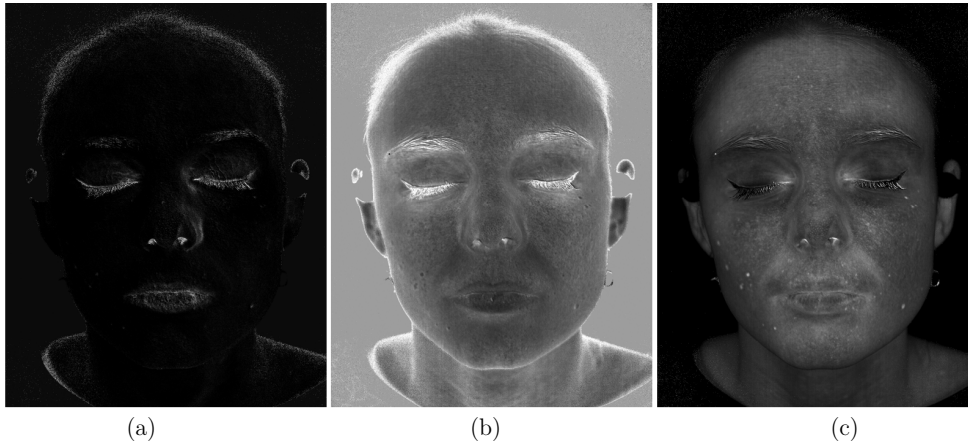


Figure 7.8. (a) Map of bilirubin concentration (displayed between 0 and 10%), (b) maps of epidermis thickness and (c) map of melanin concentration.

In addition to the 3 chromophore maps shown in Figure 7.5, the analysis method yields maps of bilirubin concentration and epidermis thickness (Figure 7.8). In the absence of pathologies such as jaundice or bruises, the bilirubin content in skin is very low. Consequently, the bilirubin map is rarely shown. Regarding the epidermis thickness map, its values are close to the typical range for healthy skin [Seroul et al. 2017], but seem to be highly correlated with the melanin concentration, which should not be the case from a biological perspective. We cannot therefore be sure that this map is actually showing skin thickness. It seems that the epidermis thickness is the free variable helping the algorithm to converge toward the closest spectrum to the spectrum measured. Questions about what it is representing and on the validity of the method in general have led us to investigate how variations in spectral reflectance are converted into variations in estimated skin parameters. We present below two approaches to assess the efficacy of the method, theoretical and experimental. Each yields particular insights on the model errors and its limitations.

7.2.a. Robustness of the analysis method: theoretical study

The theoretical study relies on creating synthetic spectral reflectance data from a set of chromophore concentration values, using the direct model described in Section 7.1. If the analysis method is accurate, applying it to synthetic data should allow us to retrieve the parameters used to generate the data. The robustness of the analysis method can therefore be assessed by computing the difference between the skin parameters estimated by the algorithm and their expected values.

In our work, we used the following set of parameters, to predict the spectral reflectance shown in Figure 7.9, considered as a reference:

$$\left\{ \alpha = 60\%, c_{blood} = 11\%, c_{mel} = 27.5\%, c_{bi} = 0.5\%, h = 42\mu m \right\}. \quad (7.18)$$

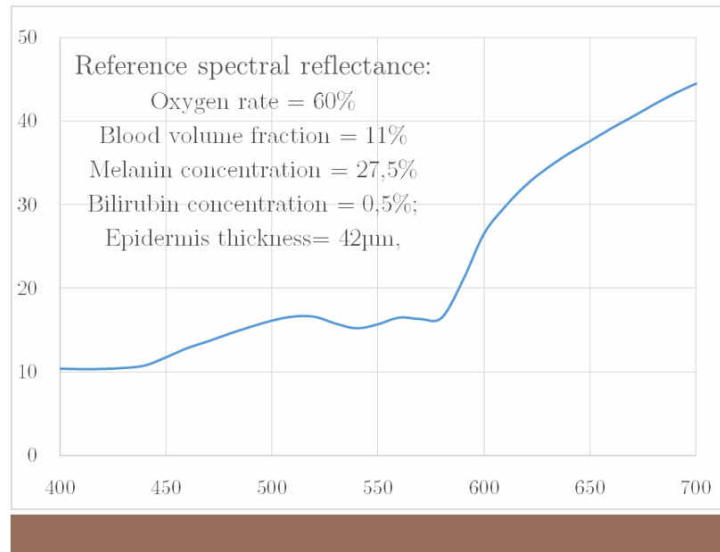


Figure 7.9. Reference spectral reflectance (%) and corresponding color.

From this reference, a dataset of spectral reflectance has been created using the direct model, varying one parameter at a time within a range of plausible values (excluding very low epidermis thicknesses). The corresponding simulated spectra are illustrated in Figure 7.10, with low values for the parameter plotted in dark shades of blue and high values plotted in light shades of blue. The color corresponding to each spectrum is represented underneath the graph, with the values of the parameter increasing from left to right.

We can notice on Figure 7.10 that the color variations due to changes in oxygen rate are almost imperceptible: variations of oxygen rate slightly affect the amplitude of the spectrum in the long wavelengths (above 600 nm) and also modify the “W” shape of the spectrum around 550 nm, which is more distinct for higher oxygen rate values.

Variations of blood volume fraction create strong spectral variations, which correspond to color variations mainly in terms of hue and chroma. These color variations, however, are less noticeable than those obtained when melanin concentration or epidermis thickness, which influence color lightness, vary. When comparing the variations induced by changes in melanin concentration and epidermis thickness, we observe a noticeable difference between the two diagrams only in the short wavelengths (between 400 and 450 nm). Melanin concentration and epidermis thickness are not totally independent from each other: for a given melanin concentration, the overall quantity of melanin varies with epidermis thickness, which partly explains why the melanin and the epidermis thickness maps are correlated. However, in the short wavelengths, light cannot travel very deep into the skin because of scattering, and the epidermis thickness has a weaker impact on reflectance. The corresponding color variations exhibit these properties: higher melanin concentration or higher epidermis thickness both result in a darker color; and low melanin concentration or thin epidermis thickness both result in a light color. When epidermis thickness is low, the hue is more yellowish.

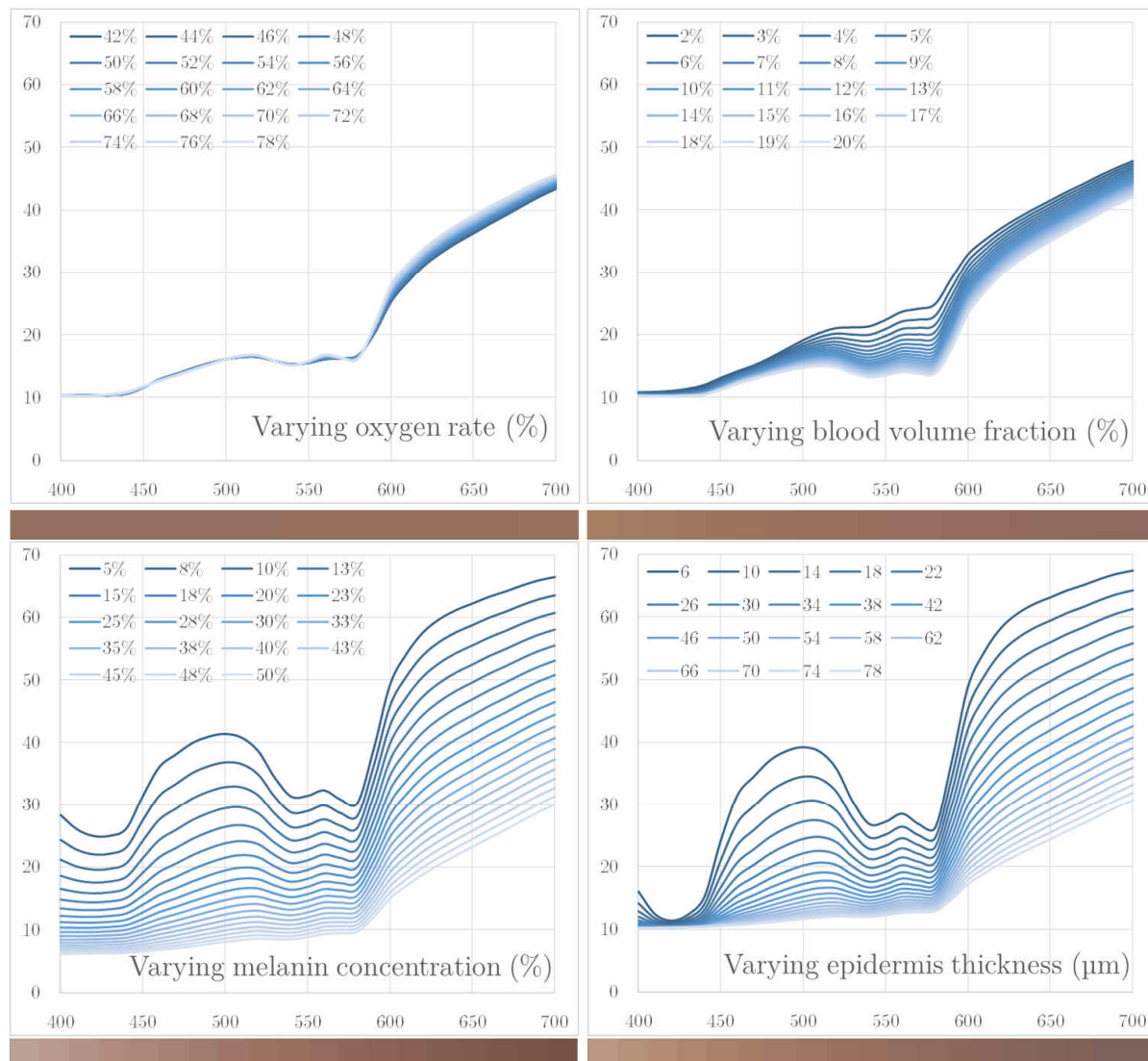


Figure 7.10. Simulated spectral reflectance (%) as a function of wavelength (nm) obtained when one parameter varies. For each graph, the color bar displayed below it depicts the color corresponding to the spectral reflectance when the parameter varies from its lowest value (left) to its highest (right).

The analysis method has been applied on synthetic spectral reflectance data, yielding estimated chromophore concentrations and epidermis thickness. The difference between the estimated parameters and the expected parameters has been plotted in Figure 7.11 in the form of relative error (%). Error on the bilirubin parameter has not been plotted on the figures of this section. In relative values, bilirubin shows a high amount of error, but we do not consider that this invalidates the analysis method, given the very small initial value of the parameter, and the fact that this information is rarely used in normal skin analysis.

Figure 7.11 shows that the model provides estimations close to the expected values when oxygen rate or blood volume fraction vary. Variations of epidermis thickness and melanin concentration yield greater error, especially on the estimation of the oxygen rate,

which is under-estimated. Relative errors are high when epidermis thickness is low, however, the very small values used to create the synthetic data do not correspond to real skin. As for melanin concentrations, for which the range of variation is representative of real skin, error is also high for high concentrations of melanin. Consequently, the analysis method might not yield accurate analysis on darker colored skin, which contains higher concentrations of melanin than lighter colored skin.

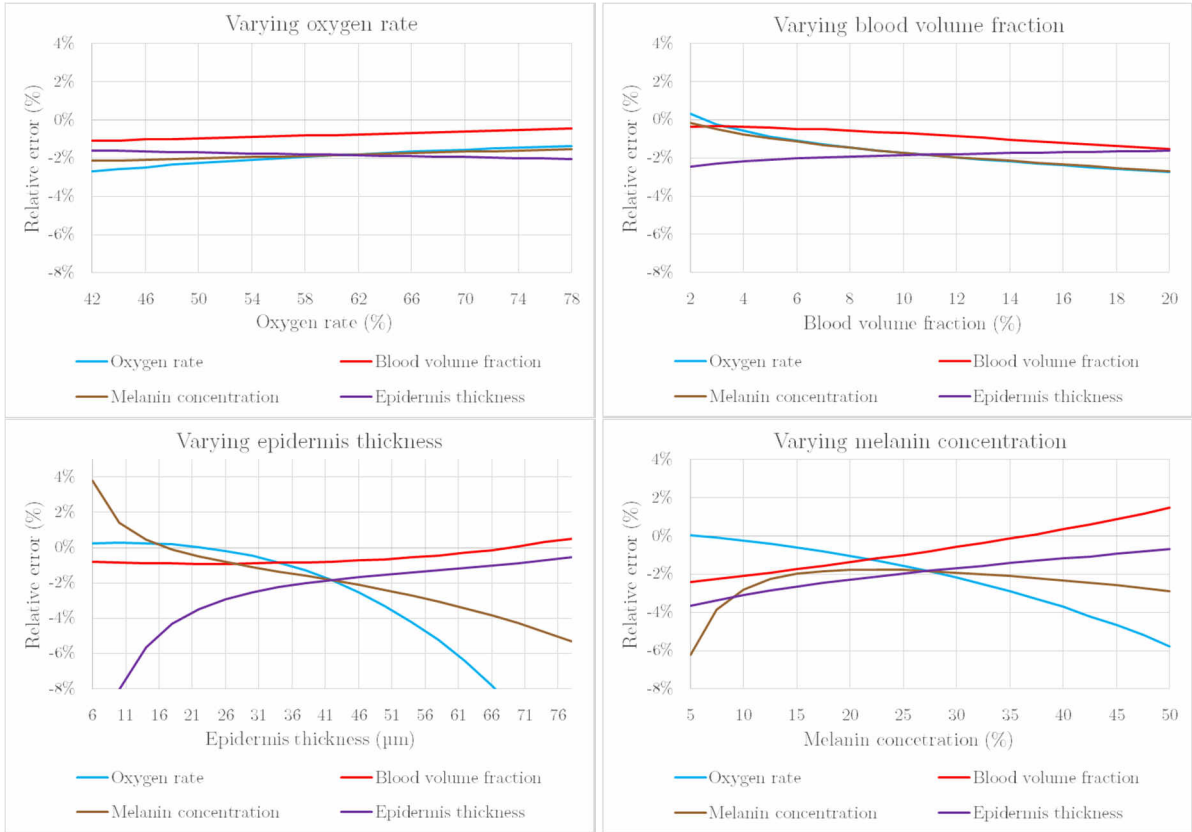


Figure 7.11. Relative error between the parameters estimated by the analysis method and the expected values of the parameters. For each graph, only one parameter varies.

In addition to oxygen rate, blood volume content, melanin concentration and epidermis thickness, the impact of skin scattering coefficient on the estimated parameter values was also evaluated. For simplicity, we described skin scattering by a Rayleigh law with two parameters b_{μ_s} and μ_{s_500} :

$$\mu_s'(\lambda) = \mu_{s_500} \left(\frac{\lambda}{500(nm)} \right)^{-b_{\mu_s}}. \quad (7.19)$$

In the analysis algorithm, $\mu_s'(\lambda)$ is fixed and can be approximated by $b_{\mu_s} = 3.1$ and $\mu_{s_500} = 49.9 \text{ cm}^{-1}$. We have created a range of synthetic spectral reflectance by varying one

or the other parameter around these reference values. The corresponding spectral reflectance values are illustrated in Figure 7.13. The parameter b_{μ_s} influences the slope of the $\mu_s'(\lambda)$ curve, and μ_{s_500} corresponds to the height of the curve. We can notice similar effects on the spectral reflectance curves of Figure 7.13, with variations of slope when b_{μ_s} varies, and translations when μ_{s_500} varies.

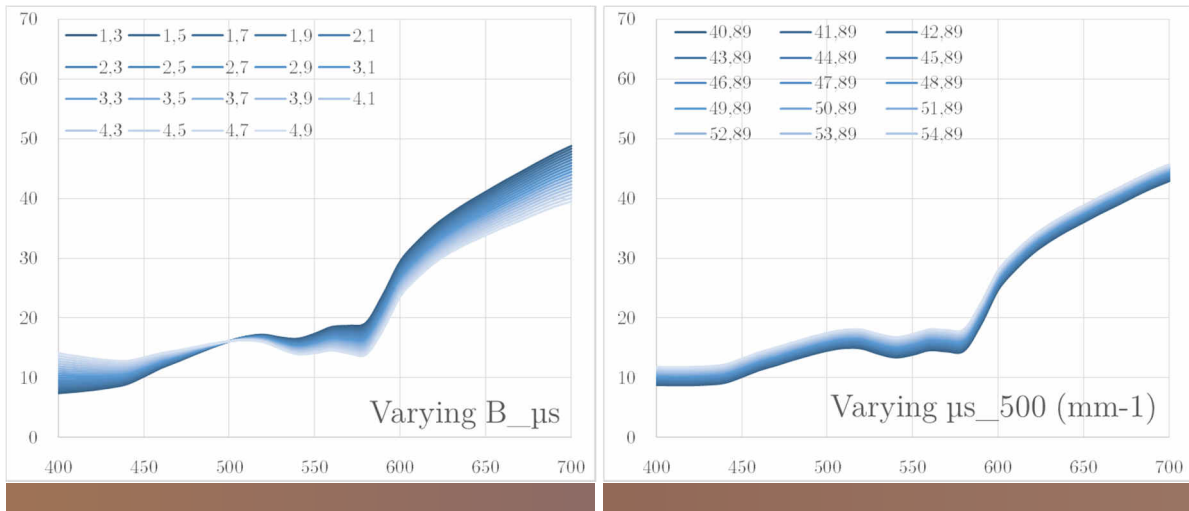


Figure 7.12. Simulated spectral reflectance (%) as function of wavelength (nm) obtained when one parameter of skin scattering properties varies, and corresponding skin color, from the lower value (left) to the highest value (right) of the varied parameter.

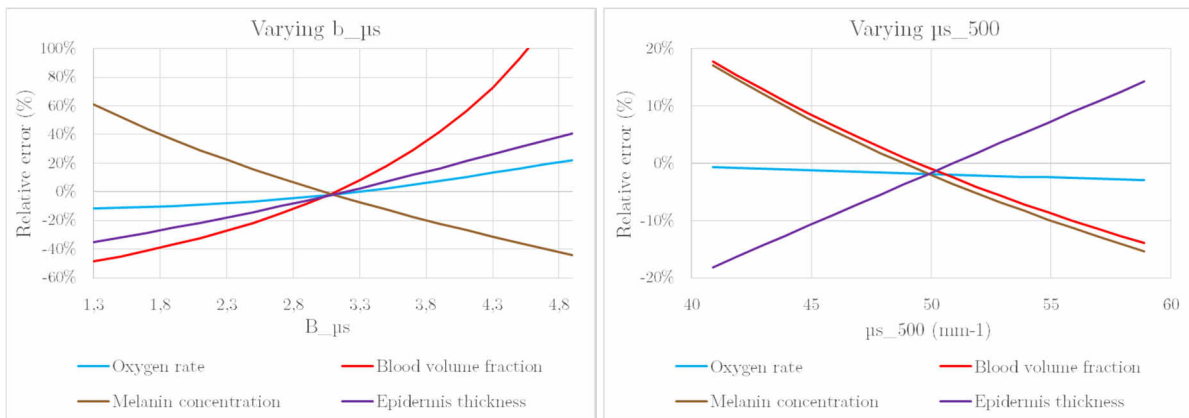


Figure 7.13. Relative error on the estimated parameter values when the parameters b_{μ_s} and μ_{s_500} vary.

Figure 7.13 shows the estimated parameter values when skin scattering coefficient varies. The relative error is high, which is expected since the scattering coefficient is not a parameter of the model and is assumed as constant on all pixels. The amount of error is especially high when b_{μ_s} varies, with a significant amount of error in the blood volume fraction estimation when b_{μ_s} is underestimated in the model. These results underline a

significant limitation of the method and the importance of accounting for skin scattering properties, which will be the theme of the next two chapters.

The analysis algorithm has been designed to be robust to irradiance drifts, which can also be verified using the same theoretical approach. The reference spectrum was multiplied by constants varying between 0.1 and 1.9 to model the effects of various illumination conditions. The modified spectra, the corresponding color and the relative error on the estimated parameter values are presented in Figure 7.14. Whatever the multiplicative constant applied on the spectral reflectance, there is no variation of relative error, which is consistent with the use of SAM, a metric robust to irradiance drifts.

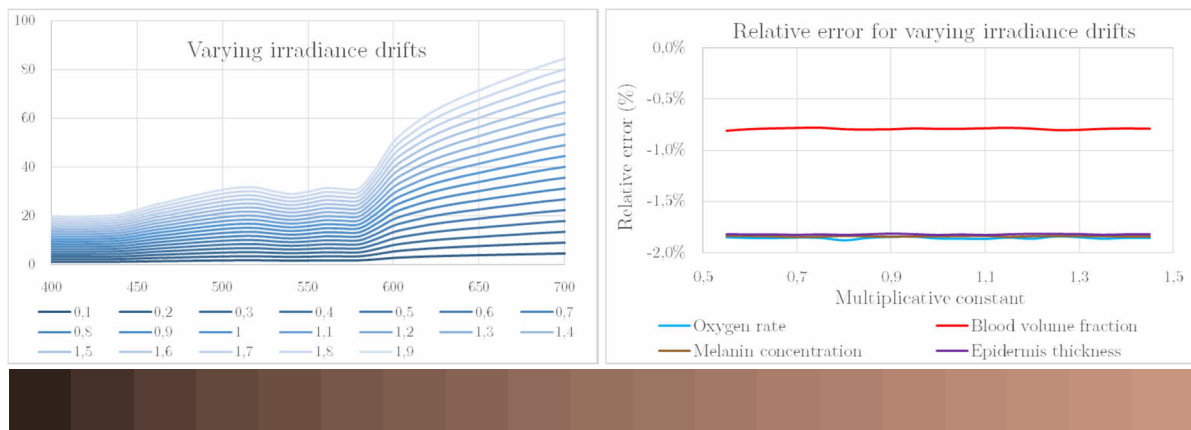


Figure 7.14. Effects of varying irradiance drifts on the spectrum, corresponding relative error and corresponding color.

Finally, to assess the robustness of the analysis method to noise, spectral reflectance data with various amounts of noise have been created. Gaussian noise with a standard deviation proportional to the reflectance at each wavelength has been added to the reference spectral reflectance. The standard deviation varies from 0 to 4.5% of the signal amplitude for the 19 small images that have been created. Their properties illustrated in Figure 7.15.

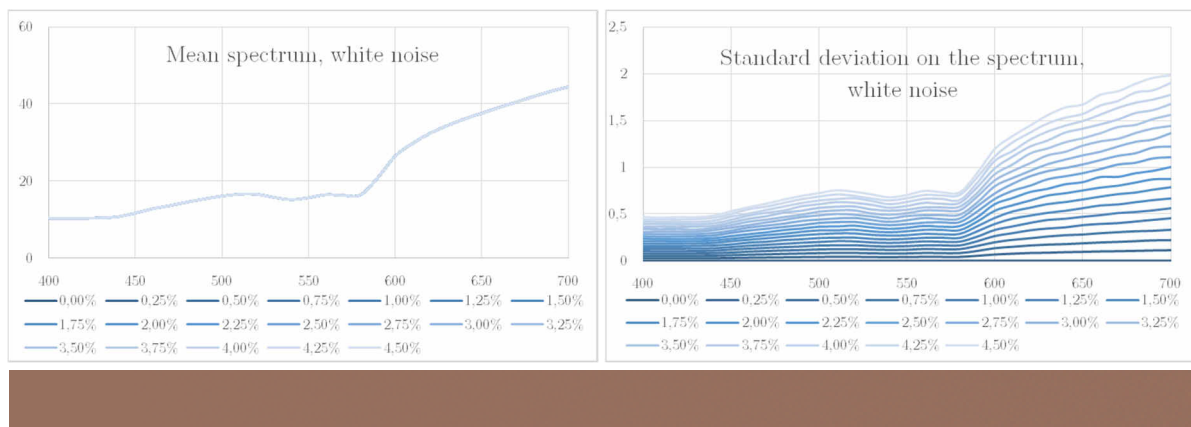


Figure 7.15. Effects of varying Gaussian noise on the average spectrum, standard deviation and color (from low noise on the left to high noise on the right).

On average, all the spectral reflectances are similar. Looking at the color bar (Figure 7.15), we can barely see any noise. However, in Figure 7.16, the effects of noise on the estimated parameter values, are clearly visible. In particular, the oxygen rate and the blood volume fraction are the two parameters that are the most sensitive to noise.

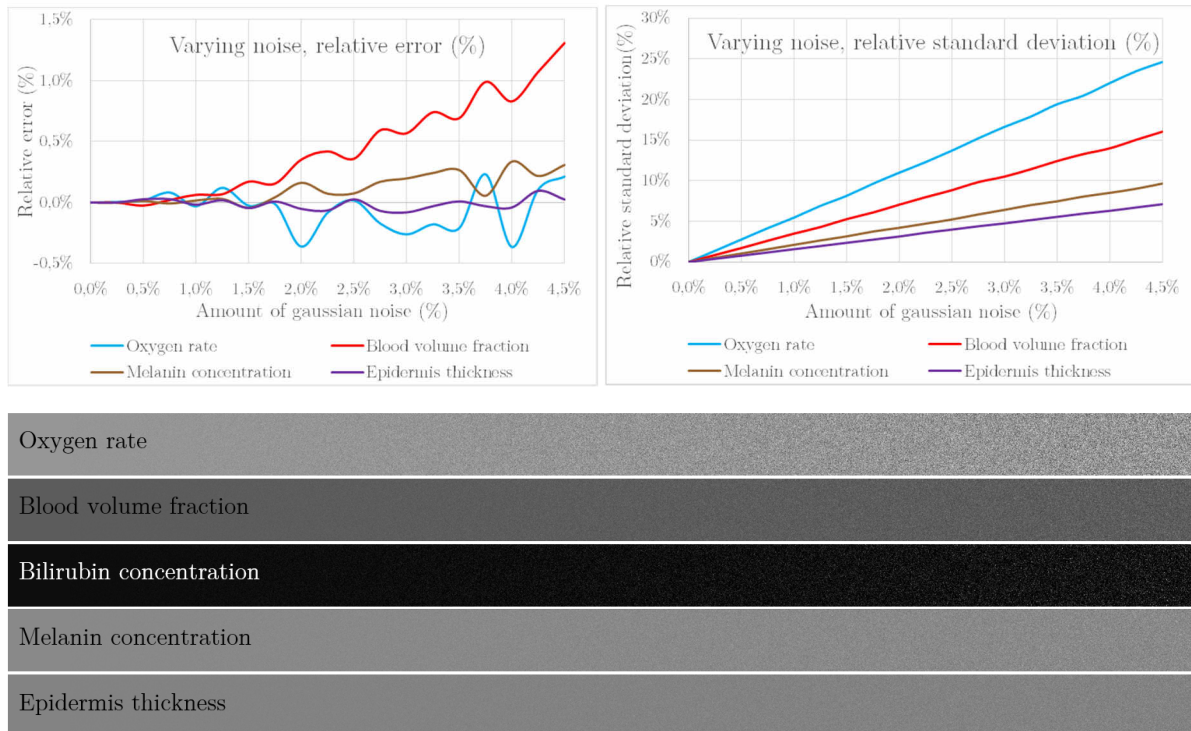


Figure 7.16. Effects of varying Gaussian noise on the estimated parameter values: relative mean error (%), relative standard deviation and corresponding chromophore maps, from low amount of noise (left) to high amount of noise (right). For these images, the display ranges are: [0%, 30%] for blood volume fraction, [0%, 10%] for bilirubin concentration, [0%, 50%] for melanin concentration and [0 μm , 80 μm] for epidermis thickness.

The analysis method shows satisfactory accuracy on light-colored skin. On dark-colored skin, however, the estimated parameter values are very noisy and not sufficiently accurate for clinical studies. This can be explained as follows. First, on dark skins, the spectrum amplitude is low and the signal to noise ratio is high, which generates noise to which the oxygen rate parameter is particularly sensitive (see Figure 7.16). Then, the simulations illustrated in Figure 7.11 shows that when the melanin concentration is high, the shape of the reflectance spectrum is relatively flat, making the “W” signature of oxygen difficult to distinguish. It also results in high amount of error on the estimation of the oxygen rate. From these two remarks and the noisy chromophore maps calculated from experimental measurements on dark-colored skin, we are forced to conclude that the current method is not adapted to their analysis.

7.2.b. Experimental validation of the method

The theoretical study developed above does not account for the shortcomings of the skin model itself, as the spectral reflectances are generated using the model. Skin spectrum simulated using Monte Carlo, which we were unable to carry out for lack of time, should be used for further theoretical analysis. Therefore, to further validate the method, we decided to observe the parameter values calculated from experimental measurements and to try to identify any variations that seem abnormal.

Error in this skin analysis method is difficult to assess as no ground truth chromophore concentration is available for in vivo measurements. It is also difficult to validate the method using skin phantoms as this would require samples made with a similar structure and spectral properties as real in vivo skin. The results of SpectraCam® have been validated by showing that the estimated chromophore concentrations are consistent with those expected in terms of melanin when measuring skin with lentigos, and in terms of blood content and oxygen rate after applying local pressure to induce blood inflow [Nkengne et al. 2018]. This study, however, is valid only for planar areas. On a full face, the proposed method can be validated by comparing two acquisitions of the same person at different orientations and verifying that the estimated chromophore concentrations remain similar. This comparison has been implemented by calculating the relative deviation between the average chromophore concentrations corresponding to the same areas on a front view and a side view.

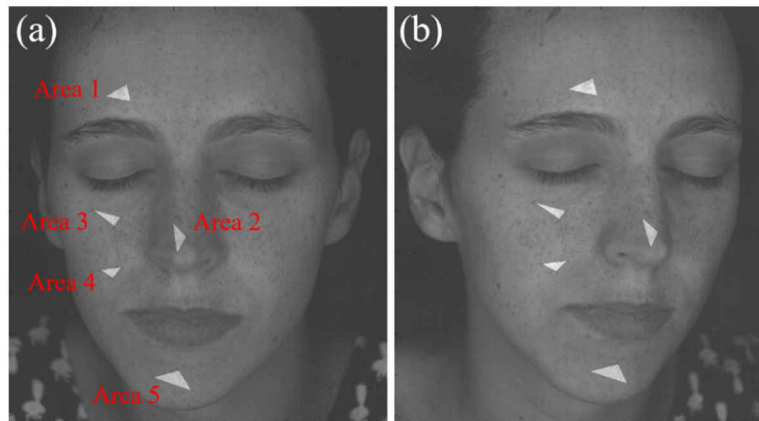


Figure 7.17. Areas selected for verifying the constancy of the estimated chromophore concentrations independently from the orientation of the face: (a) front view and (b) side view.

The areas used for front-face and side-face comparison are illustrated in Figure 7.17, and the estimated parameter values shown in Table 7.1. The chromophore concentrations estimated from both views using the analysis method are very similar on the two views of the face: for most values, the relative deviation is below 3%, with values as low as 0%. The

maximum deviation is 10.2% for melanin concentration on area 3, which corresponds to around 3% in absolute value.

		Oxygen rate	Blood volume fraction	Melanin concentration
Area 1	Front	71.2%	5.4%	28.4%
	Side	71.6%	5.3%	30.6%
	Deviation	0.6%	0.8%	7.4%
Area 2	Front	70.8%	9.0%	35.4%
	Side	72.2%	8.3%	36.5%
	Deviation	2.0%	7.7%	2.8%
Area 3	Front	80.1%	4.2%	30.2%
	Side	80.1%	4.6%	33.4%
	Deviation	0.0%	7.7%	10.2%
Area 4	Front	82.7%	6.0%	28.3%
	Side	83.8%	6.0%	29.0%
	Deviation	1.3%	0.1%	2.2%
Area 5	Front	69.3%	8.6%	34.0%
	Side	72.1%	8.4%	35.9%
	Deviation	4.0%	2.3%	5.7%

Table 7.1. Average chromophore concentrations for front and side view of the face, and relative deviation between the two measurements.

Given the median deviation value of 2.3%, we consider that this front and side view comparison validate our method. The melanin concentration deviates the most between the two measurements (the median relative deviation is 5.5% for melanin concentration). However, the average values given in Table 7.1 depend on the precision of the selection of exactly the same area on both views. Higher deviations for melanin are expected given that melanin is very heterogeneous.

The residual error map (already shown in Figure 7.7), has been displayed at two dynamic ranges in Figure 7.18 for a closer analysis of errors. While the full dynamic image (Figure 7.18.a) shows that the algorithm converged well on skin and badly on hairs, the optimized dynamic (Figure 7.18.b) reveals that the residual distance is higher on small structures such as the eyelid blood vessels or on the border of nevi. This can be caused by the chromatic aberration of the acquisition system: on small structures or on borders, the pixel spectrum is altered by chromatic aberration, affecting the pixel-by-pixel chromophore map. We can consider, however, that the number of pixels affected by this error is sufficiently low to be negligible in the final image.

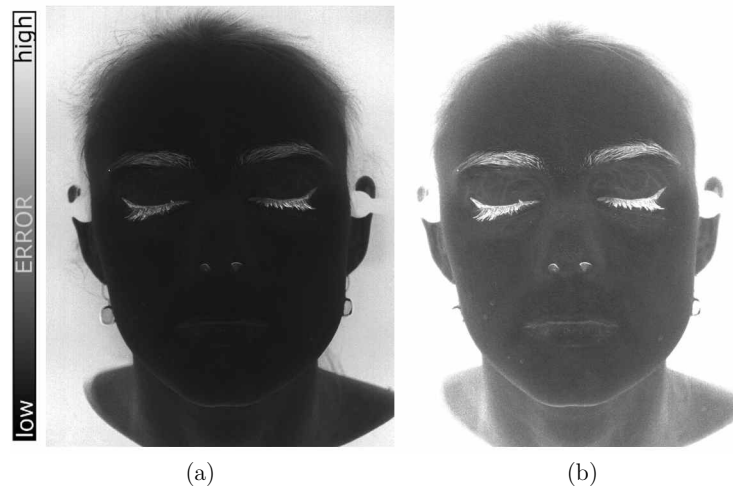


Figure 7.18. Error map from the skin optical analysis, (a) full dynamic ($SAM \in [0, 0.5]$) and (b) optimized dynamic ($SAM \in [0, 0.1]$) to observe errors on skin.

Similar errors might also result from skin scattering. The optical model relies on the assumption that, on average, light fluxes travel through a parallel plane along the vertical direction. In our application, however, the analysis method is independently applied on each pixel whose dimension is small compared to average lateral propagation distance in skin, and light propagation in directions other than vertical is not negligible, as illustrated in Figure 7.19. In the estimated maps of chromophore concentration, some spatial information is likely to be blurred. In addition, as scattering varies as a function of wavelength, the spectrum on the contours of small structures varies accordingly with the wavelength, which adds another chromatic distortion.

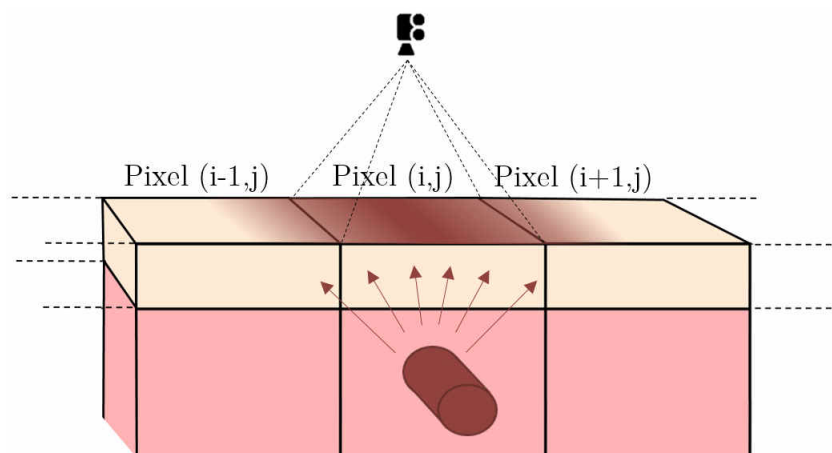


Figure 7.19. Effects of scattering on the contours of skin small elements.

Higher residual error can also be found on regions such as the sides of the nostril and the ears, where the geometry is convex. A possible explanation for this is the occurrence of interreflections [Forsyth and Zisserman 1989]. Interreflections are multiple light reflections

within a concave surface which modify the reflected radiance as a nonlinear function of the spectral reflectance. These spectral modifications impact the chromophore map reconstruction and results in an error. Table 7.2 gives an example of how the estimated chromophore maps can be affected by interreflections. In this example, a reflectance spectrum measured on skin has been associated to a flat surface. From it, reference chromophore maps have been estimated by applying the analysis algorithm, illustrated on the first row of the table. Then, the shape of the surface has been “changed” to a 45° V-cavity, and the resulting interreflections have been computed in MatLab [Saint-Pierre et al. 2018].

The effects of interreflections on the values estimated by analysis are mainly visible on the melanin concentration map. These simulations are coherent with what can be observed on the full face melanin concentration map (Figure 7.5.c): high concentrations of melanin are erroneously estimated in the corner of the eyes.

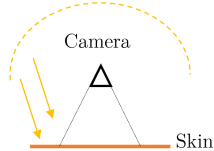




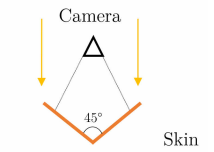




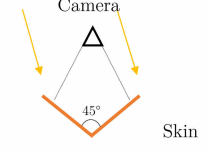
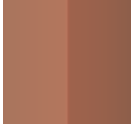
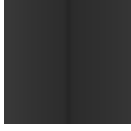
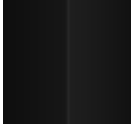
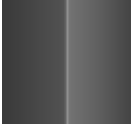
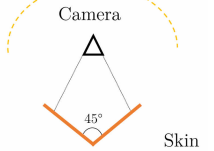



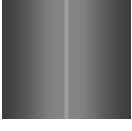
Configuration		Color	Oxygen rate	Blood volume fraction	Melanin concentration
Diffuse or collimated illumination					
Collimated normal illumination					
Collimated 10° illumination					
Diffuse illumination					

Table 7.2. Simulation of the effects of 45° V-cavity interreflections on chromophore estimation.

Finally, error is also higher on the sides of the face, where the incident light is grazing. This is especially visible in Figure 7.6.b, which represents skin color simulated from the estimated parameters, where the color on the side of the face is noticeably lighter than the

rest of the face and does not correspond to a realistic skin color as seen on the original picture. We interpret this as a limitation of the model: the optical analysis is based on the assumptions that skin is Lambertian (ignoring the specular reflection, which is discarded by the cross-polarization configuration of the hyperspectral camera) and that the Kubelka-Munk model can be applied in the same way regardless of whether the observed surface is normal to the observation direction or not. However, at grazing angles, skin cannot be modeled as a Lambertian reflector. An extended model taking into account the angular dependence of the skin reflectance would be necessary to improve the accuracy of the method.

7.2.c. Discussion

The experimental evaluation of the accuracy has shown the limitations of the method, which yields erroneous parameters on parts where incident light is grazing, where interreflections occur, on small details affected by chromatic distortion and on the artefacts that result from light scattering within skin. These limitations indicate that some parts of the maps, such as the side of the face, contain a high amount of error and cannot be used for cosmetological studies.

Error also appears when the scattering properties of skin are different to the ones used in the model. This source of error is not limited to distinct parts of the face, but is present across all pixels. As skin scattering properties can be considered relatively homogenous compared to absorption properties, we can assume in a first approximation that the error remain the same for all pixels. If this is the case, the estimated chromophore maps do not give absolute information but should rather be interpreted relatively, for comparisons between acquisitions made at two different times, between two areas or for the segmentation of objects such as vessels, stains and moles.

This limitation, however, is inherent to any analysis method that relies on the acquisition of only one parameter: the Kubelka-Munk model gives the relationship between the spectral reflectance and the ratio K/S of absorption and scattering parameters. In order to retrieve absorption, scattering must therefore be estimated by hypothetical value taken from literature. For methods using hyperspectral imaging, both scattering and absorption can be retrieved when two measurements are possible. For example, such methods can be performed on make-up, for which two samples of different thickness can be measured, or which can be applied on white and black background to create two measurement conditions [Doi et al. 2006]. In the case of skin in vivo measurement, two measurement conditions are not possible and we must find an alternative to get both absorption and scattering coefficients.

7.3. Going further: using artificial neural networks for skin chromophore map estimation

The skin acquisition and analysis method presented in this chapter has a significant computational cost: typically, around 1 hour for a 1-megapixel image representing an area of few cm² and around 5 hours for a 4-megapixel image representing a full face. In a cosmetology study context, this long computation time represents a significant limitation, as it prevents the user from previewing the results immediately after acquiring the image, and consequently from evaluating the quality of the images obtained. To tackle this limitation and reduce computation time, we trained an artificial neural network to replace the optimization algorithm.

Machine learning algorithms have shown utility for modeling non-linear functions when a lot of data is available. In the course of studies over the past years, Newton Technologies have collected a sufficient amount of data, comprising hyperspectral images and their corresponding chromophore concentration maps, to train a neural network capable of solving the inverse problem in place of the classical optimization algorithm, allowing results to be obtained within a few seconds. Machine learning applied to regression problems present an interesting alternative to time-consuming optimization-based algorithms, which have hitherto been used in many works in the field of tissue optics [Wang et al. 1994; Jäger et al. 2013; Wirkert et al. 2016; Panigrahi and Gioux 2018]. Nowadays, many machine learning tools are open source and user-friendly, which make their application relatively straightforward. Although the selection of the neural network architecture is important, we will see in this section that the dataset used to train the neural network has a high influence on the efficacy of the method. This work, done in collaboration with Newton Technologies, is somehow a preliminary study aiming at understanding whether machine learning can help us reduce computation time.

7.3.a. Architecture of the artificial neural network

The type of neural network used in our work is a *multi-layer perceptron* (MLP), a very popular class of feed-forward network [Jain et al. 1996] that can be applied to a wide variety of tasks including prediction, function approximation and pattern classification. Such a network is an ensemble of several *perceptrons*, or *artificial neurons*, organized into layers. MLP networks partly owe their emergence to the back-propagation learning algorithm for multi-layer feed-forward networks first proposed by Werbos [Werbos 1974], an optimization algorithm that uses a gradient-descent method.

The concept of the perceptron, clearly inspired by how a nerve cell processes information within a biological network, was first drafted in the works of McCulloch and Pitts in 1943 [McCulloch and Pitts 1943] and then developed by Rosenblatt in 1958

[Rosenblatt 1958]. A perceptron, illustrated in Figure 7.20 is a function of several inputs x_i , each associated with a weight w_i , that provides a single output Y . It is described by its activation function f which takes the weighted sum of the inputs as an argument, and includes a bias b , added to increase the robustness of the algorithm to noise.

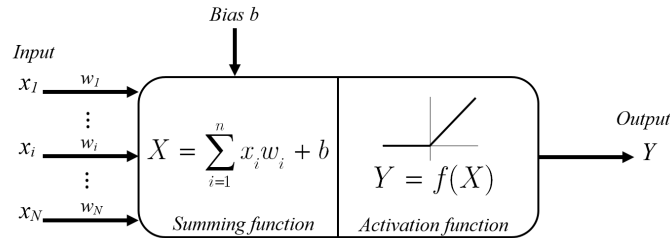


Figure 7.20. Perceptron model

The proposed method uses the Rectified Linear Unit (ReLU) activation function, which is simple and yields good results for modeling regression problems, given by:

$$Y = \max(0, X). \quad (7.20)$$

The organization of several perceptrons in parallel defines a layer. The assembly of several layers one after the other defines a multi-layer network, where the output of one layer corresponds to the inputs of the next one.

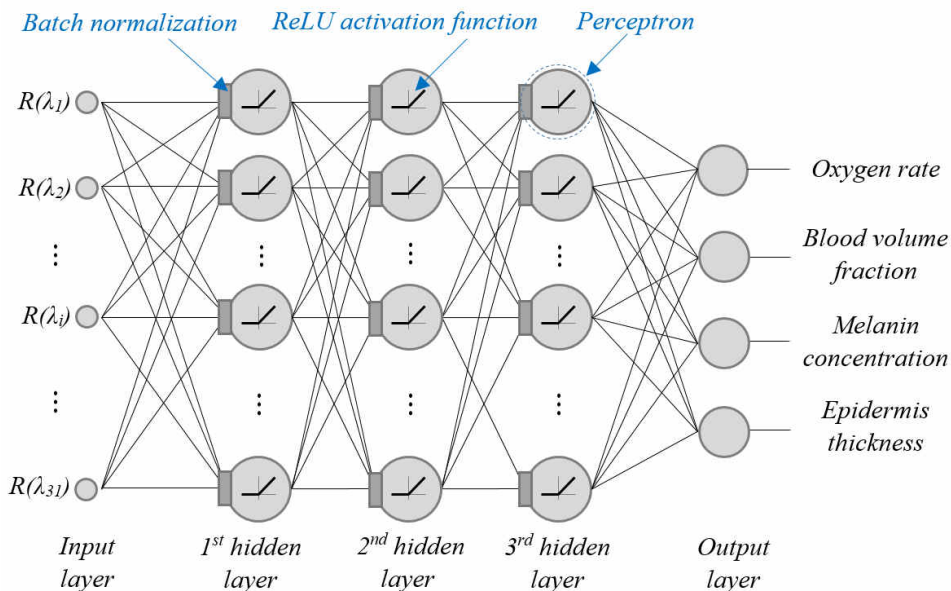


Figure 7.21. Architecture of the MLP used to model the function that relates skin spectral reflectance to skin properties.

The selected MLP architecture, shown in Figure 7.21, contains three hidden layers that are each constituted of 31 perceptrons. The entry layer connects the 31 perceptrons of

the first hidden layer with the spectral reflectance R at each wavelength λ_i . The output layer comprises 4 perceptrons that yield output signals corresponding to the oxygen rate, the blood volume fraction, the melanin concentration and the epidermis thickness. Each hidden layer is preceded by a batch normalization function according to the method developed by Ioffe and Szegedy [Ioffe and Szegedy 2015]. This method increases the performance of the training process by constraining the distribution of each layer's input. Without such a method, the distribution of the layer input changes during training, which requires the layer to adapt to the new distribution at each iteration. Batch normalization allows higher learning rates and reduces the result dependence on initialization, which makes the setting of the initial parameters easier. In total, the MLP comprises 3290 trainable parameters, which are randomly initialized according to a normal distribution of mean value 0 and standard deviation 0.01.

The choice of the number of layers and the number of perceptrons depends on the complexity of the function that has to be modeled [Gardner and Dorling 1998]. Too few trainable parameters yield a poor fitting of the function, and too many parameters yield a model that overfits the training data and has poor generalization performances, i.e. that learns very well the training set and performs very well on it, but is not able to perform well on any data that is outside of the training set. Similar issues occur in case of overtrained network. Indeed, if a network is trained for too long, it is likely to perform poorly on unseen data although the error on the training dataset is very low, especially when noisy, real world data are used. To overcome this problem, a part of the dataset is used for validation purposes. The training dataset is used to optimize the trainable parameters of the network, and the validation dataset is used at each iteration of the training process to verify the generalization abilities of the network. When the model is converging, error decreases for both the training and verification datasets. However, when the network starts to be overtrained, error on the verification dataset increases while error on the training dataset keeps decreasing. This change of trend provides a clear indication of when to stop the training.

7.3.b. Training dataset and process

The dataset used to train and test the MLP has been created from the hyperspectral images acquired during a clinical knowledge study conducted by Clarins (France) on 204 patients. For each patient, hyperspectral images were acquired on the inside of the forearm, on the cheek and on the dark circles below the eyes using SpectraCam® (Newtone Technologies, France). These images represent skin spectral reflectance at 31 wavelengths between 400 and 700 nm for 1148×948 pixels.

From these images, maps of skin parameters have been estimated using the skin analysis method described in Section 7.1. The measured skin spectral reflectance on one pixel corresponds to the input data of the MLP, and the output values that we want to

predict are the calculated skin parameters for the pixel, i.e. the oxygen rate α , blood volume fraction c_{blood} , melanin concentration c_{mel} and epidermis thickness h .

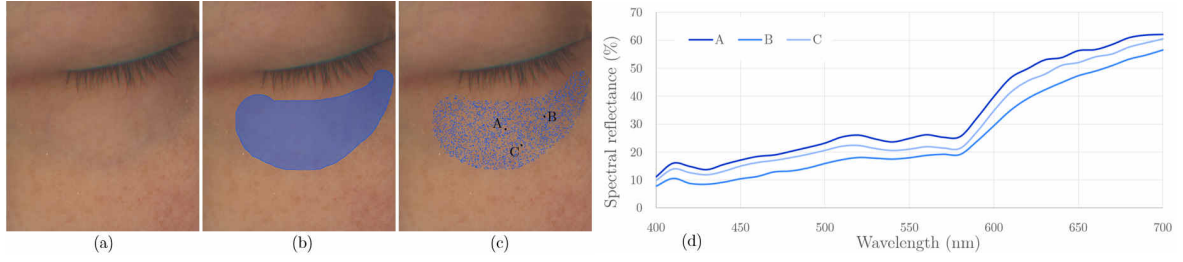


Figure 7.22. Illustration of the dataset creation process. (a) Original image, (b) selection of an area of interest, (c) random selection of pixels and (d) example of the spectral reflectance associated with the pixels labelled as A, B and C.

The dataset used to create the MLP is a collection of pixels selected among the available images, associated with their skin parameters. To train the MLP into an accurate model of the skin analysis algorithm, the training dataset must contain varied reflectance spectra that accurately represent the entire spectrum of possible skin spectral reflectance measurements, and must not contain any pixels corresponding to features that are not skin, such as the eyelashes. Hence, areas of interest corresponding to the most diversified and vascularized areas have been manually created on each image. A total of 800 000 pixels have been randomly selected from these areas to form the dataset, making sure the corresponding measured spectral reflectance is between 0 and 1, and that the estimated skin parameters are within the possible ranges of $[0, 100\%]$ for oxygen rate and the concentrations, and $[0, 150 \mu\text{m}]$ for epidermis thickness. The dataset creation process is illustrated in Figure 7.22.

A normalization step is applied to the measured skin spectral reflectance in order to create input values that are independent from irradiance drifts. In a first attempt, a normalization of the total quantity of reflected light, which corresponds to the normalization that can be found in the definition of the spectral angle mapper (SAM), was applied. Such a normalization appeared to us as the most effective solution to remove the effects of irradiance drifts. However, it didn't yield satisfying results for the training of the MLP. As an alternative that is less grounded on physics meaning, the following normalization formula was applied:

$$R(\lambda_i)' = \frac{R(\lambda_i) - \bar{R}}{\sigma}. \quad (7.21)$$

with the average value of the spectral reflectance:

$$\bar{R} = \frac{1}{31} \sum_{k=1}^{31} R(\lambda_k). \quad (7.22)$$

and σ the standard deviation:

$$\sigma = \sqrt{\frac{\sum_{k=1}^{31} (R(\lambda_k) - \bar{R})^2}{30}}. \quad (7.23)$$

The 4 skin parameters have also been normalized, using the following equation:

$$c_i' = \frac{c_i - c_{\min}}{c_{\max} - c_{\min}}, \quad (7.24)$$

where c_i' is the normalized parameter for pixel i , c_i the original value, c_{\min} and c_{\max} the minimum and maximum values of the parameter among all the dataset.

This normalization is necessary for the machine to learn from data that have the same amplitude, and ensures better results for the neural network. Indeed, for skin, the considered parameters do not vary within the same intervals. For example, melanin concentration typically varies between 1% and 43% while blood volume fraction varies between 2% and 15% [Jacques 1996]. Rescaling all the reference parameters between 0 and 1 ensures that the parameters are equally important and estimated with the same precision. If this step is not performed, the parameters that have the lower values have less weight in the training process and are estimated with less accuracy. For example, when the original values of the parameters are used in the dataset, the trained neural network yields good results on the melanin concentration parameter but very noisy results on the blood volume fraction parameter.

Finally, the 800 000 selected training patterns have been randomly dispatched between the learning dataset (which contains 516 000 data), the validation dataset (136 000 data) and the test dataset (160 000 data).

Each pixel i of the training set corresponds to a training pattern or input-output pair

$$\left(R_i(\lambda); \left\{ \alpha_i, c_{\text{blood},i}, c_{\text{mel},i}, h_i \right\} \right). \quad (7.25)$$

where $R_i(\lambda)$ refers to the spectral reflectance at 31 wavelengths, α_i to the estimated oxygen rate, $c_{\text{blood},i}$ to the estimation blood volume fraction, $c_{\text{mel},i}$ to the melanin concentration and h_i to the epidermis thickness.

The skin analysis model yields maps of bilirubin concentrations, for the neural network model, however, we decided to exclude this parameter. Bilirubin is a breakdown product of melanin, and is present only at very low concentrations in healthy skin, typically around 0.1%. Higher concentrations occur only in the incidence of pathologies such as jaundice, or on healing bruises. The maps of bilirubin estimated using the optimization algorithm are consequently very noisy and including such values in the training dataset reduces the performances of the neural network method.

With $\{A_i, C_{blood,i}, C_{mel,i}, H_i\}$ the parameters estimated by the neural network and N the number of pixels, the mean-square error between the reference values and the output values is:

$$\varepsilon = \frac{1}{N} \sum_{i=1}^N \frac{1}{4} \left[(\alpha_i - A_i)^2 + (c_{blood,i} - C_{blood,i})^2 + (c_{mel,i} - C_{mel,i})^2 + (h_i - H_i)^2 \right]. \quad (7.26)$$

The weight on the connection between the k^{th} neuron of layer $(m-1)$ and the l^{th} neuron of layer m is denoted as $w_{k,l,m}$. The combination of these weights form the trainable parameters that are determined through optimization:

$$\{w_{k,l,m}\} = \arg \min_{w_{k,l,m}} (\varepsilon). \quad (7.27)$$

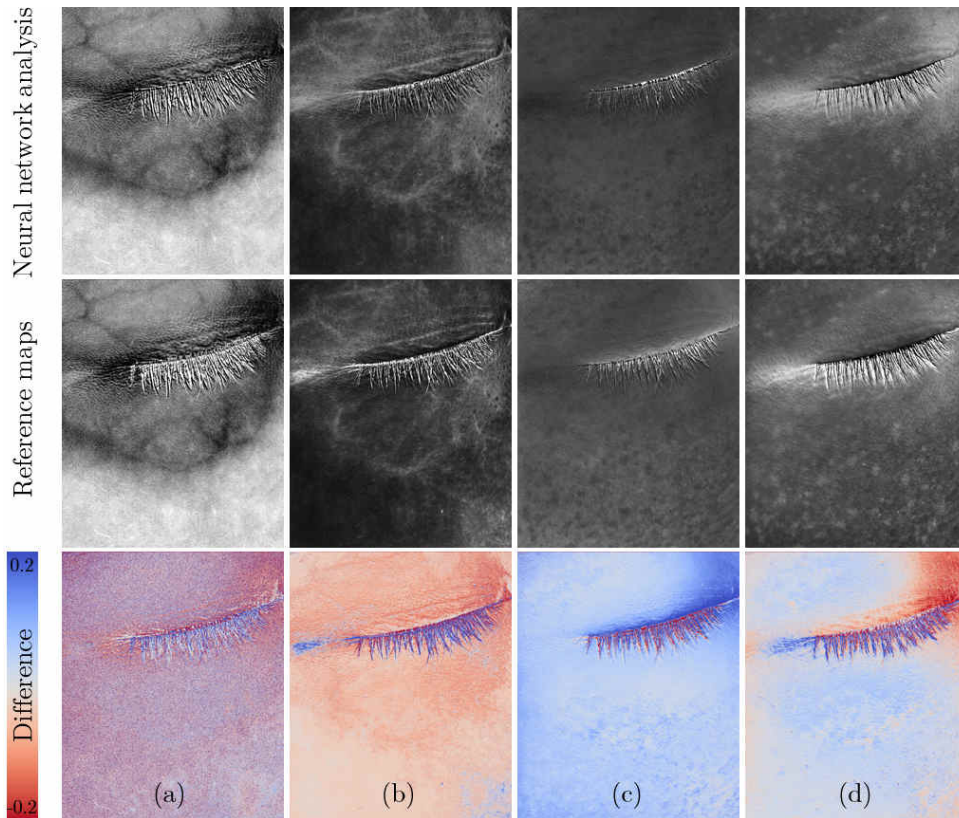


Figure 7.23. Maps of skin chromophore concentration estimated using the neural network, reference maps computed using the optimization based model (middle row) and difference between the estimated maps and the expected maps (bottom row): (a) oxygen rate, (b) blood volume fraction, (c) epidermis thickness and (d) melanin concentration.

The model has been implemented in TensorFlow 1.10 framework using Python 3.5. The training process has been performed on a single GPU NVidia 1080 Ti GTX 10Gb RAM. The model trained for around 6 days and required around 5 500 steps.

A low residual error of the MLP on the validation set is necessary, but does not guarantee reliable results on real world images. Indeed, the training data must fully represent all possible skin spectral measurements for the network to be able to generalize the function, and the best way to validate the method is to visually compare the output of the network with the expected results on an image. Maps of chromophore estimated by the neural network on an image that corresponds to the dark circles under the eyes are presented in Figure 7.23.

On Figure 7.23, the maps of difference show that the oxygen rate is very well reconstructed by the neural network method, but the result is noisy. Differences on the melanin concentration map and epidermis thickness map show that more information is lost using the neural network analysis. However, from a visual perspective, the difference is barely noticeable excepted near the eye. Finally, the map that is the most difficult to reconstruct with a machine learning approach is the blood volume fraction. This might be due to the high dynamic of the possible values, as the blood volume fraction is very high when there is a blood vessel and relatively low when it is not the case.

7.3.c. Estimated chromophore maps

While computation was about 1 hours for a 1148×948 pixels image with the optimization based algorithm, the computation time using the MLP is only 0.28 second using a GPU and 1.29 seconds using a CPU, on the same computer (Intel@Core™ i7-6700 CPU 3.40 Ghz). It is respectively 13 000 times and 2 800 times faster than classical method.

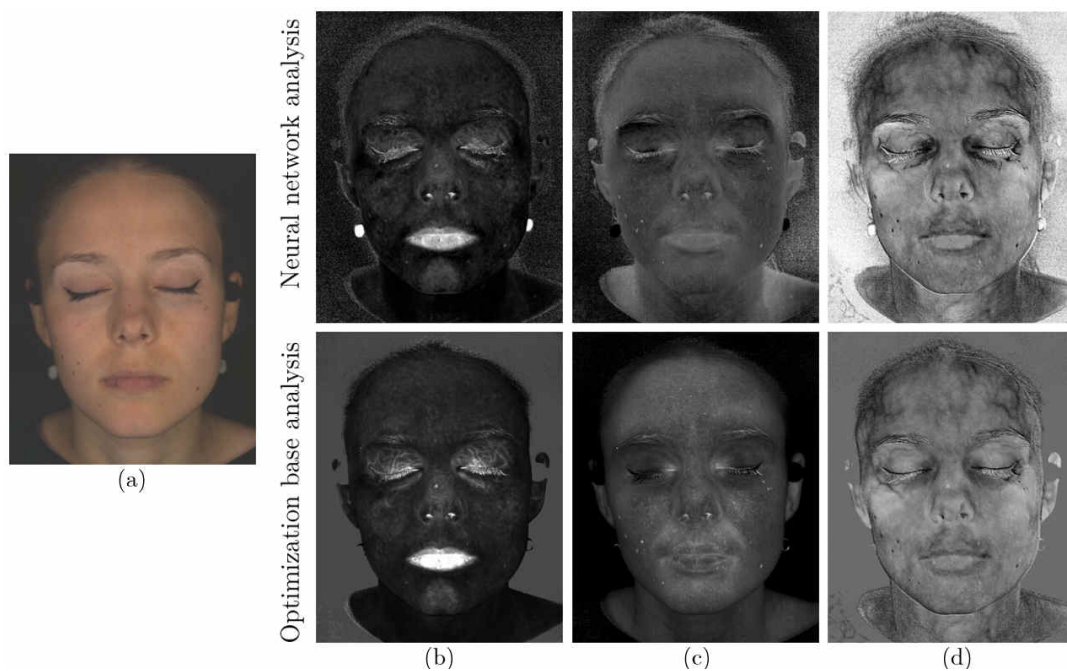


Figure 7.24. Full face analysis, comparison between the neural network analysis and the optimization based analysis: (a) color image, (b) map of blood volume fraction, (c) map of melanin concentration, (d) map of oxygen rate.

Figure 7.24 shows the maps of chromophore concentration estimated from a full face hyperspectral image, obtained by applying the neural network that has been trained on normalized spectral reflectances. These maps are noisier than the maps estimated using the optimization based method, however, they allow a preview of the result almost instantaneously (calculation time was 1.4 seconds on a 1548×1948 pixels image). The eyelid part is the less well reconstructed, possibly because no pixel representing the eyelid was part of the training dataset. Among the estimated maps, the melanin concentration map is the less well reconstructed. It might result from the loss of data implied by the spectral reflectance normalization preprocessing.

7.3.d. Discussions

The implementation of a neural network based method for the estimation of maps of chromophore concentration has shown calculation time drastically reduced, which allows a visualization of the result right after acquisition. The maps of chromophore concentration obtained with this method are close to the one computed using the model-based skin analysis method, and they are satisfying for visual inspection of the results.

In this study, we pointed out that the selection of the training dataset is critical, and that it must include as various skin spectral reflectance as possible. At the moment, our training dataset is not sufficiently representative of all possible skin properties, and a dataset created from measurement on more patients of different age, skin color and living conditions would be necessary to train a new neural network. We also showed the importance of spectral reflectance data normalization to account for irradiance drifts and make full face analysis possible. Without normalization, the neural network fails on pixels that are affected by irradiance drifts because the model has not learned at all on such pixels. As an alternative solution to data normalization, spectral reflectance data that mimic irradiance drifts could be created by applying various multiplication constants on the current training set. The extended training dataset thereby created would be more representative of the spectral reflectance measured by the hyperspectral camera on a full face.

In addition, the method presented in this paper relies on training a neural network from a dataset obtained using an optical model based method, which itself has limitations. A different approach could be investigated, using as a training dataset created using a Monte Carlo method [Panigrahi and Gioux 2018; Deeb et al. 2019; Zherebtsov et al. 2019] and a much more detailed model of skin than our two-layer model. In that case, the neural network would provide a model for skin spectral reflectance and solve the inverse approach. However, using synthetic data, we cannot be certain that this kind of approach would yield satisfactory results on noisy spectral reflectance corresponding to real skin. Conversely, our current approach has the advantage of accounting for real data, acquired with a real optical system that also induces noise.

A possibility for further developing the acquisition system is to reduce the complexity of the measured data, using a neural network to replace the optimization based analysis. Currently, the quality of the results requires high resolution skin spectral reflectance measurements as an input, as skin parameters are estimated using the shape of the spectrum. High spectral resolutions are thus required to distinguish small variations in the shape of the spectrum, corresponding to small variations in skin optical properties. However, it is possible that not all acquired wavelengths contain useful information, just as it is possible that two different wavelengths might be correlated, making it redundant to measure both. If such is the case, the quantity of acquired data could be reduced by ignoring certain wavelengths, and the analysis method could be replaced by a neural network. This would allow us to reduce acquisition time or even to consider using a multispectral camera rather than a hyperspectral camera, as illustrated in Figure 7.25.

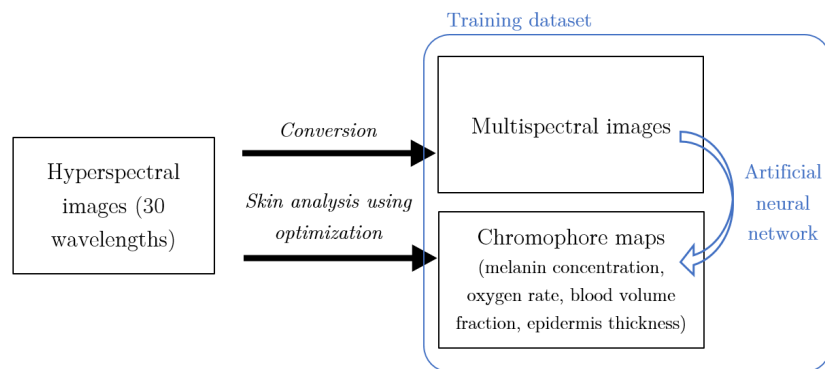


Figure 7.25. Using artificial neural network to replace hyperspectral imaging by multispectral imaging?

Using a multispectral camera would have many advantages, as it is generally lighter, less fragile and cheaper than a hyperspectral camera. Such a simplification requires a careful selection of the acquired wavelengths, retaining those that carry the most relevant information to ensure the good convergence of the neural network.

7.4. Conclusion

Several studies on the estimation of chromophore concentration maps have been published, however, most of them address relatively flat parts of the body, and to our knowledge, the estimation of full face maps is currently without precedent.

Although the chromophore maps show very promising results, one of the main limitations of the method is its long computation time. On a full face image, 5 hours are required to obtain the maps of estimated chromophore concentrations. However, a large amount of data has now been gathered and could be used to train a neural network to

replace the classical optimization-based method. The preliminary results shown in Section 7.3 demonstrates the potential of such a method to drastically shorten analysis time, from 5 hours to few seconds for full face image analysis.

Another limitation is related to one of the main assumptions of the analysis method: currently the method does not include the variation of skin scattering properties in its model. This is due to the fact that the measured information - spectral reflectance - is mainly influenced by skin absorption properties, and scattering is difficult to assess from only one measurement. Quantification of scattering could provide a better description of skin properties that could aid in the study of phenomena such as inflammation and aging. This would require the addition of spatial frequency domain imaging to the proposed method, and could be done with several minor modifications to the camera.

Chapter 8.

Measuring skin translucency: Spatial frequency domain imaging (SFDI)

Skin spectral reflectance provides information about how light interacts with the absorbing and scattering components in skin before being reflected back towards the detector. The measurement of spectral reflectance alone, however, is not sufficient to evaluate both the absorption and scattering coefficients. We have shown in Chapter 7 how skin absorption properties can be estimated with scattering coefficients taken from literature. We would like to go further and find an acquisition method that provides enough information to estimate both absorption and scattering, and that is compatible with the experimental equipment presented so far.

When observing a homogeneous and large material under uniform lighting, no visual cue can be used to judge the degree of translucency of the material. Rather, translucency can be characterized by border effects: we understand how translucent a material is from how blurred its borders are, either between a region that receives light and a region that does not, or at the border between two elements of different optical properties. The pattern observed at a border can be characterized by the point spread function (PSF) of the material, already defined in Chapter 2, which describes how light spreads at the surface of the material when illumination is punctual. Thus, translucency can be characterized by measuring the PSF, or any other quantity related to it, such as the line spread function (LSF), which describes how a line of light spreads in a homogenous material, or the modulation transfer function (MTF), which corresponds to the PSF in the spatial frequency domain.

When dealing with skin or any other biological tissue, translucency is related to the morphology and chemical composition of the tissue. Hence, the measurement of

“translucency” can provide useful information for better understanding the physiology and structure of a tissue, and can be used as a diagnosis tool [Wilson and Jacques 1990]. One of the first methods implemented to measure the optical properties of tissue was diffuse reflectance spectroscopy (DRS), which measures the PSF of a material by illuminating it punctually, collecting the diffusely reflected light and measuring the optical signal using a spectrometer. While this method has proved useful for a number of applications, DRS systems are often probes that are put into direct contact with the tissue [Koenig et al. 2015], which risks altering its optical properties depending on the pressure applied. This limitation has been overcome by the development of contactless systems relying on imaging [Foschum et al. 2011]. Yet, DRS only provides an average measurement over a small area, which provides much less information than imaging methods for the study of heterogeneous materials such as skin.

Spatial frequency domain imaging (SFDI), which is both contactless and wide field, was developed around 15 years ago [Dognitz and Wagnières 1998; Cuccia et al. 2005; Cuccia et al. 2009] to estimate the optical properties of a material from the measurement of the modulation transfer function (MTF). MTF, also defined in Chapter 2, describes the loss of contrast of a sinusoidal fringe light pattern projected onto the material, in function of the spatial frequency of the fringes. While PSF measurement requires punctual illumination (Figure 8.1.a), MTF is generally measured by projecting sinusoidal fringes on the surface (Figure 8.1.b).

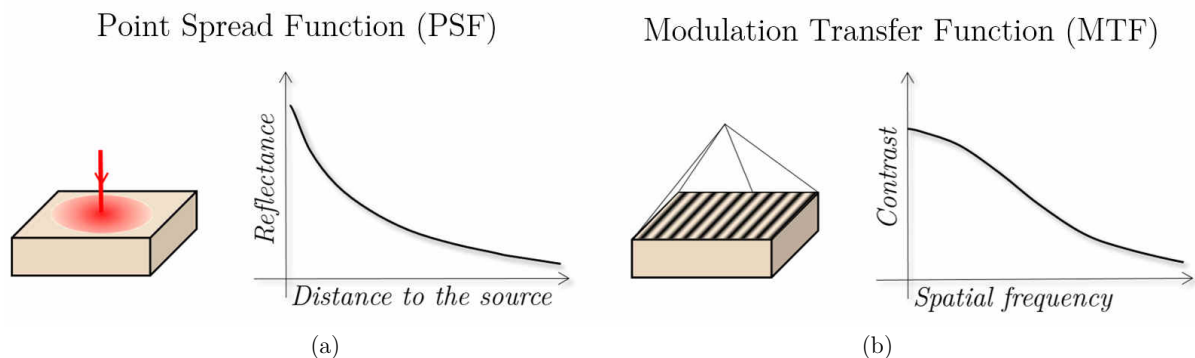


Figure 8.1. (a) Point spread function (PSF), which can be measured using DRS, and (b) modulation transfer function (MTF), which can be measured using SFDI.

The literature on SFDI methods has steadily increased in recent years, with a growing number of studies investigating its potential for medical applications [Gioux et al. 2019]. As part of this trend, open source data for building such systems has recently been made available on a dedicated website, < OpenSFDI.org > [Applegate], and suggestions on how to build SFDI systems at low cost have also been proposed by Erfanzadeh et al. [Erfanzadeh et al. 2018].

In this chapter, we propose an SFDI acquisition system that uses a digital projector, designed to study skin scattering properties on the face. This system is described in Section 8.1, and acquisition results on milk samples, wax samples and skin are presented in Section 8.2. The efficacy of the method is discussed in Section 8.3 and then conclusions are drawn.

8.1. Full face SFDI system

The measurement of MTF can be performed by projecting fringes of different frequencies and calculating their contrast. This method uses similar principles to that of 3D scanning using fringe projection, with the main difference being that 3D scanning measures phase deformation rather than loss of contrast.

The SFDI system uses the same elements as the 3D hyperspectral camera, and has been designed to fulfil the requirements of full face imaging in terms of safety, field of view, resolution and acquisition time. For the acquisition of 3D objects like a human face, the issue of irradiance drifts has to be managed. In this work, we propose to combine SFDI with hyperspectral imaging (HSI) to estimate full face scattering maps independently from irradiance drifts (discussed in further detail in Chapter 9). Thus, the acquisition system comprises all the elements necessary to HSI. For flat objects, HSI is not necessary. In that case, the SFDI system is designed to acquire MTF information within the wavebands corresponding to the digital projector emission. In this section, we describe the setup used for SFDI, the acquisition method and the calibration process.

8.1.a. Acquisition setup and software

The setup, illustrated in Figures 8.2 and 8.3, is very similar to the one used for 3D scanning. The sensor is the same 2048×2048 pixel Basler monochromatic camera (acA2040-90um, Basler, Germany) that we used for hyperspectral imaging and we kept the 35 mm focal length lens as it is well-adapted to the liquid crystal tunable filter (LCTF). The face is illuminated by structured light projected by the Optoma digital LED projector (DLP) (ML330, Optoma, Taiwan).

A panel, defining the X - and Y -axis of the Cartesian coordinate system as well as the origin of the Z -axis, is used for calibration. For 3D scanning, the sensor and the projector must be located on the same Z -plane, their respective optical axes creating an angle. For SFDI, the DLP can be placed anywhere. We have placed it next to the camera to prevent occluded areas.

The system uses a cross-polarization (CP) configuration to discard surface specular reflection. When the LCTF is used, a linear polarizing filter is placed in front of the projector, and oriented perpendicularly to the polarization direction of the LCTF. When the LCTF is not included in the acquisition system, there is not analyzer anymore in front of the camera to create a CP configuration, and another linear filter must be added.

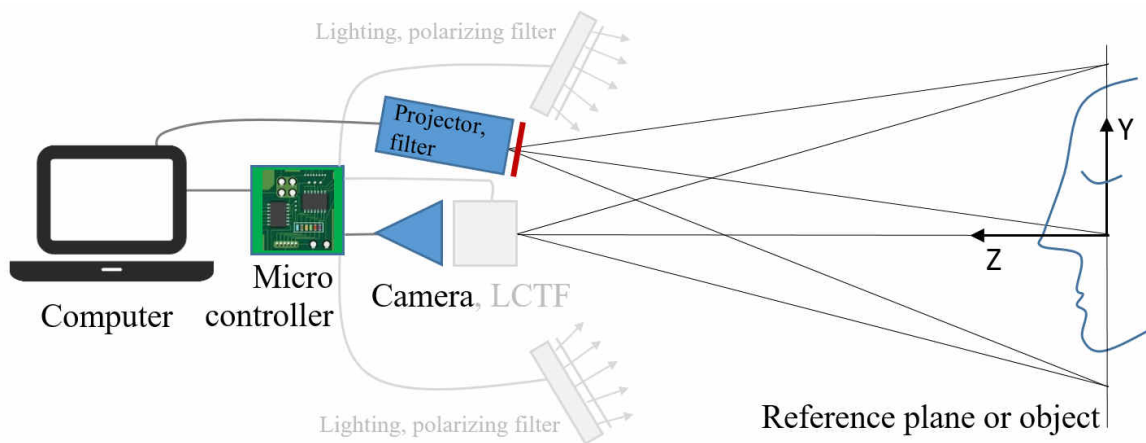


Figure 8.2. SFDI acquisition setup. Parts in gray correspond to the elements used for the hyperspectral acquisition.

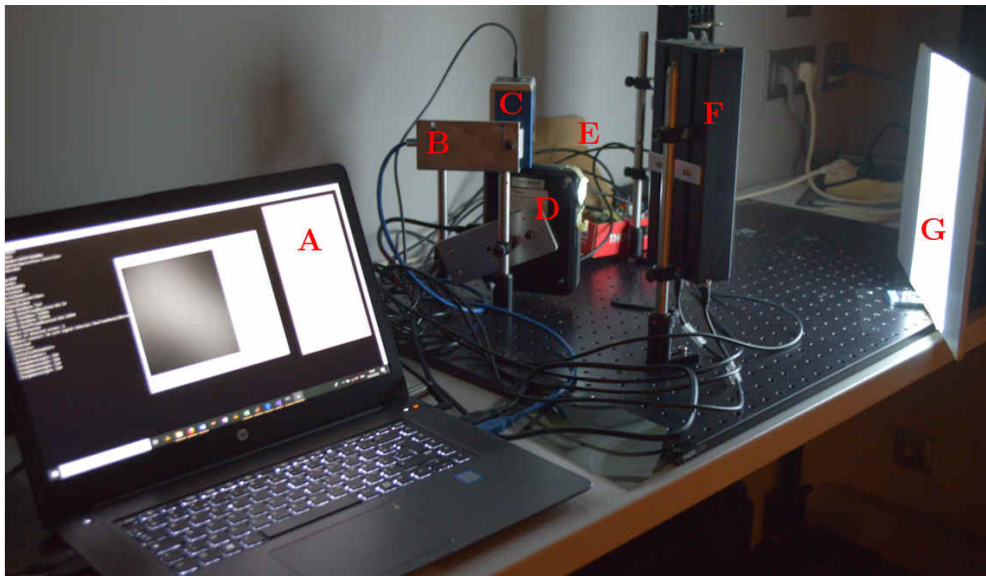


Figure 8.3. Acquisition system for SFDI and HSI, comprising: (A) a computer, (B) a camera, (C) a LCTF, (D) a DLP, (E) a microcontroller, (F) LED lighting units and (G) a reference plane.

The acquisition software has been developed in C++ with a Qt framework. It comprises a live preview tool and can be used for SFDI acquisition, HSI acquisition or both.

The parameters of the SFDI acquisition can be controlled in a settings window. The sensor parameters are the camera exposure time and the filter wavelength. The filter wavelength setting is necessary when the camera comprises a LCTF, with a choice between 450, 520 and 630 nm to match with the peaks in the emission spectrum of the DLP. The color of the projected image can also be specified. When a LCTF is used, white light can be projected, as color filtering is done by the LCTF; when only the monochromatic sensor

is used, selecting a specific color channel of the projector allows measurement of the material MTF in either the blue, green or red wavebands corresponding to the emission spectrum of each LED of the DLP. A radiometric calibration can also be performed to correct the non-linearity of the projector using the same method as that in the 3D acquisition system, detailed in Chapter 5.

Finally, the settings of the projected fringes can be specified. In particular, the number of images projected for each frequency and the fringe period can be chosen. Three non-zero frequencies are acquired in addition to the zero frequency.

After acquisition, the images of the projected fringes are treated with MatLab in order to calculate the MTF of the object in each pixel.

8.1.b. Multiple frequency contrast measurement using a projector

The implemented method is very similar to the phase-shift principle used for 3D scanning. For a given frequency, several fringe images that are successively shifted must be projected to retrieve the contrast on each pixel by applying a demodulation formula. As MTF is a function of spatial frequency, this operation must be repeated for several frequencies.

Contrast measurement at one frequency

For each frequency f , N fringe images, encoded into 8-bit gray levels such that the radiance projected onto a flat reference plane by a perfect projector is given by Eq. (8.1), are successively projected:

$$I_n(x, y, f) = I' + I'' \cos\left(2\pi fx + \frac{2\pi(n-1)}{N}\right), n=1, \dots, N, \quad (8.1)$$

where I' is the average radiance, I'' the radiance modulation, f the fringe frequency on the object and (x, y) the pixel position on the field of projection.

The camera records images that correspond to the reflected radiance J_n :

$$J_n(x, y, f) = J'(x, y) + J''(x, y, f) \cos\left(\varphi(x, y) + \frac{2\pi(n-1)}{N}\right), n=1, \dots, N, \quad (8.2)$$

with J' the average radiance, J'' the modulation, and φ the fringe phase, which are all contingent upon location (J'' is also frequency-dependent).

The quantity J'/I' corresponds to the surface reflectance, with J' measured by projecting a uniform image on the object.

In this work, MTF is defined such that its value at zero is the reflectance. It is expressed as the contrast multiplied by reflectance:

$$MTF(f=0) = \frac{J'}{I'}, \quad (8.3)$$

$$MTF(f \neq 0) = \frac{J''}{J'} \times C, \quad (8.4)$$

with

$$C = \frac{\max(J_n) - \min(J_n)}{\max(J_n) + \min(J_n)} = \frac{J''}{J'}. \quad (8.5)$$

The radiance modulation J'' can be retrieved for each pixel of the image by combining the acquired images J_n :

$$J''(x, y, f) = k \sqrt{\sum_{n=1}^N \left(J_n(x, y, f) - J_{(n+1) \bmod N}(x, y, f) \right)^2}, \quad (8.6)$$

with $k = \sqrt{3}/2$ for $N = 3$, or $k = 1/2$ for $N = 4$ (the value of k can remain unknown as a calibration is performed).

The DLP only has a “video mode”, but no “pattern projection” mode, which means that the projected images are to be observed by the human eye with a nonlinear gray level emission. This nonlinearity can be partly corrected by performing a gray scale calibration prior to image projection, as described in Chapter 5. However, this gray scale calibration is generally not sufficient, and projecting only 3 images, which is the minimum for this method, does not yield satisfactory measurements. Similarly to 3D scanning, the choice of N , the number of projected images, impacts the quality of the reconstructed radiance modulation: higher N yields better quality but extends acquisition time [Li and Li 2011]. An N value of 4 has been chosen as a compromise between acceptable quality and short acquisition time.

Multiple frequency measurement

In our system, illustrated in Figure 8.4, four different frequencies are acquired, one of which is the zero frequency. The other three frequencies have been chosen in order to obtain the best projected image quality. They correspond to periods of 8 pixels, 16 pixels and 32 pixels on the projector image. Choosing periods that are multiples of 4 is especially adapted when the phase shift method is applied with $N = 4$ to ensure the best possible signal for projection.

When projecting on an object located at around 40 cm from the projector, these periods correspond to frequencies around 0.15 mm^{-1} , 0.3 mm^{-1} and 0.6 mm^{-1} , which are adequate samples for retrieving the shape of the MTF with only 3 non-zero frequencies. The fringes described in this section are vertical, but they can also be horizontal depending on the geometry of the measured surface. Their direction should be selected to minimize the frequency variation of the fringes projected on the surface due to the 3D shape of the surface. For example, horizontal fringes yield more accurate measurement for a vertical cylinder.

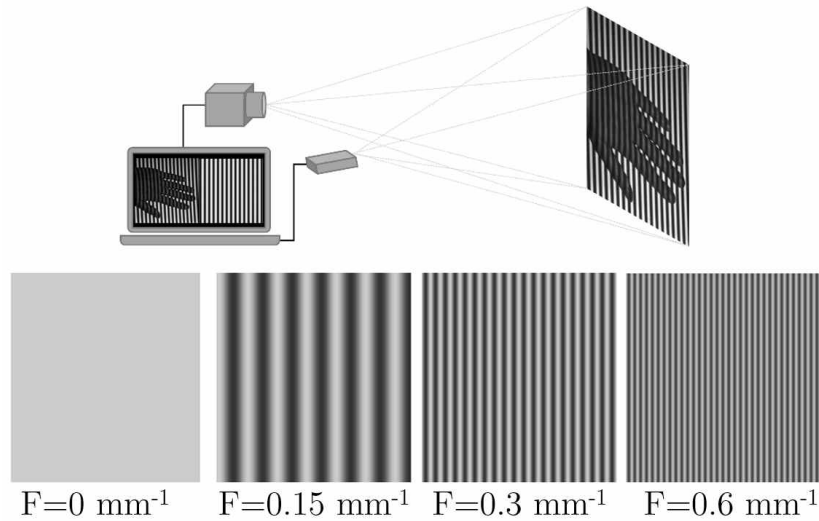


Figure 8.4. Acquisition principle of SFDI, fringes at 4 frequencies are successively projected on the object.

8.1.c. Calibration and normalization

For a perfect acquisition system, SFDI measurement on an object yields $MTF_{obj}(x, y, f)$ for each spatial frequency f and each pixel (x, y) using Eqs. (8.4), (8.5) and (8.6). For a real and imperfect acquisition system, however, the measured radiance modulation also depends on the MTF of the acquisition system $MTF_{system}(x, y, f)$:

$$J''_{obj} = I' \cdot MTF_{obj} \cdot MTF_{system}. \quad (8.7)$$

The MTF of the acquisition system depends on both the projector and camera. It is pixel-dependent, since the amount of projected light varies in the field of projection, the camera transmittance varies in the field of view, and the addition of polarizing filters affects the MTF of the projector in the field of projection.

The MTF of the object is retrieved independently from the acquisition system properties and the incident radiance through a calibration step described in Eq. (8.8). Calibration involves a white opaque reference sample whose MTF $MTF_{ref}(x, y, f)$ is one (or any other reference object for which MTF_{ref} is well known). Such a reference sample is non-absorbent and strongly scattering. Therefore, we have:

$$MTF_{obj} = \frac{J''_{obj}}{J''_{ref}} \cdot MTF_{ref}. \quad (8.8)$$

For the analysis purposes detailed in Chapter 9, MTF can be normalized to remove the effects of irradiance drifts in the following way:

$$M\bar{T}F_{obj}(x, y, f) = \frac{MTF_{obj}(x, y, f)}{MTF_{obj}(x, y, 0)}. \quad (8.9)$$

Finally, a ruler is acquired to estimate the spatial frequency of the projected fringes onto the surface, accounting for the distance between the projector and the surface. The image of the ruler gives the pixel-to-millimeter ratio for an object located near the reference plane. Fringe period in pixels is calculated from the fringe images on the reference plane, and then converted in mm to obtain the frequency in mm^{-1} .

For non-planar samples, this calibration is not accurate enough to account for the irradiance drifts that occur on curved surfaces. In such cases, SFDI acquisition yields the MTF multiplied by a constant that renders the difference between the irradiance incident on the flat reference surface and on the object. The problem of irradiance drift must be addressed before analyzing the MTF to retrieve the absorption and scattering properties of the material, which is the topic of Chapter 9. For curved surfaces like the human face, an irradiance drift correction can be performed using the method described in Chapter 6 only if the 3D geometry of the surface is known [Gioux et al. 2009]. Otherwise, one must use normalized data as an alternative.

8.2. SFDI acquisition on phantom samples and skin

In this section, we present SFDI measurement for which the LCTF has been removed from the acquisition system. The MTF was acquired on various translucent flat samples, which we can also refer to as phantoms, and on skin.

8.2.a. Milk samples

Samples of various absorption and scattering properties have been made using milk, water, agar and yellow food coloring (Figure 8.5).

Figure 8.5.c shows the average MTF measured for each sample at 13 frequencies. The SFDI system has been designed to measure only 4 frequencies. For still objects, a series of measurements can be performed for a better sampling. Here, the reference plane and the samples have been translated along the Z -axis between each acquisition to measure more than 4 frequencies.

Although the value at zero differs for each sample, we notice on Figure 8.5.c two trends: the samples with similar scattering properties have similar curves at high frequencies.

Mixing milk, water, agar and food coloring was a convenient way to create translucent samples whose optical properties are close to those of human skin. In addition, milk absorbance can be neglected and different dyes can be used to vary the scattering properties of the sample. However, samples made from milk and agar (or gelatin) are relatively fragile, and cannot keep for very long as they quickly dry out when kept for more than a few days

in the fridge. For these reasons, we chose to use samples made of wax rather than milk for further experiments.

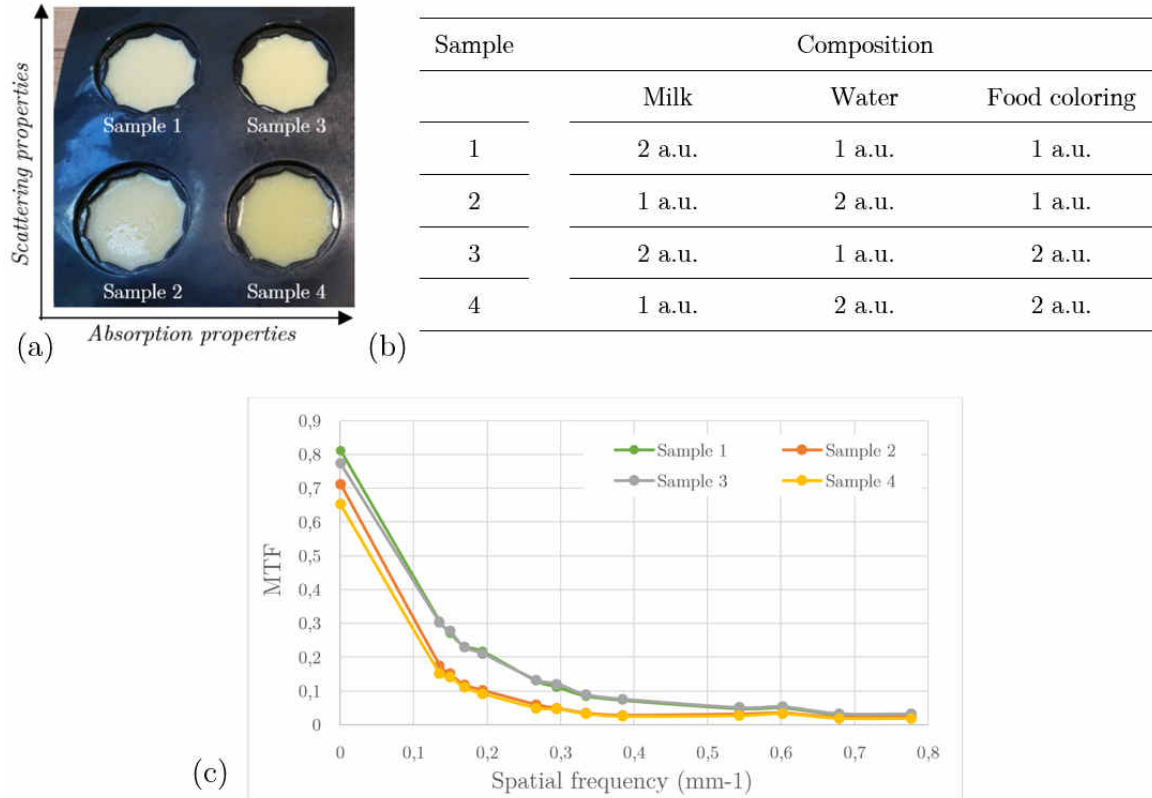


Figure 8.5. Average MTF measured at 13 frequencies on samples made of agar, milk, water and yellow coloring. Scattering properties are increased by adding more milk than water, and absorption properties are increased by adding more colorant. (a) Picture of the samples, (b) compositions and (c) corresponding MTF curves.

8.2.b. Wax samples

The wax samples are made of paraffin, palm wax, black oil paint and TiO₂ white oil paint in different proportions to obtain samples with variable absorption and scattering properties. They are homogeneous and can be molded to any shape. Paraffin, which is highly translucent, has been used as a base, and oil paints have been pre-mixed with palm wax (more scattering than paraffin), to create what we have called “black wax” and “white wax”. For the purposes of the experiment, 4 flat samples were created, with absorption properties varying depending on the quantity of black paint and scattering properties varying depending on the quantity of wax and white paint. The composition of each sample, labelled 1 to 4, is given in Table 8.1.

Sample	Composition		
	White wax	Black wax	Base wax
No 1	25%	46%	28%
No 2	50%	24%	26%
No 3	55%	44%	0%
No 4	25%	28%	47%

Table 8.1. Composition of each wax sample.

SFDI measurements were repeated 4 times to obtain the MTF of the samples at 13 frequencies, with the reference plane and samples translated between each acquisition. The green channel of the projector was used for these measurements. The fringe images obtained for one of these acquisitions are illustrated in Figure 8.6. Although the color in samples 3 and 4 are very similar (Figure 8.6.a), the translucency in sample 4 is much higher, as can be seen from the greater blurriness of the projected fringes (such as on Figure 8.6.d).

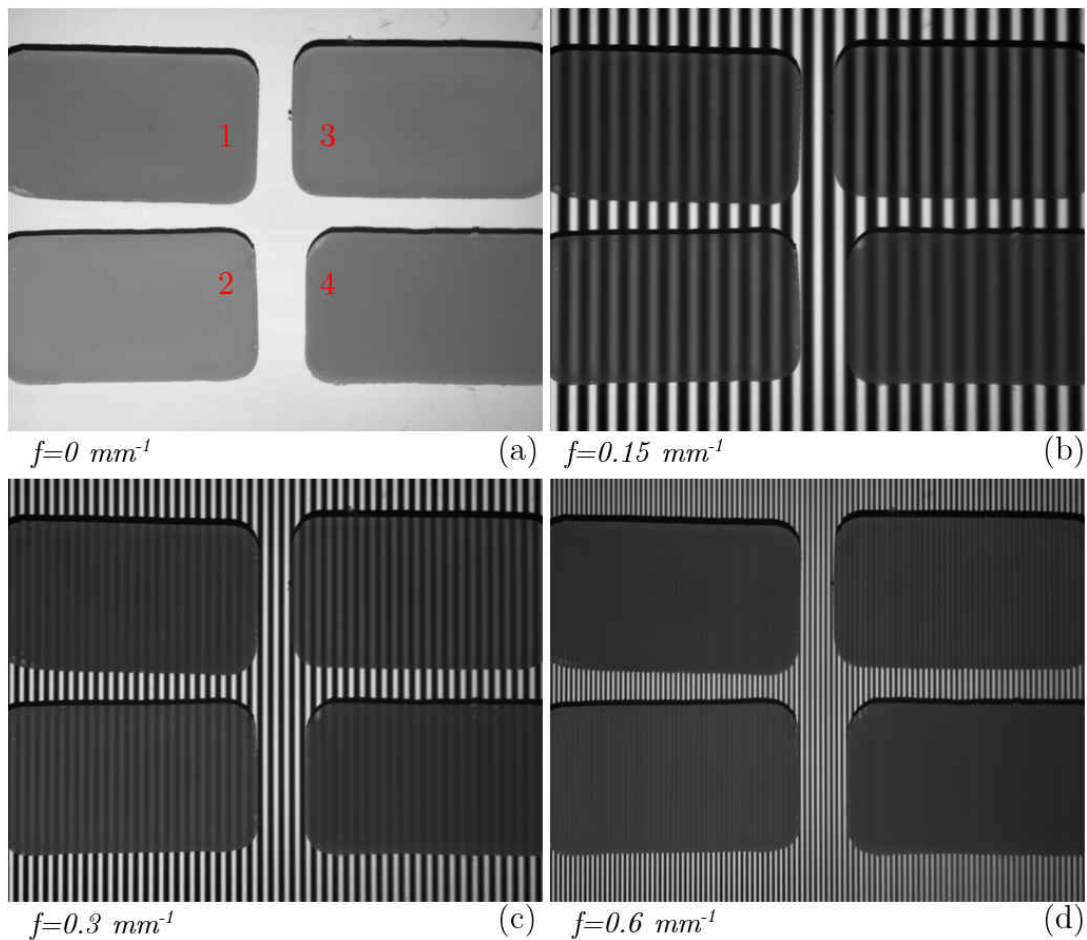


Figure 8.6. SFDI acquisition at four frequencies on wax reference samples (green channel of the digital projector).

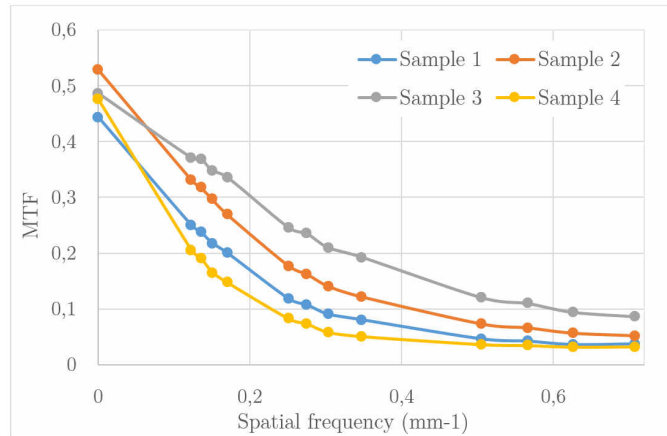


Figure 8.7. Average MTF measured on the wax samples at 13 frequencies.

Figure 8.7 represents the average MTF for each sample. The reflectance MTF at zero corresponds to the sample reflectance; for the other frequencies, the lower the scattering, the more the projected fringes are blurred and thus the lower MTF. The graph shows that sample 3 is the most scattering, which is to be expected from its composition, and that samples 4 and 1 are the most translucent, which is also to be expected as they contain a lower amount of white wax than the other two samples. These wax samples are more convenient than the milk samples, as they remain stable for a long time. However, it is difficult to determine precisely their optical properties from their composition: although they are mostly uniform on the area of interest, some pigments fall to the bottom of the mold while the wax is setting, and it is consequently difficult to use their composition to precisely determine their absorption and scattering properties.

8.2.c. Skin

SFDI measurements were performed on the inner wrist (Figure 8.8), a relatively flat part of the body which is heterogeneous in terms of color and structure, mainly due to the presence of a large number of veins close to skin surface.

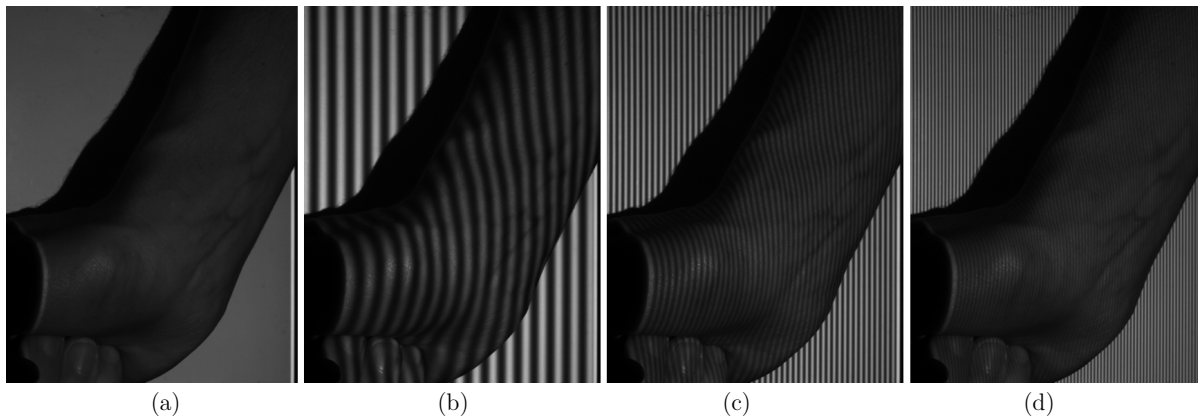


Figure 8.8. SFDI acquisition at four frequencies on the skin of the inner wrist, frequencies (mm⁻¹): (a) $f = 0$, (b) $f = 0.15$, (c) $f = 0.3$ and (d) $f = 0.8$.

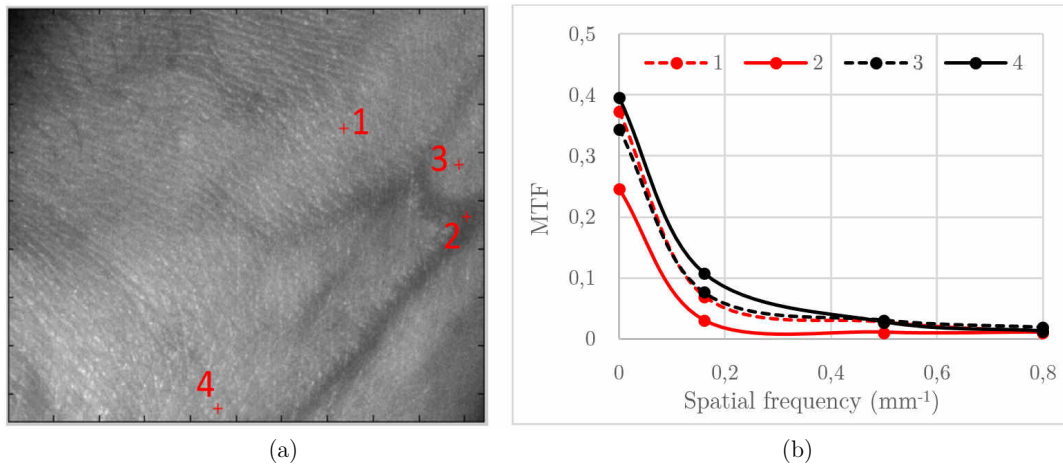


Figure 8.9. MTF measured using SFDI on the skin of the inner wrist. (a) Location of the points of interest and (b) MTF for each area.

We tried to identify different MTF properties for pixels corresponding to skin color (points 1, 2 and 4) and a visible vein (point 3). On the image and curves presented in Figure 8.9, we can observe that MTF is much lower in the region where a vein is visible (point 3) from the other regions. On Figures 8.8 and 8.9, we can notice specular reflections on the images, as no polarization filter was used for this acquisition. This introduces a significant amount of error in the analysis process, since specular reflection dramatically affects the value of the MTF at the zero frequency. For all other acquisitions, polarizing filters have been added in a CP configuration to avoid such artefacts. The effects of irradiance drifts are not especially visible on the crop of the original image displayed in Figure 8.9.a, however, it is worth asking how much of the difference between the MTF at two different region results from a change in skin optical properties and how much results from a change in the illumination conditions.

So far, the illustrations of this section have shown either projected fringes that are more or less blurry depending on the degree of translucency of the object or the corresponding MTF curves obtained by averaging the measured information on the area of interest. These curves could also be obtained using non imaging methods, such as DRS, and thus do not provide a persuasive argument in favor of the use of SFDI for the study of heterogeneous materials.

Figure 8.10 shows maps of MTF at 3 frequencies, providing a value at each pixel and thus demonstrating the potential of imaging methods. The area of skin imaged here has stretch marks. In the case of conventional imaging (corresponding to the image at the zero frequency), only horizontal stretch marks are visible and can be segmented. When using SFDI, “invisible” vertical marks can be seen at the non-zero frequencies. Such measurements are very encouraging as they demonstrate the potential input of SFDI compared to conventional imaging for applications such as the study of healing scars.

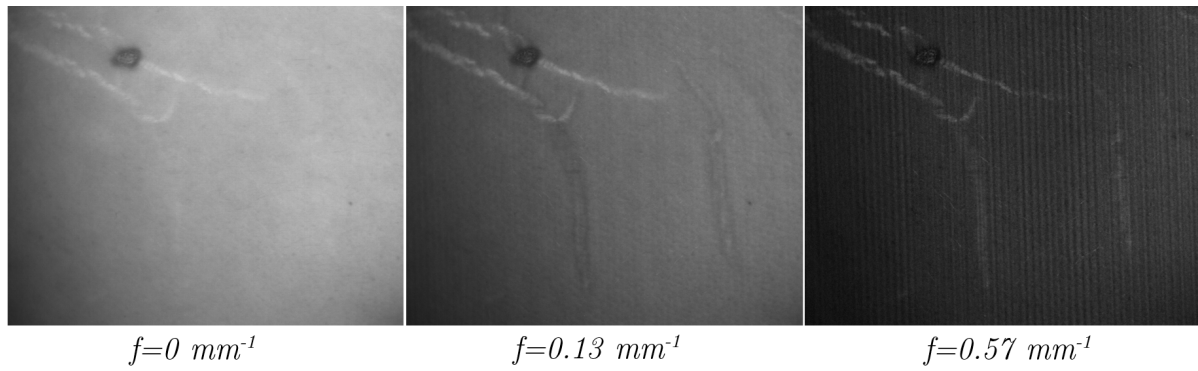


Figure 8.10. MTF at 3 frequencies on stretch marks, acquired in the red channel of the projector (the grayscale has been adjusted differently for each image for better visualization).

Finally, MTF was also measured on a full face (see Figures 8.11 and 8.12), this time combined with hyperspectral imaging (the LCTF is included in the camera).



Figure 8.11. SFDI acquisition at four frequencies on a full face, side view acquisition.

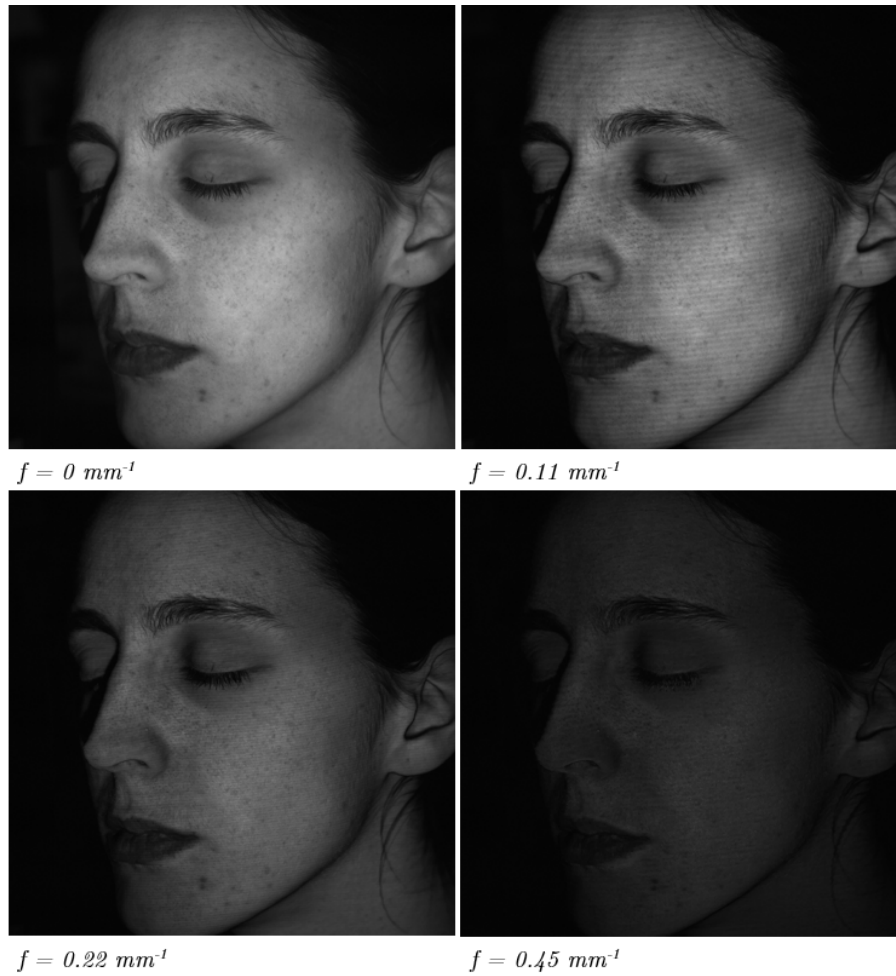


Figure 8.12. MTF at 4 frequencies acquired in the green channel of the projector.

On the images shown in Figures 8.11 and 8.12, we can notice again the presence of irradiance drifts, which must be addressed for reliable skin analysis. This point will be discussed in detail in Chapter 9. The MTF reconstructed from the SFDI acquisition shows some noise (horizontal fringes are especially visible on the image at $f = 0.11 \text{ mm}^{-1}$), which partly results from the imperfect quality of the projected fringes and partly from the person's head slightly moving during acquisition.

8.3. Efficacy of the method

As is the case for hyperspectral imaging and 3D scanning, the efficacy of the proposed SFDI method can be evaluated in terms of resolution, accuracy and acquisition speed.

The resolution of the method can be described in the spatial, spatial frequency and spectral domains, as maps of MTF are acquired at several frequencies and potentially at several wavebands. The size of a pixel of the camera depends on the distance between the object and the camera and generally varies between 70 and 100 μm for a full face acquisition,

which corresponds to the spatial resolution. For in vivo applications, the resolution in the spatial frequency domain is limited to three or four frequencies, as increasing this number can only be done at the expense of acquisition time. Moreover, the possible frequencies are limited by the resolution of the digital projector, its focal length and the distance between the projector and the object. However, for applications such as skin analysis using diffusion theory (described in Chapter 9), the maximum frequency limitation is not a significant factor, as the optical model used to describe light behavior in translucent materials is not valid for very high frequencies. Finally, spectral resolution is also limited by the properties of the projector, as acquisitions must be made in one of the three bandwidths emitted by the projector. In the current setup, multiple bandwidth acquisition is not recommended as it requires more time than is reasonable for a person to remain still (greater than 10 seconds).

The smallest detectable MTF depends on the properties of the camera. If the camera is used in 8-bit mode, the recorded images are quantified between 0 and 255. The smallest detectable MTF is obtained when:

$$J_n - J_{(n+1)} = 1, \quad n=1, \dots, N-1. \quad (8.10)$$

Using Eqs. (8.6) and (8.8), the condition given in Eq. (8.10) yields the smallest detectable MTF in theory:

$$MTF_{\min} = \frac{\sqrt{12}}{2J'_{ref}}. \quad (8.11)$$

where J'_{ref} is the gray value recorder by the camera on the reference sample. If the dynamic of the camera is fully used and J'_{ref} is 255, then MTF_{\min} is 0.7%.

The accuracy of the measured MTF is affected by many factors. First of all, as MTF is reconstructed from several projected images, subject movement can add artifacts, such as the horizontal fringes visible on the top right picture in Figures 8.12. In addition, as with 3D scanning, the quality of the projected fringes significantly affects the measured information. The choice of the reference surface for calibration can also affect the accuracy of the measurement, as its MTF must be precisely known. The accuracy of the reference MTF directly affects the accuracy of the method. In this work, we did not have time to further characterize the precision of the method, which could be done by measuring several translucent reference samples with well-known absorption and scattering properties and comparing the results of our method with the expected values. However, we were not able to build such samples by lack of time, and we therefore consider this work as a proof of concept. A complete accuracy characterization would be required if the method were to be used for cosmetic studies or in a commercial context.

Acquisition speed is determined by on a number of parameters, related to the acquisition method itself, the camera efficacy and the projector efficacy. In particular, when the SFDI system comprises a LCTF for hyperspectral imaging, the amount of light

transmitted to the sensor is drastically reduced. In such cases, acquisition time is set to 200 ms if the green channel is selected (less for acquisition in the red channel) to achieve a satisfactory signal-to-noise ratio. The method relies on the successive acquisition of 13 images, and the slow projector refresh rate imposes a time delay of 100 milliseconds between two image acquisitions. In total, taking into account additional delay due to signal transfer between the camera and the computer, SFDI acquisition time is around 5 seconds. Given that SFDI measurement is generally combined with hyperspectral imaging, which adds around 2 seconds on the total acquisition time, the acquisition speed of the system is not optimal for in vivo acquisition. In particular, it is difficult to perform SFDI measurements at several spectral bandwidths at once, such as in the green and red channels, as the person is very likely to move when acquisition time is superior to 10 seconds.

8.4. Conclusion

In this work, we have shown that a SFDI system can be built by simply using a camera and a digital projector. Although the proposed acquisition system can be improved, especially in terms of acquisition time, and further accuracy characterization is required, the described acquisition method can be applied to measure translucency properties with a relatively cheap acquisition system which is also compatible with the 3D-hyperspectral camera described in Chapters 4 and 5.

We will see in the next chapter that full face analysis is a challenge due to the presence of irradiance drifts, and that SFDI information alone is not enough to retrieve information about skin scattering properties. However, we believe that an SFDI system, even one that is limited to measuring small and relatively flat areas of the body, could be useful for many applications in cosmetology. To our knowledge, the only skin translucency measurement devices on the marketplace for cosmetology studies are Transluderm (Orion Concept, France) and Translucymètre (Monaderm, Monaco). However, both systems use probe setups that can compromise the accuracy of measurements by being in contact with the skin and are based on punctual measurements that do not provide sufficient information to separate the effects of scattering and absorption.

One of the major limitations of our acquisition system originates from the characteristics of the digital projector, which does not include a pattern projection mode. In building a new acquisition system, we would try to include a digital mirror device, such as the one recommended on the aforementioned website < opensfdi.org >.

Chapter 9.

Scattering map estimation from SFDI analysis

The optical model based analysis of hyperspectral images presented in Chapter 7 is limited to the only estimation of the absorption coefficient. The scattering coefficient has been taken from literature, and is assumed to be constant over the acquired surface [Jacques 2013]. However, as skin scattering properties can vary from one area to another one, and from one person to another, we are also interested in computing maps of scattering coefficients, which can be of use in dermatology and cosmetology. In particular, estimating skin scattering coefficients has proven to be useful for monitoring glucose rate in blood [Bruulsema et al. 1997] and for studying the severity of burns [Mazhar et al. 2014]. Skin scattering coefficients can also be used to study skin aging, as collagen fibers, whose number and diameter greatly affect skin scattering coefficients [Iglesias-Guitian et al. 2015], evolve as a person gets older [Branchet et al. 1991]. Finally skin scattering is also related to the cosmetology concept of skin “complexion radiance” [Musnier et al. 2004], a multi-factorial descriptor that involves skin color, luminosity, brightness and transparency. This complex claim is generally visually assessed by trained evaluators. Although these evaluators are specialists, different evaluators can have slightly different opinions, and for a single evaluator, perception might vary from one day to the other on such a subjective task. The evaluation of complexion radiance can therefore benefit from instrumental methods including systems able to measure skin scattering coefficient.

Skin modulation transfer function (MTF), measured using spatial frequency domain imaging (SFDI) (Chapter 8), can yield the estimation of both absorption and scattering coefficients using optical model based analysis [Cuccia et al. 2009]. This approach, however, is mainly suited to the study of flat surfaces and is difficult to implement on three-dimensional objects due to the presence of irradiance drifts. If irradiance drifts are not taken into account, analysis can be incorrect. Typically, an area that is darker because it has

received less light might be erroneously interpreted as an area with a higher absorption coefficient. For full face analysis, this issue must be addressed in order to estimate maps of scattering coefficient.

This limitation of SFDI for non-flat objects has been addressed in several works [Gioux et al. 2009; Nguyen et al. 2012] by combining SFDI with 3D measurement for correcting irradiance drifts. However, this solution, which closely resembles the method described in Chapter 6 for hyperspectral imaging (HSI), is sensitive to any errors in the 3D acquisition and does not yield satisfactory results on objects with high slopes using our 3D acquisition system. Such an irradiance correction method therefore appears inadequate to be applied to the human face. As such, we have sought to identify another solution to overcome the limitation of being only able to work on flat samples: normalizing the measured MTF to remove the effects of irradiance drifts. However, as a large amount of information about the material absorbance is contained in the MTF magnitude, normalizing the MTF results in an important loss of information that can compromise the estimation of the optical properties.

We therefore propose to combine SFDI with HSI. HSI is still used to estimate maps of skin absorption properties by optimization as described in Chapter 7. These absorption properties are then used as an input to compensate for the loss of information due to MTF normalization and to retrieve the scattering coefficient from SFDI acquisitions in a second optimization process. The spectral reflectance analysis, detailed in Chapter 7, relies on a two-layer skin model characterized by 5 parameters. In this chapter, we investigate the feasibility of a combined HSI-SFDI acquisition, in which as a starting point for the sake of simplicity, skin is modeled as a semi-infinite material and characterized using only two parameters.

In Section 9.1, a method of MTF analysis based on the diffusion approximation is presented. Then, we propose a MTF analysis method that accounts for irradiance drifts in Section 9.2. This method has been tested on phantom samples. Details on the validation process, along with experimental measurement analysis on a full face, are presented in Section 9.3. In Section 9.4, a potential future application that would allow us to “see through” a scattering material is explored. Finally, conclusions are presented in Section 9.5.

9.1. MTF model using the diffusion approximation

As with the analysis method implemented on hyperspectral images, the estimation of skin absorption and scattering properties from the measured MTF requires an optical model that describes the direct problem and a method of inversion. The direct model, which gives the relationship between skin optical properties and its MTF, includes a model of skin and a model of interactions between light and translucent materials. In this part, we present a direct model based on the diffusion equation. The material considered, illustrated in Figure

9.1, is characterized by its optical index n , absorption coefficient μ_a , reduced coefficient μ_s' and total coefficient μ_t .

As already mentioned in Chapter 2, the diffusion equation is an approximation of the radiative transfer equation that is relatively easy to apply, although it has several limitations. It is valid under the assumption that the diffusion is mainly isotropic, with poorly absorbing layers ($\mu_a \ll \mu_s'$), for a sample whose typical dimensions are larger than the scattering mean free path ($\sim \mu_s'^{-1}$). The validity of the diffusion approximation for non-pathological skin analysis has been confirmed in previous studies [Cuccia et al. 2009; Schmitt et al. 1990; Kienle et al. 1998]. Under these assumptions, the *fluence*, or *diffuse photon flux density* φ satisfies the following equation:

$$\Delta \varphi - \frac{\mu_a}{D} \varphi = -\frac{S}{D}, \quad (9.1)$$

where S is the source term that describes the propagation of the incident flux and D the diffusion coefficient given by:

$$D = \frac{1}{3(\mu_a + \mu_s')}. \quad (9.2)$$

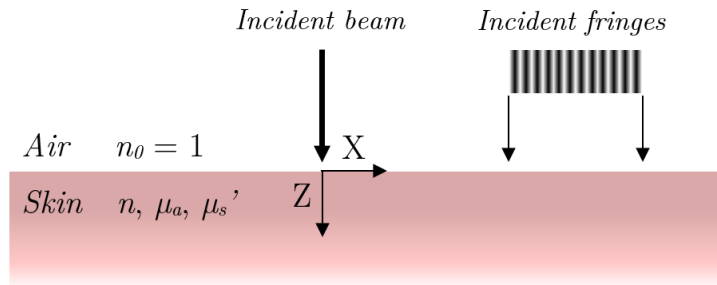


Figure 9.1. Semi-infinite model for skin.

Boundary conditions have to be specified to solve the diffusion equation. These conditions depend on how a material is modeled, for example as homogenous, or as multi-layered with interfaces between materials of different index. Although skin is more accurately described as a multi-layer material, we decided to model it as a semi-infinite material with a planar boundary, a model for which the solution of the diffusion approximation can be solved analytically in the spatial frequency domain. This model has been chosen for its ease of implementation, as the focus of this chapter is to understand the overall experimental method. A finer model, such as a multi-layer model that describes skin more accurately, could be considered in a future work. In the spatial frequency domain, the diffusion approximation also has analytical solutions for multi-layer materials [Kienle et al. 1998].

When the source term corresponds to a thin beam incident upon the material along the Z axis, as illustrated in Figure 9.1, the equation of the diffusion approximation describes the PSF of the material. Its expression in the Fourier domain can be used to describe the MTF of the material.

In the spatial domain frequency, Eq. (9.1) can be rewritten as the following expression, involving the spatial depth z and the wave vector $s = (s_x^2 + s_y^2)^{1/2}$:

$$\frac{\partial^2 \tilde{\varphi}}{\partial z^2}(s, z) - \alpha^2 \tilde{\varphi}(s, z) = -\frac{\tilde{S}(s, z)}{D}, \quad (9.3)$$

with the fluence in the frequency domain

$$\tilde{\varphi}(z, s_x, s_y) = \int_{-\infty}^{\infty} \int_{-\infty}^{\infty} \varphi(x, y, z) e^{i(s_x x + s_y y)} dx dy, \quad (9.4)$$

with the source term, that depends on φ_0 the incident irradiance

$$\tilde{S}(s, z) = \varphi_0 \mu_s^{-1} e^{-\mu_t z}, \quad (9.5)$$

and

$$\mu_t = \mu_a + \mu_s^{-1}, \quad (9.6)$$

$$\alpha^2 = 3\mu_a \mu_t + s^2. \quad (9.7)$$

The wave factor s can be replaced with the spatial frequency f according to the relationship:

$$s = 2\pi f. \quad (9.8)$$

In our application, the projected fringes correspond to a one-dimensional frequency, arbitrarily chosen along the X dimension, therefore $f = f_x$.

For semi-infinite materials, the solution to Eq. (9.3) is the sum of a general homogeneous solution and a particular solution, and can be written as:

$$\tilde{\varphi}(f, z) = C e^{-\alpha z} + \frac{3\varphi_0 \mu_s^{-1} / \mu_t}{\alpha^2 / \mu_t^2 - 1} e^{-\mu_t z}, \quad (9.9)$$

where C is a constant that has to be determined from applying boundary conditions.

At the material interface ($z = 0$), no diffuse flux oriented toward the positive Z direction is created. However, due to a change of index between the outside environment and the material, a fraction of the diffuse flux oriented toward the outside of the material is reflected back into the material according to Fresnel reflection. This yields the *partial-current boundary condition* described by Haskell [Haskell et al. 1994]:

$$\tilde{\varphi}(f, z = 0) - \frac{2b}{3\mu_t} \frac{\partial \tilde{\varphi}}{\partial z}(f, z = 0) = 0, \quad (9.10)$$

with

$$b = \frac{1 - R_{eff}}{1 + R_{eff}}, \quad (9.11)$$

and R_{eff} the effective reflection coefficient [Egan and Hilgeman 1979]

$$R_{eff} \approx 0.0636n + 0.668 + \frac{0.710}{n} - \frac{1.440}{n^2}, \quad (9.12)$$

where n is the relative index of refraction of the medium with the reflected ray to the other medium.

The combination of Eqs. (9.9) and (9.10) yields the expression of the fluence in the spatial frequency domain at the depth z :

$$\tilde{\varphi}(f, z) = \frac{3\varphi_0 \mu_s' / \mu_t}{\alpha^2 / \mu_t^2 - 1} \left(e^{-\mu_t z} - \frac{1 + 3/2b}{\alpha / \mu_t + 3/2b} e^{-\alpha z} \right). \quad (9.13)$$

The reflectance in the spatial frequency domain is related to the fluence through the exiting flux $F^-(0)$:

$$\tilde{R} = -\frac{F^-(0)}{\varphi_0}, \quad (9.14)$$

$$F^-(0) = -\frac{1}{3\mu_t} \frac{\partial \tilde{\varphi}}{\partial z}(0). \quad (9.15)$$

Finally, Eqs. (9.13), (9.14) and (9.15) yield the analytic expression of the diffuse reflectance in the spatial frequency domain (which is also the MTF):

$$\tilde{R}(f) = \frac{3\mu_s' / 2b\mu_t}{(\alpha / \mu_t + 1)(\alpha / \mu_t + 3/2b)}. \quad (9.16)$$

In the spatial domain, the diffusion approximation is valid for an area located far enough from the impact point of the incident light beam, i.e. at a distance higher than the transport mean free path, $l = 1/\mu_t$. In the spatial frequency domain, this condition means that results are valid for frequencies inferior to $1/l = \mu_t$. Since the quantity μ_t is typically superior to 1 for skin, our acquisition method meets this condition ($f < 0.7 \text{ mm}^{-1}$). At the zero frequency, $\tilde{R}(f = 0)$ depends only on the quantity μ_s' / μ_t , often called the *reduced albedo*, a quantity that does not allow us to measure μ_a or μ_s' separately. $\tilde{R}(f = 0)$ also

corresponds to the reflectance in the real domain. Consequently, the expression given in Eq. (9.16) can also be used in principle to analyze the spectral reflectance acquired by HSI [Bjorgan et al. 2014].

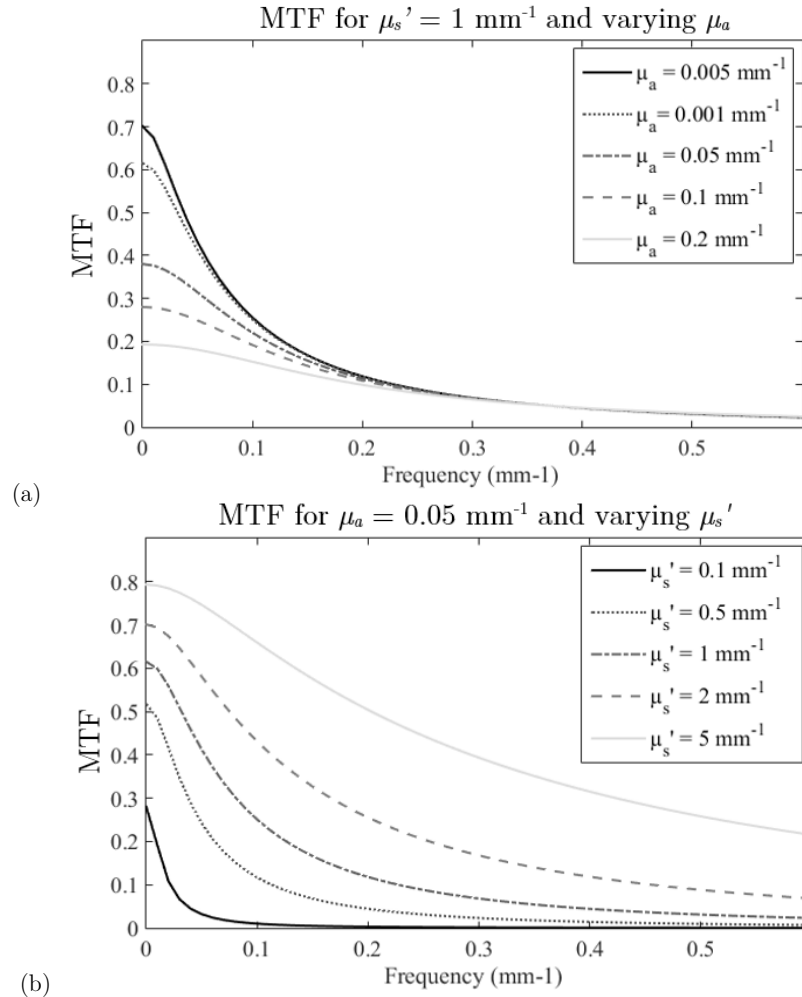
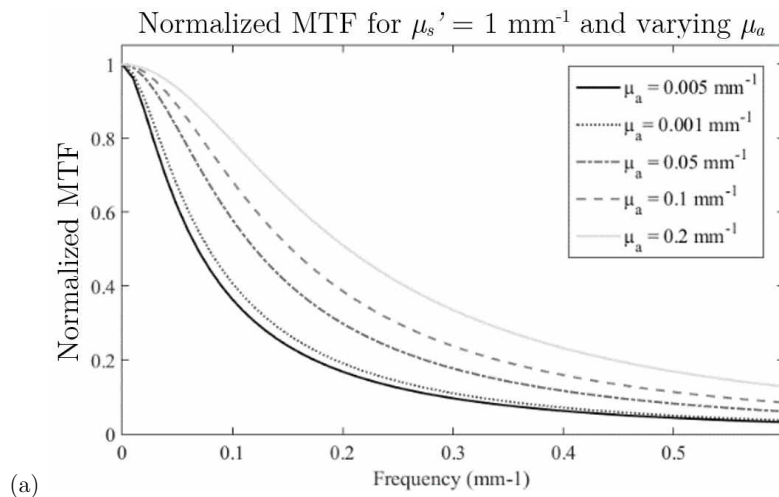
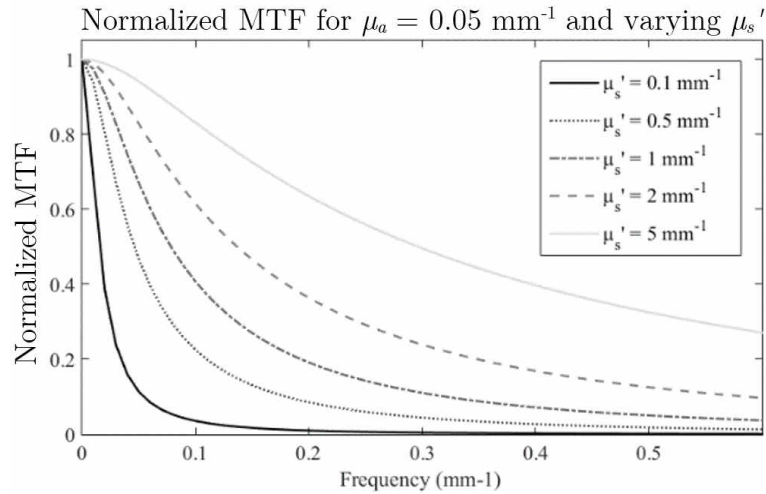


Figure 9.2. MTF variations for (a) varying absorption properties and (b) varying scattering properties (optical index $n = 1.4$).





(b)

Figure 9.3. Normalized MTF variations for (a) varying absorption properties and (b) varying scattering properties (optical index $n = 1.4$).

MTF computed from Eq. (9.16) at several frequencies are presented in Figure 9.2 to show the variations that occur when either the absorption coefficient or the scattering coefficient are fixed. Figure 9.2.a shows MTF curves corresponding to a fixed μ_s' value and varying μ_a values. Interestingly, the MTF varies with μ_a at low frequencies, but not at high frequencies, where the curves converge to the same asymptotic curve. The curves on Figure 9.2.b, which correspond to MTF for a fixed μ_a value and varying μ_s' values, show that the scattering properties of the material influence the MTF in both the low and high frequencies.

Figure 9.3 shows normalized MTF for the same optical parameters as in Figure 9.2. Figure 9.3.b shows that when the value of μ_a is fixed, the shape of the normalized MTF clearly varies with μ_s' . However, the inverse is not true: for a given μ_s' (Figure 9.3.a), changing μ_a affects less significantly the shape of the curves. This observations illustrate the difficulties of estimating μ_a from normalized data, as the variations are not strong enough to ensure an accurate estimation of μ_a using an optimization approach. In the following, a method to tackle this issue is proposed.

9.2. MTF analysis for a full face

The direct model presented in the previous section is suitable for analyzing the measured MTF as long as the acquired area of skin is flat. When curved surfaces are considered, the acquisitions are affected by irradiance drifts and the measured MTF corresponds to the surface MTF multiplied by a constant factor that is the ratio of the sample irradiance to the reference plane irradiance.

In the analysis of full face hyperspectral images, this problem was tackled using the spectral angle mapper (SAM) in the optimization process, which relies on a comparison

between normalized spectra. Spectral reflectance normalization leads to a loss of information (i.e. the total quantity of light that has been reflected), but in practice, the measured information is altered by irradiance drifts. Normalization is therefore a way to suppress the effects of irradiance drifts, but it does not impede the estimation of skin absorption properties, as it is the shape of the spectrum that provides information about skin chromophore concentrations.

In the case of MTF, normalization also removes the effects of irradiance drifts, but contrary to spectral reflectance, MTF is monotonic with respect to frequency, and estimating of the scattering coefficient using only the shape of the MTF is difficult. The loss of information caused by normalization must therefore be compensated.

To address this problem, we propose to combine SFDI with HSI in a dual-step measurement, as illustrated in Figure 9.4. The analysis of the hyperspectral image yields the skin absorption coefficient independent of irradiance drifts. Once this coefficient is known, it is possible to analyze the normalized MTF to estimate the skin scattering coefficient.

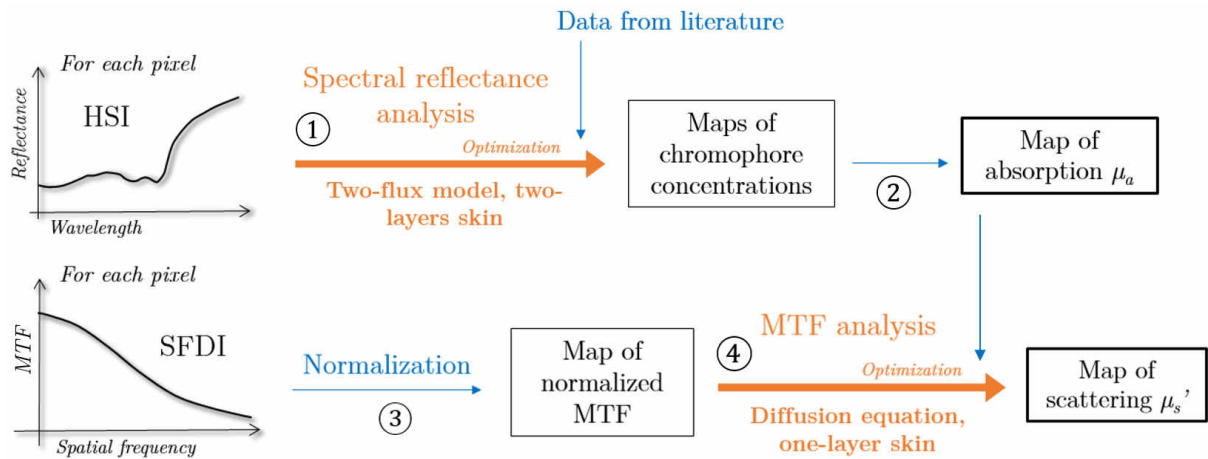


Figure 9.4. HSI and SFDI combined analysis to estimate maps of absorption and scattering coefficients.

Once the spectral reflectance analysis is completed (indicated by ① in Figure 9.4), its output parameters (oxygen rate, blood volume fraction, melanin concentration, bilirubin concentration and epidermis thickness) are converted into a map of absorption coefficients (indicated by ② in Figure 9.4). The spectral reflectance analysis method considers skin as a two-layer material. In the MTF analysis, however, skin is modeled as a one-layer material characterized by an overall absorption coefficient μ_a and an overall reduced scattering coefficient μ_s' . To compute the absorption coefficient, we refer to the Kubelka Munk theory applied to a semi-infinite homogeneous layer, which describes skin reflectance as a function of absorption and scattering parameters K_{skin} and S_{skin} , for each wavelength:

$$R_{skin} = \frac{K_{skin} + S_{skin} - \sqrt{K_{skin}(K_{skin} + 2S_{skin})}}{S_{skin}}. \quad (9.17)$$

The inversion of Eq. (9.17) yields (it also corresponds to the formula that gives the *remission function* K/S):

$$K_{skin} = \frac{S_{skin}(R_{skin} - 1)^2}{2R_{skin}}. \quad (9.18)$$

A map of the absorption parameter K_{skin} can be calculated using Eq. (9.18). The scattering parameter S_{skin} is taken from literature [Jacques 2013] and used in the spectral reflectance analysis method presented in Chapter 7 to described the scattering properties of both the epidermis and dermis. R_{skin} is the skin reflectance calculated from the estimated parameters (oxygen rate, blood volume fraction, melanin concentration, bilirubin concentration and epidermis thickness) by applying the direct model given in Eq. (7.9) in Chapter 7.

Then, the absorption coefficient μ_a is obtained from the Kubelka Munk parameter K_{skin} using:

$$K_{skin} = 2\mu_a. \quad (9.19)$$

This coefficient is used as an input in the analysis of the normalized MTF, in order to estimate the skin scattering coefficient.

The third step of the method, indicated by ③ in Figure 9.4, is the normalization of the measured MTF:

$$M\bar{T}F_m(x, y, f) = \frac{MTF(x, y, f)}{MTF(x, y, 0)}. \quad (9.20)$$

Finally, the reduced scattering coefficient μ_s' can be estimated by an optimization, indicated by ④ in Figure 9.4. The reduced scattering coefficient for each pixel (x, y) is estimated by using a least squares fitting method:

$$\mu_s'(x, y) = \arg \min_{\mu_s'} \left(d_E \left(M\bar{T}F_{th}, M\bar{T}F_m \right) (x, y) \right), \quad (9.21)$$

with the distance

$$d_E(M\bar{T}F_{th}, M\bar{T}F_m)(x, y) = \sqrt{\sum_{f_i} \left(M\bar{T}F_{th}(x, y, f_i) - M\bar{T}F_m(x, y, f_i) \right)^2}. \quad (9.22)$$

The distance is defined by a sum over f_i , where f_i designates the non-zero acquired spatial frequencies ($i = 1 \dots 3$ in for our acquisition system).

The normalization of the theoretical MTF is given by the following formula, with MTF_{th} given by Eq. (9.16):

$$MTF_{th}(x, y, f) = \frac{\tilde{R}(x, y, f)}{\tilde{R}(x, y, 0)}. \quad (9.23)$$

As the cost function described by Eq. (9.21) is unidimensional with a single minimum, simple optimization can be used. The method that we implemented is based on a look-up-table: we computed, for all μ_s ' values, the distance d_E defined in Eq. (9.22) and searched for the μ_s ' value for which d_E is the lowest.

9.3. Experimental measurement analysis

Before performing in vivo acquisition on skin, we first verified the analysis method on translucent phantoms. To create irradiance drifts, we front-tilted and side-tilted these samples at various angles, from 0 to 60 degrees, and applied the method to estimate scattering properties from normalized MTF. We then performed HSI and SFDI acquisitions on a full face. The reduced scattering coefficient maps obtained are presented in this section.

9.3.a. Phantom SFDI measurement

Four flat wax samples with varying absorption and scattering properties, as described in Chapter 8, have been used to assess the method's ability of extracting scattering coefficients independently from irradiance drifts. For this experimental test, SFDI has been performed at the green waveband emitted by the digital LED projector (the tunable filter used for HSI was not part of the acquisition system). The wax samples can be considered as infinitely thick in this waveband, as their thickness exceeds the maximum light depth propagation.

As the properties of oil paint and wax are unknown, a first SFDI measurement has been performed for calibration purposes. To retrieve both absorption and reduced scattering coefficients, we assumed that there was no irradiance drift on these flat samples and consequently, that no normalization was required. The 4 frequencies projected by the acquisition system are insufficient to precisely measure the samples' MTF. The SFDI acquisition was thus repeated 4 times, with the distance between the sample and the acquisition system varying each time, which allows for 13 frequencies to be measured instead of 4. As SFDI provides a value in each pixel, MTF has been obtained by computing the average value on the sample. The acquired data has then been analyzed in order to retrieve the optical properties of each sample. During this part of the process, the non-normalized model described in Eq. (9.16) was used within an optimization based on Euclidean distance

[Eq. (9.22)]. The optical index for wax was assumed to be $n = 1.45$. The measured MTF and estimated optical coefficients are illustrated in Figure 9.5 and Table 9.1.

On Figure 9.5, we notice that the distance between the theoretical curves (dotted lines) and the measured curves (solid lines) is relatively minor, which suggests that the diffuse approximation applied for a single-layer material is an accurate description of the MTF for this kind of sample.

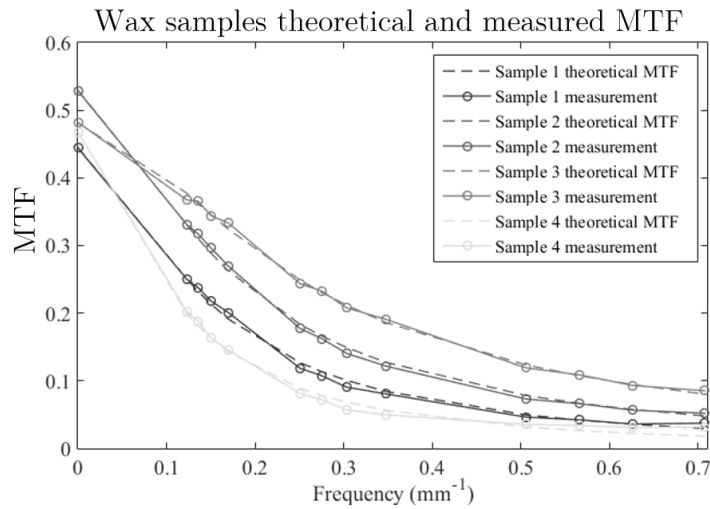


Figure 9.5. Average MTF measured on the wax samples and theoretical fitting curves yielding to values of μ_a and μ_s' for each sample (optical index $n = 1.45$).

Sample	Composition			SFDI analysis at 520 nm		
	White wax	Black wax	Base wax	μ_a (mm ⁻¹)	μ_s' (mm ⁻¹)	Error*
No 1	25%	46%	28%	0.0414	1.439	0.021
No 2	50%	24%	26%	0.0320	1.973	0.019
No 3	55%	44%	0%	0.0634	2.817	0.018
No 4	25%	28%	47%	0.0265	1.077	0.025

Table 9.1. Composition of each wax samples, estimated optical absorption and reduced scattering coefficient, and residual error after optimization (*Error denotes the residual Euclidean distance after optimization).

The 4 wax phantoms were tilted around the X -axis (front tilted) and the Y -axis (side tilted), as illustrated in Figure 9.6, and acquired at varying angles using SFDI with vertical fringes. The normalization method was then applied to estimate scattering properties, using the absorption coefficient determined in the calibration step.

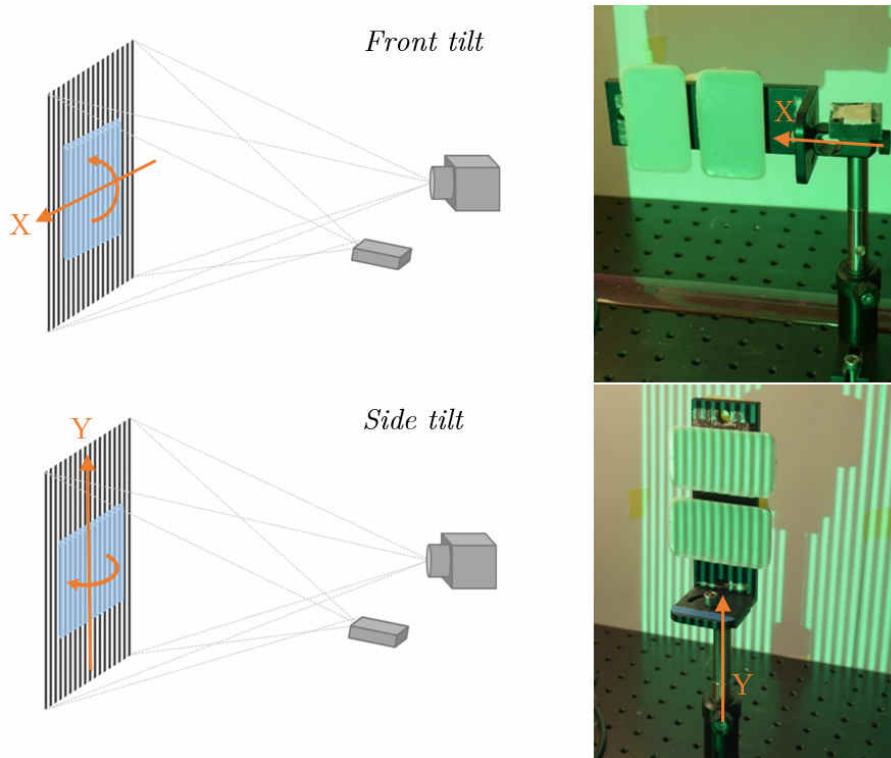


Figure 9.6. SFDI acquisition on front tilted and side tilted wax samples.

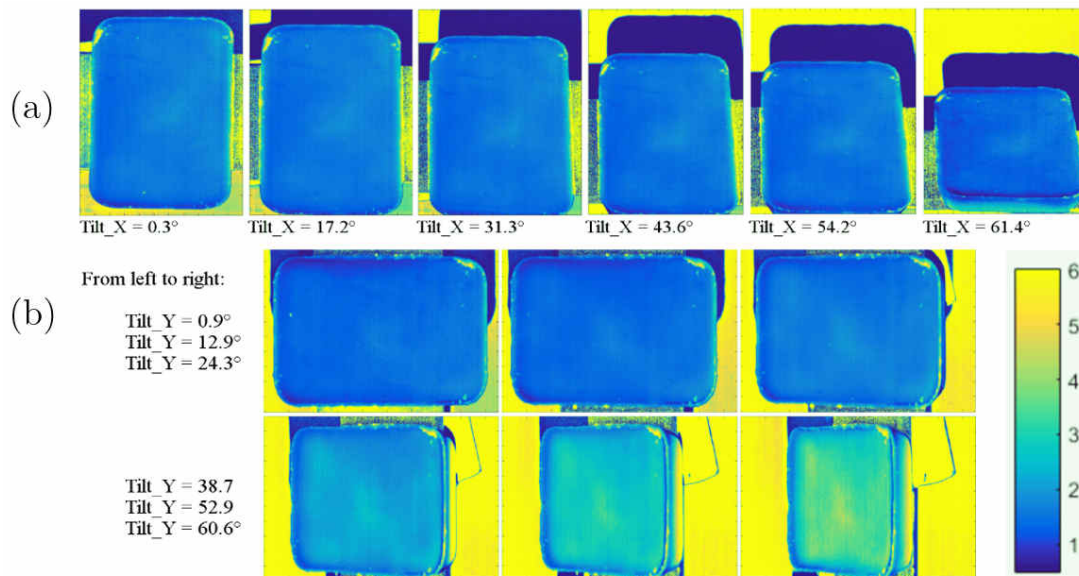


Figure 9.7. Maps of estimated reduced scattering coefficient μ_s' (mm^{-1}) obtained for sample No 1 at several tilt angles around (a) the Y-axis and (b) the X-axis.

On the estimated reduced scattering coefficients presented in Figure 9.8, we observe that the method yields values close to those expected for angles below 25 degrees when samples are side-tilted, and satisfactory results for all front-tilted measurements. The

difference between the front and side tilt, illustrated in Figure 9.7, can be explained by the variation of the fringe frequency induced by the sample's rotation. On the sample surface, fringe frequency remains almost unchanged for a front tilt when fringes are vertical, but decreases with a cosine law for a side tilt. In case of a side tilt, the frequencies used to compute MTF in the inverse problem do not correspond to the frequencies that are actually projected onto the surface, which results in errors in the optical property estimation. Given this limitation, 3D objects should be carefully positioned for SFDI acquisitions. In the case of face imaging, we limit our studies to a three-quarter view of the face (i.e. angled at 45° to the camera) and we project horizontal fringes, whose spatial frequency is less affected by the shape of the face than vertical fringes.

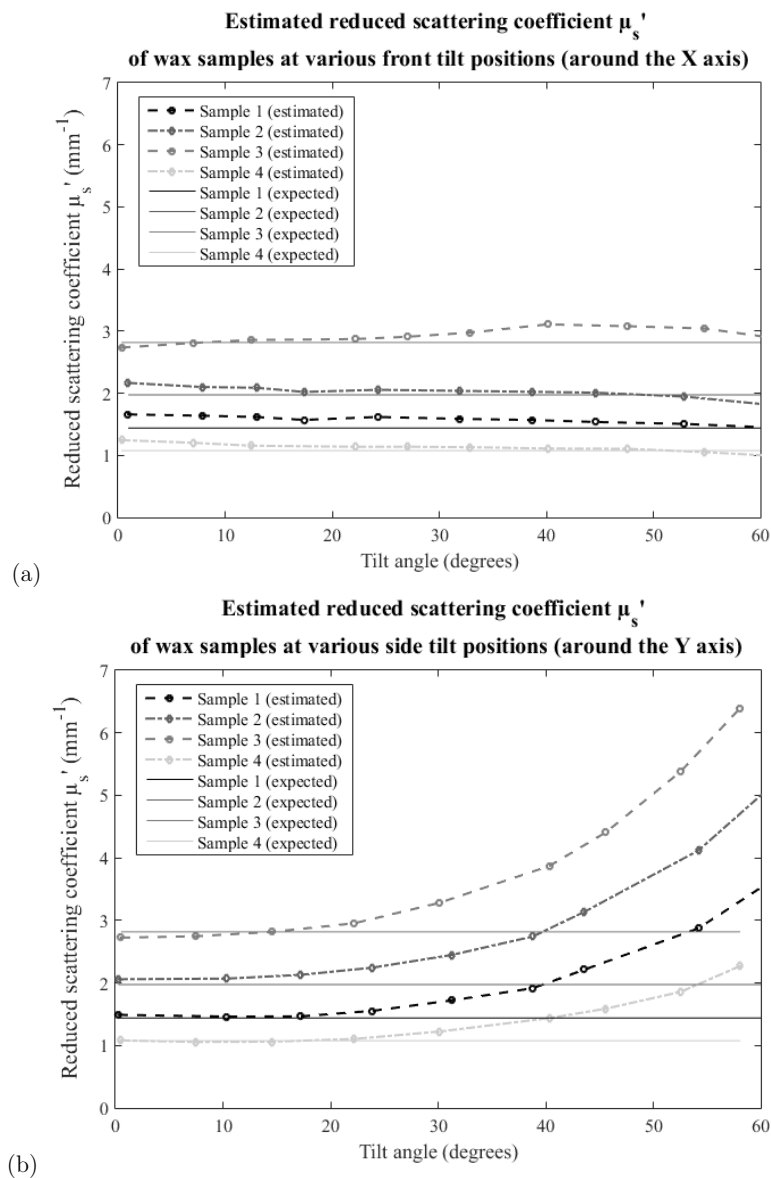


Figure 9.8. Estimated reduced scattering coefficient μ_s' of the 4 paraffin wax samples at various (a) front tilt and (b) side tilt positions.

We can also notice on Figure 9.8 that there is an error between the expected reduced scattering coefficient value, obtained from the calibration, and the estimated value using normalized MTF for the first tilt position (approximately zero degrees). This might result from errors in sample calibration, frequency measurement and reference acquisition. This error, 15% at the highest for sample No 1, provides some information about the accuracy of the analysis method. Better calibrated samples would be necessary to properly characterize the method's accuracy.

9.3.b. Face measurement using HSI and SFDI

The acquisition and analysis method combining HSI and SFDI was applied to the human face. A three-quarter view of the face was acquired using HSI and SFDI at 520 nm, which corresponds to the peak of emission of the projector green LED. Hyperspectral images have been analyzed using the method described in Chapter 7, and maps of skin reduced scattering coefficient μ_s' have been estimated using the method described in Section 9.2. Acquisition and analysis results on three different persons are presented in Figures 9.9, 9.10, 9.11 and 9.12.

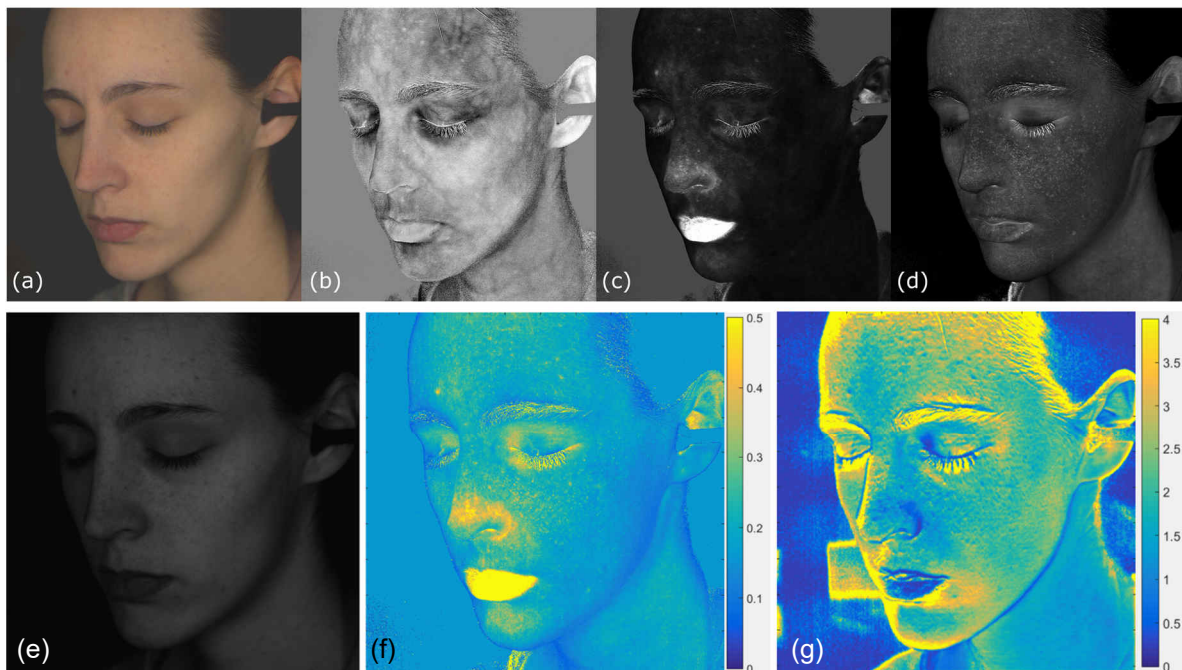


Figure 9.9. HSI and SFDI analysis images: (a) acquired hyperspectral image converted into RGB color, (b) map of oxygen rate, (c) map of blood volume fraction, (d) map of melanin concentration, (e) grayscale image at 520 nm, (f) map of absorption coefficient μ_a (mm^{-1}) and (g) estimated map of reduced scattering coefficient μ_s' (mm^{-1}).

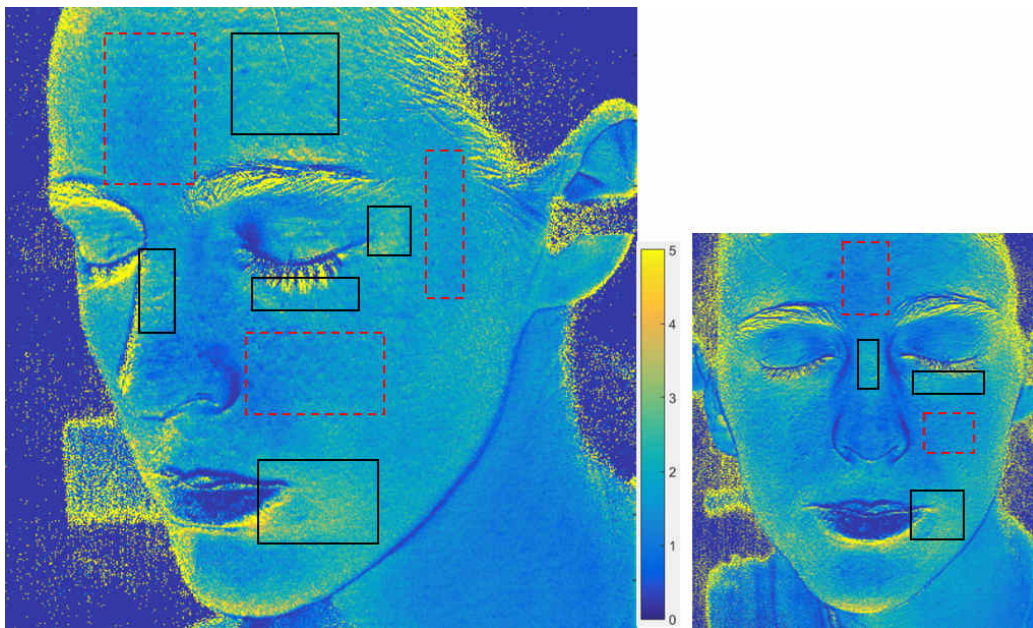


Figure 9.10. Enlarged map of reduced scattering coefficient μ_s' (mm^{-1}) from Figure 9.9.g and map from an additional front view acquisition. The parts enclosed in dotted red exhibit a lower scattering coefficient than the average and parts enclosed in black show areas for with the scattering coefficient is higher.

Figures 9.9.g and 9.10 show the computed maps of reduced scattering coefficient μ_s' at 520 nm. Except for the side of the face and the top of the nose, we observe no strong correlation between the computed μ_s' and the 3D shape of the face, which indicates that the analysis was not affected by irradiance drifts. The low correlation between the estimated reduced coefficient μ_s' and the shape of the face can also be verified by checking that the estimated values for μ_s' are similar on a side view and front view of the face, which is the case here, as illustrated in Figure 9.10.

On Figure 9.10, values for μ_s' vary between 1 and 4 mm^{-1} , which is consistent with the values found in previous works [Calin et al. 2013; Cuccia et al. 2009], however, though inferior to the ones published by Jacques [Jacques 2013]. We can also observe that μ_s' does not drastically vary on the face, which corroborates the use of a constant scattering coefficient in chromophore map estimation from HSI. However, several “patterns” of variation can be pointed out: the reduced scattering coefficient is lower on the middle of the forehead, on the tip of the nose, on the chin and on the cheek; it is higher on the bridge of the nose, on the dark circles below the eyes, on the corners of the mouth, or on the part of the forehead above the eyes. For some of these areas, such as the bridge of the nose, skin is directly on top of a bone, where the optical model of skin as semi-infinite skin may not be valid. At this stage of our research, we cannot therefore say with any certainty that the estimated scattering coefficients for these areas accurately represent skin physiology. Another limitation of the method can be noticed: on the inside corner of the eye and on the

nostril, the values estimated for μ_s' are likely to be erroneous as the light interreflections that occur on these concave parts are not a linear variation of the spectral irradiance. This issue, already mentioned in Chapter 7, is not accounted for in the model.

Figures 9.11 and 9.12 show acquisition and analysis results on two men of different ethnicity. While the chromophore maps obtained from spectral reflectance analysis (Figures 9.11.b-d and Figures 9.12.b-d) show similar patterns on the chromophore maps, e.g. a lack of oxygen around the dark circles under the eyes, the maps of reduced scattering coefficients differ (Figures 9.11.f and 9.12.f), with greater variations for the subject on Figure 9.11. While there have been studies that have aimed to measure skin reduced scattering properties on large groups of people in order to understand its typical variations [Jonasson et al. 2018], as far as we could tell, very little is known about how skin reduced scattering coefficient varies on the face, given differences of age, sex, or ethnicity. Our method could allow such a study.

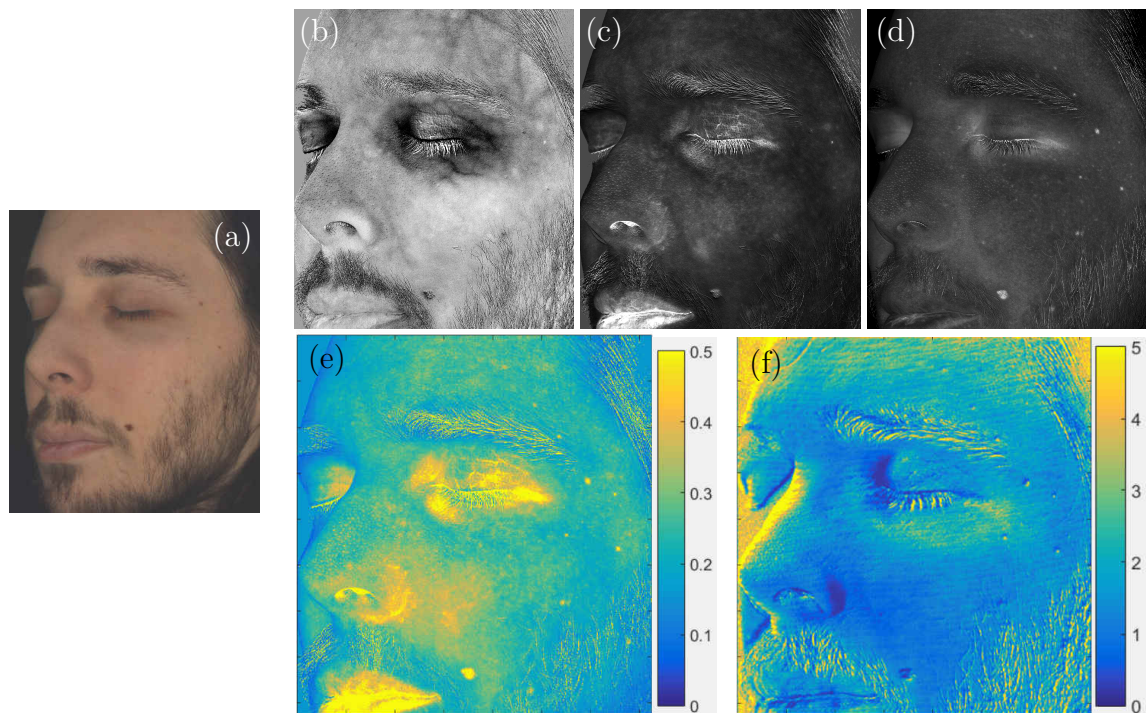


Figure 9.11. HSI and SFDI analysis images: (a) acquired hyperspectral image converted into RGB color, (b) map of oxygen rate, (c) map of blood volume fraction, (d) map of melanin concentration, (e) map of absorption coefficient μ_a (mm⁻¹) and (f) estimated map of reduced scattering coefficient μ_s' (mm⁻¹).

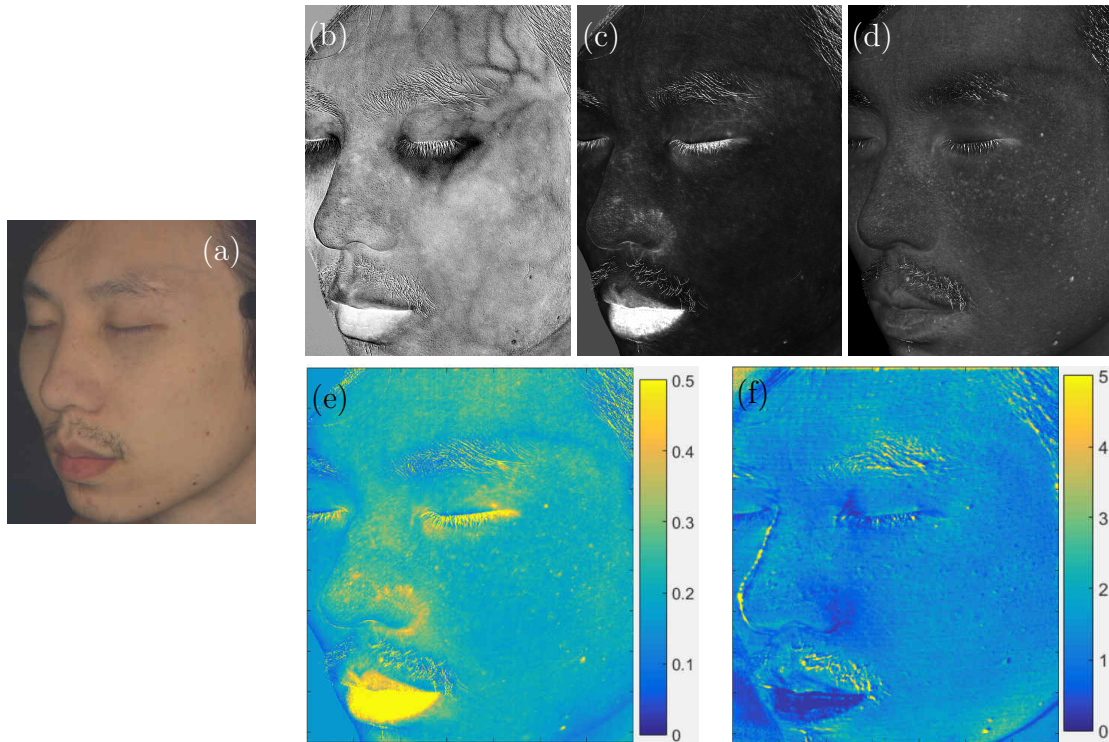


Figure 9.12. HSI and SFDI analysis images: (a) acquired hyperspectral image converted into RGB color, (b) map of oxygen rate, (c) map of blood volume fraction, (d) map of melanin concentration, (e) map of absorption coefficient μ_a (mm^{-1}) and (f) estimated map of reduced scattering coefficient μ_s' (mm^{-1}).

9.3.c. Discussion on the limitations of the method

The maps presented in § 9.3.b are currently difficult to interpret, as the one-layer optical model that is used might not be valid on parts of the face for which skin is close to a bone. Additional studies are also required to fully understand the limitations and accuracy of the method. In particular, the estimated reduced scattering coefficient values are likely to be sensitive to errors arising from calibration and fringe frequency estimation: finding the right values for the projected fringe frequency presents a challenge, as they are measured on a flat reference surface but vary on non-flat objects. To validate the acquisition method, the acquisition of well-known calibrated samples with optical coefficients comparable to human skin would be necessary. Then, to validate the analysis method on skin, the estimated reduced scattering coefficient would need to be compared with measurements obtained using an already validated method.

In this work, a one-layer model was preferred over the two-layer model used for spectral reflectance analysis. A first improvement could therefore be to model the skin as a two-layer material [Weber et al. 2006]. Working in the spatial frequency domain makes the resolution of the diffusion equation rather simple for multi-layered materials, but the complexity of the inverse problem lies in the number of parameters involved.

Finally, although using an imaging method such as SFDI for MTF measurement yields a value per pixel, the resolution of the measurement depends on the translucency properties of the material more than on the size of the pixel. At a wavelength for which skin is strongly scattering, light does not travel very far, and we can consider that it is the material delimited by a pixel that is measured. At higher wavelengths however, skin is more translucent and light can travel distances larger than the size of a pixel. In such cases, the measurement does not depict skin optical properties on each pixel, but rather corresponds to an average value within a certain radius around the pixel.

9.3.d. Using μ_s' maps to improve the analysis of hyperspectral images?

This chapter shows that the reduced scattering coefficient is relatively uniform on a person's face, an assumption on which the spectral reflectance analysis (Chapter 7) relies. While the values used in the algorithm might not exactly match the person's skin properties, its relative uniformity on the face shows that the interpretation of chromophore maps are generally valid as a relative measure, for example, when comparing two locations on the face, or at two times for the face person. However, for parts of the face such as dark circles under the eyes, which can have different scattering properties than "normal" skin, the amount of error caused by this assumption can be higher. As a next step of development, we could put back the scattering coefficient obtained by MTF analysis into the spectral reflectance analysis algorithm to better understand its impact, as illustrated in Figure 9.13. This would require an iterative optimization process, as the new estimated maps of chromophore concentration could be used in turn to estimate the reduced scattering coefficient again.

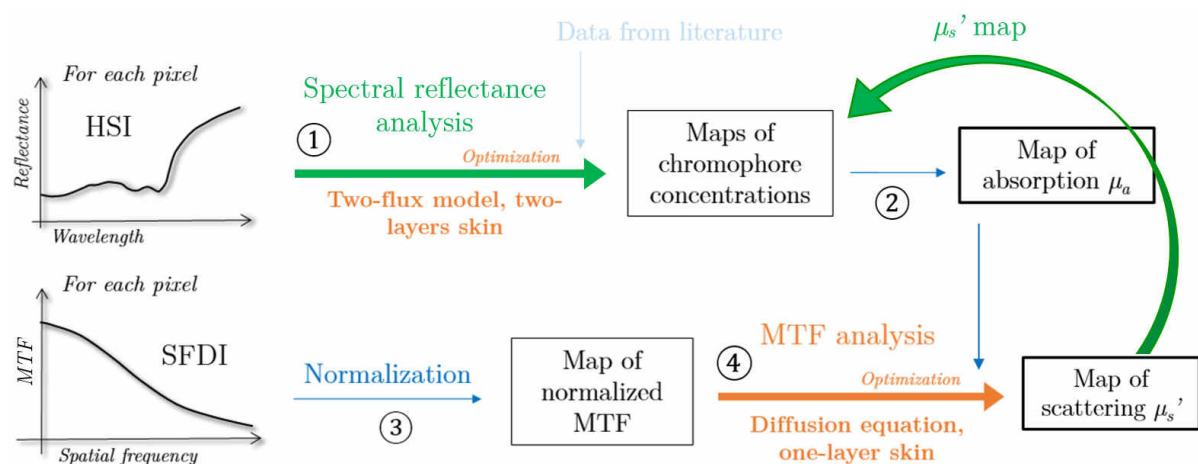


Figure 9.13. HSI and SFDI iterative analysis process to improve the estimation of chromophore concentration maps.

The reason for which this has not yet been implemented is that it would require reduced scattering coefficients at every visible wavelength. As the variation of this coefficient can be modeled by a Rayleigh law, acquisition at two or three wavelengths would suffice to interpolate data at any wavelength. However, due to limitations of the SFDI acquisition system in terms of acquisition speed, we failed to acquire maps of skin MTF at more than one wavelength at a time.

Throughout this thesis, we insist on the importance of short acquisition time. This constraint aside, another limitation is computation time. In particular, an iterative analysis method as described above would require enormous calculation time. While more than one day of computation per image is feasible from a research point of view, it is a strong limitation for applications in cosmetology studies. To tackle this issue, we could take advantage of machine learning method, which can drastically reduce computation time as illustrated in the preliminary study presented in Chapter 7.3.

9.4. Going further: “seeing” through a scattering material by using deconvolution techniques

In this chapter, we have seen that skin optical properties determine the extent to which fringes projected onto its surface are blurred. Similarly, skin optical properties also affect the contours of the objects located inside it, such as veins: the deeper in the skin a vein is located, the blurrier its contours appear.



Figure 9.14. Increasing quantity of milk on coins at different heights and screw, illuminated from underneath.

To quantify the blurring effect on an object located at a certain depth in a translucent material, the diffusion approximation theory can be applied, by considering for the boundary conditions that the object is a source point, and modeling the PSF in transmission rather than reflection. Figure 9.14 illustrates an experiment with coins, a screw, and a changing quantity of milk poured over them to show that the amount of blur increases with depth in translucent media.

In theory, if the optical properties of the translucent material and the depth of the object are known, then the contour of the object can be “unblurred” through deconvolution using the PSF of the material. The PSF is modeled according to the depth of object in the material. This method has been applied to skin, e.g. finger vein image restoration [Yang and Bai 2012].

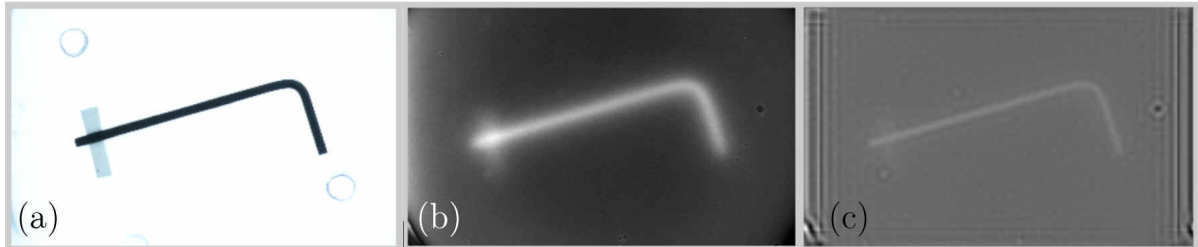


Figure 9.15. Milk on an Allen key, illuminated from underneath: (a) Allen key alone, (b) Allen key under 3.5 mm of milk and (c) deconvoluted image obtained using a PSF modeled by the diffusion approximation.

We tried to implement it on an Allen key in milk: the acquired and processed images are shown in Figure 9.15. The deconvoluted image, represented in Figure 9.15.c, shows a key whose size is similar to the one in image of the key itself (Figure 9.15.a), however, there is a noticeable loss of image quality and contrast caused by the deconvolution process is significant. For applications on skin, such methods might help to improve the contrast of skin vessels, or to estimate their depth. However, this would require a complicated process involving deconvolution with multiple PSFs.

9.5. Conclusion

We have investigated the potential of combining HSI with SFDI to estimate maps of absorption and scattering coefficients of skin independently from irradiance drifts. This preliminary study has shown the feasibility of this method, but additional measurements on calibrated samples would be required to fully identify its limitations and its sensitivity to errors. The estimated scattering values might not be reliable as an absolute measurement, however, we believe that the estimated maps of scattering properties might be of interest as a relative result that can be used for purposes of comparison (for example, at two different times, between two different regions or for two different persons), since calibration errors, frequency estimation errors, model limitations, and so on, are the same for every pixel. Additional studies are required to understand whether the method is sensitive enough to provide the sufficiently accurate information for such applications. The most conspicuous limitation of the method may be that the maximum tilt angle is relatively small (around

25°) in one of the tilt directions. This appears to be of little consequence for face acquisition when horizontal fringes are used, nevertheless, the acquired surfaces need to be carefully oriented to minimize errors resulting from 3D geometry. This limitation could be addressed by correcting both irradiance drifts and spatial frequency variations that occur when projecting fringe patterns on a complex 3D object. This approach would need additional, high precision acquisition of 3D geometry, which remains a challenge for full face acquisitions.

Chapter 10.

Conclusion

The aim of this project was to develop an imaging system and a skin analysis method that could be applied to a full face and yield information about skin composition. The challenges of this were manifold: in vivo full face imaging requires wide field imaging, fast acquisition to limit artefacts caused by a person moving during measurement, and an optical analysis method robust to irradiance drifts. In addition, obtaining images of a sufficiently high resolution was also essential if we wished to use the measurements acquired for the purpose of skin analysis. The content of this work was developed with all these requirements in mind.

In the first part, we proposed a 3D-hyperspectral camera capable of acquiring hyperspectral images of the full face and its 3D geometry in around 5 seconds. The acquisition method, detailed in Chapters 4 and 5, is safe for the skin and the eyes, non-invasive, and contactless. In terms of measurement resolutions, we succeeded in finding a good trade-off between spectral and spatial resolution: spectral reflectance is measured at 30 wavebands of 10 nm width within the visible spectrum, which adequately records the reflectance spectrum to allow for skin chromophore concentration analysis; and spatial resolution is around 0.1 mm per pixel on the face, which is sufficient for discerning fine details on the face such as blood vessels. The acquisition system was designed for applications in cosmetological studies: today, the full face hyperspectral camera, the “SpecraFace”, has been used on hundreds of patients by clients of Newton Technologies. This demonstrates that the design of the system is suited to applications outside of a research lab.

Using an optical model and an optimization algorithm, the acquired hyperspectral images can be analyzed into maps of skin properties (e.g. maps of blood volume fraction, melanin concentration, oxygen rate ...). The analysis method, which was developed prior to the undertaking of this project, was extended to the full face, with its limitations defined in Chapter 7. Using a metric that is robust to irradiance drifts in the optimization algorithm, we obtained skin composition maps for a full face, shown in Figure 10.1, even in areas where irradiance was low in the measured spectral images. While there are existing studies on the

estimation of chromophore concentration maps for flat areas, as far as we could tell from the literature, the estimation of skin component maps over the full face is without precedent.

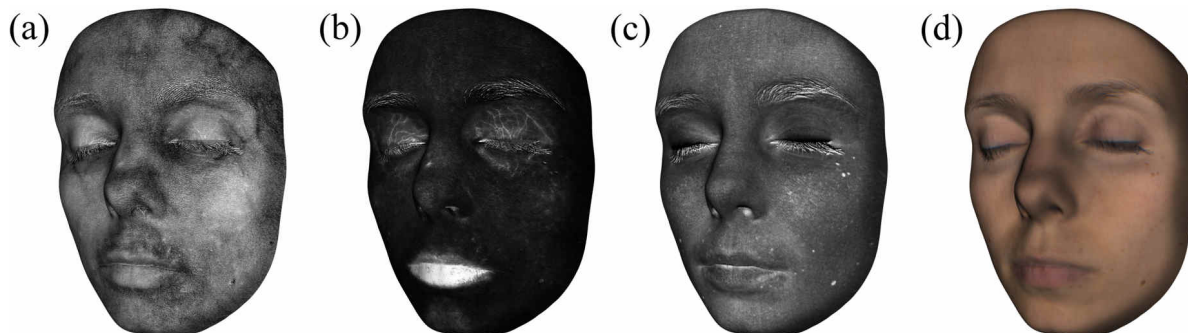


Figure 10.1. 3D hyperspectral acquisition results: (a) oxygen rate, (b) blood volume fraction, (c) melanin concentration, and (d) color.

The combination of 3D scanning with hyperspectral imaging (HSI) was originally conceived to correct irradiance drifts, as a pre-processing step before image analysis. Irradiance drift correction is relatively easy to implement for simple illumination configurations, typically when the object is illuminated by a single punctual source. In the case of HSI, however, the illumination configuration is far more complex, and finding a suitable correction method was a real challenge. We found and implemented a method whose simplicity is worth mentioning given the complexity of the problem, detailed in Chapter 6, and obtained satisfactory results on most parts of the face. It is only on highly-sloped areas, such as the nose, that the method does not yield good results, as it is very sensitive to errors in the 3D measurement, which result in over-corrected irradiance drifts. The precision and accuracy of the 3D scanner are satisfactory given the simplicity of the setup: the 3D measurement method relies on multiple fringe projection, a feature that has been added to the hyperspectral camera simply by adding a digital projector beside the camera. Unfortunately, this proved inadequate for obtaining accurate results on a full face. Using this method, it would be necessary to use more than one camera and perhaps more than one projector to achieve the precision required for suitable irradiance drift correction. Given the commercial context of the work, we decided to stick with the simple, low cost 3D measurement method we devised and did not apply the irradiance drift correction method as a pre-processing step to image analysis. Instead, we used an alternative method for addressing irradiance drift, as mentioned above.

The combination of the hyperspectral camera and a digital projector was not therefore used according to our initial intentions, but instead led us, in the second part of this work, to another imaging method: modifying the set-up, we managed to create a spatial frequency domain imaging (SFDI) using the same camera and digital projector. The system that we have built, described in Chapter 8, has been used to measure skin modulation transfer function (MTF), a quantity that contains information about both skin scattering

and absorption coefficients. We have subsequently shown, using an original approach, how combining SFDI with HSI and optical analysis can be used as a method for estimating reduced scattering coefficient maps independently from irradiance drifts. We present in Chapter 9 preliminary results on a full face that are promising. This work can be interpreted as an initial proof of concept for the feasibility of the method and used to evaluate its relevance for applications in cosmetology. Presently, similar methods are used in the medical field, but as far as we know, no such equivalents exist in cosmetology. The design of a portable and relatively cheap system for applications in cosmetology could therefore significantly strengthen the services offered by the industrial partner of the project.

Certain limitations have been encountered. First of all, the efficacy of the analysis method is difficult to evaluate, as a ground truth value for the properties that we are estimating is difficult to obtain. Throughout this dissertation, we have therefore insisted on the fact that these maps of skin properties are estimated values using a given optical method, which itself relies on assumptions. Secondly, we have not been able to obtain satisfactory skin analysis results on dark-colored skin, especially in the estimation of oxygen rate maps. To address this shortcoming, the acquisition method would need to be perfected to yield a better noise-to-signal ratio for dark-colored skin. Finally, the implemented HSI system uses a technology which is now obsolete: the key component of the system, the VariSpecTM liquid crystal tunable filter, is no longer commercially available. Further development of the method therefore relies on finding an adequate substitute.

We have also often emphasized throughout the work the importance of short acquisition time for in vivo measurements, and designed the acquisition methods with this requirement in mind. The hyperspectral image analysis method, however, is extremely time-consuming in terms of computation time (1 hour for a small image and 5 hours for a full face image). A possible approach to reduce this duration is to train neural networks to replace the classical optimization-based analysis, which could drastically shorten computation time and allow for real time analysis. We have presented the findings of a preliminary study in this direction in Chapter 7. Initial results are promising: an analysis which would require 1 hour using the classical method has been reduced to 1 second using the neural network. Another possibility that could be explored using machine learning is to replace high resolution hyperspectral imaging with a slightly less well resolved multispectral imaging method. Such a system would have the advantage of being less expensive than hyperspectral imaging, with the loss of resolution compensated by machine learning methods.

Currently, the skin analysis method presented in this work is satisfactory for characterizing cosmetological products that affect melanin concentration or oxygen rate. The scope of applications of the method is relatively limited and has not yet been fully explored. It is imperative that their full scope is investigated in the near future.

Appendix 1: Reproduction of Figure 4.18 (page 82)

Image at 420 nm



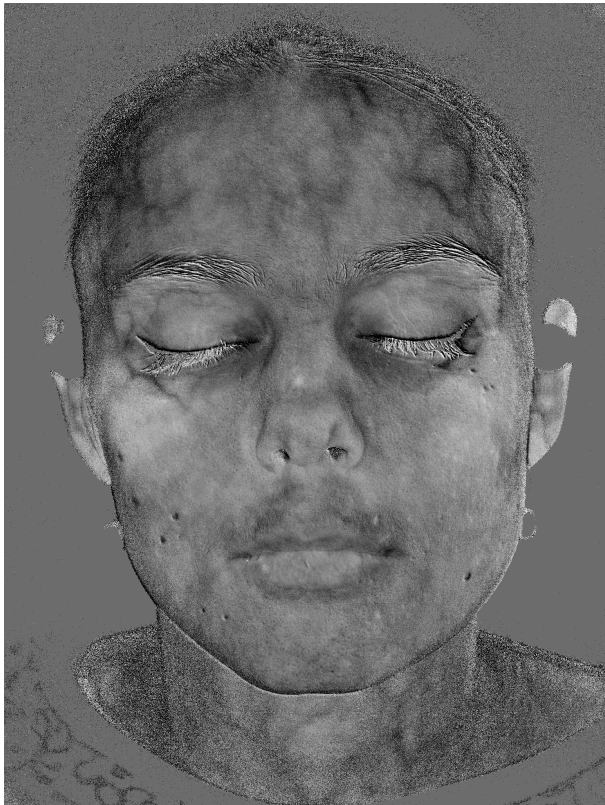
Image at 590 nm



Image at 700 nm



Color image

Appendix 2: Reproduction of Figure 7.5 (page 137)

Oxygen rate



Blood volume fraction



Melanin concentration



Reconstituted color image

Communications

Journal articles:

Lou Gevaux, Cyprien Adnet, Pierre Sérroul, Raphael Clerc, Alain Trémeau, Jean Luc Perrot, Mathieu Hébert, "Three-dimensional maps of human skin properties on full face with shadows using 3-D hyperspectral imaging," J. Biomed. Opt. 24(6) 066002 (June 2019).

Conferences with proceedings:

Lou Gevaux, Cyprien Adnet, Pierre Sérroul, Raphael Clerc, Alain Trémeau, Jean Luc Perrot, Mathieu Hébert, "Three-dimensional hyperspectral imaging: a new method for human face acquisition," Electronic Imaging. 2018 (January 2018).

Lou Gevaux, Marie Cherel, Pierre Sérroul, Raphael Clerc, Alain Trémeau, Mathieu Hébert, "Hyperspectral imaging and spatial frequency domain imaging: combined acquisition for full face skin analysis," Proc. SPIE 10881, Imaging, Manipulation, and Analysis of Biomolecules, Cells, and Tissues XVII, 108810P (March 2019).

Oral presentations:

Lou Gevaux, Pierre Sérroul, Raphael Clerc, Alain Trémeau, Mathieu Hébert, "Imagerie hyperspectrale grand champ appliquée à l'acquisition du visage humain et à l'analyse de la peau," GdR ISIS, Journée Co-conception : capteurs hybrides et algorithmes pour des systèmes innovants (November 2018).

Posters:

Lou Gevaux, Pierre Sérroul, Raphael Clerc, Alain Trémeau, Mathieu Hébert, "Three-dimensional maps of human skin properties on full face from 3-D hyperspectral imaging," Journées Jean-Paul Marty de la Société Française de Cosmétologie (December 2018).

Book chapters:

Pierre Sérroul, Lou Gevaux, Cyrielle Monpeurt, "La peau, apparence et propriétés optiques", in Quand la matière diffuse la lumière, Presse des Mines (2019).

In progress:

Lou Gevaux, Mathieu Hébert, Jean Luc Perrot, "Multispectral and Hyperspectral Imaging for skin acquisition and analysis," in Technology in Practical Dermatology - Non-Invasive Imaging, Lasers and Ulcer Management, Edited by Michele Fimiani, Pietro Rubegni and Elisa Cinotti. [Book chapter].

References

- [All3dp]. ALL3DP. 30 Best 3D Scanners of Spring 2019. <<https://all3dp.com/1/best-3d-scanner-diy-handheld-app-software/>>.
- [Applegate]. APPLGATE, M. <<https://OpenSFDI.org>>.
- [Bai et al. 2018]. BAI, C., LI, J., XU, Y., YUAN, H., AND LIU, J. Compact birefringent interferometer for Fourier transform hyperspectral imaging. *Optics Express* 26, 2, 1703. (2018)
- [Barron and Malik 2015]. BARRON, J.T. AND MALIK, J. Shape, Illumination, and Reflectance from Shading. *IEEE transactions on pattern analysis and machine intelligence* 37.8, 1670–1687. (2015)
- [Bintz et al. 2016]. Bintz, J.R., Mendenhall, M.J., Marciniak, M.A., Butler, S.D., and Lloyd, J.T. A novel image-based BRDF measurement system and its application to human skin. *Scattering, and Diffraction from Surfaces V*. Vol. 9961. International Society for Optics and Photonics. (2016)
- [Bjorgan et al. 2014].BJORGAN, A., MILANIC, M., AND RANDEBERG, L.L. Estimation of skin optical parameters for real-time hyperspectral imaging applications. *Journal of Biomedical Optics* 19, 6, 066003. (2014)
- [Blais 2004]. BLAIS, F. Review of 20 years of range sensor development. *Journal of Electronic Imaging* 13, 1, 231. (2004)
- [Bouguet]. BOUGUET, J.-Y. Camera calibration toolbox for MatLab. <http://www.vision.caltech.edu/bouguetj/calib_doc/>.
- [Bouguet 1729]. BOUGUET, P. *Essai d'optique sur la gradation de la lumiere [Optical essay on light gradation]*. Claude Jombert, Paris. (1729)
- [Branchet et al. 1991]. BRANCHET, M.C., BOISNIC, S., FRANCES, C., LESTY, C., AND ROBERT, L. Morphometric analysis of dermal collagen fibers in normal human skin as a function of age. *Archives of Gerontology and Geriatrics* 13, 1, 1–14. (1991)
- [Brauers et al. 2008]. BRAUERS, J., SCHULTE, N., AND AACH, T. Multispectral Filter-Wheel Cameras: Geometric Distortion Model and Compensation Algorithms. *IEEE Transactions on Image Processing* 17, 12, 2368–2380. (2008)
- [Bruulsema et al. 1997]. BRUULSEMA, J.T., HAYWARD, J.E., FARRELL, T.J., ET AL. Correlation between blood glucose concentration in diabetics and noninvasively measured tissue optical scattering coefficient. *Optics Letters* 22, 3, 190. (1997)
- [Calin et al. 2013]. CALIN, M.A., PARASCA, S.V., SAVASTRU, R., CALIN, M.R., AND DONTU, S. Optical techniques for the noninvasive diagnosis of skin cancer. *Journal of Cancer Research and Clinical Oncology* 139, 7, 1083–1104. (2013)
- [Calpe-Maravilla 2006]. CALPE-MARAVILLA, J. 400– to 1000–nm imaging spectrometer based on acousto-optic tunable filters. *Journal of Electronic Imaging* 15, 2, 023001.
- [Chandrasekhar 1943]. CHANDRASEKHAR, S. Stochastic problems in physics and astronomy. *Reviews of modern physics*. (1943)
- [Chandrasekhar 1960]. CHANDRASEKHAR, S. *Radiative transfer*. Dover Publications Inc., New York. (1960)
- [Chardon et al. 1991]. CHARDON, A., CRETOIS, I., AND HOURSEAU, C. Skin colour typology and suntanning pathways. *International Journal of Cosmetic Science* 13, 4, 191–208. (1991)
- [Cong et al. 2015]. CONG, P., XIONG, Z., ZHANG, Y., ZHAO, S., AND WU, F. Accurate Dynamic 3D Sensing With Fourier-Assisted Phase Shifting. *IEEE Journal of Selected Topics in Signal Processing* 9, 3, 396–408. (2015)

- [Cook and Torrance 1982]. COOK, R.L. AND TORRANCE, K.E. A Reflectance Model for Computer Graphics. *ACM Transactions on Graphics* 1, 1, 7–24. (1982)
- [Cucci et al. 2016]. CUCCI, C., DELANEY, J.K., AND PICOLLO, M. Reflectance Hyperspectral Imaging for Investigation of Works of Art: Old Master Paintings and Illuminated Manuscripts. *Accounts of Chemical Research* 49, 10, 2070–2079. (2016)
- [Cuccia et al. 2009]. CUCCIA, D.J., BEVILACQUA, F., DURKIN, A.J., AYERS, F.R., AND TROMBERG, B.J. Quantitation and mapping of tissue optical properties using modulated imaging. *Journal of Biomedical Optics* 14, 2, 024012. (2009)
- [Cuccia et al. 2005]. CUCCIA, D.J., BEVILACQUA, F., DURKIN, A.J., AND TROMBERG, B.J. Modulated imaging: quantitative analysis and tomography of turbid media in the spatial-frequency domain. *Optics Letters* 30, 11, 1354. (2005)
- [Debevec et al. 2000]. DEBEVEC, P., HAWKINS, T., TCHOU, C., DUIKER, H.P., SAROKIN, W., AND SAGAR, M. Acquiring the reflectance field of a human face. In *Proceedings of the 27th annual conference on Computer graphics and interactive techniques* (pp. 145-156). ACM Press/Addison-Wesley Publishing Co. (2000)
- [Deeb et al. 2019]. DEEB, R., VAN DE WEIJER, J., MUSELET, D., HEBERT, M., AND TREMEAU, A. Deep spectral reflectance and illuminant estimation from self-interreflections. *Journal of the Optical Society of America A* 36, 1, 105. (2019)
- [Del Bino et al. 2015]. DEL BINO, S., ITO, S., SOK, J., ET AL. Chemical analysis of constitutive pigmentation of human epidermis reveals constant eumelanin to pheomelanin ratio. *Pigment Cell & Melanoma Research* 28, 6, 707–717. (2015)
- [Dognits and Wagnières 1998]. DOGNITZ, N. AND WAGNIÈRES, G. Determination of tissue optical properties by steady-state spatial frequency-domain reflectometry. *Lasers in Medical Science* 13, 1, 55–65. (1998)
- [Doi et al. 2016]. DOI, M., KIMACHI, A., NISHI, S., AND TOMINAGA, S. Estimation of Local Skin Properties from Spectral Images and its Application to Appearance Reproduction. *Journal of Imaging Science and Technology* 60, 5, 504041–5040411. (2016)
- [Doi et al. 2019]. DOI, M., NISHIDA, N., KIMACHI, A., AND NISHI, S. Acquisition of 3D Data and Spectral Color by Using RGBD Camera and Programmable Light Source. *7th International Workshop*. (2019)
- [Doi et al. 2006]. DOI, M., OHTSUKI, R., AND TOMINAGA, S. Spectral estimation of made-up skin color under various conditions. In *Spectral Imaging: Eighth International Symposium on Multispectral Color Science* (Vol. 6062, p. 606204). International Society for Optics and Photonics. (2006)
- [Duempelmann et al. 2017]. DUEMPELMANN, L., GALLINET, B., AND NOVOTNY, L. Multispectral Imaging with Tunable Plasmonic Filters. *ACS Photonics* 4, 2, 236–241. (2017)
- [Egan et al. 1979]. EGAN, W.G. AND HILGEMAN, T.W. *Optical Properties of Inhomogeneous Materials*. New York Academic Press. (1979)
- [Elbaum et al. 2001]. ELBAUM, M., KOPF, A.W., RABINOVITZ, H.S., ET AL. Automatic differentiation of melanoma from melanocytic nevi with multispectral digital dermoscopy: A feasibility study. *Journal of the American Academy of Dermatology* 44, 2, 207–218. (2001)
- [Elias and Cotte 2008]. ELIAS, M. AND COTTE, P. 2008. Multispectral camera and radiative transfer equation used to depict Leonardo’s sfumato in Mona Lisa. *Applied Optics* 47, 12, 2146. (2008)
- [Erfanzadeh et al. 2018]. ERFANZADEH, M., NANDY, S., KUMAVOR, P.D., AND ZHU, Q. Low-cost compact multispectral spatial frequency domain imaging prototype for tissue characterization. *Biomedical Optics Express* 9, 11, 5503. (2018)
- [Forsyth and Zisserman 1989]. FORSYTH, D. AND ZISSERMAN, A. Mutual illumination. In *Proceedings CVPR’89: IEEE Computer Society Conference on Computer Vision and Pattern Recognition* (pp. 466-473). IEEE, 466–473. (1989)

- [Foschum et al. 2011]. FOSCHUM, F., JÄGER, M., AND KIENLE, A. Fully automated spatially resolved reflectance spectrometer for the determination of the absorption and scattering in turbid media. *Review of Scientific Instruments* 82, 10, 103104. (2011)
- [FOX 2002]. FOX, M. Optical properties of solids. AAPT. (2002)
- [Gardner and Dorling 1998]. GARDNER, M.W. AND DORLING, S.R. Artificial neural networks (the multilayer perceptron)—a review of applications in the atmospheric sciences. *Atmospheric Environment* 32, 14–15, 2627–2636. (1998)
- [Garini et al. 2006]. GARINI, Y., YOUNG, I.T., AND MCNAMARA, G. Spectral imaging: Principles and applications. *Cytometry Part A* 69A, 8, 735–747. (2006)
- [Gat 2000]. GAT, N. Imaging Spectroscopy Using Tunable Filters: A Review. 50–64. In *Wavelet Applications VII* (Vol. 4056, pp. 50–64). International Society for Optics and Photonics. (2000)
- [Geng 2011]. GENG, J. Structured-light 3D surface imaging: a tutorial. *Advances in Optics and Photonics* 3, 2, 128. (2011)
- [Gevaux et al. 2018]. GEVAUX, L., ADNET, C., SÉROUL, P., ET AL. Three-dimensional hyperspectral imaging: a new method for human face acquisition. *Electronic Imaging 2018*, 8, 152-1-152–10. (2018)
- [Gevaux et al. 2019a]. GEVAUX, L., ADNET, C., SEROUL, P., ET AL. Three-dimensional maps of human skin properties on full face with shadows using 3-D hyperspectral imaging. *Journal of Biomedical Optics* 24, 06, 1. (2019)
- [Gevaux et al. 2019b]. GEVAUX, L., CHEREL, M., SEROUL, P., CLERC, R., TRÉMEAU, A., AND HÉBERT, M. Hyperspectral imaging and spatial frequency domain imaging: combined acquisition for full face skin analysis. *Imaging, Manipulation, and Analysis of Biomolecules, Cells, and Tissues XVII*, SPIE, 24. (2019)
- [Ghiglia and Pritt 1998]. GHIGLIA, D.C. AND PRITT, M.D. *Two-dimensional phase unwrapping: theory, algorithms, and software*. Wiley New York. (1998)
- [Ghiglia and Romero 1994]. GHIGLIA, D.C. AND ROMERO, L.A. Robust two-dimensional weighted and unweighted phase unwrapping that uses fast transforms and iterative methods. *Journal of the Optical Society of America A* 11, 1, 107. (1994)
- [Gioux et al. 2019]. GIOUX, S., MAZHAR, A., AND CUCCIA, D.J. Spatial frequency domain imaging in 2019: principles, applications, and perspectives. *Journal of Biomedical Optics* 24, 07, 1. (2019)
- [Gioux et al. 2009]. GIOUX, S., MAZHAR, A., CUCCIA, D.J., DURKIN, A.J., TROMBERG, B.J., AND FRANGIONI, J.V. Three-dimensional surface profile intensity correction for spatially modulated imaging. *Journal of Biomedical Optics* 14, 3, 034045. (2009)
- [Goel et al. 2015]. GOEL, M., PATEL, S.N., WHITMIRE, E., ET AL. HyperCam: hyperspectral imaging for ubiquitous computing applications. *Proceedings of the 2015 ACM International Joint Conference on Pervasive and Ubiquitous Computing - UbiComp '15*, ACM Press, 145–156. (2015)
- [Gorthi and Rastogi 2010]. GORTHI, S.S. AND RASTOGI, P. Fringe projection techniques: Whither we are? *Optics and Lasers in Engineering* 48, 2, 133–140. (2010)
- [Grove et al. 1989]. GROVE, G.L., GROVE, M.J., AND LEYDEN, J.J. Optical profilometry: An objective method for quantification of facial wrinkles. *Journal of the American Academy of Dermatology* 21, 3, 631–637. (1989)
- [Gutiérrez-Gutiérrez et al. 2019]. GUTIÉRREZ-GUTIÉRREZ, J.A., PARDO, A., REAL, E., LÓPEZ-HIGUERA, J.M., AND CONDE, O.M. Custom Scanning Hyperspectral Imaging System for Biomedical Applications: Modeling, Benchmarking, and Specifications. *Sensors* 19, 7, 1692. (2019)
- [Hagen and Kudenov 2013]. HAGEN, N. AND KUDENOV, M.W. Review of snapshot spectral imaging technologies. *Optical Engineering* 52, 9, 090901. (2013)

- [Haskell et al. 1994]. HASKELL, R.C., SVAASAND, L.O., TSAY, T.-T., FENG, T.-C., TROMBERG, B.J., AND MCADAMS, M.S. Boundary conditions for the diffusion equation in radiative transfer. *Journal of the Optical Society of America A* 11, 10, 2727. (1994)
- [Hatzis 2004]. HATZIS, J. The wrinkle and its measurement. *Micron* 35, 3, 201–219. (2004)
- [Hébert et al. 2014]. HÉBERT, M., HERSCH, R.D., AND EMMEL, P. Fundamentals of Optics and Radiometry for Color Reproduction. In: M. Kriss, ed., *Handbook of Digital Imaging*. John Wiley & Sons, Ltd, Chichester, UK, 1–57. (2014)
- [Henyey and Greenstein 1941]. HENYEY, L.G. AND GREENSTEIN, J.L. Diffuse radiation in the Galaxy. *Astrophysical Journal* 93, 70–83. (1941)
- [Herakleous and Poullis]. HERAKLEOUS, K. AND POULLIS, C. FabScan open source 3D laser scanner. <<https://mariolukas.github.io/FabScanPi-Server/>>.
- [Hirai et al. 2016]. HIRAI, K., NAKAHATA, R., AND HORIUCHI, T. Measuring Spectral Reflectance and 3D Shape Using Multi-primary Image Projector. In: A. Mansouri, F. Nouboud, A. Chalifour, D. Mammass, J. Meunier and A. Elmoataz, eds., *Image and Signal Processing*. Springer International Publishing, Cham, 137–147. (2016)
- [Hirose et al. 2016]. HIROSE, M., AKAHO, R., MAITA, C., SUGAWARA, M., AND TSUMURA, N. Optimization of spectral sensitivities of mosaic five-band camera for estimating chromophore densities from skin images including shading and surface reflections. *Optical Review* 23, 3, 544–548. (2016)
- [Hofmann-Wellenhof et al. 2012]. HOFMANN-WELLENHOF, R., PELLACANI, G., MALVEHY, J., AND SOYER, H.P. *Reflectance confocal microscopy for skin diseases*. Springer Science & Business Media. (2012)
- [Igarashi et al. 2007]. IGARASHI, T., NISHINO, K., AND NAYAR, S.K. The Appearance of Human Skin: A Survey. *Foundations and Trends® in Computer Graphics and Vision* 3, 1, 1–95. (2007)
- [Iglesias-Guitian et al. 2015]. IGLESIAS-GUITIAN, J.A., ALIAGA, C., JARABO, A., AND GUTIERREZ, D. A Biophysically-Based Model of the Optical Properties of Skin Aging. *Computer Graphics Forum* 34, 2, 45–55. (2015)
- [Ioffe and Szegedy 2015]. IOFFE, S. AND SZEGEDY, C. Batch Normalization: Accelerating Deep Network Training by Reducing Internal Covariate Shift. *arXiv:1502.03167 [cs]*. (2015)
- [Ishimaru 1978]. ISHIMARU, A. *Wave propagation and scattering in random media, single scattering and transport theory*. New York: Academic Press. (1978)
- [Islam et al. 2017]. ISLAM, K., PLOSCHNER, M., AND GOLDDYS, E.M. Multi-LED light source for hyperspectral imaging. *Optics Express* 25, 26, 32659. (2017)
- [ISO/CIE 1999]. ISO/CIE. *CIE standard illuminant for colorimetry*. ISO/CIE. (1999)
- [Jacques 1996]. JACQUES, S.L. Origins of tissue optical properties in the UVA, visible, and NIR regions. *OSA TOPS on advances in optical imaging and photon migration* 2, 364–369. (1996)
- [JACQUES 2013]. JACQUES, S.L. Optical properties of biological tissues: a review. *Physics in Medicine and Biology* 58, 11, R37–R61. (2013)
- [JACQUES]. JACQUES, S.L. <<https://omlc.org/spectra/melanin/>>.
- [Jäger et al. 2013]. JÄGER, M., FOSCHUM, F., AND KIENLE, A. Application of multiple artificial neural networks for the determination of the optical properties of turbid media. *Journal of Biomedical Optics* 18, 5, 057005. (2013)
- [Jain et al. 1996]. JAIN, A.K., MAO, J., AND MOHIUDDIN, K.M. Artificial Neural Networks: A Tutorial. *Computer* 3, 31–44. (1996)
- [Jensen et al. 2001]. JENSEN, H.W., MARSCHNER, S.R., LEVOY, M., AND HANRAHAN, P. A practical model for subsurface light transport. *Proceedings of the 28th annual conference on Computer graphics and interactive techniques - SIGGRAPH '01*, ACM Press, 511–518. (2001)
- [Jia et al. 2007]. JIA, P., KOFMAN, J., AND ENGLISH, C. Comparison of linear and nonlinear calibration methods for phase-measuring profilometry. *Optical Engineering* 46, 4, 043601. (2007)

- [Jolivot et al. 2013]. JOLIVOT, R., BENEZETH, Y., AND MARZANI, F. Skin Parameter Map Retrieval from a Dedicated Multispectral Imaging System Applied to Dermatology/Cosmetology. *International Journal of Biomedical Imaging* 2013, 1–15. (2013)
- [Jonasson et al. 2018]. JONASSON, H., FREDRIKSSON, I., BERGSTRAND, S., ÖSTGREN, C.J., LARSSON, M., AND STRÖMBERG, T. In vivo characterization of light scattering properties of human skin in the 475- to 850-nm wavelength range in a Swedish cohort. *Journal of Biomedical Optics* 23, 12, 1. (2018)
- [Jullien et al. 2017]. JULLIEN, A., PASCAL, R., BORTOLOZZO, U., FORGET, N., AND RESIDORI, S. High-resolution hyperspectral imaging with cascaded liquid crystal cells. *Optica* 4, 4, 400. (2017)
- [Kainerstorfer et al. 2010]. KAINERSTORFER, J.M., AMYOT, F., EHLER, M., ET AL. Direct curvature correction for noncontact imaging modalities applied to multispectral imaging. *Journal of Biomedical Optics* 15, 4, 046013. (2010)
- [Kienle et al. 1998]. KIENLE, A., PATTERSON, M.S., DÖGNITZ, N., BAYS, R., WAGNIÈRES, G., AND VAN DEN BERGH, H. Noninvasive determination of the optical properties of two-layered turbid media. *Applied Optics* 37, 4, 779. (1998)
- [Kim 2013]. KIM, M.H. 3D Graphics Techniques for Capturing and Inspecting Hyperspectral Appearance. *2013 International Symposium on Ubiquitous Virtual Reality*, IEEE, 15–18. (2013)
- [Kitware]. KITWARE. The Visual Toolkit. <<https://www.vtk.org/>>.
- [Koenig et al. 2015]. KOENIG, A., ROIG, B., LE DIGABEL, J., JOSSE, G., AND DINTEN, J.M. Accessing deep optical properties of skin using diffuse reflectance spectroscopy. In *European Conference on Biomedical Optics* (p. 95370E). Optical Society of America. (2015)
- [Kubelka 1954]. KUBELKA, P. New Contributions to the Optics of Intensely Light-Scattering Materials Part II: Nonhomogeneous Layers*. *Journal of the Optical Society of America* 44, 4, 330. (1954)
- [Kubelka and Munk 1931]. KUBELKA, P. AND MUNK, F. An Article on Optics of Paint Layers. *Z. Tech. Phys*, 12 (593-601). (1931)
- [Kupetsky and Ferris 2013]. KUPETSKY, E.A. AND FERRIS, L.K. The diagnostic evaluation of MelaFind multi-spectral objective computer vision system. *Expert Opinion on Medical Diagnostics* 7, 4, 405–411. (2013)
- [Lanman and Taubin 2009]. LANMAN, D. AND TAUBIN, G. Build your own 3D scanner: 3D photography for beginners. *ACM SIGGRAPH 2009 Courses on - SIGGRAPH '09*, ACM Press, 1–94. (2009)
- [Li et al. 2012]. LI, H., FENG, J., YANG, W., ET AL. Multi-spectral imaging using LED illuminations. *2012 5th International Congress on Image and Signal Processing*, IEEE, 538–542. (2012)
- [Li et al. 2013]. LI, Q., HE, X., WANG, Y., LIU, H., XU, D., AND GUO, F. Review of spectral imaging technology in biomedical engineering: achievements and challenges. *Journal of Biomedical Optics* 18, 10, 100901. (2013)
- [Li and Li 2011]. LI, Z. AND LI, Y. Gamma-distorted fringe image modeling and accurate gamma correction for fast phase measuring profilometry. *Optics Letters* 36, 2, 154. (2011)
- [Liang 2012]. LIANG, H. Advances in multispectral and hyperspectral imaging for archaeology and art conservation. *Applied Physics A* 106, 2, 309–323. (2012)
- [Lorente et al. 2012]. LORENTE, D., ALEIXOS, N., GÓMEZ-SANCHIS, J., CUBERO, S., GARCÍA-NAVARRETE, O.L., AND BLASCO, J. Recent Advances and Applications of Hyperspectral Imaging for Fruit and Vegetable Quality Assessment. *Food and Bioprocess Technology* 5, 4, 1121–1142. (2012)
- [Lu et al. 2017]. LU, F., HE, L., YOU, S., CHEN, X., AND HAO, Z. Identifying Surface BRDF From a Single 4-D Light Field Image via Deep Neural Network. *IEEE Journal of Selected Topics in Signal Processing* 11, 7, 1047–1057. (2017)
- [Lu and Fei 2014]. LU, G. AND FEI, B. Medical hyperspectral imaging: a review. *Journal of Biomedical Optics* 19, 1, 010901. (2014)

- [Magnain 2009]. MAGNAIN, C. *Modélisation de la couleur de la peau et sa représentation dans les œuvres d'art*. PhD diss. (2009)
- [Magnain et al. 2007]. MAGNAIN, C., ELIAS, M., AND FRIGERIO, J.-M. Skin color modeling using the radiative transfer equation solved by the auxiliary function method. *Journal of the Optical Society of America A* 24, 8, 2196. (2007)
- [Manley 2014]. MANLEY, M. Near-infrared spectroscopy and hyperspectral imaging: non-destructive analysis of biological materials. *Chem. Soc. Rev.* 43, 24, 8200–8214. (2014)
- [Marschner et al. 1999b]. MARSCHNER, S.R., WESTIN, S.H., LAFORTUNE, E.P.F., TORRANCE, K.E., AND GREENBERG, D.P. Reflectance Measurements of Human Skin. (1999)
- [Marschner et al. 1999a]. MARSCHNER, S.R., WESTIN, S.H., LAFORTUNE, E.P.F., TORRANCE, K.E., AND GREENBERG, D.P. Image-Based BRDF Measurement Including Human Skin. In *Rendering Techniques' 99* (pp. 131-144). Springer, Vienna (1999)
- [Matts et al. 2007]. MATTS, P.J., FINK, B., GRAMMER, K., AND BURQUEST, M. Color homogeneity and visual perception of age, health, and attractiveness of female facial skin. *Journal of the American Academy of Dermatology* 57, 6, 977–984. (2007)
- [Mazhar et al. 2014]. MAZHAR, A., SAGGESE, S., POLLINS, A.C., CARDWELL, N.L., NANNEY, L., AND CUCCIA, D.J. Noncontact imaging of burn depth and extent in a porcine model using spatial frequency domain imaging. *Journal of Biomedical Optics* 19, 8, 086019. (2014)
- [McCluney 1994]. MCCLUNEY, R. Introduction to Radiometry and Photometry. *Artech House*. (1994)
- [McCulloch and Pitts 1943]. MCCULLOCH, W.S. AND PITTS, W. A logical calculus of the ideas immanent in nervous activity. *The bulletin of mathematical biophysics* 5, 4, 115–133. (1943)
- [Meglinski and Matcher 2003]. MEGLINSKI, I.V. AND MATCHER, S.J. Computer simulation of the skin reflectance spectra. *Computer Methods and Programs in Biomedicine* 70, 2, 179–186. (2003)
- [Mie 1908]. MIE, G. Beiträge zur Optiktrübe Medien, speziell kolloidaler Metallösungen. *Annalen der Physik*, 377–445. (1908)
- [Moeller et al. 2015]. MOELLER, M., BENNING, M., SCHONLIEB, C., AND CREMERS, D. Variational Depth From Focus Reconstruction. *IEEE Transactions on Image Processing* 24, 12, 5369–5378. (2015)
- [Moncrieff et al. 2002]. MONCRIEFF, M., COTTON, S., CLARIDGE, E., AND HALL, P. Spectrophotometric intracutaneous analysis: a new technique for imaging pigmented skin lesions. *British Journal of Dermatology* 146, 3, 448–457. (2002)
- [Monheit et al. 2011]. MONHEIT, G., COGNETTA, A.B., FERRIS, L., ET AL. The Performance of MelaFind: A Prospective Multicenter Study. *Archives of Dermatology* 147, 2, 188. (2011)
- [Moreno and Taubin 2012]. MORENO, D. AND TAUBIN, G. Simple, Accurate, and Robust Projector-Camera Calibration. *2012 Second International Conference on 3D Imaging, Modeling, Processing, Visualization & Transmission*, IEEE, 464–471. (2012)
- [Musnier et al. 2004]. MUSNIER, C., PIQUEMAL, P., BEAU, P., AND PITTET, J.C. Visual evaluation in vivo of “complexion radiance” using the C.L.B.T.tm sensory methodology. *Skin Research and Technology* 10, 1, 50–56. (2004)
- [Newton et al. 2017]. NEWTON, V.L., BRADLEY, R.S., SEROUL, P., ET AL. Novel approaches to characterize age-related remodelling of the dermal-epidermal junction in 2D, 3D and *in vivo*. *Skin Research and Technology* 23, 2, 131–148. (2017)
- [Nguyen et al. 2012]. NGUYEN, T.T.A., LE, H.N.D., VO, M., WANG, Z., LUU, L., AND RAMELLA-ROMAN, J.C. Three-dimensional phantoms for curvature correction in spatial frequency domain imaging. *Biomedical Optics Express* 3, 6, 1200. (2012)
- [Nickell et al. 2000]. NICKELL, S., HERMANN, M., ESSENPREIS, M., FARRELL, T.J., KRÄMER, U., AND PATTERSON, M.S. Anisotropy of light propagation in human skin. *Physics in Medicine and Biology* 45, 10, 2873–2886. (2000)

- [Nicodemus et al. 1977]. NICODEMUS, F.E., RICHMOND, J.C., HSIA, J.J., GINSBERG, I.W., AND LIMPERIS, T. *Geometrical considerations and nomenclature for reflectance*. National Bureau of Standards, Gaithersburg, MD. (1977)
- [Nielsen et al. 2017]. NIELSEN, J.B., STETS, J.D., LYNGBY, R.A., AANAS, H., DAHL, A.B., AND FRISVAD, J.R. A Variational Study on BRDF Reconstruction in a Structured Light Scanner. *2017 IEEE International Conference on Computer Vision Workshops (ICCVW)*, IEEE, 143–152. (2017)
- [Nishidate et al. 2004]. NISHIDATE, I., AIZU, Y., AND MISHINA, H. Estimation of melanin and hemoglobin in skin tissue using multiple regression analysis aided by Monte Carlo simulation. *Journal of Biomedical Optics* 9, 4, 700. (2004)
- [Nkengne et al. 2018]. NKENGNE, A., ROBIC, J., SEROUL, P., GUEHEUNNEUX, S., JOMIER, M., AND VIE, K. SpectraCam[®]: A new polarized hyperspectral imaging system for repeatable and reproducible in vivo skin quantification of melanin, total hemoglobin, and oxygen saturation. *Skin Research and Technology* 24, 1, 99–107. (2018)
- [Ohsaki et al. 2017]. OHSAKI, M., NAGAHARA, H., IKEDA, T., AND TANIGUCHI, R.I. Hyperspectral imaging using flickerless active LED illumination. *Thirteenth International Conference on Quality Control by Artificial Vision 2017* (Vol. 10338, p. 103380Z). International Society for Optics and Photonics. (2017)
- [Panigrahi and Gioux 2018]. PANIGRAHI, S. AND GIOUX, S. Machine learning approach for rapid and accurate estimation of optical properties using spatial frequency domain imaging. *Journal of Biomedical Optics* 24, 07, 1. (2018)
- [Paquit et al. 2008]. PAQUIT, V.C., MERIAUDEAU, F., PRICE, J.R., AND TOBIN, K.W. Simulation of skin reflectance images using 3D tissue modeling and multispectral Monte Carlo light propagation. *30th Annual International Conference of the IEEE Engineering in Medicine and Biology Society*, IEEE, 447–450. (2008)
- [Paquit et al. 2009]. PAQUIT, V.C., TOBIN, K.W., PRICE, J.R., AND MERIAUDEAU, F. 3D and Multispectral Imaging for Subcutaneous Veins Detection. *Optics express* 17.14 (2009): 11360–11365. (2009)
- [Pham et al. 2000]. PHAM, T.H., BEVILACQUA, F., SPOTT, T., DAM, J.S., TROMBERG, B.J., AND ANDERSSON-ENGELS, S. Quantifying the absorption and reduced scattering coefficients of tissuelike turbid media over a broad spectral range with noncontact Fourier-transform hyperspectral imaging. *Applied Optics* 39, 34, 6487. (2000)
- [Phong 1975]. PHONG, B.T. Illumination for computer generated pictures. *Communications of the ACM* 18, 6, 311–317. (1975)
- [Poh et al. 2010]. POH, M.-Z., MCDUFF, D.J., AND PICARD, R.W. Non-contact, automated cardiac pulse measurements using video imaging and blind source separation. *Optics Express* 18, 10, 10762. (2010)
- [Pottier et al. 2019]. POTTIER, F., MICHELIN, A., KWIMANG, S., ANDRAUD, C., GOUBARD, F., AND LAVÉDRINE, B. Macroscopic reflectance spectral imaging to reveal multiple and complementary types of information for the non-invasive study of an entire polychromatic manuscript. *Journal of Cultural Heritage* 35, 1–15. (2019)
- [Prahl]. PRAHL, S. <<https://omlc.org/spectra/hemoglobin/>>.
- [Rayleigh 1871]. RAYLEIGH, L.J.S. On light from the sky, its polarization and colour. *Philosophical Magazine*, 107–120. (1871)
- [Remondino and El-Hakim 2006]. REMONDINO, F. AND EL-HAKIM, S. Image-based 3D Modelling: A Review: Image-based 3D modelling: a review. *The Photogrammetric Record* 21, 115, 269–291. (2006)
- [Rosenblatt 1958]. ROSENBLATT, F. The perceptron: a probabilistic model for information storage and organization in the brain. *Psychological review* 65.6, 386. (1958)

- [Saint-Pierre et al. 2018]. SAINT-PIERRE, D., DEEB, R., MUSELET, D., SIMONOT, L., AND HÉBERT, M. Light Interreflections and Shadowing Effects in a Lambertian V-Cavity under Diffuse Illumination. *Electronic Imaging 2018*, 8, 166-1-166-10. (2018)
- [Saunderson 1942]. SAUNDERSON, J.L. Calculation of the Color of Pigmented Plastics. *J. Opt. Soc. Am* 32, 727-736. (1942)
- [Schmitt et al. 1990]. SCHMITT, J.M., WALL, R.T., ZHOU, G.X., AND WALKER, E.C. Multilayer model of photon diffusion in skin. *Journal of the Optical Society of America A* 7, 11, 2141. (1990)
- [Seroul et al. 2017]. SEROUL, P., HÉBERT, M., CHEREL, M., VERNET, R., CLERC, R., AND JOMIER, M. Model-based Skin Pigment Cartography by High-Resolution Hyperspectral Imaging. *Journal of Imaging Science and Technology* 60 (6), 60404-1. (2017)
- [Setiadi and Nasution 2019]. SETIADI, I.C. AND NASUTION, A.M.T. Reconstruction hyperspectral reflectance cube based on artificial neural networks for multispectral imaging system applied to dermatology. *Third International Seminar on Photonics, Optics, and Its Applications (ISPhOA 2018)* (Vol. 11044, p. 110440G). International Society for Optics and Photonics. (2019)
- [Sole et al. 2018]. SOLE, A., FARUP, I., NUSSBAUM, P., AND TOMINAGA, S. Bidirectional Reflectance Measurement and Reflection Model Fitting of Complex Materials Using an Image-Based Measurement Setup. *Journal of Imaging* 4, 11, 136. (2018)
- [Thennadil 2008]. THENNADIL, S.N. Relationship between the Kubelka-Munk scattering and radiative transfer coefficients. *Journal of the Optical Society of America A* 25, 7, 1480. (2008)
- [Tomatis et al. 2005]. TOMATIS, S., CARRARA, M., BONO, A., ET AL. Automated melanoma detection with a novel multispectral imaging system: results of a prospective study. *Physics in Medicine and Biology* 50, 8, 1675-1687. (2005)
- [Torrance and Sparrow 1967]. TORRANCE K.E. AND SPARROW E.M. Theory for Off-Specular Reflection From Roughened Surfaces*. *Journal of the Optical Society of America* 57, 9, 1105. (1967)
- [Varani et al. 2006]. VARANI, J., DAME, M.K., RITTIE, L., ET AL. Decreased Collagen Production in Chronologically Aged Skin. *The American Journal of Pathology* 168, 6, 1861-1868. (2006)
- [Vidovič et al. 2015]. VIDOVIČ, L., MILANIČ, M., RANDEBERG, L.L., AND MAJARON, B. Quantitative characterization of traumatic bruises by combined pulsed photothermal radiometry and diffuse reflectance spectroscopy. *Photonic Therapeutics and Diagnostics XI* (Vol. 9303, p. 930307). International Society for Optics and Photonics. (2015)
- [Wang et al. 1994]. WANG, L., ZHAO, X., AND JACQUES, S.L. Computation of the optical properties of tissues from light reflectance using a neural network. *Laser-Tissue Interaction V; and Ultraviolet Radiation Hazards*, International Society for Optics and Photonics, 391-400. (1994)
- [Wang et al. 2013]. WANG, Y., LAUGHNER, J.I., EFIMOV, I.R., AND ZHANG, S. 3D absolute shape measurement of live rabbit hearts with a superfast two-frequency phase-shifting technique. *Optics Express* 21, 5, 5822. (2013)
- [Weber et al. 2006]. WEBER, J.R., CUCCIA, D.J., AND TROMBERG, B.J. Modulated imaging in layered media. *2006 International Conference of the IEEE Engineering in Medicine and Biology Society*, IEEE, 6674-6676. (2006)
- [Werbos 1974]. WERBOS, P. Beyond Regression: New Tools for Prediction and Analysis in the Behavioral Sciences. PhD diss. (1974)
- [Westhäuser et al. 2008]. WESTHÄUSER, M., BISCHOFF, G., BÖRÖCZ, Z., KLEINHEINZ, J., VON BALLY, G., AND DIRKSEN, D. Optimizing color reproduction of a topometric measurement system for medical applications. *Medical Engineering & Physics* 30, 8, 1065-1070. (2008)
- [Wilson and Jacques 1990]. WILSON, B.C. AND JACQUES, S.L. Optical reflectance and transmittance of tissues: principles and applications. *IEEE Journal of Quantum Electronics* 26, 12, 2186-2199. (1990)

- [Wirkert et al. 2016]. WIRKERT, S.J., KENNGOTT, H., MAYER, B., ET AL. Robust near real-time estimation of physiological parameters from megapixel multispectral images with inverse Monte Carlo and random forest regression. *International Journal of Computer Assisted Radiology and Surgery* 11, 6, 909–917. (2016)
- [Wu et al. 2012]. WU, H.-Y., RUBINSTEIN, M., SHIH, E., GUTTAG, J., DURAND, F., AND FREEMAN, W. Eulerian video magnification for revealing subtle changes in the world. *ACM Transactions on Graphics* 31, 4, 1–8. (2012)
- [Wyszecki and Stiles 1982]. WYSZECKI, G. AND STILES, W.S. *Color science: concepts and methods, quantitative data and formulae, 2nd ed.* Wiley New York. (1982)
- [Yalla and Hassebrook 2005]. YALLA, V.G. AND HASSEBROOK, L.G. Very high resolution 3D surface scanning using multi-frequency phase measuring profilometry. *Spaceborne Sensors II* (Vol. 5798, pp. 44-53). International Society for Optics and Photonics. (2005)
- [Yang and Bai 2012]. YANG, J. AND BAI, G. Finger-vein image restoration based on skin optical property. *2012 IEEE 11th International Conference on Signal Processing*, IEEE, 749–752. (2012)
- [Yuhas et al. 1992]. YUHAS, R., GOETZ, A., AND BOARDMAN, J. Discrimination among semiarid landscape endmembers using the spectral angle mapper (sam) algorithm. JPL Publication, 147–149. (1992)
- [Zhang et al. 2016]. ZHANG, C., ROSENBERGER, M., BREITBARTH, A., AND NOTNI, G. A novel 3D multispectral vision system based on filter wheel cameras. *2016 IEEE International Conference on Imaging Systems and Techniques (IST)*, IEEE, 267–272. (2016)
- [Zhang and Huang 2006]. ZHANG, S. AND HUANG, P.S. Novel method for structured light system calibration. *Optical Engineering* 45, 8, 083601. (2006)
- [Zhand et al. 2017]. ZHANG, S. AND HUANG, P.S. Phase error compensation for a 3-D shape measurement system based on the phase-shifting method. *Optical Engineering* 46, 9. (2017)
- [Zhang and Yau 2006]. ZHANG, S. AND YAU, S.-T. High-resolution, real-time 3D absolute coordinate measurement based on a phase-shifting method. *Optics Express* 14, 7, 2644. (2006)
- [Zheng et al. 2007]. ZHENG, Y., CHANG, J., ZHENG, Z., AND WANG, Z. 3D Face Reconstruction from Stereo: A Model Based Approach. *2007 IEEE International Conference on Image Processing*, IEEE, III-65-III-68. (2007)
- [Zherebtsov et al. 2019]. ZHEREBTSOV, E., DREMIN, V., POPOV, A., ET AL. Hyperspectral imaging of human skin aided by artificial neural networks. *Biomedical Optics Express* 10, 7, 3545. (2019)
- [Zhu and Liu 2013]. ZHU, C. AND LIU, Q. Review of Monte Carlo modeling of light transport in tissues. *Journal of Biomedical Optics* 18, 5, 050902. (2013)
- [Zonios and Dimou 2006]. ZONIOS, G. AND DIMOU, A. Modeling diffuse reflectance from semi-infinite turbid media: application to the study of skin optical properties. *Optics Express* 14, 19, 8661. (2006)
- [Zuo et al. 2016]. ZUO, C., HUANG, L., ZHANG, M., CHEN, Q., AND ASUNDI, A. Temporal phase unwrapping algorithms for fringe projection profilometry: A comparative review. *Optics and Lasers in Engineering* 85, 84–103. (2016)